UNIVERSITY OF SOUTHAMPTON
FACULTY OF PHYSICAL AND APPLIED SCIENCES
OPTOELECTRONICS RESEARCH CENTRE

All-Optical Signal Processing using Cascaded Quadratic Interactions in Periodically Poled Lithium Niobate Waveguides

by

Sheng Liu

Thesis for the degree of Doctor of Philosophy
January 2012

UNIVERSITY OF SOUTHAMPTON

ABSTRACT

FACULTY OF PHYSICAL AND APPLIED SCIENCES
OPTOELECTRONICS RESEARCH CENTRE

Doctor of Philosophy

ALL-OPTICAL SIGNAL PROCESSING USING CASCADED QUADRATIC INTERACTIONS IN PERIODICALLY POLED LITHIUM NIOBATE WAVEGUIDES

by Sheng Liu

This thesis investigates all-optical signal processing using cascaded quadratic nonlinearities in periodically poled lithium niobate (PPLN) waveguides for telecommunication applications. PPLN waveguides which possess high second-order nonlinearity are attractive due to their suitable properties with respect to high compactness, high operating speed and resistance to parasitic effects. They allow the implementation of various advanced signal processing functionalities which will be required in future ultrahigh speed fibre-optic communication systems.

Several novel all-optical signal processing techniques relying on two types of cascaded quadratic processes in PPLN waveguides, namely cascaded second harmonic generation and difference frequency generation (cSHG/DFG) and cascaded sum frequency generation and difference frequency generation (cSFG/DFG), are demonstrated. These two processes are conventionally employed for wavelength conversion in the telecommunication band. To facilitate the use of these wavelength converters, a systematic study of the acceptance bandwidths of cSHG/DFG and cSFG/DFG in PPLN waveguides is presented. Following this study, an optical time-division-multiplexing to wavelength-division multiplexing format conversion scheme, which relies on the generation of linearly chirped pulses which are then optically switched with data pulses using cSHG/DFG in a PPLN waveguide, is demonstrated. Signal regeneration techniques exploiting cascaded quadratic nonlinearities in PPLN waveguides are also investigated. An all-optical signal retiming system for on-off keying signals relying on pulse shaping and cSHG/DFG-based switching in a PPLN waveguide is demonstrated. Subsequently, two novel configurations of PPLN-based phase sensitive amplifiers (PSA) which have the potential as regenerators for phase-shift keying signals are demonstrated. Finally, a novel method for the elimination of arbitrary frequency chirp from short optical pulses is presented.

In addition, the thesis contains a study on the use of OFCGs as telecommunication sub-picosecond pulse sources. Both a theoretical and experimental study of the intensity and phase properties of the pulses generated by an OFCG is presented. Furthermore, two approaches are proposed to compensate for the intrinsic chirp of the OFCGs.

Contents

List of Figures

Declaration of Authorship

I, Sheng Liu, declare that this thesis titled, 'All-Optical Signal Processing in Periodically Poled Lithium Niobate' and the work presented in the thesis are both my own, and have been generated by me as the result of my own original research. I confirm that:

- this work was done wholly or mainly while in candidature for a research degree at this University;
- where any part of this thesis has previously been submitted for a degree or any other qualification at this University or any other institution, this has been clearly stated;
- where I have consulted the published work of others, this is always clearly attributed;
- where I have quoted from the work of others, the source is always given. With the exception of such quotations, this thesis is entirely my own work;
- I have acknowledged all main sources of help;
- where the thesis is based on work done by myself jointly with others, I have made clear exactly what was done by others and what I have contributed myself;
- parts of this work have been published as listed in appendix List of Publications.

Signed:

Date:

Acknowledgements

Firstly, a very special thank to my PhD. supervisor Dr. Periklis Petropolous, for all his efforts in supervising, supporting and encouraging me. I could not imagine having a better supervisor for my PhD. Periklis does not only teach me academically, but also influences me with his personality. He is very nice, likes to give others as much support as he can, and always keeps smile to his students. However when starting to discuss the technical problems, his face sometimes turns serious at once. He is so dedicated to research and very responsible for his students. I feel very lucky to have him as my PhD supervisor. Finally, I would like to say sorry for my English, thanks for your great patience.

I also would like to thank Prof. David Richardson. He is very knowledgable, very social, and so easy to talk to. Although he is a famous and busy professor, he still has time for every student and likes to take care of every student, unbelievable. I clearly remember that every time I gave a presentation in a conference, he always appeared in the hall on time, no matter whether my presentation was important and how early my presentation was held. Having a chance to study in his group makes these four years unique and unforgettable.

This thesis would not appear here without the kind assistance and support of my ORC colleagues. Dr. Kwang Jo Lee who led me onto the way and accompanied me during the whole PhD. Dr. Francesca Parmigiani for her initial guidance to the group and the labs. Dr Katia Gallo who is the final saver of the project. Dr. Trina Ng who taught me how to use FROG. Joseph Kakande with who we fighted together for the experiment results to meet the deadline of the conference. Dr. Radan Slavik who is very knowledgable in this area and always gives me helpful comments. Dr. Angela Camerlingo, who helped me a lot at the beginning of my project. I also would like to give my thanks to Eric and Dr. Yongjun Ying who gave me great help during my thesis writing. Also Eve Smith, Kevin Sumner and David Oliver who gave me various supports during my PhD.

Thanks my parents, for the consistent support throughout my PhD.

Finally, thanks for the ORC scholarship.

Abbreviations

ASE	**A**mplified **S**pontaneous **E**mission
AWG	**A**rrayed **W**aveguide **G**rating
BER	**B**it-**E**rror **R**ate
BPF	**B**and **P**ass **F**ilter
BPM	**B**irefringent **P**hase **M**atching
BPSK	**B**ipolar **P**hase **S**hift **K**eying
cSFG/DFG	cascaded **S**um **F**requency **G**eneration and **D**ifference **F**requency **G**eneration
cSHG/DFG	cascaded **S**econd **H**armonic **G**eneration and **D**ifference **F**requency **G**eneration
CSRZ	**C**arrier-**S**uppressed **R**eturn to **Z**ero
CW	**C**ontinuous **W**ave
DCF	**D**ispersion **C**ompensating **F**ibre
DF	**D**ifference **F**requency
DFG	**D**ifference **F**requency **G**eneration
DPSK	**D**ifferential **P**hase **S**hift **K**eying
EDFA	**E**rbium-**D**oped **F**ibre **A**mplifier
EOM	**E**lectro-**O**ptic **M**odulator
ERGO	**ER**bium **G**lass **O**scillator
ETDM	**E**lectrical **T**ime **D**ivision **M**ultiplexing
FBG	**F**ibre **B**ragg **G**rating
FF	**F**undamental **F**requency
FP	**F**abry **P**erot
FROG	**F**requency-**R**esolved **O**ptical **G**ating

FSR	**F**ree **S**pectral **R**ange
FWM	**F**our **W**ave **M**ixing
FWHM	**F**ull **W**idth at **H**alf-**M**aximum
GSL	**G**ain **S**witched **L**aser
GVD	**G**roup-**V**elocity **D**ispersion
GVM	**G**roup-**V**elocity **M**ismatch
HNLF	**H**ighly **N**on**L**inear Optical **F**ibre
IFWM	**I**ntrachennel **F**our **W**ave textbfMixng
IGVD	**I**ntra-pulse **G**roup-**V**elocity **D**ispersion
ISI	**I**nter**S**ymbol **I**nterference
IXPM	**I**ntrachannel **C**ross **P**hase **M**odulation
LCoS	**L**iquid **C**rystal on **S**ilicon
L-FROG	**L**inear-**F**requency **R**esolved **O**ptical **G**ating
NOLM	**N**onlinear **O**ptical **L**oop **M**irror
NRZ	**N**on **R**eturn-to-**Z**ero
O-E-O	**O**ptical-**E**lectronic-**O**ptical
OFC	**O**ptical **F**requency **C**omb
OFCG	**O**ptical **F**requency **C**omb **G**enerator
OOK	**O**n-**O**ff **K**eying
OP	**O**ptical **P**rocessor
OPA	**O**ptical **P**arametric **A**mplification
OSA	**O**ptical **S**pectrum **A**nalyser
OSNR	**O**ptical **S**ignal-to-**N**oise **R**atio
OSO	**O**ptical **S**ampling **O**scilloscope
OTDM	**O**ptical **T**ime-**D**ivision-**M**ultiplexing
PA	**P**arametric **A**mplification
PE	**P**roton **E**xchange
PIA	**P**hase-**I**nsensitive **A**mplifier
PLL	**P**hase-**L**ocked **L**oop
PMD	**P**olarization **M**ode **D**ispersion
PPLN	**P**eriodically **P**oled **L**ithium **N**iobate

PRBS	**P**seudo**R**andom **B**it **S**equence
PR-WC	**P**hase **R**egenerative-**W**avelength **C**onversion
PSA	**P**hase **S**ensitive **A**mplifier
PSK	**P**hase **S**hift **K**eying
PSS	**P**hase-**S**ensitive **S**wing
QPM	**Q**uasi-**P**hase **M**atching
RZ	**R**eturn-to-**Z**ero
SBS	**S**timulated **B**rillouin **S**cattering
SF	**S**um **F**requency
SFG	**S**um **F**requency **G**eneration
SH	**S**econd **H**armonic
SHG	**S**econd **H**armonic **G**eneration
SMF	**S**ingle **M**ode **F**ibre
SOA	**S**emiconductor **O**ptical **A**mplifier
SPM	**S**elf-**P**hase **M**odulation
SRS	**S**timulated **R**aman **S**cattering
SSFBG	**S**uper**S**tructure **F**ibre **B**ragg **G**rating
TDM	**T**ime **D**ivision **M**ultiplexing
TDMA	**T**ime **D**ivision **M**ultiplexing **A**ccess
TBF	**T**unable **B**andpass **F**ilter
WDM	**W**avelength **D**ivision **M**ultiplexing
XGM	**C**ross **G**ain **M**odulation
XPM	**C**ross **P**hase **M**odulation

1

Introduction

1.1 Motivation

Optical networks have revolutionized modern communications enabling massive amounts of data to be rapidly transmitted around the globe. Traffic on the global communication infrastructure is predicted to continue to grow by ∼70 % annually, driven by bandwidth-hungry applications such as video sharing websites, E-commerce, video conferencing, cloud computing, virtual reality games, and the introduction of smart mobile phones [Cis , Ria].

However, as line rates keep increasing, electronic processing of data packets at routers in an optical network and the required optical-electronic-optical (O-E-O) conversions may present a bottleneck in speed. In order to mitigate the problem, and at the same time increase network functionality and flexibility, it will become increasingly more attractive, if not essential, to process the data signals within the optical layer. Therefore, highly functional optical devices will be required at the nodes of these advanced telecommunication networks to assist or replace some of the electronic modules used in current network routers, and they are expected to be capable of seamlessly processing multiple signals in parallel at extremely high speeds (40 Gbit/s and above). These optical devices need to perform various processing tasks such as data package routing, add-drop multiplexing, regeneration and format conversion as required in electrical systems, the implementation of which generally requires the use of nonlinear effects in optical devices.

Intensive research has already been done on various nonlinear optical devices. For instance, highly nonlinear optical fibres (HNLFs) possess an ultrafast response but are prone to environmental instabilities associated with their long lengths and suffer from stimulated Brillouin scattering (SBS), the mitigation of which would either impose serious performance limitations or add significant complexity to the system. On the other hand, semiconductor materials such as the semiconductor optical amplifier (SOA) are compact. However, the carrier lifetime of semiconductor materials is typically of the order of few hundreds of picoseconds and thus comparable to the period of the modulated optical signal. As a consequence, the output of SOA does not only depend on the current input data bit, but also depends on the preceding input data bits. This undesirable phenomenon is referred to as patterning effect, and leads to relatively low switching speeds for SOA [Manning 97, Zoiros 08].

In this project I have investigated the use of periodically poled lithium niobate (PPLN) waveguides as nonlinear optical devices for telecommunication applications. In order to obtain an efficient conversion in nonlinear interactions, the relative phase between the interacting waves must be maintained. Quasi-phase matching (QPM), which was first devised by Armstrong *et al.* [Armstrong 62] and Franken *et al.* [Franken 63], is a technique to correct the interacting waves' relative phase at regular intervals using a structural periodicity built into the nonlinear medium. Lithium niobate which is a type of ferroelectric materials and displays second-order nonlinearities was proposed for QPM in the 1970s [Okada 76]. Lithium niobate crystals having periodically alternating ferroelectric domain structures are named as PPLN. With the developments of the QPM technology by improved lithographically controlled patterning and low-loss waveguide fabrication technology, the efficiency of the second-order interactions in lithium niobate devices has increased by several orders of magnitude, which enables PPLN waveguides to rival third-order nonlinearities-based nonlinear optical devices [Fejer 92, Hum 07].

The use of quadratic nonlinearities in PPLN waveguides for all-optical signal processing applications offers several advantages, including a high nonlinear coefficient, ultra-fast optical response, compactness, less sensitivity to SBS, low spontaneous emission noise, low cross talk, no intrinsic frequency chirp, transparency to both bit rate and modulation format owing to the phase-preserving nature of parametric conversion [Langrock 06, Gallo 06]. To date, PPLN-based all-optical signal processing techniques for telecommunication applications have been demonstrated to operate at ultrahigh speeds. For instance, add/drop multiplexing using PPLN waveguides at 640 Gbit/s has been reported by Bogoni *et al.* [Bogoni 10]. Tunable wavelength conversion using PPLN waveguides at 160 Gbit/s has been reported by Furukawa *et al.* [Furukawa 07]. Also, channel-selective data exchange for multiple WDM channels using PPLN waveguides has been demonstrated by Wang *et al.* at 40 Gb/s [Wang 10].

Compared to other nonlinear optical devices, PPLN waveguides still remain relatively unexplored in the telecommunication area. By exploiting the use of cascaded nonlinear effects in PPLN waveguides, in this thesis I will demonstrate several novel all-optical processing modules capable of operating at modest optical power levels and that are able to meet the stringent requirements of ultrahigh capacity telecommunication systems.

1.2 Contribution to knowledge

The objectives of this project have been to study the physics and engineering aspects of second-order guided-wave interactions in the ultrafast regime and their applications in telecommunication signals. By the end of the study, a number of novel results have been produced, which are outlined below:

◇ The first systematic and comparative study of the acceptance bandwidths of two cascaded quadratic nonlinear processes, cascaded second harmonic generation and difference frequency generation (cSHG/DFG) and cascaded sum frequency generation and difference frequency generation (cSFG/DFG), in PPLN waveguides, both in the continuous wave (CW) and pulsed-pump regimes.

◇ An optical time-division-multiplexing (OTDM) to wavelength-division multiplexing (WDM) format conversion scheme using the cSHG/DFG process in a fiberized PPLN waveguide.

◇ An all-optical retiming scheme based on pulse shaping and cSHG/DFG-based optical switching in a PPLN waveguide.

◇ A novel frequency non-degenerate phase sensitive amplification configuration based on the cSHG/DFG process within a single PPLN waveguide.

◇ A new scheme for phase-regenerative wavelength conversion (PR-WC) based on a combination of the cSHG/DFG process and the cSFG/DFG process within PPLN waveguides has been devised and experimentally demonstrated. With the novel PR-WC configurations, phase regeneration for differential (bipolar) phase shift keying (D(B)PSK) signals using PPLN waveguides is demonstrated for the first time.

◇ A novel scheme to erase the chirp of ps-long pulses and yield chirp-free output pulses, relying on a combination of the cSHG/DFG process and the cSFG/DFG process in two different PPLN waveguides, and operating independently of the input chirp characteristics.

◇ Finally, beyond applications in second-order nonlinear media, this thesis investigates the use of optical frequency comb generators (OFCGs) as short pulse sources for telecommunication application. This thesis presents a first numerical analysis of the output of OFCGs in the time domain, neglecting the intra-cavity dispersion. Based on that, two approaches are proposed to compensate for the intrinsic chirp of the OFCGs, by using either a properly designed compensating filter or a free-space delay line interferometer.

1.3 Outline

This thesis is organised as follows:

Chapter 2 contains the general background needed to understand the work developed in this thesis. The origin of the second-order nonlinearity of lithium niobate crystals, various second-order nonlinear interactions in PPLN waveguides, the QPM technique, and the PPLN waveguide fabrication technique are introduced. Subsequently, the second harmonic generation (SHG), sum frequency generation (SFG), difference frequency generation (DFG), cSHG/DFG and cSFG/DFG interactions in PPLN waveguides are modelled and the properties of these second-order nonlinear interactions are analysed. This chapter finally includes an introduction to an optical processor filter as well as to linear frequency resolved optical gating (L-FROG) technologies, which are used in the subsequent experiments in this thesis.

Chapter 3 presents a systematic and comparative study of the acceptance bandwidths of two cascaded quadratic nonlinear processes, cSHG/DFG and cSFG/DFG, in PPLN waveguides. The acceptance bandwidths of both the individual SHG and SFG processes in the CW and pulsed-pump regimes are theoretically and experimentally studied.

Chapter 4 presents an optical time-division-multiplexing (OTDM) to wavelength-division multiplexing (WDM) format conversion scheme using the cSHG/DFG process in a fiberized PPLN waveguide. The operational principle and theoretical model of the format conversion scheme is presented first, followed by experimental results.

In Chapter 5, an all-optical retiming scheme based on pulse shaping and cSHG/DFG-based switching in a PPLN waveguide is demonstrated. This chapter starts with a brief introduction of a variety of degradations in fiber-optic communication system and a review of regeneration techniques which generally involve three basic functions, reamplification, reshaping and retiming. The chapter then focuses on all-optical retiming techniques and a new all-optical retiming scheme for return-to-zero on-off keying (RZ-OOK) signals is proposed. The chapter closes with experimental evidence supporting this novel retiming scheme.

Chapter 6 demonstrates two novel configurations of phase sensitive amplification based on cascaded quadratic effects in PPLN waveguides. The first one is frequency non-degenerate phase sensitive amplifier (PSA) based on the cSHG/DFG process within a single PPLN waveguide, demonstrated in Section 6.2. The second configuration of PSA is phase-regenerative wavelength conversion (PR-WC) based on a combination of the cSHG/DFG process and the cSFG/DFG process within PPLN waveguides, demonstrated in Section

6.3. The phase regenerative properties of the PR-WC configuration as a D(B)PSK phase regenerator are also investigated in Section 6.3.

Chapter 7 presents an effective method to erase the chirp of ps-long pulses and yield chirp-free output pulses. The technique, which is based on a combination of cascaded nonlinear effects in two different PPLN waveguides, operates independently of the input chirp characteristics and requires only limited knowledge of the input pulse shape. Simulations with different input chirp profiles have been performed, all resulting in chirp-free output pulses after this chirp-elimination system. Finally, the experimental results validated the simulations and confirmed the capability of the scheme to remove a broad range of chirp profiles.

Chapter A presents supplementary studies that I have carried out on OFCGs. Both a theoretical and experimental study of the intensity and phase properties of the pulses generated by an OFCG is presented, which aids the use of OFCGs as short pulse sources for communication applications. Furthermore, two approaches are proposed to compensate for the intrinsic chirp of the OFCGs, by using either a properly designed compensating filter or a free-space delay line interferometer.

Finally, this thesis is concluded in Chapter 8 along with a discussion on the direction of future work.

References

[Armstrong 62] J. A. Armstrong, N. Bloembergen, J. Ducuing & P. S. Pershan, *Interactions between Light Waves in a Nonlinear Dielectric*, Phys. Rev., vol. 127, no. 6, pages 1918–, September 1962.

[Bogoni 10] Antonella Bogoni, Xiaoxia Wu, Zahra Bakhtiari, Scott Nuccio, Robert W. Hellwarth & Alan E. Willner. *640 Gb/s All-Optical Add/Drop Multiplexing Based on Pump Depletion in a PPLN Waveguide.* In Photonics in Switching, page PTuB6. Optical Society of America, 2010.

[Cis] *http://www.cisco.com/en/US/solutions/collateral/ns341/ns525 /ns537/ns705/ns827/white_paper_c11-481360.pdf.*

[Fejer 92] M. M. Fejer, G. A. Magel, D. H. Jundt & R. L. Byer, *Quasi-phase-matched 2nd Harmonic-generation - Tuning and Tolerances*, Ieee Journal of Quantum Electronics, vol. 28, no. 11, pages 2631–2654, November 1992.

[Franken 63] P. A. Franken & J. F. Ward, *Optical Harmonics and Nonlinear Phenomena*, Rev. Mod. Phys., vol. 35, no. 1, pages 23–, January 1963.

[Furukawa 07] H. Furukawa, A. Nirmalathas, N. Wada, S. Shinada, H. Tsuboya & T. Miyazaki, *Tunable all-optical wavelength conversion of 160-Gb/s RZ optical signals by cascaded SFG-DFG generation in PPLN waveguide*, Ieee Photonics Technology Letters, vol. 19, no. 5-8, pages 384–386, March 2007.

[Gallo 06] K. Gallo, J. Prawiharjo, F. Parmigiani, P. Almeida, P. Petropoulos & D. J. Richardson. *Processing ultrafast optical signals in broadband telecom systems by means of cascaded quadratic nonlinearities*, 2006.

[Hum 07] D. S. Hum & M. M. Fejer, *Quasi-phasematching*, Comptes Rendus Physique, vol. 8, no. 2, pages 180–198, March 2007.

[Langrock 06] C. Langrock, S. Kumar, J. E. McGeehan, A. E. Willner & M. M. Fejer, *All-optical signal processing using chi((2)) nonlinearities in guided-wave* *devices*, Journal of Lightwave Technology, vol. 24, no. 7, pages 2579–2592, July 2006.

[Manning 97] R. J. Manning, A. D. Ellis, A. J. Poustie & K. J. Blow, *Semiconductor laser amplifiers for ultrafast all-optical signal processing*, Journal of the Optical Society of America B-optical Physics, vol. 14, no. 11, pages 3204–3216, November 1997.

[Okada 76] M. Okada, K. Takizawa & S. Ieiri, *2nd Harmonic-generation By Periodic Laminar Structure of Nonlinear Optical Crystal*, Optics Communications, vol. 18, no. 3, pages 331–334, 1976.

[Ria] *http://www.siliconiran.com/magazine/technology_ editorial/index.shtml.*

[Wang 10] J. Wang, S. Nuccio, X. X. Wu, O. F. Yilmaz, L. Zhang, I. Fazal, J. Y. Yang, Y. Yue & A. E. Willner, *40 Gbit/s optical data exchange between wavelength-division-multiplexed channels using a periodically poled lithium niobate waveguide*, Optics Letters, vol. 35, no. 7, pages 1067–1069, April 2010.

[Zoiros 08] K. E. Zoiros, T. Siarkos & C. S. Koukourlis, *Theoretical analysis of pattern effect suppression in semiconductor optical amplifier utilizing optical delay interferometer*, Optics Communications, vol. 281, no. 14, pages 3648–3657, July 2008.

2

Background

In this chapter, I lay the background theory necessary to understand the subsequent chapters. The origin of the second-order nonlinearity of lithium niobate crystals and various second-order nonlinear interactions in PPLN waveguides are introduced at the beginning of this chapter followed by a brief introduction of the quasi-phase matching (QPM) technique and the PPLN waveguide fabrication techniques. After that, the characterisation of the PPLN waveguide samples used in the subsequent experiments is presented. Subsequently, the SHG, SFG, DFG, cSHG/DFG and cSFG/DFG interactions in PPLN waveguides are modelled and the properties of these second-order nonlinear interactions are analysed. The chapter finally includes an introduction to two tools used in the experiments of the following chapters, namely linear frequency resolved optical gating (L-FROG) technologies, and an optical processor (OP) which is a programmable phase and amplitude filter based on the liquid crystal on silicon (LCoS) technology.

2.1 Theory of periodically poled lithium niobate waveguide

2.1.1 Second-order nonlinearity in lithium niobate crystals

In nonlinear optics, the polarization $P(t)$ can be written in terms of the applied electric field $E(t)$ as [Boyd 03]

$$\begin{aligned} P(t) &= \varepsilon_0[\chi^{(1)}E(t) + \chi^{(2)}E^2(t) + \chi^{(3)}E^3(t) + \cdots] \\ &= P^{(1)}(t) + P^{(2)}(t) + P^{(3)}(t) + \cdots \end{aligned} \tag{2.1}$$

where $P^{(1)}(t) = \varepsilon_0\chi^{(1)}E(t)$ is the linear polarization which depends linearly on the electric field strength, $P^{(2)}(t) = \varepsilon_0\chi^{(2)}E^2(t)$ is the second-order nonlinear polarization and $P^{(3)}(t) = \varepsilon_0\chi^{(3)}E^3(t)$ is the third-order nonlinear polarization. $\chi^{(2)}$ and $\chi^{(3)}$ denote the second- and third-order nonlinear optical susceptibilities, respectively. In general, the polarisation at a certain point and time t_0 depends on the electric field at that place and instant as well as the electric field at nearby points for time $\leq t_0$, which means the nonlinear susceptibilities depend on the frequencies of the applied fields [Boyd 03].

The applied electric field $E_i(t)$ can be expressed as a summation of frequency components

$$E_i(t) = \sum_n E_i(\omega_n)e^{-i\omega_n t} \tag{2.2}$$

The second-order susceptibility tensor $\chi^{(2)}_{ijk}(\omega_n + \omega_m, \omega_n, \omega_m)$ can be defined as the constants of proportionality relating the amplitude of the nonlinear polarization to the product of field amplitudes as follows [Boyd 03]:

$$P_i(\omega_n + \omega_m) = \varepsilon_0 \sum_{jk} \sum_{(nm)} \chi^{(2)}_{ijk}(\omega_n + \omega_m, \omega_n, \omega_m)E_j(\omega_n)E_k(\omega_m) \tag{2.3}$$

where the indices ijk refer to the Cartesian components of the fields, and the sum $\omega_n + \omega_m$ should be held fixed in performing the summation over n and m in Eq. 2.3.

In the following, the second-order nonlinearities in lithium niobate crystals will be briefly introduced. Lithium niobate ($LiNbO_3$) is a kind of artificial dielectric crystals, first reported to be a type of ferroelectric material in 1949 [Schweinler 52]. Ferroelectricity is a property of certain materials which possess a spontaneous electric polarization P_s that can be reversed by the application of an external electric field [Kanzig 57, Volk 08]. The lattice of lithium niobate is shown in Fig. 2.1. The shift of an ion from a symmetrical site makes lithium niobate crystals to not display inversion symmetry, resulting in spontaneous polarization P_s and nonzero $\chi^{(2)}$, from which second-order nonlinearities originate. These kinds of crystals, such as $LiNbO_3$, which do not possess inversion symmetry are referred to as non-centrosymmetric crystals, and second-order nonlinear optical interactions only occur in non-centrosymmetric media. In contrast, third-order nonlinear optical interactions can occur in both centrosymmetric and non-centrosymmetric media [Boyd 03].

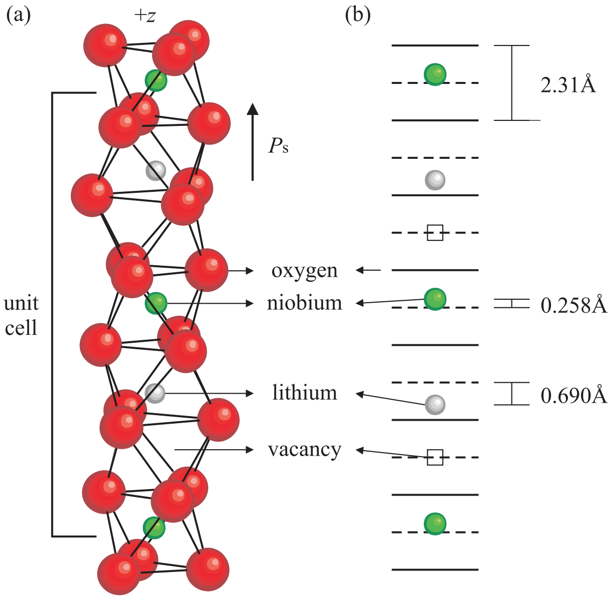

FIGURE 2.1: Lattice of lithium niobate crystal. Redrawn from [Gopalan 07].

Lithium niobate offers several attractive properties as a kind of nonlinear optical devices. Congruent lithium niobate (undoped) can be grown in large sizes with excellent homogeneity [Volk 08]. Also, lithium niobate has one of the largest nonlinear coefficients $d_{33} = \frac{1}{2}\chi_{333} = 27$ pm/V among ferroelectric materials [Fejer 92]. Furthermore, it is transparent within a large wavelength range between 325 nm and 4500 nm [Weiss 02]. However, lithium niobate usually suffers from photorefractive effects [Ashkin 66]. The general understanding of photorefractive effects is that the photo excited carriers come from Fe_{++} impurities in the LiNbO_3 crystal and that the photorefractive sensitivity of the crystal is proportional to its Fe_{++} concentration [Glass 74]. In order to mitigate the photorefractive effect, the most commonly used composition of lithium niobate for optical applications is magnesium-doped lithium niobate [Weiss 02]. By addition of 4.6 mol% of MgO to undoped LiNbO_3 crystal, a hundred-fold increase in the resistance against optical damage over the pure crystal was reported [Polgár 86].

2.1.2 Second-order nonlinear interactions

The optical wave is an electromagnetic wave, so the propagation of optical fields is governed by Maxwell's equation as follows [Agrawal 07]:

$$
\begin{aligned}
&\nabla \times E = -\frac{\partial B}{\partial t} \\
&\nabla \times H = \frac{\partial D}{\partial t} + J \\
&\nabla \cdot D = \rho \\
&\nabla \cdot B = 0
\end{aligned}
\tag{2.4}
$$

where E and H are the electric and magnetic field vectors, respectively; D and B are the electric displacement and magnetic induction, respectively; The current density vector J and the charge density ρ denote the sources for the electromagnetic field.

D and B arise in response to the electric field E and magnetic field H propagating inside the fibres, and the relationship between them is given by the constitutive relations as follows [Agrawal 07]:

$$
\begin{aligned}
&D = \varepsilon_0 E + P \\
&B = \mu_0 (H + M)
\end{aligned}
\tag{2.5}
$$

It is noted that the set of Maxwell's equations cannot be solved uniquely without the constitutive relations [Agrawal 07].

From the set of Maxwell's equations (Eq. 2.4) and the constitutive relations (Eq. 2.5), it can be derived that

$$\nabla^2 E - \frac{1}{c^2}\frac{\partial^2}{\partial t^2}E = \frac{1}{\varepsilon_0 c^2}\frac{\partial^2 P}{\partial t^2} \tag{2.6}$$

Polarisation P can be separated into two parts:

$$P = P^{(1)} + P^{NL} \tag{2.7}$$

where $P^{(1)}$ is the linear part which depends linearly on the electric field E, and P^{NL} is the nonlinear part.

The displacement field D can also be separated into linear and nonlinear parts:

$$D = D^{(1)} + P^{NL} \tag{2.8}$$

Because $D^{(1)} = \varepsilon_0 E + P^{(1)} = \varepsilon_0 \varepsilon^{(1)} E$, Eq. 2.6 can be written as

$$\nabla^2 E - \frac{\varepsilon^{(1)}}{c^2}\frac{\partial^2}{\partial t^2}E = \frac{1}{\varepsilon_0 c^2}\frac{\partial^2 P^{NL}}{\partial t^2} \tag{2.9}$$

Observing the right hand side of Eq. 2.9, time-varying polarization can act as the source of new components of the electromagnetic field.

For the case of a dispersive medium, we must consider each frequency component of the field separately. We represent the electric, linear displacement, and polarization field as the sums of their various frequency components:

$$\begin{aligned} E(r,t) &= \sum_n E_n(r,t) \\ D(r,t) &= \sum_n D_n(r,t) \\ P^{NL}(r,t) &= \sum_n P_n^{NL}(r,t) \end{aligned} \tag{2.10}$$

where the summation is to be performed over positive field frequencies only, and we represent each frequency component in terms of its complex amplitude as

$$\begin{aligned} E_n(r,t) &= E_n(r)e^{-i\omega_n t} + c.c. \\ D_n(r,t) &= D_n(r)e^{-i\omega_n t} + c.c. \\ P_n^{NL}(r,t) &= P_n^{NL}(r)e^{-i\omega_n t} + c.c. \end{aligned} \tag{2.11}$$

If dissipation can be neglected, the relationship between $D_n^{(1)}$ and E_n can be expressed in terms of a real, frequency-dependent dielectric tensor according to [Boyd 03]

$$D_n^{(1)}(r,t) = \epsilon_0 \epsilon^{(1)}(\omega_n) E_n(r,t) \tag{2.12}$$

Substituting Eq. 2.10 and Eq. 2.12 into Eq. 2.9, we obtain a wave equation that is valid for each frequency component of the field [Boyd 03]

$$\nabla^2 E_n - \frac{\varepsilon^{(1)}(\omega_n)}{c^2}\frac{\partial^2 E_n}{\partial t^2} = \frac{1}{\varepsilon_0 c^2}\frac{\partial^2 P_n^{NL}}{\partial t^2} \tag{2.13}$$

2.1.2.1 Second harmonic generation

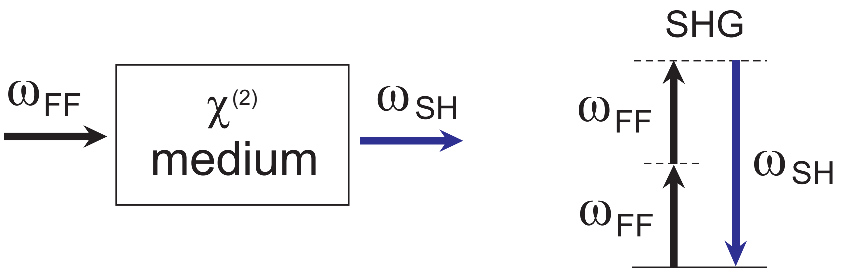

FIGURE 2.2: Illustration of the SHG process.

In second harmonic generation, a fundamental frequency (FF) wave at frequency ω_{FF} passes through a medium with second-order nonlinear susceptibility, generating a second harmonic (SH) wave at frequency $\omega_{SH} = 2\omega_{FF}$, as illustrated in Fig. 2.2. The electric fields of the FF and the SH can be written respectively as

$$\begin{aligned} E_{FF}(z,t) &= E_{FF}e^{-i\omega_{FF}t} + c.c. \\ &= A_{FF}e^{i(\beta_{FF}z-\omega_{FF}t)} + c.c. \\ E_{SH}(z,t) &= E_{SH}e^{-i\omega_{SH}t} + c.c. \\ &= A_{SH}e^{i(\beta_{SH}z-\omega_{SH}t)} + c.c. \end{aligned} \tag{2.14}$$

where A_{FF} and A_{SH} denote the electric field amplitudes of the FF and SH waves which are constants in time, whereas E_{FF} and E_{SH} denote the amplitudes of the electric fields which vary rapidly in time. β_{FF} and β_{SH} denote the propagation constants of the FF and the SH waves respectively. Propagation constant is defined as $\beta = \frac{2\pi}{\lambda}n_{eff}$, and the effective refractive index n_{eff} depends on the geometry of the PPLN waveguides.

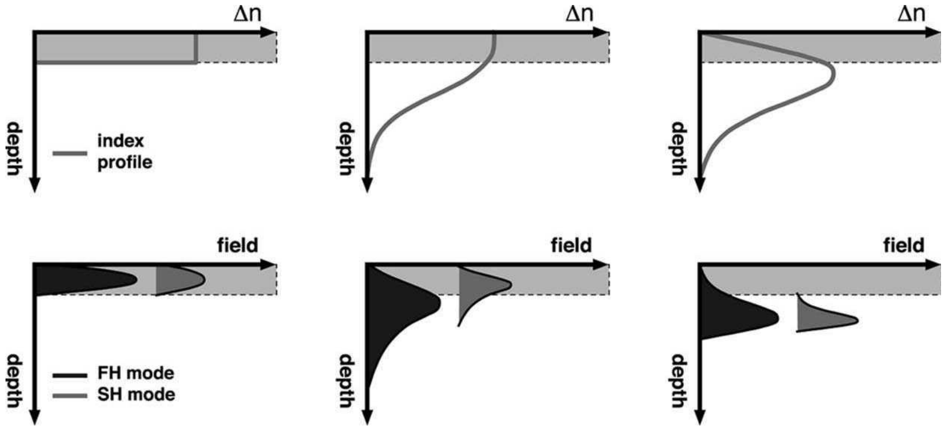

Figure 2.3: Comparison between PE, APE, and RPE indexes and mode profiles in the depth dimension. Ref.[Langrock 06]

Figure 2.3 shows the refractive index profiles of proton exchange (PE) PPLN, annealing proton exchange (APE) PPLN and reverse proton exchange (RPE) PPLN. For proton exchange PPLN, lithium ions are exchanged with hydrogen ions in the channels. After that, for APE PPLN high-temperature annealing diffuses the protons deeper into the substrate, increasing the effective nonlinear coefficient and reducing the propagation losses by pushing the propagating fields farther from the substrate surface. Because of the asymmetric APE refractive index profile along the depth dimension, the peaks of the interacting modes at different wavelengths are not well aligned, reducing the overlap integral and the maximum normalized efficiency. The index profile can be buried to create a more symmetric waveguide by an additional exchange step in a lithium-rich melt, replacing protons by lithium ions in the top layer of the waveguiding structure. The reverse proton exchange step also increases the separation between the propagating fields and the substrate surface, further decreasing the propagation losses [Langrock 06]. Figure 2.4 illustrates a simulation of a mode profile in a RPE PPLN waveguide.

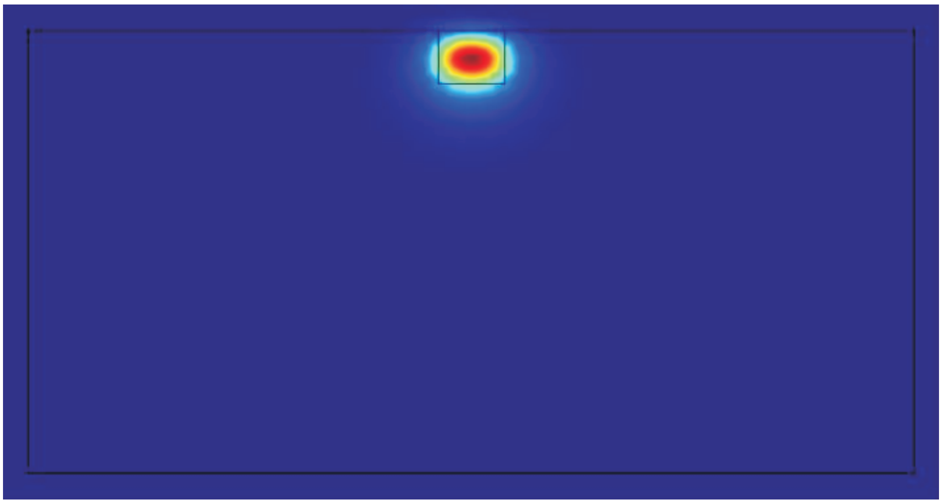

FIGURE 2.4: Simulation of a mode profile in a RPE PPLN waveguide using software Comsol.

According to Eq. 2.3, the amplitude of the nonlinear polarizations of the FF and SH waves can be expressed as:

$$P_{FF} = 4\varepsilon_0 d_{eff} E_{FF}^* E_{SH} = 4\varepsilon_0 d_{eff} A_{FF} A_{SH} e^{i(\beta_{SH}-\beta_{FF})z} \tag{2.15}$$

$$P_{SH} = 2\varepsilon_0 d_{eff} E_{FF}^2 = 2\varepsilon_0 d_{eff} A_{FF}^2 e^{i2\beta_{FF}z} \tag{2.16}$$

where $d_{eff} = \frac{1}{2}\chi^{(2)}$ denotes the effective nonlinear coefficient.

Assuming the field is invariant in the waveguide cross-section, we replace ∇^2 in Eq. 2.13 by d^2/dz^2, and obtain:

$$\frac{d^2 A_{FF}}{dz^2} + 2i\beta_{FF}\frac{A_{FF}}{dz} = \frac{-4d_{eff}\omega_{FF}^2}{c^2} A_{FF}^* A_{SH} e^{i(-2\beta_{FF}+\beta_{SH})z} \tag{2.17}$$

$$\frac{d^2 A_{SH}}{dz^2} + 2i\beta_{SH}\frac{A_{SH}}{dz} = \frac{-2d_{eff}\omega_{SH}^2}{c^2} A_{FF}^2 e^{i(2\beta_{FF}-\beta_{SH})z} \tag{2.18}$$

Under the following slowly varying amplitude approximation

$$|\frac{d^2A_i}{dz^2}| \ll |\beta_i \frac{A_i}{dz}|, \qquad \text{where} \qquad i = FF, SH \tag{2.19}$$

we obtain the coupled mode equations for the SHG process as follows:

$$\frac{dA_{FF}}{dz} = \frac{2id_{eff}\omega_{FF}^2}{\beta_{FF}c^2} A_{FF}^* A_{SH} e^{-i\Delta\beta z} \tag{2.20}$$

$$\frac{dA_{SH}}{dz} = \frac{id_{eff}\omega_{SH}^2}{\beta_{SH}c^2} A_{FF}^2 e^{i\Delta\beta z} \tag{2.21}$$

where $\Delta\beta = 2\beta_{FF} - \beta_{SH}$ is the phase mismatch of the SHG process.

The amplitude of the SH wave at the end of the nonlinear medium is given by integrating Eq. 2.21 along the length of the medium L, yielding:

$$A_{SH} = \frac{id_{eff}\omega_{SH}^2}{\beta_{SH}c^2} A_{FF}^2 \int_0^L e^{i\Delta\beta z} dz = \frac{id_{eff}\omega_{SH}^2 A_{FF}^2}{\beta_{SH}c^2} \frac{\sin^2(\Delta kL/2)}{\Delta kL/2} L \tag{2.22}$$

Because $I_i = 2n_i\varepsilon_0 c|A_i|^2$, the intensity of the SHG output can be written as

$$\begin{aligned} I_{SH} &= \frac{2n_{SH}\varepsilon_0 d_{eff}^2 \omega_{SH}^4 |A_{FF}|^4}{\beta_{SH}^2 c^4} sinc^2(\Delta\beta L/2)L^2 \\ &= \frac{2d_{eff}^2 \omega_{SH}^2 I_{FF}^2}{n_{FF}^2 n_{SH}\varepsilon_0 c^2} sinc^2(\Delta\beta L/2)L^2 \end{aligned} \tag{2.23}$$

2.1.2.2 Sum frequency generation

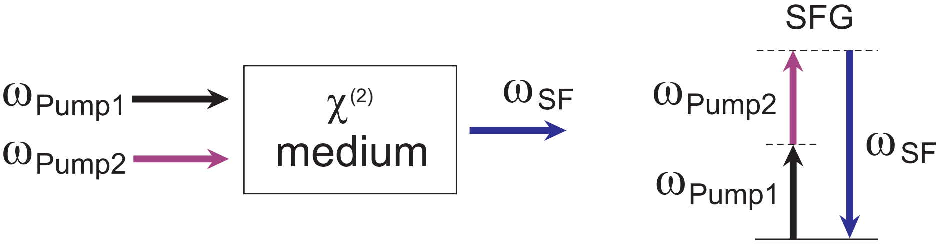

FIGURE 2.5: Illustration of the SFG process.

In sum frequency generation, Pump 1 at frequency ω_{Pump1} and Pump 2 at frequency ω_{Pump2} pass through a medium with second-order nonlinear susceptibility, generating a sum frequency (SF) wave at frequency $\omega_{SF} = \omega_{Pump1} + \omega_{Pump2}$, as illustrated in Fig. 2.5.

According to Eq. 2.3, the amplitude of the nonlinear polarizations of Pump 1, Pump 2 and the SF can be expressed as:

$$P_{Pump1} = 4\varepsilon_0 d_{eff} E^*_{Pump2} E_{SF} \tag{2.24}$$

$$P_{Pump2} = 4\varepsilon_0 d_{eff} E^*_{Pump1} E_{SF} \tag{2.25}$$

$$P_{SF} = 4\varepsilon_0 d_{eff} E_{Pump1} E_{Pump2} \tag{2.26}$$

In comparing Eq. 2.26 to Eq. 2.16, the extra factor of 2 comes from the summation over n and m in Eq. 2.3, which also means the degeneracy factors appearing in SHG and SFG are different [Boyd 03].

The derivation of the coupled-mode equations for SFG is analogous to that of SHG, and the coupled-mode equations are given by:

$$\frac{dA_{Pump1}}{dz} = \frac{2id_{eff}\omega^2_{Pump1}}{\beta_{Pump1}c^2} A_{SF} A^*_{Pump2} e^{-i\Delta\beta z} \tag{2.27}$$

$$\frac{dA_{Pump2}}{dz} = \frac{2id_{eff}\omega^2_{Pump2}}{\beta_{Pump2}c^2} A_{SF} A^*_{Pump1} e^{-i\Delta\beta z} \tag{2.28}$$

$$\frac{dA_{SF}}{dz} = \frac{2id_{eff}\omega^2_{SF}}{\beta_{SF}c^2} A_{Pump1} A_{Pump2} e^{i\Delta\beta z} \tag{2.29}$$

where $\Delta\beta = \beta_{Pump1} + \beta_{Pump2} - \beta_{SF}$ is the phase mismatch of the SFG process. β_{Pump1}, β_{Pump2} and β_{SF} denote the wave vectors of the Pump 1, Pump 2 and SF waves respectively. The output amplitude of the SFG process can be written as

$$A_{SF} = \frac{2id_{eff}\omega^2_{SF}}{\beta_{SF}c^2} A_{Pump1} A_{Pump2} \int_0^L e^{i\Delta\beta z} dz = \frac{2id_{eff}\omega^2_{SF} A_{Pump1} A_{Pump2}}{\beta_{SF}c^2} \frac{\sin^2(\Delta\beta L/2)}{\Delta\beta L/2} L \tag{2.30}$$

The intensity of the SFG output can be written as

$$\begin{aligned} I_{SF} &= \frac{8n_{SF}\varepsilon_0 d_{eff}^2 \omega_{SF}^4 |A_{Pump1}|^2 |A_{Pump2}|^2}{\beta_{SF}^2 c^4} sinc^2(\Delta\beta L/2)L^2 \\ &= \frac{8d_{eff}^2 \omega_{SF}^2 I_{Pump1} I_{Pump2}}{n_{Pump1} n_{Pump2} n_{SF} \varepsilon_0 c^2} sinc^2(\Delta\beta L/2)L^2 \end{aligned} \tag{2.31}$$

2.1.2.3 Difference frequency generation

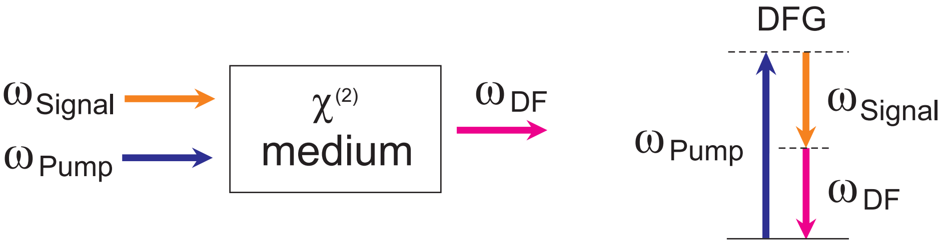

FIGURE 2.6: Illustration of the DFG process.

In difference frequency generation, a Pump at frequency ω_{Pump} and a signal at frequency ω_{Signal} pass through a medium with second-order nonlinear susceptibility, generating a difference frequency (DF) wave at frequency $\omega_{DF} = \omega_{Pump} - \omega_{Signal}$, as illustrated in Fig. 2.6.

According to Eq. 2.3, the amplitude of the nonlinear polarizations of the signal, pump and DF can be expressed as:

$$P_{Signal} = 4\varepsilon_0 d_{eff} E_{Pump} E_{DF}^* \tag{2.32}$$

$$P_{Pump} = 4\varepsilon_0 d_{eff} E_{DF} E_{Signal} \tag{2.33}$$

$$P_{DF} = 4\varepsilon_0 d_{eff} E_{Pump} E_{Signal}^* \tag{2.34}$$

The coupled-mode equations for DFG are given by:

$$\frac{dA_{Signal}}{dz} = \frac{2id_{eff}\omega_{Signal}^2}{\beta_{Signal}c^2} A_{Pump} A_{DF}^* e^{-i\Delta\beta z} \tag{2.35}$$

$$\frac{dA_{Pump}}{dz} = \frac{2id_{eff}\omega_{Pump}^2}{\beta_{Pump}c^2} A_{DF} A_{Signal} e^{i\Delta\beta z} \tag{2.36}$$

$$\frac{dA_{DF}}{dz} = \frac{2id_{eff}\omega_{DF}^2}{\beta_{DF}c^2} A_{Pump} A_{Signal}^* e^{-i\Delta\beta z} \tag{2.37}$$

where $\Delta\beta = \beta_{Pump} - \beta_{DF} - \beta_{Signal}$ is the phase mismatch of the DFG process. β_{Pump}, β_{DF} and β_{Signal} denote the wave vectors of the pump, the output and the signal waves respectively.

2.1.2.4 Cascaded second-order nonlinear interactions

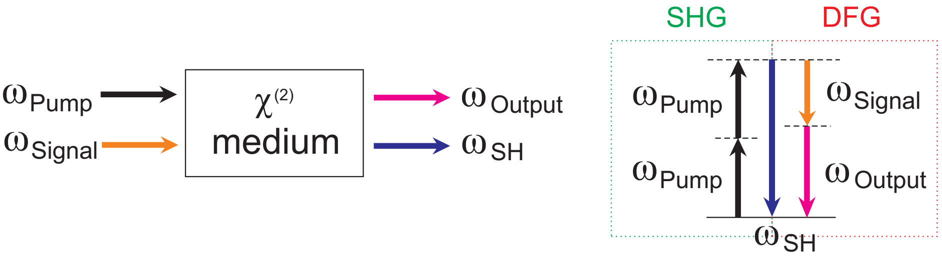

Figure 2.7: Illustration of the cSHG/DFG process.

In the previous sections, the SHG, SFG,and DFG interactions have been introduced. In addition to these single-stage second-order interactions, the SHG (SFG) process and the DFG process can also develop simultaneously in a PPLN waveguide. These are known as cascaded quadratic interactions. Cascaded quadratic interactions mimic the four wave mixing (FWM) process. FWM generates the outputs in the same wavelength band as the signal and the pump with the third order nonlinearity directly, whereas cascaded quadratic interactions generate the outputs with two second-order interactions in two steps. Firstly, the SH (SF) is generated from the pump(s) through the SHG (SFG) process which is followed by DFG with the signal, finally generating the output in the same wavelength band as the signal and the pump(s), as shown in Fig. 2.7 and 2.8.

In cascaded second harmonic generation and difference frequency generation (cSHG/DFG), the pump at frequency ω_{Pump} and the signal at frequency ω_{Signal} are simultaneously launched into a medium with second-order nonlinear susceptibility. The pump generates a SH wave at frequency $\omega_{SH} = 2\omega_{Pump}$ through SHG, accompanied by the DFG process between the SH wave and the signal, generating the output at frequency $\omega_{Output} = \omega_{SH} - \omega_{Signal}$, as illustrated in Fig. 2.7. The coupled-mode equations for the cSHG/DFG process are given by:

$$\frac{dA_{Pump}}{dz} = \frac{2id_{eff}\omega_{Pump}^2}{\beta_{Pump}c^2} A_{Pump}^* A_{SH} e^{-i\Delta\beta_{SHG}z} \tag{2.38}$$

$$\frac{dA_{SH}}{dz} = \frac{id_{eff}\omega_{SH}^2}{\beta_{SH}c^2} A_{Pump}^2 e^{i\Delta\beta_{SHG}z} + \frac{2id_{eff}\omega_{SH}^2}{\beta_{SH}c^2} A_{Signal} A_{Output} e^{i\Delta\beta_{DFG}z} \tag{2.39}$$

$$\frac{dA_{Signal}}{dz} = \frac{2id_{eff}\omega_{Signal}^2}{\beta_{Signal}c^2} A_{Output}^* A_{SH} e^{-i\Delta\beta_{DFG}z} \tag{2.40}$$

$$\frac{dA_{Output}}{dz} = \frac{2id_{eff}\omega_{Output}^2}{\beta_{Output}c^2} A_{Signal}^* A_{SH} e^{-i\Delta\beta_{DFG}z} \tag{2.41}$$

where $\Delta\beta_{SHG} = 2\beta_{Pump} - \beta_{SH}$ is the phase mismatch of the SHG process, and $\Delta\beta_{DFG} = \beta_{SH} - \beta_{Signal} - \beta_{Output}$ is the phase mismatch of the DFG process. β_{Pump}, β_{SH}, β_{Signal} and β_{Output} denote the wave vectors of the pump, the SH, the signal and the output waves respectively.

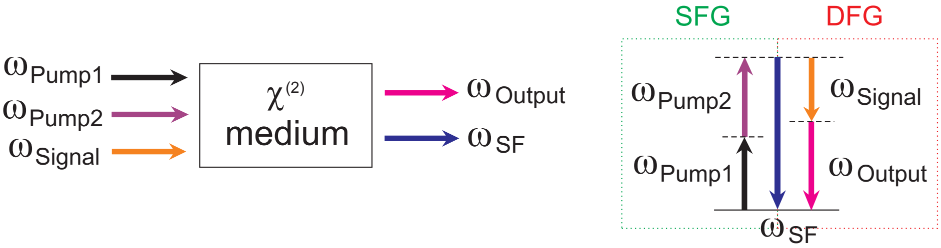

FIGURE 2.8: Illustration of the cSFG/DFG process.

The second type of cascaded quadratic interactions is cascaded sum frequency generation and difference frequency generation (cSFG/SHG). Pump 1 at frequency ω_{Pump1}, Pump 2 at frequency ω_{Pump2}, and the signal at frequency ω_{Signal} are simultaneously launched into a second-order nonlinear medium. Pump 1 and Pump 2 interact with each other and generate a SF wave at frequency $\omega_{SF} = \omega_{Pump1} + \omega_{Pump2}$ through SFG, accompanied by the DFG process between the SF wave and the signal, generating the output at frequency $\omega_{Output} = \omega_{SF} - \omega_{Signal}$, as illustrated in Fig. 2.8. The coupled-mode equations for the cSFG/DFG process are given by:

$$\frac{dA_{Pump1}}{dz} = \frac{2id_{eff}\omega_{Pump1}^2}{\beta_{Pump1}c^2} A_{Pump2}^* A_{SF} e^{-i\Delta\beta_{SFG}z} \tag{2.42}$$

$$\frac{dA_{Pump2}}{dz} = \frac{2id_{eff}\omega_{Pump2}^2}{\beta_{Pump2}c^2} A_{Pump1}^* A_{SF} e^{-i\Delta\beta_{SFG}z} \tag{2.43}$$

$$\frac{dA_{SF}}{dz} = \frac{2id_{eff}\omega_{SF}^2}{\beta_{SF}c^2} A_{Pump1} A_{Pump2} e^{i\Delta\beta_{SFG}z} + \frac{2id_{eff}\omega_{SF}^2}{\beta_{SF}c^2} A_{Signal} A_{Output} e^{i\Delta\beta_{DFG}z} \tag{2.44}$$

$$\frac{dA_{Signal}}{dz} = \frac{2id_{eff}\omega_{Signal}^2}{\beta_{Signal}c^2} A_{Output}^* A_{SF} e^{-i\Delta\beta_{DFG}z} \tag{2.45}$$

$$\frac{dA_{Output}}{dz} = \frac{2id_{eff}\omega_{Output}^2}{\beta_{Output}c^2} A_{Signal}^* A_{SF} e^{-i\Delta\beta_{DFG}z} \tag{2.46}$$

where $\Delta\beta_{SFG} = \beta_{Pump1} + \beta_{Pump2} - \beta_{SF}$ is the phase mismatch of the SFG process, and $\Delta\beta_{DFG} = \beta_{SF} - \beta_{Signal} - \beta_{Output}$ is the phase mismatch of the DFG process. β_{Pump1}, β_{Pump2}, β_{SF}, β_{Signal} and β_{Output} denote the wave vectors of Pump 1, Pump 2, the SF, the signal and the output waves respectively.

2.1.3 Quasi-phase matching

In this section, the theory of the QPM technique will be introduced. SHG is the simplest case of second-order interaction and will be analysed as a prototypical interaction in the following. A FF wave at frequency ω interacts with the medium via its second-order nonlinear susceptibility and generates a polarization wave at frequency 2ω. The polarization wave propagates at the same phase velocity as the FF wave and radiates a SH wave. In $LiNbO_3$, the SH wave propagates slower than the FF wave, because the refractive index of the SH is larger than that of the FF wave (see Fig. 2.9). The difference in the phase velocities of the FF wave and SH wave leads to variations in the relative phase between these two interacting waves. The continuous phase slip between these waves results in a periodic alternation in the direction of the power flow. Hence, the SH periodically grows and decays along the length of crystal, and the SH wave is not able to grow continuously, as shown in Fig. 2.10. Therefore, it is necessary that the relative phase between the interacting waves should be maintained for an efficient second-order nonlinear interaction.

In order to overcome this limit, two approaches are conventionally employed, namely birefringent phasematching (BPM) and QPM [Fejer 92]. In the early years of nonlinear

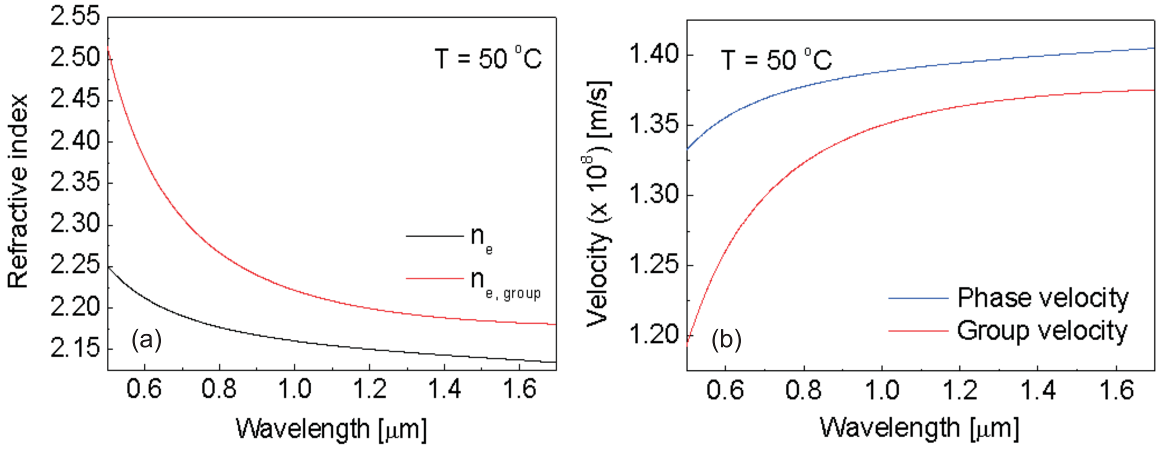

FIGURE 2.9: (a): Refractive index and group index for MgO-doped lithium niobate (e-wave). (b): Phase and group velocities for MgO-doped lithium niobate.

optics, the dominant approach was BPM, in which the phase velocities of the FF wave and the SH wave are balanced by setting them with orthogonal states of polarization and making use of the difference in the refractive indices for orthogonally polarized waves.

With the development of lithographically controlled patterning of nonlinear media, an alternative method, the QPM technique, in which the ferroelectric domains of the material are periodically inverted to correct the interacting waves' relative phase at regular intervals, has received much attention for an efficient second-order nonlinear interaction [Armstrong 62, Franken 63]. For instance, PPLN, first proposed by [Okada 76], periodically reverses the ferroelectric domains and thus periodically reverses the spontaneous polarization P_S such that the sign of nonlinear coefficient also varies periodically. By changing the sign of nonlinear susceptibility at every coherent length $l_c = \lambda/4(n_2 - n_1)$, which is defined as the distance over which the relative phase between the FF and SH waves accumulates a difference of π due to temporal walk-off effect, the phase of the polarization wave is shifted by π, effectively rephasing the interaction and resulting in a monotonic growth of the SH, as shown in Fig. 2.10. It should be noted that except for changing the sign of nonlinear susceptibility at every coherent length, any Fourier component of the QPM grating at the correct spatial frequency will also contribute to a QPM interaction [Fejer 92], as shown in Fig. 2.10. The QPM technique offers several advantages over BPM. Because QPM does not rely on birefringence, any convenient choice of the polarization states for the FF wave and SH wave can be used. All interacting waves

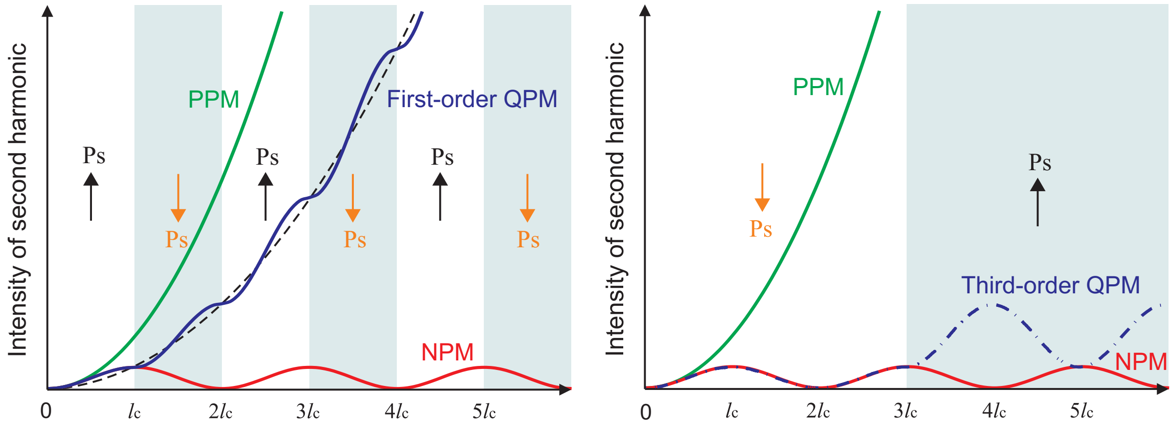

FIGURE 2.10: Effect of phase matching on the growth of second harmonic intensity. PPM: perfect phase matching, QPM: quasi-phase match, NPM: non phase matching. Replotted from [Fejer 92].

can be set with parallel polarization states and aligned to the largest component of the nonlinear susceptibility tensor in common ferroelectric media like $LiNbO_3$. However, it is noted that as shown in Fig. 2.10, the average growth rate of the QPM harmonic wave is lower than that of a perfectly phasematched wave in the same medium.

2.1.4 PPLN waveguides

The fabrication of PPLN waveguides can usually be divided into two processes. The first is the inversion of the ferroelectric domains by poling the PPLN substrate. The second is the formation of a waveguide structure [Fejer 92].

Several approaches have been reported to fabricate the QPM grating on a single-domain z-cut $LiNbO_3$ wafer. Electric-field poling is the most widely used technique, in which a high-voltage pulse is applied to electrodes lithographically patterned on the surface of the wafer [Fejer 92, Miller 96].

A guided-wave geometry can prevent optical beam diffraction by providing tight optical confinement over a long interaction length, so waveguide structures in second-order nonlinear materials can achieve long interaction lengths and high efficiency. It was reported that PPLN waveguides provided conversion efficiency enhancement up to two orders of magnitude compared to bulk PPLNs [Parameswaran 02]. Two standard methods for fabricating optical waveguides in $\mathrm{LiNbO_3}$ are titanium-diffusion and proton exchange (PE) [Schmidt 74, Jackel 82]. Ti-diffused waveguides are easily fabricated with low loss and guide both polarizations, but suffer from photorefractive damage at near-infrared power levels exceeding tens of milliwatts [Ashkin 66]. As an alternative, proton exchanged waveguides are much more resistant to photorefractive damage but PE only increases the refractive index for the extraordinary wave (n_e). Therefore, waveguides made by this method can only confine the extraordinary polarization (TM mode) when the substrate is Z-cut $\mathrm{LiNbO_3}$ [Langrock 06].

As introduced in Section 2.1.1, magnesium-doped lithium niobate is commonly used as the PPLN substrate for optical applications to mitigate the photorefractive effect. In the following, the refractive index of MgO-doped lithium niobate will be calculated to support the numerical simulation in Section 2.3. The refractive index of $\mathrm{LiNbO_3}$ depends on the polarisation of the light, the wavelength, the material composition and the temperature. For MgO-doped PE PPLN waveguides, the polarisation of light needs to be aligned along the z-axis, so light propagation is governed by the extraordinary refractive index n_e. The extraordinary refractive index n_e of $\mathrm{LiNbO_3}$ with the addition of ~ 5 mol% MgO which is wavelength-dependent and temperature-dependent can be approximated by the Sellmeier equation as follows [Jundt 97]

$$\begin{aligned} n_e^2(\lambda, T) = {} & 5.35583 + 4.629 \times 10^{-7} \times (T - 24.5)(T + 570.82) \\ & + \frac{0.100473 + 3.862 \times 10^{-8} \times (T - 24.5)(T + 570.82)}{\lambda^2 - (0.20692 - 0.89 \times 10^{-8} \times (T - 24.5)(T + 570.82))^2} \\ & + \frac{100 + 2.657 \times 10^{-5} \times (T - 24.5)(T + 570.82)}{\lambda^2 - 11.34927^2} - 1.5334 \times 10^{-2} \lambda^2 \end{aligned} \tag{2.47}$$

where λ is the wavelength and T is the temperature.

According to Eq. 2.47, Fig. 2.9(a) shows the relationship between the refractive index n_e, the group index $n_{e,group} = n_e + \omega \frac{dn_e}{d\omega}$ and the wavelength λ for MgO-doped lithium niobate. The envelope of an optical pulse moves at the group velocity, which is given by $v_g = c/n_{e,group}$. The phase velocity $v = c/n_e$ and the group velocity v_g for MgO-doped lithium niobate are shown in Fig. 2.9(b). Also, the group velocity dispersion (GVD) parameter β_2 and the dispersion parameter $D = \frac{d}{d\lambda}(\frac{1}{v_g}) = -\frac{2\pi c}{\lambda^2}\beta_2 = -\frac{\lambda}{c}\frac{d^2 n_e}{d\lambda^2}$ versus the wavelength for MgO-doped lithium niobate are shown in Fig. 2.11.

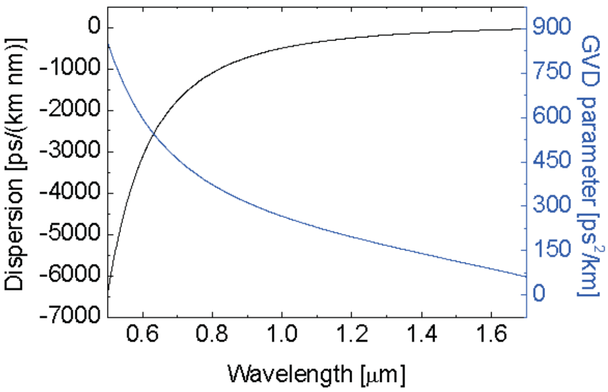

FIGURE 2.11: Dispersion parameter and GVD parameter for MgO-doped lithium niobate.

2.2 Characterisation of the PPLN waveguide samples

Two PPLN waveguide samples fabricated by HC Photonics Inc. were used in all of the experiments that will be presented in my thesis. Both these PPLN waveguides are MgO-doped PE PPLN waveguides and have a length $L = 30$ mm, but have slightly different grating periods. In this section, I will present the characterisation of the fundamental properties of these PPLN waveguide samples. This characterisation allowed me to model their behaviour (see Section 2.3) and subsequently use the PPLN samples properly in the experiments. I will investigate the period of the PPLN grating, tolerances for the variations in temperature and pump wavelength for the SHG process, and the conversion efficiency of these PPLN waveguide samples.

The QPM wavelength is a function of the PPLN grating period Λ given by [Fejer 92]

$$\lambda_{QPM} = \Lambda * 2(n_2 - n_1) \tag{2.48}$$

where n_1 and n_2 are the refractive indices at the wavelength of the FF wave and the SH wave respectively. In terms of Fig. 2.9, $n_1 = 2.138$, $n_2 = 2.182$. The calculated PPLN grating period as a function of the QPM wavelength is shown in Fig. 2.12(a). According to Eq. 2.48, $\Lambda \approx 18$ μm at the QPM wavelength of 1546 nm. Figure 2.12(b) shows the QPM wavelength as a function of the temperature for fixed PPLN grating periods. The square dots represent the experimental results, and the curves represent the numerical fits. As shown in the figure, the difference in the QPM wavelength of PPLN Sample 1 and PPLN Sample 2 used in the subsequent experiments is $\sim$ 1.1 nm at 50^oC, which corresponds to a slight grating period difference of $\sim$ 13 nm in terms of Eq. 2.48.

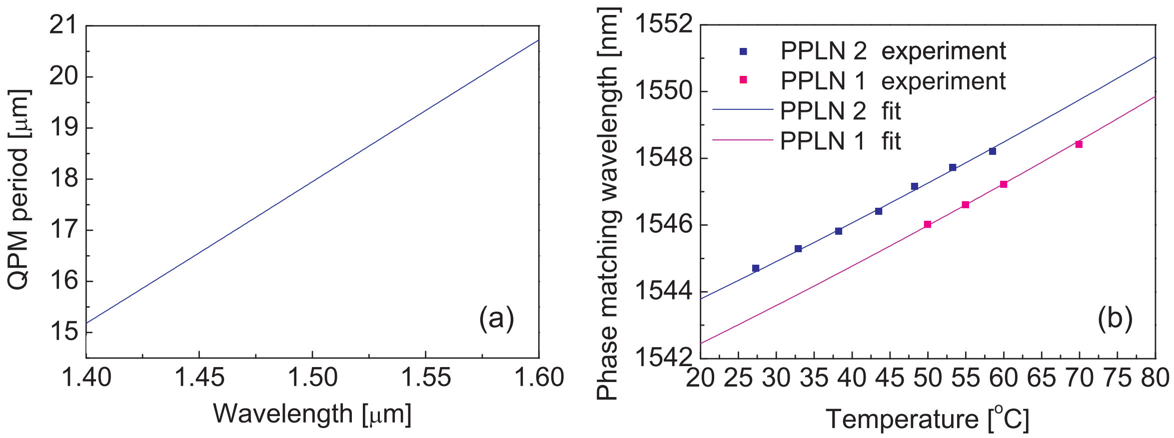

FIGURE 2.12: (a): Calculated PPLN grating period as a function of the QPM wavelength at 50^oC. (b): QPM wavelength as a function of the temperature for fixed PPLN grating periods.

To facilitate the use of the PPLN waveguides in the subsequent experiments of this thesis, it is important to evaluate the tolerances to temperature and pump wavelength variations for the SHG process. The spectral acceptance bandwidth is determined by the phase-mismatch between the FF wave and the SH wave, which is related to the length of the PPLN waveguide samples L and the refractive indices at the wavelength of the FF wave (n_1) and SH wave (n_2). Also, the refractive indices vary with the temperature. Theoretically, the spectral acceptance bandwidth of the SHG process in terms of the pump wavelength can be expressed as [Fejer 92]

$$\delta\lambda = \frac{0.4429\lambda}{L}\left|\frac{n_2 - n_1}{\lambda} + \frac{\partial n_1}{\partial\lambda} - \frac{1}{2}\frac{\partial n_2}{\partial\lambda}\right|^{-1} \tag{2.49}$$

For temperature tolerance, firstly the refractive indices are temperature-dependent. In addition, thermal expansion can alter both the period Λ and the total length L of the device.

The temperature acceptance width of the SHG process can be expressed as [Fejer 92]

$$\delta T = \frac{0.4429\lambda}{L} \left| \frac{\partial \triangle n}{\partial T} + \alpha \Delta n \right|^{-1} \tag{2.50}$$

where $\Delta n = n_2 - n_1$, λ is the wavelength at the FF wave, and α is the coefficient of linear thermal expansion.

By tuning the wavelength of the pump λ_p, the spectral acceptance bandwidth of the PPLN waveguide sample at 50^oC is measured to be $\sim$ 0.4 nm, and the experimental tuning curve is shown in Fig. 2.13(a), which is consistent with the calculated curve in terms of Eq. 2.23. By tuning the temperature of the PPLN device and with the pump at 1546 nm, the temperature acceptance bandwidth of the PPLN waveguide sample is measured to be $\sim 2.5^oC$, and the experimental tuning curve is shown in Fig. 2.13(b), which also matches the calculated curve.

[Schiek 99]

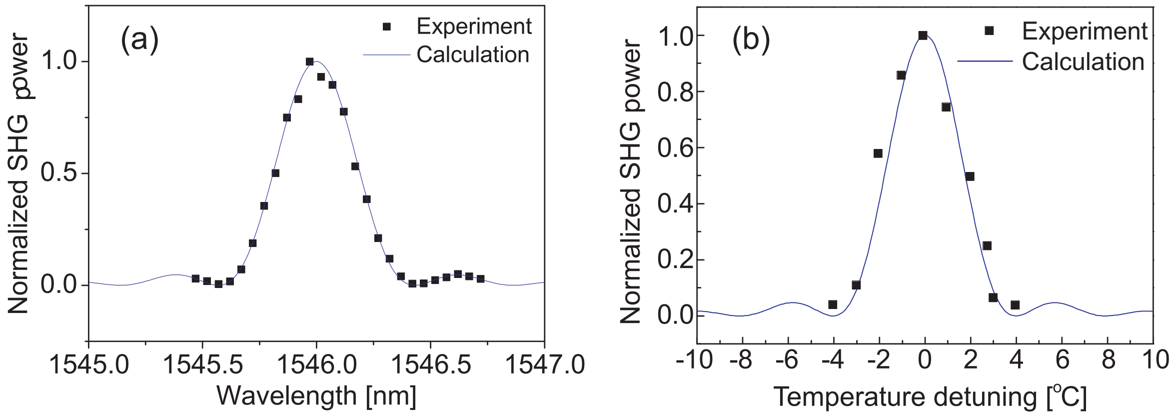

FIGURE 2.13: (a): SHG tuning curve of acceptance wavelength bandwidth at 50^oC. (b): Acceptable temperature bandwidth at 1546 nm.

Finally, the conversion efficiency is calculated in terms of the power relationship between the cSHG/DFG output and the input signal. Under the low gain and non-depleted pump assumption, the power of the SH can be written as [Banfi 98]

$$P_{SH} = \eta_{nor} L^2 P_{pump}^2 \tag{2.51}$$

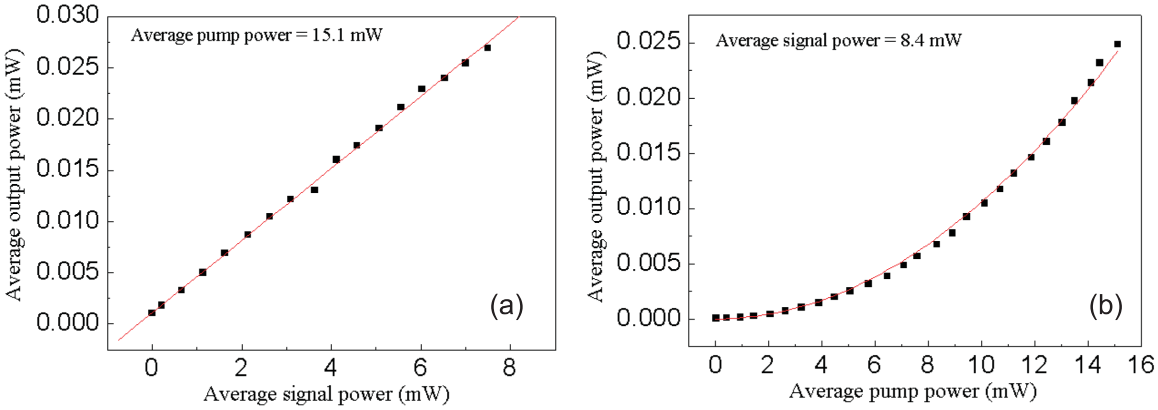

FIGURE 2.14: (a): The output power of the cSHG/DFG process as a function of the signal power. (b): The output power of the cSHG/DFG process as a function of the pump power.

where $\eta_{nor} = (\omega_{SH}\kappa)^2$ is the normalised conversion efficiency of the SHG interaction. In the subsequent DFG interaction, the output power can be written as [Langrock 06]

$$P_{DFG} = \eta_{nor(DFG)} L^2 P_{SH} P_{signal} = \frac{1}{4}\eta_{nor} L^2 P_{SH} P_{signal} \tag{2.52}$$

where $\eta_{nor(DFG)} = (\omega_{out}\kappa)^2$ is the normalised conversion efficiency of the DFG interaction. Hence, under the nondepleted pump assumption, the output power generated in a cSHG/DHG interaction can be written as [Langrock 06]

$$P_{out} = (\eta_{nor} L^2 P_{pump}/2)^2 P_{signal} \tag{2.53}$$

Hence, the average power of the cSHG/DFG output P_{out} is proportional to the average power of the input signal P_{signal}, while it grows quadratically with the average power of the pump P_{pump}. In the experiment, the wavelength arrangement followed Fig. 2.7. Two CW lasers operating at 1556 nm and 1546 nm were used as the signal and the pump respectively and launched into PPLN 1. The output was generated through cSHG/DFG at 1536 nm. PPLN 1 operated at $50^o C$. The total insertion loss of PPLN 1 was measured to be 3.8 dB, and the propagation loss in the 3-cm PPLN waveguides was assumed to be $\sim$ 1 dB (assuming a typical propagation loss of 0.3 dB/cm for fundamental frequency wave and 0.6 dB/cm for SH wave, Ref. [Schiek 99]). Therefore, each coupling loss between the fibre pigtail and the PPLN waveguide was assumed to be 1.4 dB ((3.8 dB − 1 dB) / 2).

The external input power of the signal and the pump was measured using a power meter. Subtracting the coupling loss (1.4 dB) from the external input power, the internal input power could be obtained. Also, by monitoring with an OSA, the power ratios between the signal, the pump and the output were known and the power of the output could be calculated accordingly. The experimental results are shown in Fig. 2.14. The normalised conversion efficiency of the PPLN sample was calculated to be $\eta_{nor} \approx 81.2\%(\text{W}\cdot\text{cm}^2)^{-1}$ through substituting the experimental input and output powers shown in Fig. 2.14 into numerical modelling which will be introduced in the following section.

2.3 Numerical simulations of second-order interactions in PPLN

In this section, numerical simulations of the SHG, SFG, DFG, cSHG/DFG and cSFG/DFG interactions in PPLN waveguides are performed to support the experiments presented in the subsequent chapters.

2.3.1 Second harmonic generation

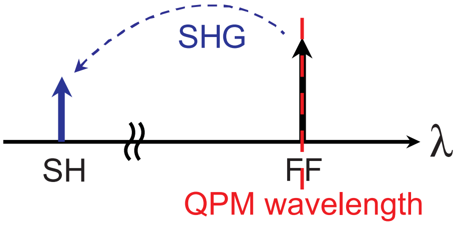

Figure 2.15: Illustration of second harmonic generation.

The SHG process in PPLN waveguides as illustrated in Fig. 2.15 is modelled firstly. When loss, pump depletion, phase mismatch, group-velocity mismatch (GVM) and GVD are taken into account, the propagation of the FF and SH pulses and the coupling between them during the SHG process are modelled by the coupled-mode (pulse propagation) equations [Boyd 03, Agrawal 07]:

$$\frac{\partial A_{FF}(z)}{\partial z}+\beta_{1FF}\frac{\partial A_{FF}(z)}{\partial t}+i\frac{\beta_{2FF}}{2}\frac{\partial^2 A_{FF}(z)}{\partial t^2}-\frac{\alpha_{FF}}{2}A_{FF}=-i\omega_{FF}\kappa_{SHG}A^*_{FF}(z)A_{SH}(z)e^{-i\Delta\beta z} \tag{2.54}$$

$$\frac{\partial A_{SH}(z)}{\partial z}+\beta_{1SH}\frac{\partial A_{SH}(z)}{\partial t}+i\frac{\beta_{2SH}}{2}\frac{\partial^2 A_{SH}(z)}{\partial t^2}-\frac{\alpha_{SH}}{2}A_{SH}=-i\omega_{FF}\kappa_{SHG}A^2_{FF}(z)e^{i\Delta\beta z} \tag{2.55}$$

where $\Delta\beta = \beta(\omega_{SH}) - 2\beta(\omega_{FF}) - 2\pi/\Lambda$ is the phase mismatch of the SHG process, β_{1FF} and β_{1SH} denote the inverse of the group velocity at the FF and SH frequencies respectively, β_{2FF} and β_{2SH} denote the intra-pulse group-velocity dispersion (IGVD) parameter at the FF and SH frequencies respectively. Briefly, the pulse envelope moves at the group velocity $v_g = 1/\beta_1$, while β_2 is responsible for pulse broadening. α_{FF} and α_{SH} are the waveguide propagation losses at the FF and SH frequencies respectively. There is no analytical solution for the set of Equations 2.54 and 2.55, so they were numerically solved using the symmetric split-step Fourier method as introduced in Ref. [Agrawal 07] with a Runge-Kutta algorithm.

The left hand sides of Equations 2.54 and 2.55 are pulse propagation equations which account for the loss, the GVM, and IGVD of the FF and SH pulses, as they propagate through the PPLN waveguides [Agrawal 07]. On the right hand side of Equations 2.54 and 2.55, the coupled-mode differential equations which are given by Eq. 2.20 and Eq. 2.21 describe the coupling between the FF and SH pulses during the SHG interaction [Boyd 03]. The effects of dispersion (GVM and IGVD) and the effect of coupling act together along the length of the PPLN waveguide. With the split-step Fourier method, an approximate solution is obtained by assuming that the dispersion effects and the coupling effects act independently over a small distance. The length of the PPLN device was divided into large number of small segments. In each small segment, the GVM and IGVD effects were modelled in the frequency domain first. Subsequently, Fourier transform was performed to convert the optical signal from the frequency domain to the time domain, and then Fourth-order Runge-Kutta algorithm was employed to solve the coupled-mode equations above in the time domain.

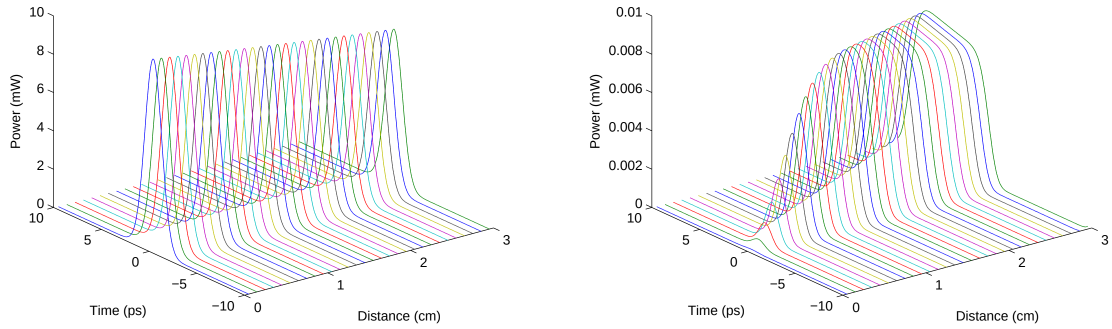

(a) Fundamental frequency pulse (b) SH pulse

FIGURE 2.16: Propagation of (a) the FF pulse (b) the SH pulse in SHG (2-ps input pulse with 10 mW peak power, and in a 30-mm-long PPLN waveguide)

In the simulation, the group velocity of the FF pulse at 1546 nm is $v_g = 1/\beta_{1FF} = 1.37386 \times 10^8$m/s, and the group velocity of the SH pulse at 773 nm is $v_g = 1/\beta_{1SH} = 1.318089 \times 10^8$ m/s as shown in Fig. 2.9. The normalized efficiency is $\eta_{nor} = 75\%(\text{Wcm}^2)^{-1}$ as calculated in Section 2.2 above. The central wavelength of the FF pulse is set at the QPM wavelength of the PPLN waveguide. In bulk PPLNs, the GVD parameter of the FF pulse at 1546 nm is $\beta_{2FF} = 1.02173 \times 10^{-25}$ s^2/m, and the GVD parameter of the SH pulse at 773 nm is $\beta_{2SH} = 3.93251 \times 10^{-25}$ s^2/m as shown in Fig. 2.11. The length of the PPLN device is 3 cm. The waveguide propagation losses α_{FF} and α_{SH} are set to be 0.3 dB/cm and 0.6 dB/cm. The input FF pulse is a 2-ps transform-limited Gaussian pulse with peak power of 10 mW. As shown in Fig. 2.16(a), as the FF pulse propagates through the PPLN waveguide, the peak power of the FF pulse remains almost constant with only a slight attenuation due to the propagation loss of the waveguide, which indicates that there is no severe pump depletion during the SHG interaction. As shown in the simulation result in Fig. 2.16(b), the GVM plays the prominent role in the shaping of the SH pulses. Because of the short length of the PPLN waveguide, the effects of intra-pulse GVD on the SH pulse shapes are negligible for pulses which are $\sim$ 50 fs or longer, but the effects of intra-pulse GVD on the SH pulse shapes are not negligible for pulses which are $\sim$ 10 fs or shorter [Sidick 95]. In the time domain, due to the difference in group velocities, the FF pulse propagates faster than the SH pulse in lithium niobate waveguides, resulting in a temporal walk-off effect. The length over which the FF pulse walks through the SH pulse is named the walk-off length $L_{walk\ off}$, which is defined as

$$L_{walk\ off} = \frac{\tau}{\delta v} \tag{2.56}$$

where τ is the pulse width of the FF pulse, and $\delta v = \beta_{1FF} - \beta_{1SH}$ is the GVM parameter between the FF and SH pulses.

In the frequency domain, the temporal walk-off effect can be understood as a finite SHG acceptance bandwidth for the SHG interaction. In a PPLN waveguide with a length of L, the relationship between the output SH pulses and the input FF pulses was derived in [Imeshev 00, Prawiharjo 05] and is (see also Chapter 3):

$$A_{SH}(L, \Omega) = D_{SHG}(\Omega)[A_{FF}(\Omega) * A_{FF}(\Omega)] \tag{2.57}$$

where $*$ denotes convolution and D_{SHG} denotes the filtering function between the output SH's spectrum and the auto-correlation of the input FF wave's spectrum.

In the case that the pulse width of the input FF pulse is shorter than the walk-off length of the PPLN waveguide and the spectral bandwidth of the input FF pulse is wider than the SHG acceptance bandwidth of the PPLN waveguides, the SHG acceptance bandwidth is insufficient to accommodate the FF pulse's spectrum. As a result, the generated SH pulses become broader than the input FF pulse as shown in Fig. 2.16(b). In contrast, in the case that the pulse width of the input FF pulse is longer than the walk-off length of the PPLN waveguide and the spectral bandwidth of the input FF pulse is narrower than the SHG acceptance bandwidth of the PPLN waveguides, the SHG acceptance bandwidth is sufficient to accommodate the FF pulse's spectrum. As a result, the temporal width of the SH pulse is equal to the square of the temporal width of the FF pulse as shown at the distance of $z = 6.7\text{mm} = L_{walk\ off}$ in Fig. 2.16(b).

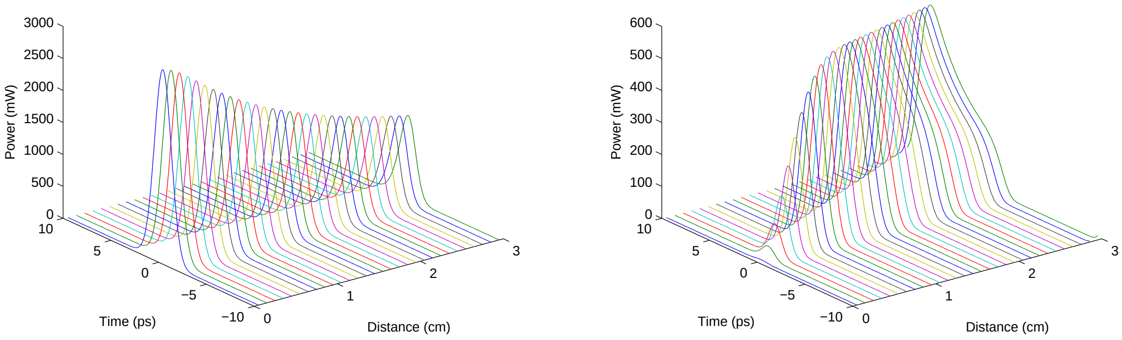

(a) Fundamental frequency pulse

(b) SH pulse

FIGURE 2.17: In depleted pump case, propagation of (a) the FF pulse (b) the SH pulse in the SHG interaction (2-ps input pulse with 3 W peak power, and in a 30-mm-long PPLN waveguide)

In order to investigate the effect of pump depletion, the peak power of the FF pulses was increased from 10 mW to 3 W in the simulation, while the length of the PPLN device was maintained to 3 cm. As shown in the simulation result of Fig. 2.17(a), the peak power of the FF pulse decreases significantly as it propagates through the PPLN waveguide owing to the pump depletion.The SH pulse still broadens as it propagates through the PPLN waveguide due to the GVM effect, but the top of the generated SH is not flat, compared to the case of no severe pump depletion.

2.3.2 Sum frequency generation

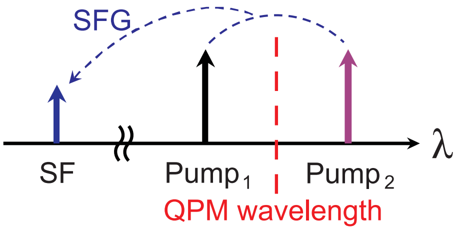

FIGURE 2.18: Illustration of the sum frequency generation interaction.

The coupled-mode equations for the SFG interaction in the PPLN waveguides which is shown in Fig. 2.18 can be written as

$$\frac{\partial A_{P1}(z)}{\partial z} + \beta_{1P1}\frac{\partial A_{P1}(z)}{\partial t} + i\frac{\beta_{2P1}}{2}\frac{\partial^2 A_{P1}(z)}{\partial t^2} - \frac{\alpha_{P1}}{2}A_{P1} = -i\omega_{P1}\kappa_{SFG}A^*_{P2}(z)A_{SF}(z)e^{-i\Delta kz} \tag{2.58}$$

$$\frac{\partial A_{P2}(z)}{\partial z} + \beta_{1P2}\frac{\partial A_{P2}(z)}{\partial t} + i\frac{\beta_{2P2}}{2}\frac{\partial^2 A_{P2}(z)}{\partial t^2} - \frac{\alpha_{P2}}{2}A_{P2} = -i\omega_{P2}\kappa_{SFG}A^*_{P1}(z)A_{SF}(z)e^{-i\Delta kz} \tag{2.59}$$

$$\frac{\partial A_{SF}(z)}{\partial z} + \beta_{1SF}\frac{\partial A_{SF}(z)}{\partial t} + i\frac{\beta_{2SF}}{2}\frac{\partial^2 A_{SF}(z)}{\partial t^2} - \frac{\alpha_{SF}}{2}A_{SF} = -i\omega_{SF}\kappa_{SFG}A_{P1}(z)A_{P2}(z)e^{i\Delta kz} \tag{2.60}$$

where $\Delta k = k(\omega_{SF}) - k(\omega_{P1}) - k(\omega_{P2}) - 2\pi/\Lambda$ is the phase mismatch of the SFG interaction. κ_{SFG} is the conversion efficiency of the SFG interaction. β_{1x}, β_{2x}, and α_x (at each wavelength x, with $x = P1$, $P2$, SF) are the inverse of the group velocity, the GVD parameter and the attenuation coefficients of Pump 1, Pump 2 and the SF respectively. It is noted that

In the simulation, the phase-matching condition in the PPLN waveguide is satisfied. The length of the PPLN device is 3 cm. Both Pump 1 and Pump 2 are both 2-ps transform-limited Gaussian pulses with peak power 5 mW as shown in Fig. 2.19(a) and Fig. 2.19(b). As shown in Fig. 2.19(c), the SF pulse becomes broader due to the GVM effect, similar to the case of SHG. In the case that the peak power of the input pumps in SFG is half of the peak power of the input FF pulse in SHG, the outputs of SHG and SFG are equal in power, which is consistent with the theory (Eq. 2.23 and 2.31).

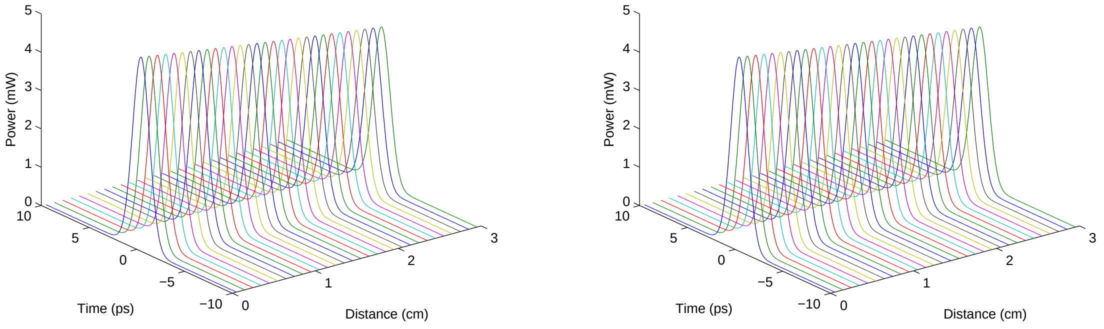

(a) Pump 1

(b) Pump 2

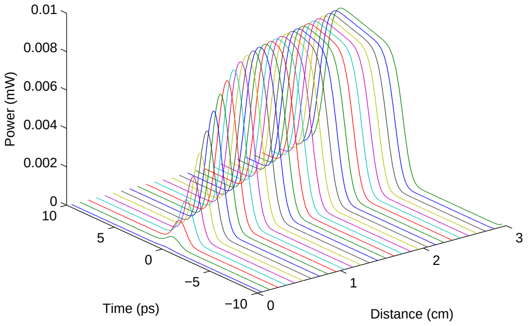

(c) SF pulse

FIGURE 2.19: Propagation of (a) Pump 1 pulse (b) Pump 2 pulse (C) the SF pulse in SFG (2-ps input pulse, 30-mm-long PPLN waveguide)

2.3.3 Difference frequency generation

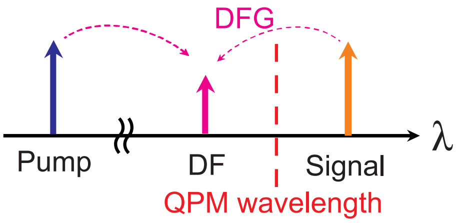

FIGURE 2.20: Illustration of difference frequency generation.

The coupled-mode equations for the DFG interaction in the PPLN waveguides which is illustrated in Fig. 2.20 can be written as:

$$\frac{\partial A_S(z)}{\partial z} + \beta_{1S}\frac{\partial A_S(z)}{\partial t} + i\frac{\beta_{2S}}{2}\frac{\partial^2 A_S(z)}{\partial t^2} - \frac{\alpha_S}{2}A_S = -i\omega_S\kappa_{DFG}A^*_{DF}(z)A_P(z)e^{-i\Delta kz} \tag{2.61}$$

$$\frac{\partial A_P(z)}{\partial z} + \beta_{1P}\frac{\partial A_P(z)}{\partial t} + i\frac{\beta_{2P}}{2}\frac{\partial^2 A_P(z)}{\partial t^2} - \frac{\alpha_P}{2}A_P = -i\omega_P\kappa_{DFG}A_{DF}(z)A_S(z)e^{i\Delta kz} \tag{2.62}$$

$$\frac{\partial A_{DF}(z)}{\partial z} + \beta_{1DF}\frac{\partial A_{DF}(z)}{\partial t} + i\frac{\beta_{2DF}}{2}\frac{\partial^2 A_{DF}(z)}{\partial t^2} - \frac{\alpha_{DF}}{2}A_{DF} = -i\omega_{DF}\kappa_{DFG}A^*_S(z)A_P(z)e^{-i\Delta kz} \tag{2.63}$$

where $\Delta k = k(\omega_P) - k(\omega_S) - k(\omega_{DF}) - 2\pi/\Lambda$ is the phase mismatch of the DFG interaction. κ_{DFG} is the conversion efficiency of the DFG interaction. β_{1x}, β_{2x}, and α_x (at each wavelength x, with $x = P$, S, DF) are the inverse of the group velocity, the GVD parameter and the attenuation coefficients of the pump, the signal and the DF wave respectively.

In the simulation, the phase-matching condition in the PPLN crystal is satisfied. Both the input signal pulse and pump pulse are 2-ps FWHM transform-limited Gaussians with peak power 10 mW as shown in Fig. 2.21(a) and Fig. 2.21(b). Because of the GVM effect, the signal pulse and the pump pulse propagate at different group velocities. After one walk-off length, the signal and pump pulses completely walk through each other. As shown in Fig. 2.21(c), the DF pulse grows at the beginning of the crystal via DFG interaction. But when the signal and pump pulses completely walk through each other, DFG interaction stops and the DF pulse ceases to build up.

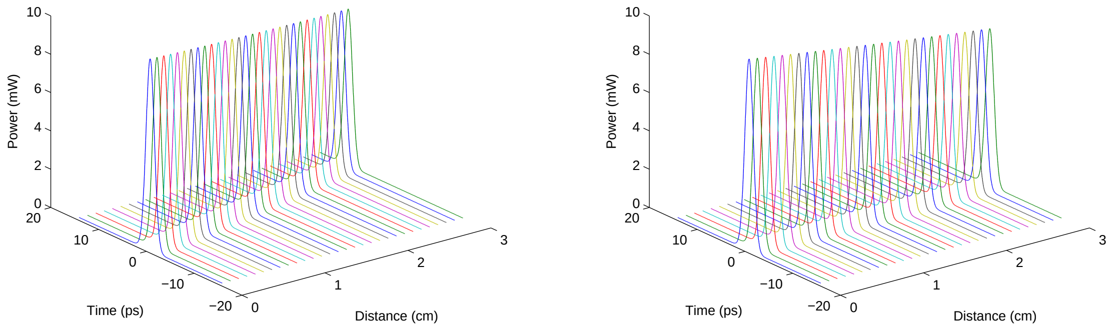

(a) Pump pulse

(b) Signal pulse

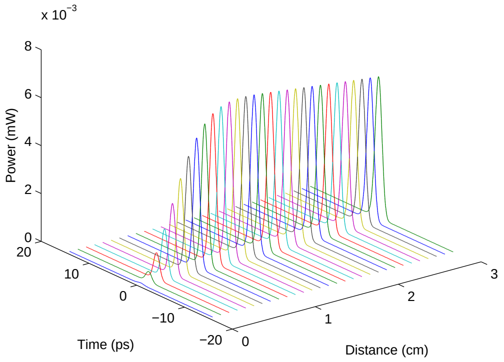

(c) DF pulse

FIGURE 2.21: Propagation of (a) the pump pulse (b) the signal pulse (C) the DF pulse in DFG (2-ps input pulse, 30-mm-long PPLN waveguide)

In the frequency domain, the relationship between the output DF pulses and the input pulses in a PPLN waveguide with a length of L was derived in Ref. [Prawiharjo 05] and is:

$$A_{DF}(L,\Omega) = A'_P(L,\Omega) * A^*_S(-\Omega) \tag{2.64}$$

where A'_P is the effective pump and can be expressed as $A'_P = G_{DFG}(\Omega)A_P(\Omega)$ and G_{DFG} is the filtering function between the effective pump and the pump.

The SHG interaction's filtering function applies on the convolution of the input pulses, so the temporal walk-off effect yields a broad output pulse. The DFG filtering function applies on the pump pulse. Therefore, the temporal walk-off effect has a less dramatic effect on the output pulse in DFG than in SFG, and the output pulse of DFG does not broaden significantly as shown in Fig. 2.21(c) [Prawiharjo 05].

2.3.4 Cascaded quadratic interactions (cSHG/DFG, cSFG/DFG)

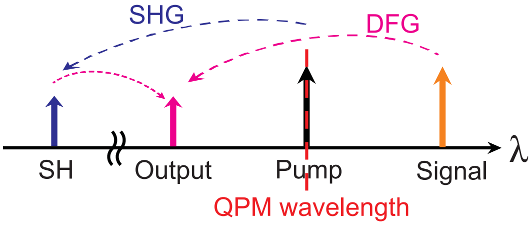

FIGURE 2.22: Illustration of cascaded second harmonic generation and difference frequency generation.

The coupled-mode equations for the cSHG/DFG interaction in the PPLN waveguides which is illustrated in Fig. 2.22 can be written as:

$$\frac{\partial A_P(z)}{\partial z} + \beta_{1P}\frac{\partial A_P(z)}{\partial t} + i\frac{\beta_{2P}}{2}\frac{\partial^2 A_P(z)}{\partial t^2} - \frac{\alpha_P}{2}A_P = -i\omega_P\kappa_{SHG}A_P^*(z)A_{SH}(z)e^{-i\Delta k_{SHG}z} \tag{2.65}$$

$$\begin{aligned}\frac{\partial A_{SH}(z)}{\partial z} + \beta_{1SH}\frac{\partial A_{SH}(z)}{\partial t} + i\frac{\beta_{2SH}}{2}\frac{\partial^2 A_{SH}(z)}{\partial t^2} - \frac{\alpha_{SH}}{2}A_{SH} &= -i\omega_P\kappa_{SHG}A_P^2(z)e^{i\Delta k_{SHG}z} \\ &\quad - i\omega_{SH}\kappa_{DFG}A_O(z)A_S(z)e^{i\Delta k_{DFG}z}\end{aligned} \tag{2.66}$$

$$\frac{\partial A_S(z)}{\partial z} + \beta_{1S}\frac{\partial A_S(z)}{\partial t} + i\frac{\beta_{2S}}{2}\frac{\partial^2 A_S(z)}{\partial t^2} - \frac{\alpha_S}{2}A_S = -i\omega_S\kappa_{DFG}A_O^*(z)A_{SH}(z)e^{-i\Delta k_{DFG}z} \tag{2.67}$$

$$\frac{\partial A_O(z)}{\partial z} + \beta_{1O}\frac{\partial A_O(z)}{\partial t} + i\frac{\beta_{2O}}{2}\frac{\partial^2 A_O(z)}{\partial t^2} - \frac{\alpha_O}{2}A_O = -i\omega_O\kappa_{DFG}A_S^*(z)A_{SH}(z)e^{-i\Delta k_{DFG}z} \tag{2.68}$$

where $\Delta k_{SHG} = k(\omega_{SH}) - 2k(\omega_P) - 2\pi/\Lambda$ is the phase mismatch of the SHG interaction and $\Delta k_{DFG} = k(\omega_{SH}) - k(\omega_{signal}) - k(\omega_{output}) - 2\pi/\Lambda$ is the phase mismatch of the DFG interaction. κ_{SHG} and κ_{DFG} are the conversion efficiency of the SHG and DFG interaction respectively. β_{1x}, β_{2x}, and α_x (at each wavelength x, with $x = P, SH, S, O$) are the inverse of the group velocity, the GVD parameter and the attenuation coefficients of the pump, the SH, the signal and the output respectively.

In the simulation, the phase-matching condition in the PPLN waveguide is satisfied. Both the input signal pulse and the pump pulse are 2-ps transform-limited Gaussian pulses with peak power 10 mW as shown in Fig. 2.23(a) and Fig. 2.23(c). In the cSHG/DFG interaction, the difference in the group velocities between the pump, signal and output pulses is small. The pump generates SH, and the walk-off effect makes SH broadening in time as shown in Fig. 2.23(b). The pump keeps generating SH which overlaps with the signal pulse in time. Hence, the broadening of the effective SH extends the distance over which the DFG interaction between the SH and signal pulse takes place. Similar to the simple DFG interaction, the output pulse of cSHG/DFG interaction does not broaden significantly as shown in Fig. 2.23(d) [Prawiharjo 05].

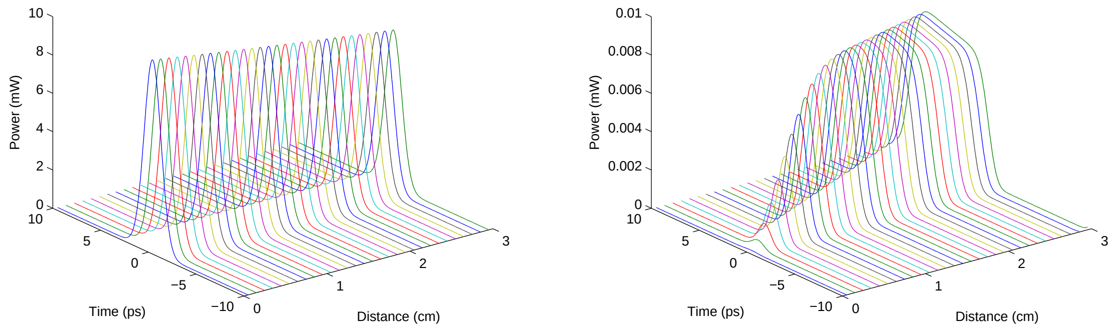

(a) Pump pulse (b) SH pulse

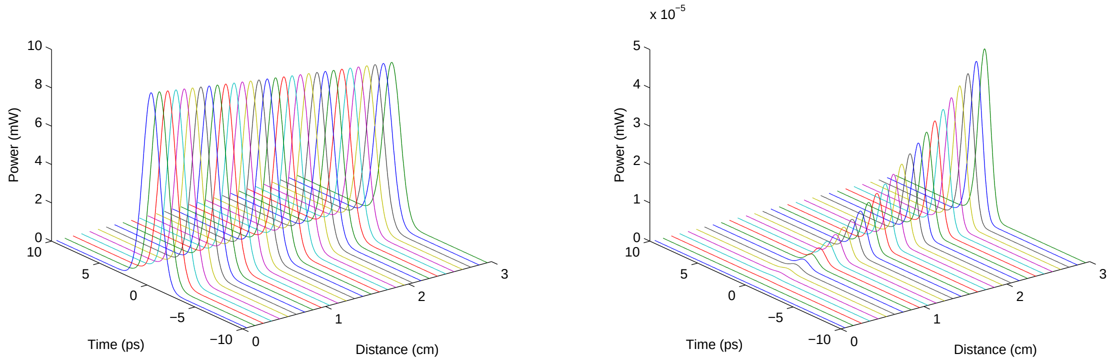

(c) Signal pulse (d) Output pulse

FIGURE 2.23: Propagation of (a) the pump pulse (b) the SH pulse (c) the signal pulse (d) the output pulse in cSHG/DFG (2-ps input pulse, 30-mm-long PPLN waveguide)

In the frequency domain, the relationship between the output pulses and the input pulses in a PPLN waveguide with a length of L was derived in [Prawiharjo 05] as follows:

$$A_O(L, \Omega) = A'_{SH}(L, \Omega) * A^*_S(-\Omega) \tag{2.69}$$

where $A'_{SH} = G_C(\Omega)(A_P(\Omega) * A_P(\Omega))$ is the effective SH, and $G_C(\Omega)$ is the filtering function of cSHG/DFG interaction.

Due to the similarity between Eqns. 2.69 and 2.64, the cSHG/DFG interaction inherits most of its features from the DFG interaction compared to the SHG interaction. In cSHG/DFG interaction, the spectral filtering function applies on the pump pulse rather than the signal pulse [Prawiharjo 05].

In order to investigate the effect of pump depletion, the peak power of the pump pulse was increased to 3 W, and the signal pulse was increased to 0.1 W. As shown in the simulation results in Fig. 2.24(a), the peak power of the pump pulse decreases as it propagates through the PPLN waveguide due to pump depletion. As shown in Fig. 2.24(b), the SH pulse still broadens as it propagates through the PPLN waveguide due to the GVM effect. But compared to the case of no severe pump depletion, the top of the generated SH is not flat. In Fig. 2.24(c), the signal pulse is amplified as it propagates through the PPLN waveguide, because when a photon of SH is destroyed, both a photon of frequency ω_O and a signal photon are created. This process is also known as optical parametric amplification (OPA). As shown in Fig. 2.24(d), the shape of the output pulse of the cascaded quadratic interaction is not distorted, but the rate of growth slows down due to pump depletion.

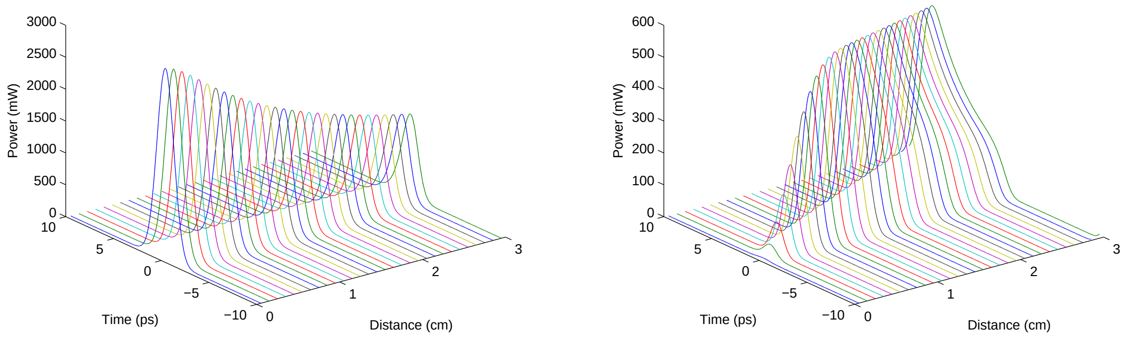

(a) Pump pulse (b) SH pulse

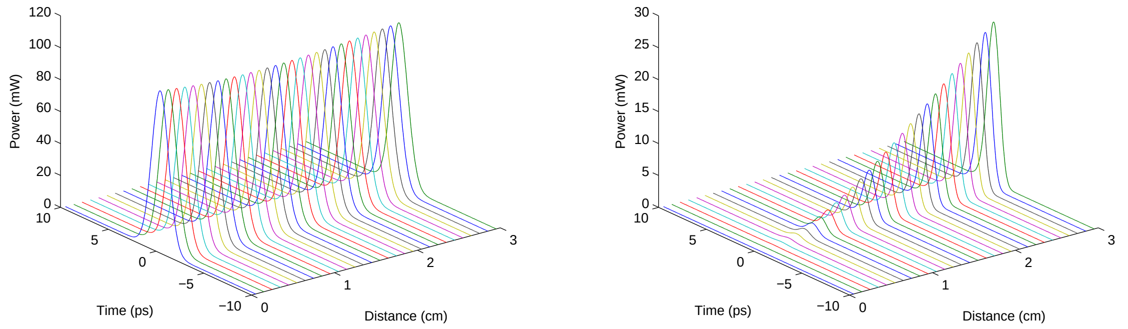

(c) Signal pulse (d) Output pulse

FIGURE 2.24: Propagation of (a) the pump pulse (b) the SH pulse (c) the signal pulse (d) the output pulse in cSHG/DFG (2-ps pump pulse with peak power of 3 W and 2-ps signal pulse with peak power of 0.1 W, 30-mm-long PPLN waveguide)

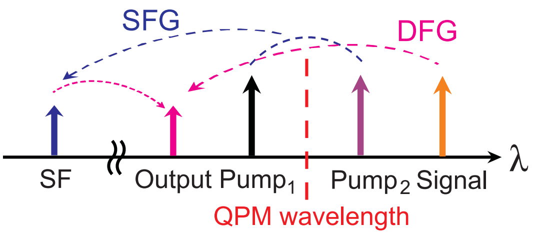

FIGURE 2.25: Illustration of the cascaded sum frequency generation and difference frequency generation interaction.

The coupled-mode equations for the cSFG/DFG interaction in the PPLN waveguides which is illustrated in Fig. 2.25 can be written as

$$\frac{\partial A_{P1}(z)}{\partial z}+\beta_{1P1}\frac{\partial A_{P1}(z)}{\partial t}+i\frac{\beta_{2P1}}{2}\frac{\partial^2 A_{P1}(z)}{\partial t^2}-\frac{\alpha_{P1}}{2}A_{P1}=-i\omega_{P1}\kappa_{SFG}A^*_{P2}(z)A_{SF}(z)e^{-i\Delta k_{SFG}z} \tag{2.70}$$

$$\frac{\partial A_{P2}(z)}{\partial z}+\beta_{1P2}\frac{\partial A_{P2}(z)}{\partial t}+i\frac{\beta_{2P2}}{2}\frac{\partial^2 A_{P2}(z)}{\partial t^2}-\frac{\alpha_{P2}}{2}A_{P2}=-i\omega_{P2}\kappa_{SFG}A^*_{P1}(z)A_{SF}(z)e^{-i\Delta k_{SFG}z} \tag{2.71}$$

$$\begin{aligned}\frac{\partial A_{SF}(z)}{\partial z}+\beta_{1SF}\frac{\partial A_{SF}(z)}{\partial t}+i\frac{\beta_{2SF}}{2}\frac{\partial^2 A_{SF}(z)}{\partial t^2}-\frac{\alpha_{SF}}{2}A_{SF}&=-i\omega_{SF}\kappa_{SFG}A_{P1}A_{P2}(z)e^{i\Delta k_{SFG}z}\\&\quad-i\omega_{SF}\kappa_{DFG}A_O(z)A_S(z)e^{i\Delta k_{DFG}z}\end{aligned} \tag{2.72}$$

$$\frac{\partial A_S(z)}{\partial z}+\beta_{1S}\frac{\partial A_S(z)}{\partial t}+i\frac{\beta_{2S}}{2}\frac{\partial^2 A_S(z)}{\partial t^2}-\frac{\alpha_S}{2}A_S=-i\omega_S\kappa_{DFG}A^*_O(z)A_{SF}(z)e^{-i\Delta k_{DFG}z} \tag{2.73}$$

$$\frac{\partial A_O(z)}{\partial z}+\beta_{1O}\frac{\partial A_O(z)}{\partial t}+i\frac{\beta_{2O}}{2}\frac{\partial^2 A_O(z)}{\partial t^2}-\frac{\alpha_O}{2}A_O=-i\omega_O\kappa_{DFG}A^*_S(z)A_{SF}(z)e^{-i\Delta k_{DFG}z} \tag{2.74}$$

where $\Delta k_{SFG}=k(\omega_{SF})-k(\omega_{P1})-k(\omega_{P2})-2\pi/\Lambda$ is the phase mismatch of the SFG interaction and $\Delta k_{DFG}=k(\omega_{SF})-k(\omega_{signal})-k(\omega_{output})-2\pi/\Lambda$ is the phase mismatch of the DFG interaction. κ_{SFG} and κ_{DFG} are the conversion efficiency of the SFG and DFG interaction respectively. β_{1x}, β_{2x}, and α_x (at each wavelength x, with $x = P1$, $P2$, SF, S, O) are the inverse of the group velocity, the GVD parameter and the attenuation coefficients of Pump 1, Pump 2, the SF, signal and output respectively.

In the simulation, the phase-matching condition in the PPLN waveguide is satisfied. The length of the PPLN device is 3 cm. Pump 1, Pump 2 and the signal are all 2-ps transform-limited Gaussian pulses. The peak power of Pump 1 and Pump 2 is 5 mW, and the peak power of signal is 10 mW. As shown in Fig. 2.26(a), 2.26(b), 2.26(c), 2.26(d) and 2.26(e), the behavior of the cSFG/DFG interaction is analogous to that of cSHG/DFG.

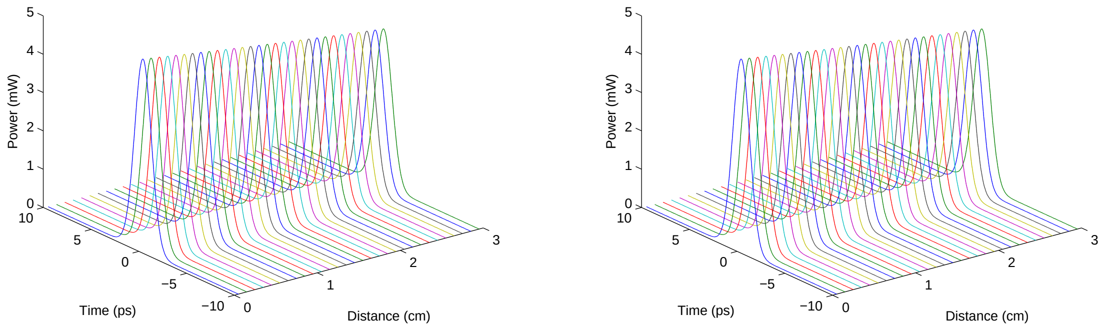

(a) Pump 1

(b) Pump 2

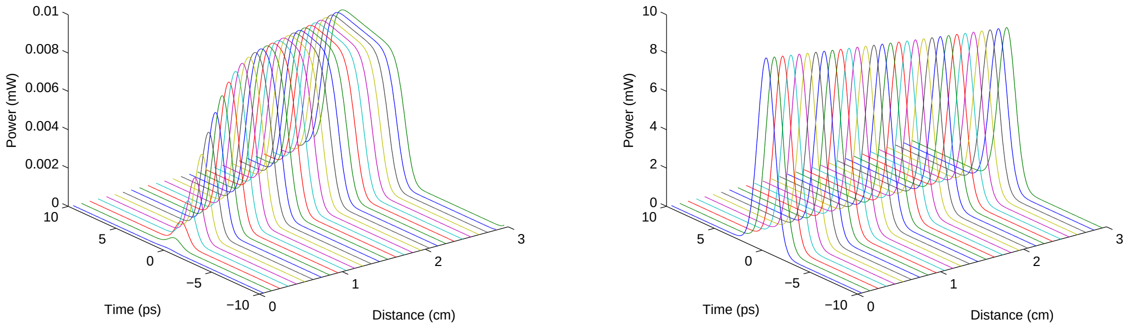

(c) SH pulse

(d) Signal pulse

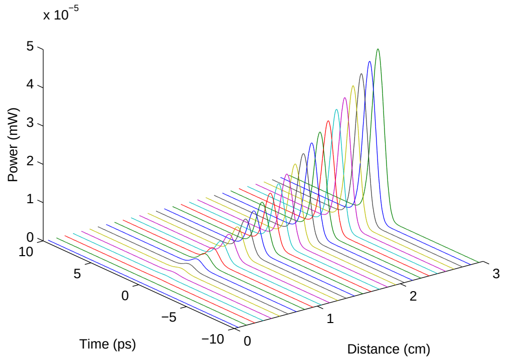

(e) Output pulse

FIGURE 2.26: Propagation of (a) Pump 1 (b) Pump 2 (c) the SF pulse (d) the signal pulse (e) the output pulse in cSFG/DFG (2-ps input pulse, 30-mm-long PPLN waveguide)

2.4 Previous works on all-optical signal processing with PPLN waveguides

All-optical signal processing using second-order nonlinearities in PPLN waveguides is of high interest for telecommunications applications. For instance, all-optical wavelength conversion relying on cSHG/DFG and cSFG/DFG were demonstrated by Gallo *et al.* [Gallo 97] and Lee *et al.* [Lee 03], respectively. All-optical demultiplexing based on the cSHG/DFG effect has been demonstrated by Fukuchi *et al.* [Fukuchi 03]. Mid-span spectral inversion using a PPLN waveguide-based phase conjugator for the dispersion compensation was demonstrated by Chou *et al.* [Chou 00]. In this chromatic dispersion compensation scheme, the chirp of the signal induced by the dispersion of fibre span was inverted by PPLN waveguides placed at the middle point of the transmission link through the cSHG/DFG effect, and the inverted chirp was subsequently negated by the second half of the fibre link.

The demonstration of all-optical continuously-tunable delay elements using PPLN waveguides were reported by Wang *et al.* [Wang 05]. In that scheme, two PPLN waveguides were employed as two wideband tunable wavelength converters. The input signal was converted to a calculated wavelength by the first PPLN waveguide, and subsequently propagated through a length of dispersion compensating fibre (DCF) which resulted in a wavelength-dependent group delay. Finally the signal was converted back to the original wavelength by the second PPLN waveguide.

Optical phase erasure relying on the cascaded quadratic processes in PPLN waveguides was proposed by Wang *et al.* [Wang 08b]. When the signal was set at the QPM wavelength, its phase was doubled through the cSHG/DFG process, and input signals with binary value of "0" or "π" phase would have the same output phase owing to the periodicity of 2π for optical phase.

Clock recovery using a PPLN waveguide and based on opto-electronic phase-locked loop (PLL) was demonstrated by Ware *et al.* [Ware 08]. In that scheme, the phase comparison operation in the opto-electronic PLL was performed by SFG in the PPLN waveguide. Also, all-optical retiming relying on the manipulation of the temporal walk-off between the FF pulses and the SH pulses in PPLN waveguides was demonstrated by Hasegawa *et al.* [Hasegawa 04]. In that scheme, the input data pulses affected by timing jitter generated SH pulses through SHG. The slower-propagating SH pulses were subsequently gated by a slightly later incident clock pulse train through DFG, generating an output signal with suppressed timing jitter at a different wavelength.

PPLN-based add/drop multiplexing at 640 Gbit/s exploiting pump depletion effect and the cSFG/DFG process was demonstrated by Bogoni *et al.* [Bogoni 10]. By means of proper control of the pump powers, the dropped channels were depleted through the SFG process and converted to another wavelength through the subsequent DFG process. Also, based on the pump depletion effect, channel-selective data exchange for multiple WDM channels at 40 Gbit/s using PPLN waveguides was demonstrated by Wang *et al.* [Wang 10].

Frequency-resolved optical gating based on cascaded quadratic interactions in a PPLN waveguide for ultrashort-pulse diagnostics application was reported by Prawiharjo *et al.* [Prawiharjo 05]. Finally, several other applications, such as all-optical format conversions e.g. from carrier-suppressed return-to-zero (CSRZ) to return-to-zero (RZ) [Wang 08b], and non return-to-zero (NRZ) to RZ [Wang 07b, Wang 07c], as well as all-optical logic gates have also been reported, e.g. AND/NAND [Lee 06], OR [Wang 07a], NOT [Wang 06], XOR [Wang 07a], half-subtracter [Wang 08a] and half-adder [Bogoni 09].

2.5 Enabling technologies in the thesis

In this closing section of this chapter, I describe briefly two unconventional components, which have been frequently used in the experimental work that will be described in the following chapters. The first is a frequency resolved optical gating (FROG) system, where the gating is implemented using an electro-optic modulator, and which allows the simultaneous intensity and phase characterisation of ps-wide optical pulses. It had originally been constructed by a previous member of our group (Dr. M. Roelens) and sufficient understanding of its operation was required in order to use it properly. The second is a commercial programmable optical filter (Finiser Waveshaper) which allows fine control of both the phase and intensity of spectral components and which has only appeared in the market and was acquired in our lab during the course of my studies.

2.5.1 Linear frequency resolved optical gating

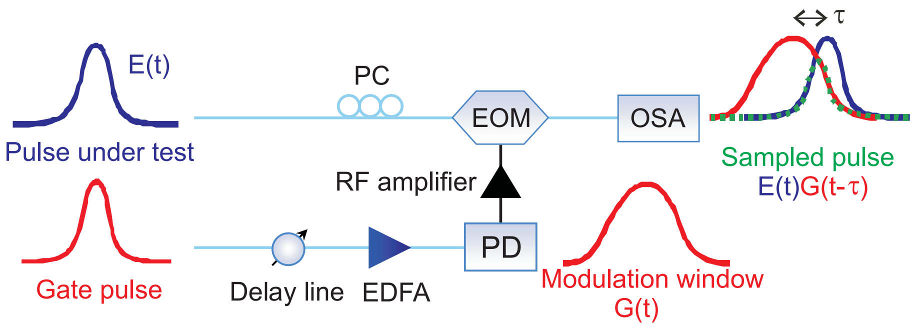

FIGURE 2.27: Illustration of a frequency resolved optical gating.

Since the time scale of the optical pulses of interest is much faster than the temporal response of any existing photo detectors, optical gating schemes, such as FROG, are employed to measure ultrashort pulses. FROG is a technique for the characterization of ultrashort pulses. FROG is capable of measuring the full time-dependent electric field including both the temporal amplitude and the temporal phase or equivalently measuring the optical spectrum including the frequency-dependent spectral phase [Kane 93].

In various configurations of nonlinear FROG, a pulse under test is optically gated by the replica of the same pulse (or by another pulse) through some nonlinear effect. Instead of using nonlinear effects, an alternative approach is to implement the gating using electro-optic modulators [Dorrer 02], namely linear FROG (L-FROG). L-FROG offers the benefit that only commonly available and fully fiberised devices are needed for its implementation. A schematic diagram of the L-FROG configuration is shown in Fig. 2.27. The pulse under test (with electric field $E(t)$) is sent to an electro-optic modulator (EOM) after polarization optimization, while the gate pulse is sent to a variable delay line, after which it is launched into a constant gain optical amplifier. This is to provide the correct input power for the receiving photodiode. The electrical pulse signal (with electric field $G(t-\tau)$) from the photodiode is amplified and sent to drive the EOM (τ is the relative delay between signal pulse and electrical signal in time, and tuned by the variable delay line). In terms of the modulation curve of the EOM, with proper bias current, the optical output of the EOM is more transparent as the driving radio-frequency electrical signal increases, and thus the electrical pulse signal is able to gate the optical pulse stream passing through the EOM. The gated signal is then spectrally resolved with an OSA. A spectrogram $I_{FROG}(\omega, \tau)$ with a very good spectral resolution can be obtained by sweeping the variable delay line, given by [Roelens 04, Reid 07]

$$I_{FROG}(\omega, \tau) = |\int_{-\infty}^{\infty} E(t)G(t-\tau)exp(i\omega t)dt|^2 \tag{2.75}$$

After obtaining the spectrogram, iterative retrieval algorithms can then be applied for reconstructing the intensity and phase profile of the pulse from the FROG spectrogram trace. Firstly, an initial guess of $E(t)$ and $G(t)$ is given. The calculated intensity $I_{Calculated}(\omega, \tau)$ and calculated phase $\phi_{Calculated}(\omega, \tau)$ can be retrieved as

$$\sqrt{I_{Calculated}(\omega, \tau)}\phi_{Calculated}(\omega, \tau) = \int_{-\infty}^{\infty} E(t)G(t)exp(-i\omega t)dt \tag{2.76}$$

Then the calculated intensity is replaced by the measured intensity. By doing inverse Fourier transform, the following semi-experimental and semi-calculated pulse is obtained

$$E(t, \tau) = F^{-1}\{\sqrt{I_{Measured}(\omega, \tau)}\phi_{Calculated}(\omega, \tau)\} \tag{2.77}$$

Ideally, the next guess for $E(t)$ represents a better estimation for the phase of the pulse. After a number of such iterations, the pulse converges to a solution eventually and the following error ε is minimized.

$$\varepsilon = \sqrt{\frac{1}{N^2}\sum_{i=1}^{N}\sum_{j=1}^{N}[I_{Calculated}(\omega_i, \tau_j) - I_{Measured}(\omega_i, \tau_j)]^2} \tag{2.78}$$

where N is the number of time points and frequency points in the spectrogram, ω_i is the i-th frequency point and τ_j is the j-th delay in the measured spectrogram.

2.5.2 Optical processor filter

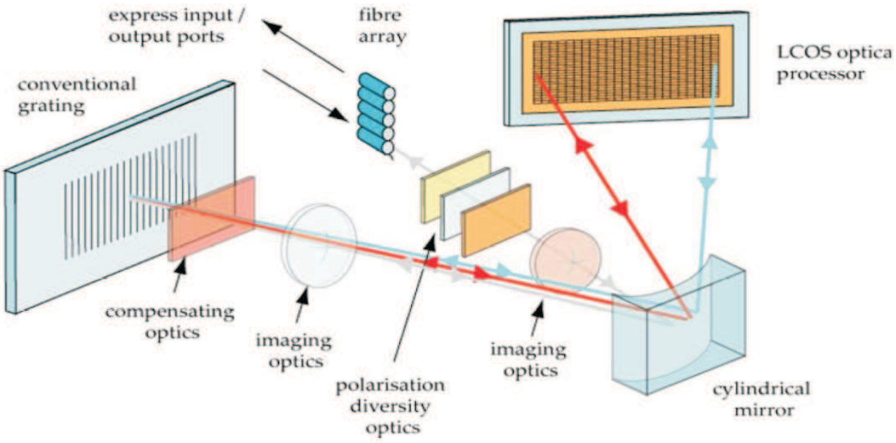

FIGURE 2.28: Illustration of an optical processor (wave shaper). Ref. [Opt].

In some of the experiments I present in the following chapters, I need the capability of accurately controlling the phase and/or intensity of optical wavelengths. This is facilitated by a commercial piece of equipment (Waveshaper, Finisar), which I will briefly describe below.

As shown in Fig. 2.28, a Waveshaper consists of a fibre array, polarization diversity optics, 4 - f wavelength imaging optics, a cylindrical mirror, compensating optics, a conventional grating and a liquid crystal on silicon (LCoS) optical processor. The fibre array consists of one common input port and several output ports. The 4 - f wavelength imaging optics images in the dispersive axis of the LCoS and provides integrated switching and optical power control. Polarization diversity optics is used to both separate and align the orthogonal polarization states to be in the high efficiency s-polarization state of the diffraction grating. The conventional grating disperses the input light. The LCoS array is the core element of the optical processor. The phase of the light at each pixel of the LCoS is controlled by driving electrical signals, forming an electrically-programmable grating. The vertical direction of the beam deflection is varied by tuning the pitch of the grating, while the number of pixel columns selected in the horizontal direction determines the bandwidth of each spectral feature of the transfer function of the grating [Opt].

In operation, light from the input fibre (one of the ports in the fibre array) firstly passes through the polarization diversity optics. Subsequently, the light is reflected from the cylindrical mirror, and angularly dispersed by the grating. After that, the light is reflected back to the cylindrical mirror which directs each optical frequency to a different portion of the LCoS. The path for each frequency is then retraced upon reflection from the LCoS, with the beam-steering image applied on the LCoS directing the light to a particular port of the fibre array [Opt].

Optical processors can be employed as spectral filters and allow individual control of the intensity and phase of spectral components. Optical processors offer a range of attractive features including simple implementation, robust polarization insensitive operation, and ready integration into fiber systems. Moreover, an optical processor is fully programmable and is able to generate arbitrary user-designed filter shape (both amplitude and phase). The optical processor (Finisar WaveShaper 4000E) used in the subsequent experiments has a resolution of 4 GHz, and an insertion loss of $\sim$ 4.5 dB.

The design methodology for a specific filter is as follows. In the time domain, the output pulse $y(t)$ is given by the convolution of the input signal $x(t)$ with the designed filter's impulse response $h(t)$

$$y(t) = x(t) * h(t) \tag{2.79}$$

Alternatively, in the frequency domain, the output signal $Y(\omega)$ is the product of the input signal $X(\omega)$ with the designed filter's frequency response $H(\omega)$

$$Y(\omega) = X(\omega)H(\omega) \tag{2.80}$$

where $X(\omega)$ and $Y(\omega)$ are the Fourier transforms of $x(t)$ and $y(t)$ respectively. In terms of Fourier transform, the relationship between $h(t)$ and $H(\omega)$ is given by:

$$H(\omega) = \int_{-\infty}^{+\infty} h(t)e^{j\omega t}dt \tag{2.81}$$

To achieve a specific output, we need to design a filter with a spectral response $H(\omega)$ as follows

$$H(\omega) = Y_{output}(\omega)/X_{input}(\omega) \tag{2.82}$$

where $Y_{output}(\omega)$ is the spectrum of the output pulse and $X_{input}(\omega)$ is the spectrum of the input pulse.

2.6 Conclusion

In this chapter, the origin of the second-order nonlinearity in lithium niobate crystals and various second-order nonlinear interactions in PPLN waveguides were introduced. The theory of the QPM technique and the PPLN waveguide fabrication techniques were presented. The PPLN waveguide samples used in the subsequent experiments were experimentally characterized. The SHG, SFG, DFG, cSHG/DFG and cSFG/DFG interactions in PPLN waveguides were modelled and the properties of these second-order nonlinear interactions were analysed. This chapter has finally included an introduction of the L-FROG technology and the optical processor technology, which are used in the subsequent experiments in my thesis.

References

[Agrawal 07] G. P. Agrawal, Nonlinear fiber optics, Elsevier, 2007.

[Armstrong 62] J. A. Armstrong, N. Bloembergen, J. Ducuing & P. S. Pershan, *Interactions between Light Waves in a Nonlinear Dielectric*, Phys. Rev., vol. 127, no. 6, pages 1918–, September 1962.

[Ashkin 66] A. Ashkin, G.D. Boyd, J.M. Dziedzic, R.G. Smith, A.A. Ballman, J.J. Levinstein & K. Nassau, *Optically-Induced Refractive Index Inhomogeneities in LiNbO3 and LiTaO3*, Applied Physics Letters, vol. 9, no. 1, pages 72–74, 1966.

[Banfi 98] G. P. Banfi, P. K. Datta, V. Degiorgio & D. Fortusini, *Wavelength shifting and amplification of optical pulses through cascaded second-order processes in periodically poled lithium niobate*, Applied Physics Letters, vol. 73, no. 2, pages 136–138, July 1998.

[Bogoni 09] Antonella Bogoni, Xiaoxia Wu, Irfan Fazal & Alan E. Willner, *Photonic processing of 320 Gbits/s based on sum-/difference-frequency generation and pump depletion in a single PPLN waveguide*, Opt. Lett., vol. 34, no. 12, pages 1825–1827, Jun 2009.

[Bogoni 10] Antonella Bogoni, Xiaoxia Wu, Zahra Bakhtiari, Scott Nuccio, Robert W. Hellwarth & Alan E. Willner. *640 Gb/s All-Optical Add/-Drop Multiplexing Based on Pump Depletion in a PPLN Waveguide.* In Photonics in Switching, page PTuB6. Optical Society of America, 2010.

[Boyd 03] R. W. Boyd, Nonlinear optics, Academic press, 2003.

[Chou 00] M. H. Chou, I. Brener, G. Lenz, R. Scotti, E. E. Chaban, J. Shmulovich, D. Philen, S. Kosinski, K. R. Parameswaran & M. M. Fejer, *Efficient wide-band and tunable midspan spectral inverter using cascaded nonlinearities in LiNbO3 waveguides*, Ieee Photonics Technology Letters, vol. 12, no. 1, pages 82–84, January 2000.

[Dorrer 02] C. Dorrer & I. Kang, *Simultaneous temporal characterization of telecommunication optical pulses and modulators by use of spectrograms*, Optics Letters, vol. 27, no. 15, pages 1315–1317, August 2002.

[Fejer 92] M. M. Fejer, G. A. Magel, D. H. Jundt & R. L. Byer, *Quasi-phase-matched 2nd Harmonic-generation - Tuning and Tolerances*, Ieee Journal of Quantum Electronics, vol. 28, no. 11, pages 2631–2654, November 1992.

[Franken 63] P. A. Franken & J. F. Ward, *Optical Harmonics and Nonlinear Phenomena*, Rev. Mod. Phys., vol. 35, no. 1, pages 23–, January 1963.

[Fukuchi 03] Y. Fukuchi, T. Sakamoto, K. Taira & K. Kikuchi, *All-optical time-division demultiplexing of 160 Gbit/s signal using cascaded second-order nonlinear effect in quasi-phase matched LiNbO3 waveguide device*, Electronics Letters, vol. 39, no. 10, pages 789–790, May 2003.

[Gallo 97] K. Gallo, G. Assanto & G. I. Stegeman, *Efficient wavelength shifting over the erbium amplifier bandwidth via cascaded second order processes in lithium niobate waveguides*, Applied Physics Letters, vol. 71, no. 8, pages 1020–1022, August 1997.

[Glass 74] A. M. Glass, D. V. D. Linde & T. J. Negran, *High-voltage Bulk Photovoltaic Effect and the Photorefractive Process In Linbo3*, Applied Physics Letters, vol. 25, no. 4, pages 233–235, 1974.

[Gopalan 07] V. Gopalan, V. Dierolf & D. A. Scrymgeour, *Defect-domain wall interactions in trigonal ferroelectrics*, Annual Review of Materials Research, vol. 37, pages 449–489, 2007.

[Hasegawa 04] T. Hasegawa, X. Wang & A. Suzuki, *Retiming of picosecond pulses by a cascaded second-order nonlinear process in quasi-phase-matched LiNbO3 waveguides*, Optics Letters, vol. 29, no. 23, pages 2776–2778, December 2004.

[Imeshev 00] G. Imeshev, M. A. Arbore, M. M. Fejer, A. Galvanauskas, M. Fermann & D. Harter, *Ultrashort-pulse second-harmonic generation with longitudinally nonuniform quasi-phase-matching gratings: pulse compression and shaping*, Journal of the Optical Society of America B-optical Physics, vol. 17, no. 2, pages 304–318, February 2000.

[Jackel 82] J. L. Jackel, C. E. Rice & J. J. Veselka, *Proton exchange for high-index waveguides in LiNbO3*, Applied Physics Letters, vol. 41, no. 7, pages 607 –608, October 1982.

[Jundt 97] D. H. Jundt, *Temperature-dependent Sellmeier equation for the index of refraction, n(e), in congruent lithium niobate*, Optics Letters, vol. 22, no. 20, pages 1553–1555, October 1997.

[Kane 93] D. J. Kane & R. Trebino, *Characterization of Arbitrary Femtosecond Pulses Using Frequency-resolved Optical Gating*, Ieee Journal of Quantum Electronics, vol. 29, no. 2, pages 571–579, February 1993.

[Kanzig 57] Werner Kanzig, Ferroelectrics and antiferroelectrics, Aca, 1957.

[Langrock 06] C. Langrock, S. Kumar, J. E. McGeehan, A. E. Willner & M. M. Fejer, *All-optical signal processing using chi((2)) nonlinearities in guided-wave devices*, Journal of Lightwave Technology, vol. 24, no. 7, pages 2579–2592, July 2006.

[Lee 03] J. H. Lee, Y. H. Min, W. Grundkotter, V. Quiring & W. Sohler. *All-optical wavelength selective switching exploiting the nonlinear phase shift induced by cascaded sum and difference frequency generation (cSFG/DFG) in a Ti:PPLN channel waveguide*, 2003.

[Lee 06] Y. L. Lee, B. A. Yu, T. J. Eom, W. Shin, C. Jung, Y. C. Noh, J. Lee, D. K. Ko & K. Oh, *All-optical AND and NAND gates based on cascaded second-order nonlinear processes in a Ti-diffused periodically poled LiNbO3 waveguide*, Optics Express, vol. 14, no. 7, pages 2776–2782, April 2006.

[Miller 96] G. D. Miller, R. G. Batchko, M. M. Fejer & R. L. Bver. *Visible quasi-phasematched harmonic generation by electric-field-poled lithium niobate*, 1996.

[Okada 76] M. Okada, K. Takizawa & S. Ieiri, *2nd Harmonic-generation By Periodic Laminar Structure of Nonlinear Optical Crystal*, Optics Communications, vol. 18, no. 3, pages 331–334, 1976.

[Opt] *http://investor.finisar.com/releasedetail.cfm?releaseid=360495.*

[Parameswaran 02] K. R. Parameswaran, R. K. Route, J. R. Kurz, R. V. Roussev, M. M. Fejer & M. Fujimura, *Highly efficient second-harmonic generation in buried waveguides formed by annealed and reverse proton exchange in periodically poled lithium niobate*, Optics Letters, vol. 27, no. 3, pages 179–181, February 2002.

[Polgár 86] K. Polgár, L. Kovács, I. Földvári & I. Cravero, *Spectroscopic and electrical conductivity investigation of Mg doped LiNbO3 single crystals*, Solid State Communications, vol. 59, no. 6, pages 375 – 379, 1986.

[Prawiharjo 05] J. Prawiharjo, K. Gallo, N. G. R. Broderick & D. J. Richardson, *Frequency-resolved optical gating in the 1.55 mu m band via cascaded ((2))(chi) processes*, Journal of the Optical Society of America B-optical Physics, vol. 22, no. 9, pages 1985–1993, September 2005.

[Reid 07] D. Reid & J. Harvey, *Linear spectrograms using electrooptic modulators*, Ieee Photonics Technology Letters, vol. 19, no. 5-8, pages 535–537, March 2007.

[Roelens 04] M. A. F. Roelens, B. C. Thomsen & D. J. Richardson. *Multiwavelength EAM based optical sampling for performance monitoring in high bit-rate WDM systems*, 2004.

[Schiek 99] R. Schiek, L. Friedrich, H. Fang, G. I. Stegeman, K. R. Parameswaran, M.-H. Chou & M. M. Fejer, *Nonlinear directional coupler in periodically poled lithium niobate*, Opt. Lett., vol. 24, no. 22, pages 1617–1619, Nov 1999.

[Schmidt 74] R. V. Schmidt & I. P. Kaminow, *Metal -diffused optical waveguides in LiNbO3*, Applied Physics Letters, vol. 25, no. 8, pages 458 –460, October 1974.

[Schweinler 52] H. C. Schweinler, *Ferroelectricity in the Ilmenite Structure*, Phys. Rev., vol. 87, no. 1, pages 5–, July 1952.

[Sidick 95] E. Sidick, A. Knoesen & A. Dienes, *Ultrashort-pulse 2nd-harmonic Generation .1. Transform-limited Fundamental Pulses*, Journal of the Optical Society of America B-optical Physics, vol. 12, no. 9, pages 1704–1712, September 1995.

[Volk 08] Tatyana Volk & Manfred Wohlecke, Lithium niobate-defects, photorefraction and ferroelectric switching, Springer-Verlag Berlin Heidelberg, 2008.

[Wang 05] Y. Wang, C. Yu, L. Yan, A. E. Willner, R. Roussev, C. Langrock & M. M. Fejer. *Continuously-tunable dispersionless 44-ns all optical delay element using a two-pump PPLN, DCF, and a dispersion compensator*, 2005.

[Wang 06] J. Wang, J. Q. Sun & Q. Z. Sun, *Experimental observation of a 1.5 mu m band wavelength conversion and logic NOT gate at 40 Gbit/s based on sum-frequency generation*, Optics Letters, vol. 31, no. 11, pages 1711–1713, June 2006.

[Wang 07a] J. Wang, J. Q. Sun & Q. Z. Sun, *Single-PPLN-based simultaneous half-adder, half-subtracter, and OR logic gate: proposal and simulation*, Optics Express, vol. 15, no. 4, pages 1690–1699, February 2007.

[Wang 07b] J. Wang, J. Q. Sun, Q. Z. Sun, D. L. Wang, M. J. Zhou, X. L. Zhang & D. X. Huang, *All-optical format conversion using a periodically poled lithium niobate waveguide and a reflective semiconductor optical amplifier*, Applied Physics Letters, vol. 91, no. 5, page 051107, July 2007.

[Wang 07c] J. Wang, L. Q. Sun & Q. Z. Sun, *Proposal for all-optical format conversion based on a periodically poled lithium niobate loop mirror*, Optics Letters, vol. 32, no. 11, pages 1477–1479, June 2007.

[Wang 08a] J. Wang, J. Q. Sun, Q. Z. Sun, X. L. Zhang & D. X. Huang, *All-optical dual-direction half-subtracter based on sum-frequency generation*, Optics Communications, vol. 281, no. 4, pages 788–792, February 2008.

[Wang 08b] J. Wang, J. Q. Sun, X. L. Zhang, D. X. Huang & M. M. Fejer, *Optical phase erasure and its application to format conversion through cascaded second-order processes in periodically poled lithium niobate*, Optics Letters, vol. 33, no. 16, pages 1804–1806, August 2008.

[Wang 10] J. Wang, S. Nuccio, X. X. Wu, O. F. Yilmaz, L. Zhang, I. Fazal, J. Y. Yang, Y. Yue & A. E. Willner, *40 Gbit/s optical data exchange between wavelength-division-multiplexed channels using a periodically poled lithium niobate waveguide*, Optics Letters, vol. 35, no. 7, pages 1067–1069, April 2010.

[Ware 08] C. Ware, L. K. Oxenlowe, F. G. Agis, H. C. H. Mulvad, M. Galili, S. Kurimura, H. Nakajima, J. Ichikawa, D. Erasme, A. T. Clausen & P. Jeppesen, *320 Gbps to 10 GHz sub-clock recovery using a PPLN-based opto-electronic phase-locked loop*, Optics Express, vol. 16, no. 7, pages 5007–5012, March 2008.

[Weiss 02] B. L. Weiss, Properties of lithium niobate, The institution of electrical engineers, 2002.

3

Analysis of acceptable spectral windows of quadratic cascaded nonlinear processes in a periodically poled lithium niobate waveguide

3.1 Introduction

Efficient all-optical wavelength conversion is likely to be a key functionality within future WDM networks [Yoo 96]. WDM technology offers an effective utilisation of the fibre bandwidth, and allows flexible interconnections based on wavelength routing. However, wavelength contention becomes a serious problem in high capacity WDM networks. The use of wavelength converters at the network nodes can mitigate the wavelength contention in WDM networks by swapping and reusing the WDM channels. All-optical wavelength converters, which can overcome the speed bottleneck of electronic components used for O-E-O wavelength converters, have become attractive. Various approaches for all-optical wavelength conversion have previously been reported, including: cross gain modulation (XGM) in semiconductor optical amplifiers (SOAs) [Wiesenfeld 94]; cross phase modulation (XPM) in either SOAs [Schilling 94] or nonlinear optical loop mirrors (NOLMs) [Rauschenbach 94]; four-wave-mixing (FWM) in either optical fibres [Inoue 92, Inoue 94, Fok 07], SOAs [Agrawal 88], or semiconductor waveguides [Le 92].

Wavelength conversion techniques exploiting cascaded second-order nonlinear processes in PPLN waveguides have attracted much interest in recent years due to a number of attractive features relative to competitor approaches [Gallo 97, Chen 04, Langrock 06]. These features include high conversion efficiency, broad wavelength conversion bandwidths within the telecom-band, bit-rate and modulation format transparency, and no excess noise accumulation during wavelength conversion. An all-optical wavelength conversion scheme based on the cSHG/DFG process in PPLN waveguides was proposed by Gallo *et al.* [Gallo 97], and was later demonstrated using a 10 GHz pulse train by Schreiber *et al.* [Schreiber 01]. All-optical wavelength conversion based on the cSFG/DFG process in PPLN waveguides was proposed by Lee *et al.* [Lee 03]. Tunable all-optical wavelength conversion of short pulses based on cSFG/DFG in a single PPLN waveguide was first demonstrated by Min *et al.* [Min 03]. Since then, tunable all-optical wavelength conversion of 160-Gb/s RZ signals based on cSFG/DFG in a PPLN waveguide has been reported by Furukawa *et al.* [Furukawa 07]. One important parameter in all these schemes is the acceptance bandwidth, since this will determine the pulse widths that the wavelength converter can handle. There have been several theoretical and experimental studies of the cascaded processes in the CW-pump regime and the results show that the acceptable pump bandwidth for the SHG based approach is relatively narrow compared to the SFG case because of restrictions imposed by the QPM requirements [Chen 04]. However, in order to apply these cascaded processes to practical digital communication systems, the transmitted signals should have the form of pulsed waves rather than CW signals - making a proper investigation of the wavelength conversion properties in the pulsed-pump regime especially important. No consistent study has been performed to compare the cSHG/DFG and cSFG/DFG schemes in the pulsed-pump regime to date, in which the acceptance bandwidth should have a somewhat different definition since it actually depends on the input pump conditions.

In this chapter, I report the first systematic study on the acceptance bandwidths under pulsed pump operation of the cSHG/DFG and the cSFG/DFG processes. The acceptance bandwidths of SHG and SFG are carefully compared in the CW and the pulsed-pump regimes via both modelling and experiments. Unlike the CW-pump regime, where the SHG bandwidth is known to be half that of SFG, my results show that these two bandwidths are comparable when pulsed signals are involved.

3.2 Theoretical analysis

3.2.1 CW-pumped SHG and SFG

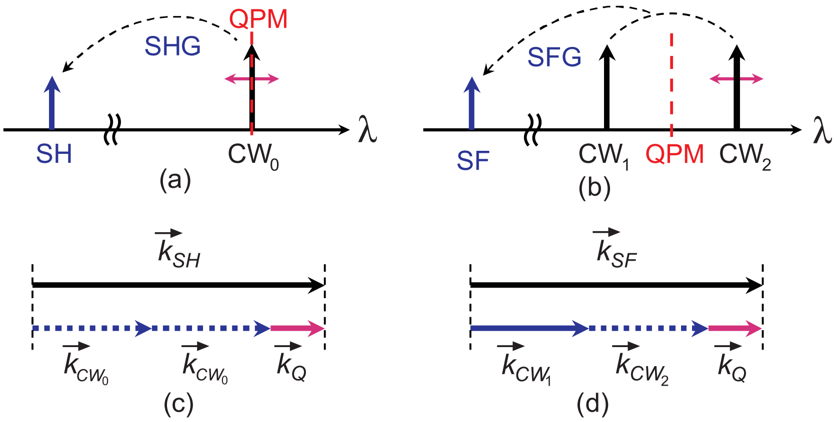

FIGURE 3.1: Schematic diagrams of the (a) SHG and (b) SFG processes in the CW-pump regime. The wave vector mismatches for (c) SHG and (d) SFG. The solid and dashed lines representing each vector correspond to the fixed and the tunable wavelength, respectively.

The schematic diagrams of the CW-pumped SHG and SFG processes in a PPLN waveguide are illustrated in Fig. 3.1. The second harmonic (SH) wave of an input pump (CW$_0$) is generated by the SHG process as shown in Fig. 3.1(a), whereas the sum-frequency (SF) wave is generated from two pump beams (CW$_1$ and CW$_2$) by the SFG process as shown in Fig. 3.1(b). In this section I theoretically investigate the bandwidth of these two effects, and in order to do this, I allow the wavelengths of CW$_0$ in Fig. 3.1(a) and CW$_2$ in Fig. 3.1(b) to be tuned around the resonant wavelengths that satisfy the QPM condition in the PPLN device. As presented in the background chapter, the output power of the SHG and SFG processes can be expressed as:

$$P_{SH} \propto sinc^2(\frac{\Delta k_{SHG} L}{2}) \tag{3.1}$$

$$P_{SF} \propto sinc^2(\frac{\Delta k_{SFG} L}{2}) \tag{3.2}$$

where Δk_{SHG} and Δk_{SFG} denote the phase mismatches of the SHG and SFG processes, respectively. The phase mismatch for SHG around the resonant pump frequency (ω_0) is defined as,

$$\Delta k_{SHG}(\Delta\omega) = 2k(\omega) - k(2\omega) = 2k(\omega_0 + \Delta\omega) - k(2\omega_0 + 2\Delta\omega) \tag{3.3}$$

which can be rewritten using a Taylor expansion as follows:

$$\begin{aligned} \Delta k_{SHG}(\Delta\omega) &= 2k(\omega_0) - k(2\omega_0) + 2[\frac{\partial k}{\partial\omega}|_{\omega_0} - \frac{\partial k}{\partial\omega}|_{2\omega_0}]\Delta\omega + O(\Delta\omega^2) \\ &= \Delta k_{0,SHG} + 2[\frac{1}{u_0} - \frac{1}{u_{SH}}]\Delta\omega + O(\Delta\omega^2) \end{aligned} \tag{3.4}$$

Here, $\Delta k_{0,SHG}$, u_0, and u_{SH} denote the phase mismatch at ω_0 and the group-velocities of the pump (CW_0) and SH waves, respectively. The function O denotes the rest of the series beyond the second order.

In the same way, the phase mismatch for SFG around the resonance by tuning the pump frequency (ω_2) can be derived as,

$$\begin{aligned} \Delta k_{SFG}(\Delta\omega) &= k(\omega_1) + k(\omega_2 + \Delta\omega) - k(\omega_1 + \omega_2 + \Delta\omega) \\ &= \Delta k_{0,SFG} + [\frac{1}{u_2} - \frac{1}{u_{SF}}]\Delta\omega + O(\Delta\omega^2) \end{aligned} \tag{3.5}$$

where, $\Delta k_{0,SFG}$, u_2, and u_{SF} also denote the phase mismatch at resonance and the group-velocities of the tunable pump (CW_2) and SF waves, respectively.

If the pumps in both the SHG and SFG cases are in the same frequency band, i.e. $\omega_0 = \omega_2$ (and as a consequence, ω_{SH}, ω_{SF}), the group velocity mismatches (GVMs) in each case can be considered to take approximately the same value, as follows:

$$\frac{1}{u_0} - \frac{1}{u_{SH}} \approx \frac{1}{u_2} - \frac{1}{u_{SF}} \approx \delta\nu \tag{3.6}$$

In the experiments described in Section 3.3, their difference is only 0.05% due to the low dispersion of lithium niobate crystals at wavelengths around 1550 nm, and thus is negligible in our analysis. Since both $\Delta k_{0,SHG}$ and $\Delta k_{0,SFG}$ in Eq. 3.4 and 3.5 are equal to zero at the QPM resonance, the phase mismatches in each case [Eq. 3.4 and 3.5] can be rewritten as,

$$\Delta k_{SHG} \approx 2\delta\nu \cdot \Delta\omega \tag{3.7}$$

$$\Delta k_{SFG} \approx \delta\nu \cdot \Delta\omega \tag{3.8}$$

which indicates that the phase mismatch for SHG varies almost twice as rapidly as for the SFG counterpart. The output powers of SH and SF can then be expressed as,

$$P_{SH} \propto sinc^2(\frac{\Delta k_{SHG}L}{2}) \approx sinc^2(\delta\nu \cdot \Delta\omega) \tag{3.9}$$

$$P_{SF} \propto sinc^2(\frac{\Delta k_{SFG}L}{2}) \approx sinc^2(\frac{\delta\nu \cdot \Delta\omega}{2}) \tag{3.10}$$

showing that the CW acceptance bandwidth for SFG is twice as broad as for the SHG counterpart. The broader pump bandwidth in the SFG case can also be explained in Fig. 3.1(c) and (d) illustrating the wave-vector mismatches for each case. Here, each k vector denotes the wave-vectors of the SH, SF, CW$_0$, CW$_1$, and CW$_2$, respectively. The QPM grating vector, k_Q, is defined by $2\pi/\Lambda$, where Λ denotes the QPM grating period. The solid and dashed lines of each vector also represent the fixed and the tunable wavelength, respectively. In the SFG case [Fig. 3.1(d)], CW$_2$ is tunable while the wavelength of CW$_1$ is fixed as defined in Fig. 3.1(b). Therefore, the wavelength tuning of CW$_2$ affects only the wave vector of CW$_2$. In the SHG case, however, the tuning of the pump wave (CW$_0$) simultaneously changes two degenerate pump vectors as shown in Fig. 3.1(c), which means that the QPM condition is more readily broken under wavelength tuning as compared to the SFG case. Therefore, the SH power is more sensitive to variation of the pump wavelength than the SF power, resulting in a narrower acceptance bandwidth as compared to the SFG case. There conclusions are common to what has been published previously in Ref. [Chen 04]. However, in the following, I will repeat this study, but now for the more relevant case of pulsed signals. The results of this study might look surprising at first.

3.2.2 Pulsed-pump SHG and SFG

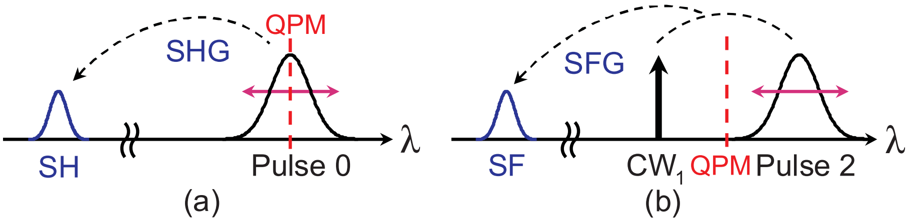

FIGURE 3.2: Schematic diagrams of the (a) SHG and (b) SFG processes in the pulsed-pump regime.

Now the pulsed-pumped SHG and SFG processes in a PPLN waveguide are investigated. The schematic diagrams for each case are illustrated in Fig. 3.2(a) and (b), respectively. The configuration of the interacting waves is very similar to that of Fig. 3.1, other than that two wavelength-tunable pulsed-pumps (Pulse 0, 2) are used instead of the CW pumps.

In order to deal with the short-pulse nonlinear frequency conversion schemes, we consider the simpler frequency domain picture rather than the time domain model. As presented in Ref. [Imeshev 00] and in the background chapter, the coupled mode equation between the second harmonic wave and the polarization wave is given by

$$\frac{\partial^2}{\partial z^2}\tilde{E}_{SH}(z,\omega) + k^2(\omega_{SH})\tilde{E}_{SH}(z,\omega) = -\mu_0\omega_0^2\tilde{P}_{NL}(z,\omega) \tag{3.11}$$

where $\tilde{E}_i$ is the Fourier transform of the temporal electric-field at frequency ω_i, $k(\omega_i)$ is the wave vector at frequency ω_i, and $\tilde{P}_{NL}$ is the electric nonlinear polarization components at SH frequency.

In a medium that is negligibly dispersive in $\chi^{(2)}$, the nonlinear polarization spectrum $P_{NL}(z,\omega)$, which radiates the SH wave, can be described as [Boyd 03]

$$\tilde{P}_{NL}(z,\omega) = \frac{1}{2}\epsilon_0\chi^{(2)}\int_{-\infty}^{+\infty}\tilde{E}_0(z,\omega')\tilde{E}_0(z,\omega-\omega')d\omega' \tag{3.12}$$

where $\chi^{(2)}$ is the second-order nonlinear susceptibility of the material.

Let us set $\tilde{E}_i(z,\omega) = \tilde{A}_i(z,\Omega_i)e^{ik(\Omega_i)z}$, where $\Omega = \omega - \omega_1$ denotes the frequency offset and $\tilde{A}_i(z,\Omega)$ denotes the Fourier transforms of the interacting waves, respectively. Under slowly varying envelope approximation $d^2\tilde{A}_i/dz^2 \ll k(d\tilde{A}_i/dz)$, the output frequency-domain envelope of the SH wave can be obtained by integrating Eq. 3.11:

$$\tilde{A}_{SH}(L,\Omega) = -\frac{i\mu_0\omega_{sh}^2}{2k_{SH}}\int_0^L \tilde{P}_{NL}(z,\Omega)e^{ik(\omega_{SH}+\Omega)z}dz \tag{3.13}$$

Substituting $\tilde{P}_{NL}(z,\Omega) = \frac{\chi^{(2)}}{2}\epsilon_0 \int_{-\infty}^{+\infty} \tilde{A}_0(z,\Omega')\tilde{A}_0(z,\Omega-\Omega')e^{-i(k(\omega_1+\Omega')+k(\omega_0+\Omega-\Omega'))z}dz$ (where $\Omega' = \omega' - \omega_1$) into Eq. 3.13, we can obtain:

$$\tilde{A}_{SH}(L,\Omega) = -i\gamma\int_0^L dz\int_{-\infty}^{\infty} \tilde{A}_0(\Omega')\tilde{A}_0(\Omega-\Omega')e^{-i\Delta k_{SHG}(\Omega)z}d\Omega \tag{3.14}$$

By manipulating Eq. 3.14, the converted output fields can be expressed as the product of the Fourier transforms of the input pump fields and the spectral filter function (D) associated to the QPM grating in the PPLN waveguide [Imeshev 00]. In our cases, the output SH and the SF fields can be expressed as follows:

$$\tilde{A}_{SH}(\Omega) = D_{SHG}(\Omega)\cdot[\tilde{A}_0^2(\Omega)] \tag{3.15}$$

$$\tilde{A}_{SF}(\Omega) = D_{SFG}(\Omega)\cdot[\tilde{A}_1(\Omega) * \tilde{A}_2(\Omega)] \tag{3.16}$$

where $D_{SHG}(\Omega)$ and $D_{SFG}(\Omega)$ denote the filter functions of the SHG and SFG processes respectively, and $*$ in Eq. 3.16 denotes the convolution integral between two interacting pump fields (CW$_1$ and Pulse 2). In the SFG case of Fig. 3.2(b), the optical fields of the CW- and the pulsed-pumps in the frequency domain are expressed as:

$$A_1(t) \equiv CW \rightarrow \tilde{A}_1(\omega) = \delta(\omega-\omega_1) \tag{3.17}$$

$$A_2(t) \equiv Pulsed \rightarrow \tilde{A}_2(\omega) \tag{3.18}$$

and therefore, Eq. 3.16 can be rewritten as follows:

$$\tilde{A}_{SF}(\Omega) = D_{SFG}(\Omega)\cdot[\tilde{A}_2(\Omega)] \tag{3.19}$$

In order to correctly investigate the acceptance bandwidths for the SHG and SFG processes in the pulsed-pump regime, the spectral widths of input fields [$A_0(\Omega)$ and $A_2(\Omega)$] in Eq. 3.15 and 3.19 are assumed to be broader than the bandwidths of their filter functions. In this instance then the filter functions primarily determine the widths of both the SH and the SF fields. These filter functions depend on the following phase mismatches for each process. The phase mismatches are originally to be derived as a function of two variables (frequency offsets) as in Ref. [Imeshev 00], yet to first-order they reduce to a function of only one of them (namely the pump frequency offset from resonance hereafter denoted by Ω) and can be expressed as follows:

$$\Delta k_{SHG}(\Omega) = \Delta k_{0,SHG} + [\frac{1}{u_0} - \frac{1}{u_{SH}}]\Omega + O(\Omega^2) \tag{3.20}$$

$$\Delta k_{SFG}(\Omega) = \Delta k_{0,SFG} + [\frac{1}{u_2} - \frac{1}{u_{SF}}]\Omega + O(\Omega^2) \tag{3.21}$$

Here, u_0, u_2, u_{SH}, and u_{SF} denote the group-velocities of Pulse 0, Pulse 2, SH and SF waves, respectively. In the same pump frequency band, the GVM values can be assumed to have the same value again as given in Eq. 3.6, and then we can get the phase mismatches in Eq. 3.20 and 3.21 as follows:

$$\Delta k_{SHG}(\Omega) \approx \delta\nu \cdot \Omega \tag{3.22}$$

$$\Delta k_{SFG}(\Omega) \approx \delta\nu \cdot \Omega \tag{3.23}$$

It should be noted that the factor of 2 in the CW-pump case [Eq. 3.7] has disappeared in the pulsed-pump case [Eq. 3.22] and that the two phase mismatches vary in the same way with Ω. Now the filter functions can be expressed as follows:

$$D_{SHG}(\Omega) \propto \int_0^L e^{-i\Delta k_{SHG}(\Omega)z}dz = \int_0^L e^{-i\delta\nu\cdot\Omega z}dz \tag{3.24}$$

$$D_{SFG}(\Omega) \propto \int_0^L e^{-i\Delta k_{SFG}(\Omega)z}dz = \int_0^L e^{-i\delta\nu\cdot\Omega z}dz = D_{SHG}(\Omega) \tag{3.25}$$

which means that both the SHG and the SFG cases have essentially the same filter function. Although the SH and the SF output fields are determined by Eq. 3.15 and

3.19, the relatively narrower filter functions select only a certain part of the spectral components from their input pump fields, which leads to similar widths for both the SH and the SF output fields. Therefore, the acceptance pump bandwidths for the SHG and the SFG processes are comparable with each other in the pulsed-pump regime. This observation can be intuitively explained by the following physical considerations: In the case of Fig. 3.2(a), the symmetric spectral components on both sides of the resonant wavelength for the SHG also interact with each other as two pulsed pumps for SFG. Therefore, the energy of the input pulse that falls outside of the SHG filter bandwidth is not wasted but used to generate SF pulses at the same wavelength as the SH.

3.3 Experiments

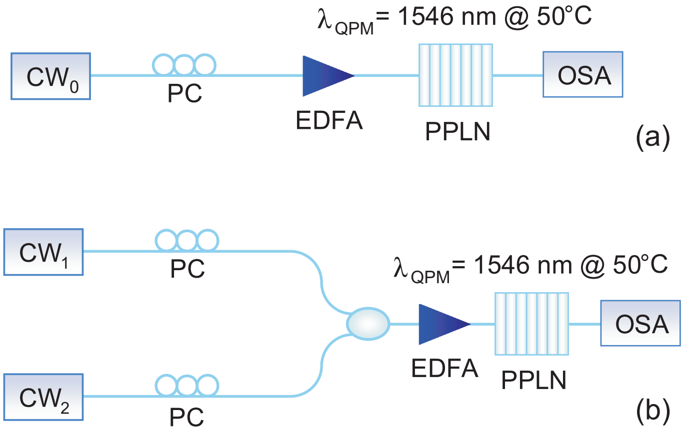

FIGURE 3.3: Experimental setup used to measure the acceptance bandwidths for (a) the SHG case and (b) the SFG case in the CW-pump regime. PC: polarisation controller, EDFA: erbium-doped fibre amplifier, OSA: optical spectrum analyser.

Figure 3.3 shows the experimental setup I used to measure the acceptance bandwidths for the SHG and the SFG in the CW-pump regime. A 30-mm-long fibre pigtailed PPLN waveguide as introduced in the background chapter was used for both the SHG and the SFG processes, and its SHG phase matching wavelength was 1546 nm at 50°C. In the SHG case, only the tunable source CW_0 was launched into the waveguide, while both the CW_1 with a fixed wavelength and the tunable CW_2 were used as two pump sources for the SFG case. Figure 3.4(a) and (b) show the normalised powers of the SH and the SF waves plotted as a function of the pump wavelength, respectively. The bandwidths measured in each case were 0.38 nm for SHG and 0.73 nm for SFG respectively. As discussed in the previous section, the SHG bandwidth was approximately half of its SFG counterpart, which confirms the ideas mentioned above and in Ref. [Chen 04]. As can be seen in Fig. 3.4(a) and (b), they are well matched with the points in the theoretical curves calculated using Eqns. 3.9 and 3.10.

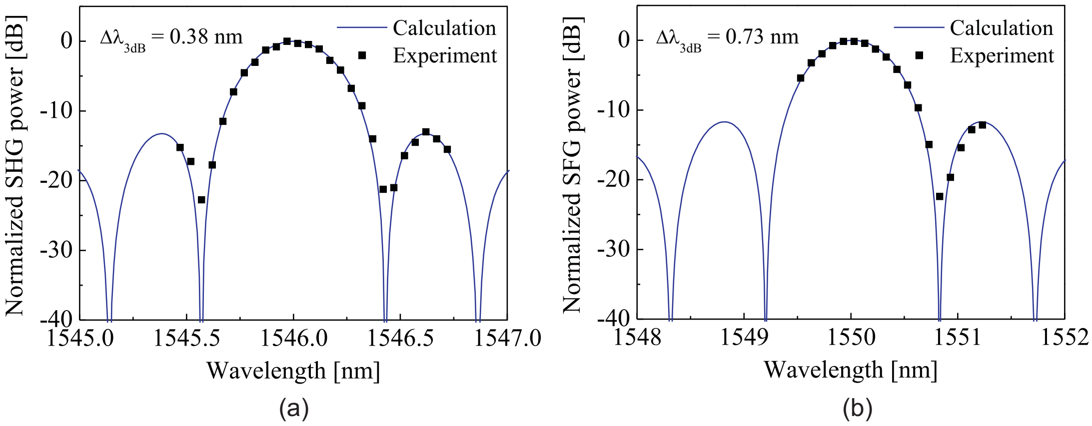

FIGURE 3.4: Measured and calculated bandwidths for (a) the SHG process and (b) the SFG process.

Next the pulsed-pump quadratic cascaded processes were investigated. Due to restrictions in the operation wavelengths of our diagnostic equipment, it was difficult to measure the output pulses of SHG or SFG directly at the 780 nm band. Thus the cSHG/DFG and cSFG/DFG processes which converted the SH/SF pulses back to the C-band were employed to assess the acceptance bandwidths of the SHG and SFG processes. The schematic diagrams of the cSHG/DFG and the cSFG/DFG in a PPLN waveguide are shown in Fig. 3.5(a) and (b), respectively. In the case of cSHG/DFG, a short pulse with a spectral width broader than the CW acceptable bandwidth for the SHG was used as the pump beam. The generated SH pulse then interacted with the CW signal (CW_1) by the DFG process, resulting in the output pulse as shown in Fig. 3.5(a). In the cSFG/DFG process, a CW_1 and a pulsed signal interacted with each other as the two pump sources for the SFG process. Then the generated SF wave interacted with CW_2 through DFG to produce the output pulsed signal as shown in Fig. 3.5(b). The experimental setup used to measure the acceptance bandwidths for the two cases are illustrated in Fig. 3.6. An erbium glass oscillator (ERGO) was used as the pulsed pump source. It generated 10 GHz, 2-ps pulses with a corresponding spectral bandwidth of $\sim$ 2.1 nm. The central wavelengths of the ERGO were 1546 nm for the cSHG/DFG [Fig. 3.5(a)] and 1550 nm for the cSFG/DFG [Fig. 3.5(b)], respectively. There was the option to filter the pump pulses using a 1.0 nm-bandpass filter which restricted their temporal width to 4 ps. The pulses were then modulated by a $2^{31}-1$ pseudorandom bit sequence (PRBS) using a lithium niobate modulator. In the case of cSHG/DFG as shown in Fig. 3.5(a), only CW_1 (1538 nm) was used, while both CW_1 (1542 nm) and CW_2 (1558 nm) were used for the case of cSFG/DFG as shown in Fig. 3.5(b), respectively. The inputs were then combined in a 3-dB coupler and launched into the PPLN waveguide after amplification.

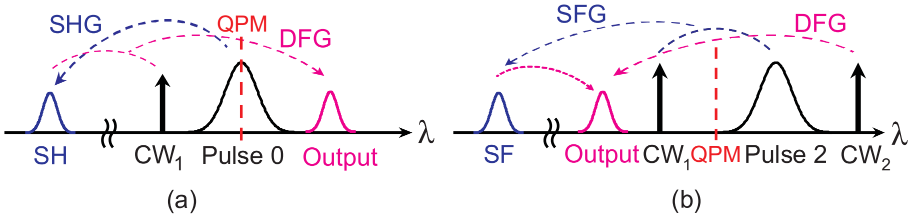

FIGURE 3.5: Schematic diagrams of (a) the cSHG/DFG and (b) the cSFG/DFG processes in the pulsed pump-regime.

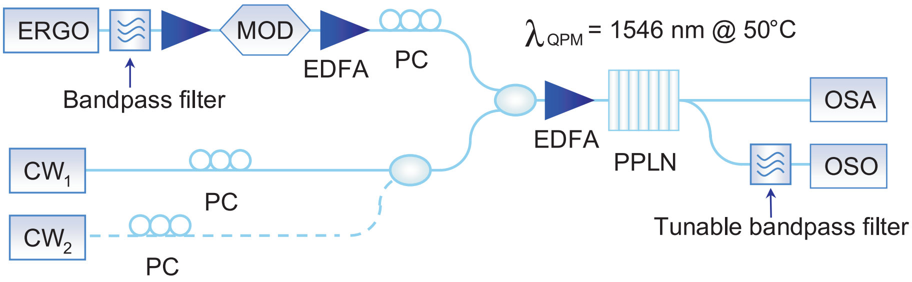

FIGURE 3.6: Experimental setup used to measure the acceptable bandwidths for the cSHG/DFG and the cSFG/DFG processes. Only CW_1 is used for the case of the cSHG/DFG process where CW_1 is labelled as CW_0, while both CW_1 and CW_2 are used for the case of the cSFG/DFG process. ERGO: Erbium doped glass oscillator, MOD: modulator, OSO: optical sampling oscilloscope.

The spectral and temporal shapes for each case, as monitored with an optical spectrum analyser (OSA) and an optical sampling oscilloscope (OSO), are presented in Fig. 3.7, 3.8, 3.9 and 3.10, respectively. The measured optical signal-to-noise ratios (OSNR) of the converted output waves were 16 dB at 1554.1 nm for the cSHG/DFG process and 15.7 dB at 1534.2 nm for the cSFG/DFG process, respectively. The temporal shapes of the output pulses measured without the 1.0-nm filter (i.e. corresponding to a pulse width of 2 ps) were distorted as shown in Fig. 3.7(b) and Fig. 3.8(b), which is due to the distortion of the SH (or SF) waves caused by the group delay between the SH (or the SF) and the pump waves in the PPLN waveguide. Next the results measured with the 1.0-nm filter in place are compared. In the case of cSHG/DFG, if the acceptance bandwidth for the SHG was approximately half of the SFG bandwidth as in the case of the CW-pump regime, then one would expect the temporal width of the output pulse [Fig. 3.9(b)] to be much broader than the pulse width in the cSFG/DFG case [Fig. 3.10(b)]. However, as indicated in Figs. 3.9(b) and 3.10(b), the temporal width of the cSHG/DFG output was comparable with its cSFG/DFG counterpart in the pulsed-pump regime, and the measured spectral bandwidths of each case were both 0.6 nm for cSHG/DFG and cSFG/DFG [Fig. 3.9(a) and Fig. 3.10(a)]. As discussed in Section 3.2.2, this is because the filter functions for the SHG and SFG processes are essentially the same in the pulsed-pump regime, which leads to the comparable output pulse widths in the two cascaded processes. Compared Fig. 3.7 and 3.8 with Fig. 3.9 and 3.10, the small difference between the measured temporal (and spectral) widths arises because in the absence of the filter, the 2-ps input pulse was severely distorted from the initial Gaussian-like shape due to the walk-off effect, whereas when the 1.0 nm filter was used the output pulses still maintained close to Gaussian shape.

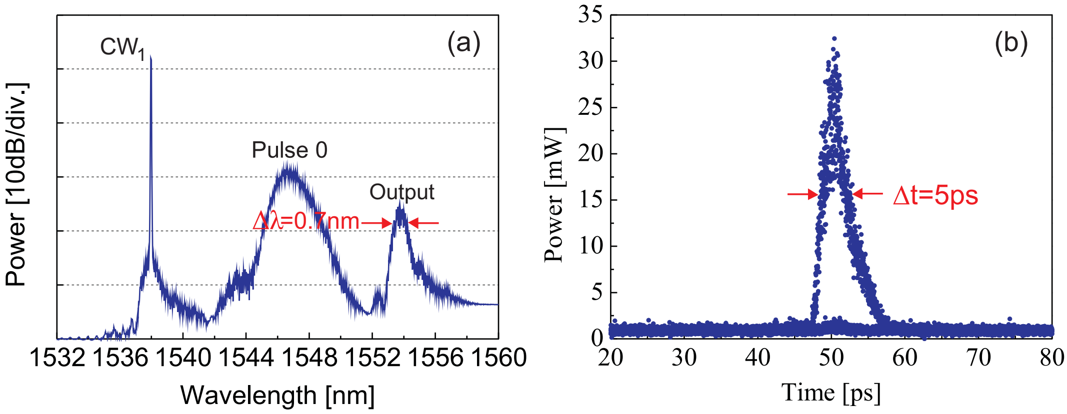

FIGURE 3.7: (a) Measured spectral and (b) temporal shapes without the filter in the cSHG/DFG.

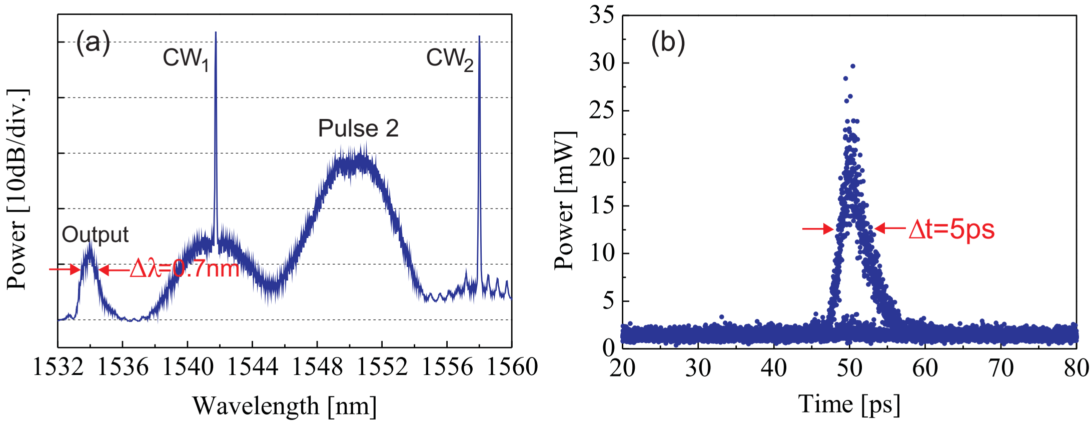

FIGURE 3.8: (a) Measured spectral and (b) temporal shapes without the filter in the cSFG/DFG.

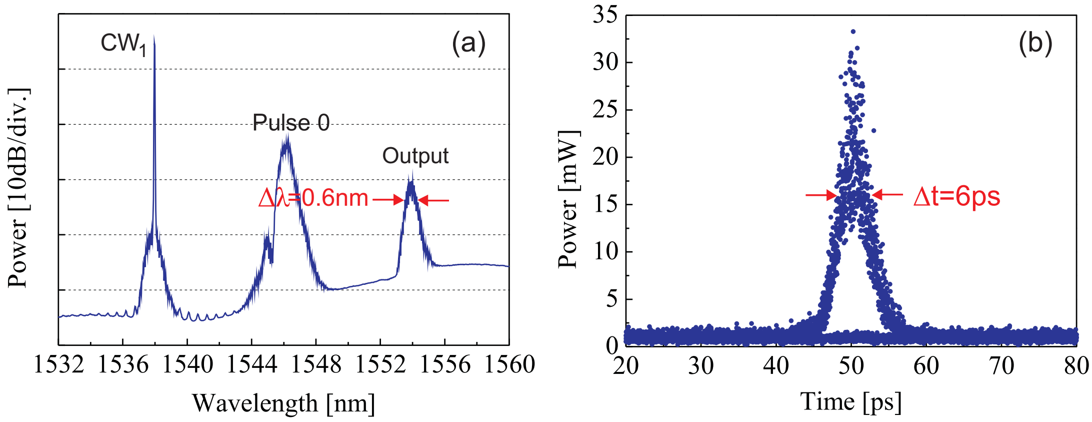

FIGURE 3.9: (a) Measured spectral and (b) temporal shapes for 1.0 nm filters in the cSHG/DFG.

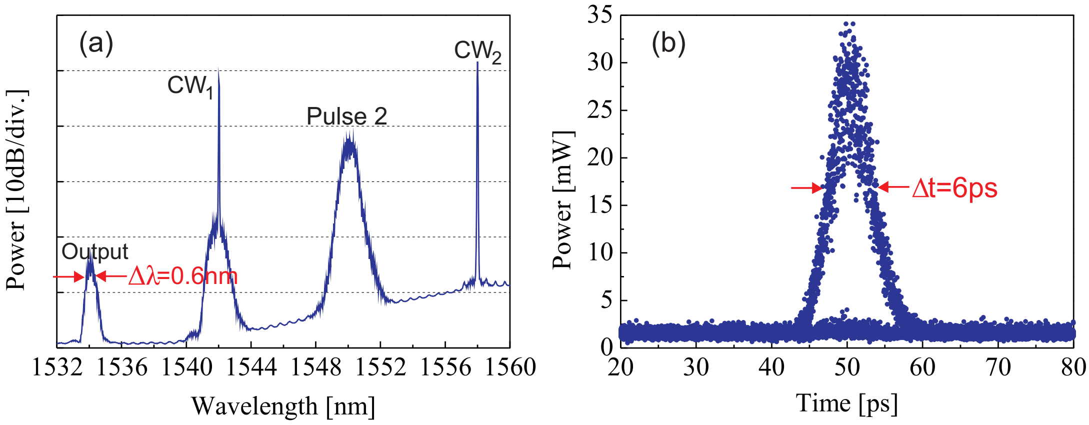

FIGURE 3.10: (a) Measured spectral and (b) temporal shapes for 1.0 nm filters in the cSFG/DFG.

3.4 Conclusion

When the pump signals involved in quadratic processes in a quasi-phase-matched waveguide, such as a PPLN device, are CW waves, the acceptance bandwidth for SFG is almost twice as broad as compared to the corresponding bandwidth of the SHG process. This is because phase matching of the two degenerate pump vectors involved in SHG is more sensitive to small detunings from the nominal wavelength than in the corresponding case of SFG. This relation is no longer valid when spectrally broader pumps are considered, i.e. when the pumps are pulsed. In this case, the spectral wings of the pulses interact with each other in a similar fashion as the different pump signals in SFG, resulting in an effectively broader acceptance bandwidth than in the CW-case. I have demonstrated this effect both analytically as well as experimentally, where nonlinear conversion experiments based on either cSHG/DFG or cSFG/DFG with a broadband pump have confirmed that the width of the converted signal was similar in both cases, even if the pump bandwidth exceeded the nominal (CW-based) acceptance bandwidth of the SHG process. In both cases, the ultimate bandwidth limitation is dictated by the walk-off effect between the signal and the SH. Comparing cSHG/DFG-based wavelength converters to cSFG/DFG-based counterparts, the merit of cSHG/DFG-based ones is that only one CW laser is required in the configuration, but the input signal has to be set at the QPM wavelength of the PPLN devices. In contrast, for cSFG/DFG-based wavelength converters, by placing Pump 1 symmetrically opposite the signal with respect to the QPM wavelength, the operating wavelength of the wavelength converter is no longer tied to the PPLN characteristics (within certain bounds). This of course, comes to the expense of using two tunable lasers (in cSFG/DFG) instead of one (in cSHG/DFG). The results in this chapter are expected to be useful for applying the two quadratic cascaded processes to short-pulse wavelength converters in practical digital communication systems.

References

[Agrawal 88] G. P. Agrawal, *Population Pulsations and Nondegenerate 4-wave Mixing In Semiconductor-lasers and Amplifiers*, Journal of the Optical Society of America B-optical Physics, vol. 5, no. 1, pages 147–159, January 1988.

[Boyd 03] R. W. Boyd, Nonlinear optics, Academic press, 2003.

[Chen 04] B. Chen & C. Q. Xu, *Analysis of novel cascaded chi((2)) (SFG+DFG) wavelength conversions in quasi-phase-matched waveguides*, Ieee Journal of Quantum Electronics, vol. 40, no. 3, pages 256–261, March 2004.

[Fok 07] M. P. Fok, C. Shu & D. J. Blumenthal. *Dual-pump four-wave mixing in bismuth-oxide highly nonlinear fiber for wide-band DPSK wavelength conversion.* Optical Fiber Communication Conference and Exposition National Fiber Optic Engineers Conference. Technical Digest. OFCNFOEC 2007, 2007.

[Furukawa 07] H. Furukawa, A. Nirmalathas, N. Wada, S. Shinada, H. Tsuboya & T. Miyazaki, *Tunable all-optical wavelength conversion of 160-Gb/s RZ optical signals by cascaded SFG-DFG generation in PPLN waveguide*, Ieee Photonics Technology Letters, vol. 19, no. 5-8, pages 384–386, March 2007.

[Gallo 97] K. Gallo, G. Assanto & G. I. Stegeman, *Efficient wavelength shifting over the erbium amplifier bandwidth via cascaded second order processes in lithium niobate waveguides*, Applied Physics Letters, vol. 71, no. 8, pages 1020–1022, August 1997.

[Imeshev 00] G. Imeshev, M. A. Arbore, M. M. Fejer, A. Galvanauskas, M. Fermann & D. Harter, *Ultrashort-pulse second-harmonic generation with longitudinally nonuniform quasi-phase-matching gratings: pulse compression and shaping*, Journal of the Optical Society of America B-optical Physics, vol. 17, no. 2, pages 304–318, February 2000.

[Inoue 92] K. Inoue & H. Toba, *Wavelength Conversion Experiment Using Fiber 4-wave-mixing*, Ieee Photonics Technology Letters, vol. 4, no. 1, pages 69–72, January 1992.

[Inoue 94] K. Inoue, *Tunable and Selective Wavelength Conversion Using Fiber 4-wave-mixing With 2 Pump Lights*, Ieee Photonics Technology Letters, vol. 6, no. 12, pages 1451–1453, December 1994.

[Langrock 06] C. Langrock, S. Kumar, J. E. McGeehan, A. E. Willner & M. M. Fejer, *All-optical signal processing using chi((2)) nonlinearities in guided-wave devices*, Journal of Lightwave Technology, vol. 24, no. 7, pages 2579–2592, July 2006.

[Le 92] H. Q. Le & S. Dicecca, *Ultrafast, Multi-thz-detuning, 3rd-order Frequency-conversion In Semiconductor Quantum-well Waveguides*, IEEE Photonics Technology Letters, vol. 4, no. 8, pages 878–880, August 1992.

[Lee 03] J. H. Lee, Y. H. Min, W. Grundkotter, V. Quiring & W. Sohler. *All-optical wavelength selective switching exploiting the nonlinear phase shift induced by cascaded sum and difference frequency generation (cS-FG/DFG) in a Ti:PPLN channel waveguide.* 11th European Conference on Integrated Optics, 2003.

[Min 03] Yoo H. Min, Jie H. Lee, Yeung L. Lee, Werner Grundkoetter, Victor Quiring & Wolfgang Sohler. *Tunable All-Optical Control of Wavelength Conversion of 5 ps Pulses by Cascaded Sum- and Difference Frequency Generation (cSFG/DFG) in a Ti:PPLN Waveguide.* In Optical Fiber Communication Conference, page FP4. Optical Society of America, 2003.

[Rauschenbach 94] K. A. Rauschenbach, K. L. Hall, J. C. Livas & G. Raybon, *All-optical Pulse-width and Wavelength Conversion At 10-gb/s Using A Nonlinear-optical Loop Mirror*, Ieee Photonics Technology Letters, vol. 6, no. 9, pages 1130–1132, September 1994.

[Schilling 94] M. Schilling, K. Daub, W. Idler, D. Baums, U. Koerner, E. Lach, G. Laube & K. Wunstel, *Wavelength Converter Based On Integrated All-active 3-port Mach-zehnder Interferometer*, Electronics Letters, vol. 30, no. 25, pages 2128–2130, December 1994.

[Schreiber 01] G. Schreiber, H. Suche, Y.L. Lee, W. GrundkÃűtter, V. Quiring, R. Ricken & W. Sohler, *Efficient cascaded difference frequency conversion in periodically poled Ti:LiNbO3 waveguides using pulsed and cw pumping*, Applied Physics B: Lasers and Optics, vol. 73, pages 501–504, 2001. 10.1007/s003400100708.

[Wiesenfeld 94] J. M. Wiesenfeld, J. S. Perino, A. H. Gnauck & B. Glance, *Bit Error Rate Performance For Wavelength Conversion At 20 Gbit/s*, Electronics Letters, vol. 30, no. 9, pages 720–721, April 1994.

[Yoo 96] S. J. B. Yoo, *Wavelength conversion technologies for WDM network applications*, Journal of Lightwave Technology, vol. 14, no. 6, pages 955–966, June 1996.

4

OTDM to WDM format conversion based on quadratic cascading in a periodically poled lithium niobate waveguide

4.1 Introduction

The demand for increased capacity in optical communication systems presents us with several challenges. In the proposed "photonic networks" where ultra-fast optical signals of any bit rate and modulation format will be transmitted and processed from end to end without O-E-O conversion. In this scenario, several flexible node functions at the network interface, such as wavelength conversion, format conversion, add-drop multiplexing, packet compression and expansion, routing, buffering, and address recognition, are required to be implemented by optical signal processing. Hence, optical signal processing technologies have the potential to play an essential role in future ultra-high-speed fibre-optic communication systems.

Current optical networks are based on both the time division multiplexing (TDM) and WDM technologies. TDM is a technique where several signals are interleaved in time, transmitted together, and separated again based on different arrival times so that the interleaving pulse trains can carry different data channels in a single fiber. As a result, the use of multiple channels allows increased overall data transmission capacities without increasing the data rates of the single channels, or transmission of data of different users simultaneously [Tucker 88, Weber 06]. Electrical time division multiplexing (ETDM) and optical time division multiplexing (OTDM) are two types of TDM techniques. In ETDM systems which are used in current commercial networks, several low speed data channels are interleaved into one high speed data channel, and high speed electrical multiplexers and modulators are needed. In contrast, in OTDM systems several sets of low speed optical signals are directly multiplexed into one set of high speed optical signal, and short optical pulse trains are needed to reduce the crosstalk between OTDM channels.

WDM is a technology where data channels are assigned to different wavelengths and combined in a single fibre, transmitted together, and separated again at the receiver. In this way, the transmission capacity of fiber-optic links can be increased significantly, therefore, both fibers and active components such as fiber amplifiers are efficiently used [Ishio 84, Keiser 99]. TDM and WDM are individually mature technologies and have been deployed in different networks. For instance, transoceanic systems are likely to continue using WDM, as a large amount of data can be aggregated in a straightforward manner and long-haul transmission is achieved without complex and expensive regeneration schemes, while access networks may opt for high-speed time division multiplexing access (TDMA), because TDMA technology needs simple network management and control. However, conversion between high-speed TDM signals and WDM signals will be required in future digital communication systems in order to combine WDM network topologies with ultra-high speed OTDM networks. In addition to that, such format conversions have also been proposed for other applications. In fibre-optic communication systems, some of network-node functions are convenient to implement in the time domain, whereas others are more convenient to implement in the frequency domain. For instance, functions such as channel add/drop multiplexing can be performed by passive spectral filtering and channel coupling in the frequency domain [Almeida 06]. In contrast, functions such as clock recovery which requires beating with a local oscillator in the time domain [von Lerber 07] and Q-factor measurements which are implemented in the time domain and used for optical performance monitoring applications [Shake 02, Kilper 04]. As illustrated in Fig. 4.1, a conversion of high-speed OTDM signals to mixed TDM-WDM signals shifts the carrier wavelength of each tributary channel onto a different wavelength without affecting the temporal bit-interleaving, which allows the implementation of networking functions by manipulating the signal in both the temporal and spectral domains [Almeida 04, Almeida 06]. With these advantages, applications for OTDM to mixed TDM-WDM format conversion, such as OTDM add-drop multiplexing [Uchiyama 01, Almeida 06] and packet compression /expansion [Almeida 04], have also been demonstrated.

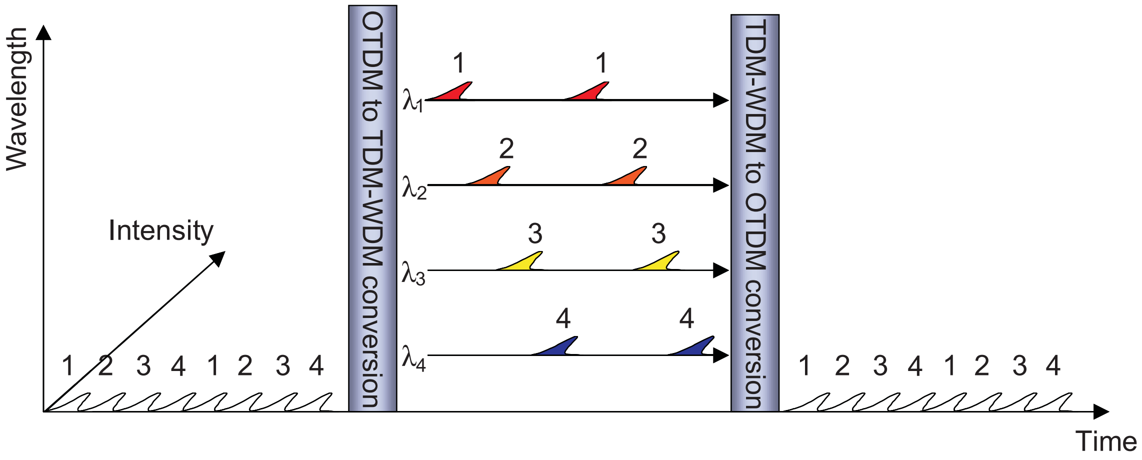

Figure 4.1: Illustration of the format conversions between OTDM signals and mixed TDM-WDM signals in the time and frequency domains. 1, 2, 3, and 4 represent Channel 1, Channel 2, Channel 3, and Channel 4, respectively.

To date various approaches for the conversion of TDM to a mixed TDM-WDM format have been reported using either self-phase modulation (SPM) followed by optical time gating [Hashimoto 00, Sotobayashi 02]; cross-gain compression in a semiconductor optical amplifier [Norte 96]; cross-phase modulation in a nonlinear optical loop mirror [Almeida 06]; or four-wave mixing [Sotobayashi 01] in highly nonlinear fibers. Except from the first approach based on SPM, all the other approaches rely on gating linearly-chirped pulses in an ultrafast nonlinear interaction controlled by the incoming OTDM data signal, as illustrated in Fig. 4.2. Following the same operational principle, I will present a novel scheme to achieve OTDM to mixed TDM-WDM format conversion using the cSHG/DFG process in a fiberized PPLN waveguide in this chapter.

This chapter is organized as follows: the operational principle and theoretical model of the format conversion scheme will be presented first, followed by experimental results, and a conclusion will be given at the end of the chapter.

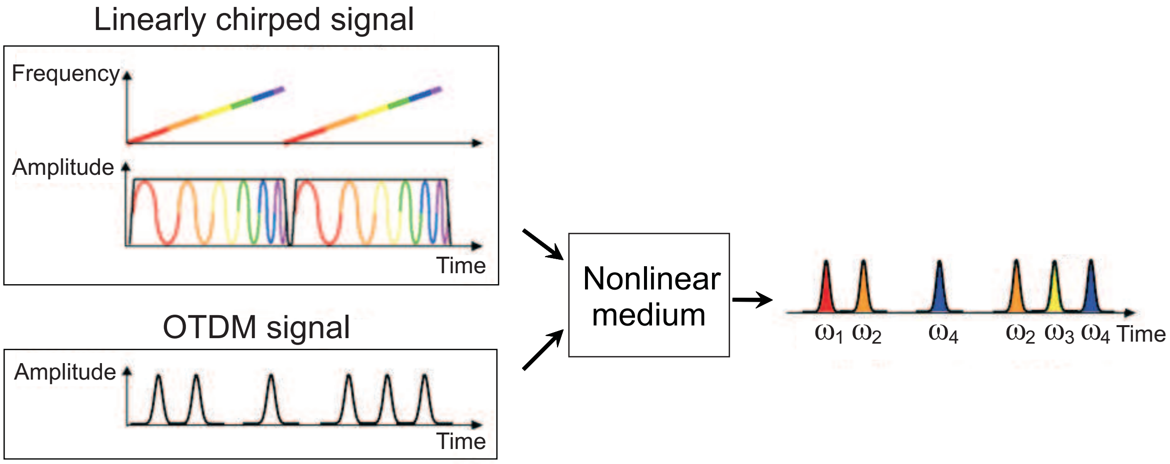

FIGURE 4.2: Illustration of the OTDM to mixed TDM-WDM format conversion based on gating linearly chirped pulses in nonlinear media controlled by the incoming OTDM signal.

4.2 Operational principle and theoretical model

Fig. 4.3 illustrates the block diagram of our OTDM to mixed TDM-WDM conversion scheme based on cSHG/DFG in a PPLN waveguide in more detail. For a more quantitative evaluation of the device performance, a numerical simulation which corresponded to the following system experiment was performed by Katia Gallo. The simulation results are also plotted in Fig. 4.3.

Two inputs are launched into the PPLN waveguide simultaneously. The first is an OTDM data signal at the aggregate bit rate comprising N temporally interleaved tributary channels, having a bit period T_p and optical frequency ω_p which is within the acceptance bandwidth of the PPLN, as shown in Fig. 4.3(b). The second input is a train of synchronized linearly-chirped rectangular pulses, with a duration spanning across the N

tributary channels ($\Delta\tau_{cp} \sim NT_p$) and a repetition rate equal to that of the individual TDM tributaries ($1/NT_p$), as shown in Fig. 4.3(a).

In the PPLN waveguide the two input signals undergo a nonlinear frequency mixing process as a consequence of the following $\chi^{(2)}$ interactions: the incoming OTDM data signal at ω_p generates an up-converted OTDM data stream at $2\omega_p$ [Fig. 4.3(d)] via the SHG process. The SHG process is followed by the DFG process between the $2\omega_p$ signal and the input rectangular pulse train, which makes each tributary channel interact with a different portion of the linearly chirped signal spectrum, thereby acquiring a different frequency shift ($\omega'_k = 2\omega_p - \omega_k$). As a result of the cSHG/DFG process, the various OTDM channels are mapped onto discrete separate output wavelengths (ω'_k) while retaining the critical pulse-timing information on a bit-by-bit basis, as indicated in Fig. 4.3(c).

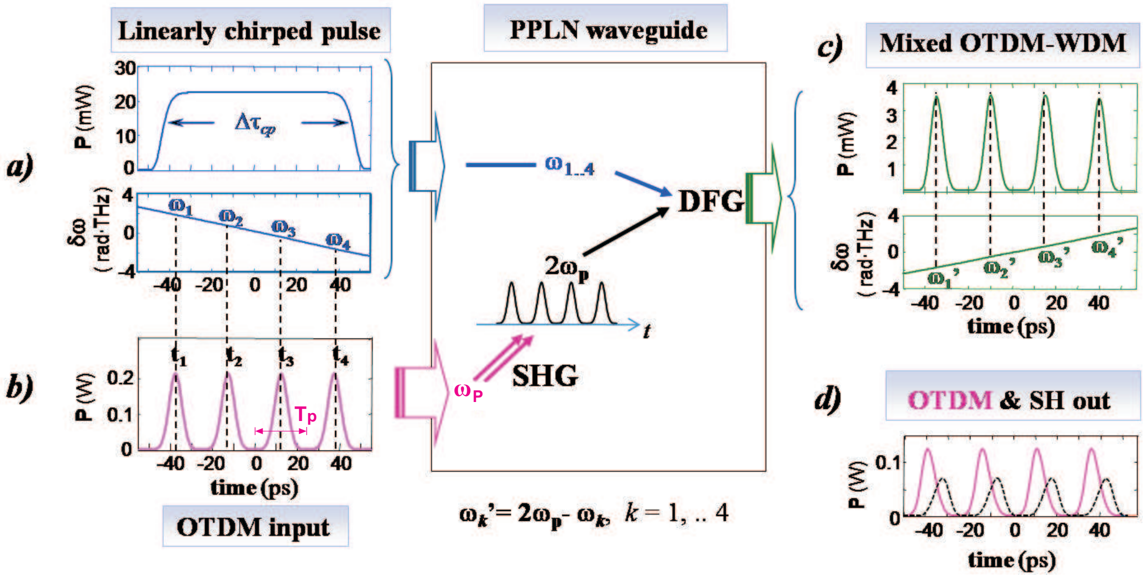

Figure 4.3: Illustration of the OTDM to mixed TDM-WDM conversion based on cSHG/DFG in a PPLN waveguide.

In the following, a theoretical model of the proposed OTDM to mixed TDM-WDM conversion scheme will be introduced. The accompanying simulations were performed for a PPLN waveguide, characterized by a length $L = 30$ mm, a normalized SHG conversion efficiency $\eta_{nor} = 60\%$ W^{-1}cm^{-2}, and 80% input coupling losses. In the model we used the dispersion parameters of bulk LiNbO$_3$ [Jundt 97]. For typical fabrication conditions of buried waveguides in this wavelength range [Gallo 08], the main effect of waveguide dispersion is a shift of $2 \sim 3$ μm of the optimum period with respect to the bulk, while group velocity mismatch and group velocity dispersion are not significantly affected.

The results shown in Fig. 4.3 were calculated for the following inputs [electric field envelopes $A(z=0,t)$]:
◇ OTDM signal at the SHG phase matching wavelength λ_p, with average power P_p and a Gaussian field profile [Fig. 4.3(b)] of the form: $A_{in}(0,t) = A_p \cdot exp\{-[(t-nT_p)/\tau_p]^2\}$ with $n = \pm 1/2, \pm 3/2$, $T_p = 25$ ps, $\tau_p = 6$ ps, corresponding to a FWHM pulse duration of 7 ps (power) $[\tau = \tau_p(2 \cdot ln2)^{1/2}]$, $A_p = [P_pT_p/(\tau_p\sqrt{2}\pi)]^{1/2}$;
◇ Chirped pulse with a spectrum spanning $\Delta\lambda_{cp} = 6$ nm around λ_{cp}, average power P_{cp} and a field profile of the form: $A_{cp}(0,t) = A_{cp0} \cdot exp\{-(ln2)/2[2(t-\delta t)/\Delta\tau_{cp}]^{18}\} \cdot exp[iC_p(t-\delta t)^2]$, with $\Delta\tau_{cp} = 90$ ps, $A_{cp} = (P_{cp}T_p/\Delta\tau_{cp})^{1/2}$, a chirp $C_{cp} = 0.023$ ps^{-2}, and a time delay δt with respect to the OTDM input ($\delta t = 2$ ps for Fig. 4.3, to optimize the response with respect to SHG walk-off).

The temporal evolution of the interacting waves associated with cSHG/DFG mixing in the PPLN waveguide was modeled through the following set of coupled mode equations:

$$\begin{aligned}
\frac{\partial A_{in}}{\partial z} + \delta v_p \frac{\partial A_{in}}{\partial t} &= -i\kappa_{SHG}\omega_p A_{sh} A_{in}^* exp(-i\Delta k_{SHG} z) \\
\frac{\partial A_{cp}}{\partial z} + \delta v_{cp} \frac{\partial A_{cp}}{\partial t} &= -i\kappa_{DFG}\omega_{cp} A_{sh} A_{out}^* exp(-i\Delta k_{DFG} z) \\
\frac{\partial A_{out}}{\partial z} + \delta v_{out} \frac{\partial A_{out}}{\partial t} &= -i\kappa_{DFG}\omega_{out} A_{sh} A_{cp}^* exp(-i\Delta k_{DFG} z) \\
\frac{\partial A_{sh}}{\partial z} + \delta v_{sh} \frac{\partial A_{sh}}{\partial t} &= -i\kappa_{SHG}\omega_{in} A_{in}^2 exp(i\Delta k_{SHG} z) - i\kappa_{DFG}\omega_{sh} A_{cp} A_{out} exp(i\Delta k_{DFG} z)
\end{aligned} \tag{4.1}$$

where A_{in}, A_{cp}, A_{sh}, and A_{out} denote the slowly varying envelopes of the input OTDM signal (the pump), the chirped pulse, the SH and the output TDM-WDM signal, respectively. $\delta v_p = v_p^{-1}$, $\delta v_{cp} = v_{cp}^{-1}$, $\delta v_{out} = v_{out}^{-1}$, $\delta v_{sh} = v_{sh}^{-1}$, and v are the group velocities at the corresponding frequency. κ_{SHG} and κ_{DFG} denote the nonlinear coupling coefficients of SHG and DFG respectively. $\Delta k_{SHG} = k_{sh} - 2k_{in} - 2\pi/\Lambda$ and $\Delta k_{DFG} = k_{cp} + k_{out} - k_{sh} + 2\pi/\Lambda$ are the phase-mismatches of SHG and DFG respectively (where Λ is the period of the QPM grating and each k is the wave vector at the corresponding frequency). The set of equations in Eq. 4.1 was solved numerically by means of a symmetric split-step Fourier method [Agrawal 07].

Figure 4.3(c) plots the calculated amplitude and chirp of the generated output mixed TDM-WDM pulses, for $\lambda_p = 1546$ nm, $P_p = 16$ dBm, $\lambda_{cp} = 1551$ nm, $P_{cp} = 14$ dBm, and $\lambda_{out} \sim 2\lambda_p - \lambda_{cp} = 1541$ nm, simulating the experiments described in the following section. Figure 4.3(d) shows the expected OTDM pump throughput and SH output (solid and dotted lines, respectively). No distortion is apparent in the format converter output [Fig. 4.3(c)], despite the presence of SHG walk-off [Fig. 4.3(d)]. This confirms the capability of the cSHG/DFG scheme to work with pulses (7-ps FWHM in the simulations) shorter than the SHG walk-off limit ($\sim$ 10 ps for our device).

4.3 Experiment and discussion

4.3.1 Generation of linearly-chirped rectangular-like pulses

As discussed in the section above, linearly-chirped rectangular-like pulses are crucial in the OTDM to mixed TDM-WDM format conversion scheme and should have the following characteristics: First, the duration of the linearly-chirped pulses should be sufficiently long to overlap with all the tributaries of the OTDM signal. Second, the top of the linearly-chirped rectangular-like pulses should be flat across the full envelope to ensure that all converted WDM channels have equal power. Third, the pulses should have linear chirp to ensure all the tributary channels are mapped onto WDM channels which are equally spaced in frequency and with identical spectral bandwidths. Finally, the full bandwidth of the linearly-chirped pulses should be sufficiently wide to allow clear spectral separation between all the converted tributary channels.

Figure 4.4 shows the experimental setup used to generate the 10 GHz linearly-chirped rectangular-like pulses. The output of a 10 GHz, 1.5 ps mode-locked ERGO was first amplified to 21 dBm and launched into a 490-m long HNLF with a nonlinear coefficient of $\sim$ 20 /W/km, a dispersion of -0.64 ps/nm/km at 1550 nm, a dispersion slope of +0.030 ps/nm^2/km and an attenuation of 0.49 dB/km. The generated SPM spectral bandwidth was 25 nm, as shown in Fig. 4.6(a). Subsequently the wavelength range between 1548 nm and 1554 nm was selected using two cascaded fiber Bragg grating (FBG) filters.

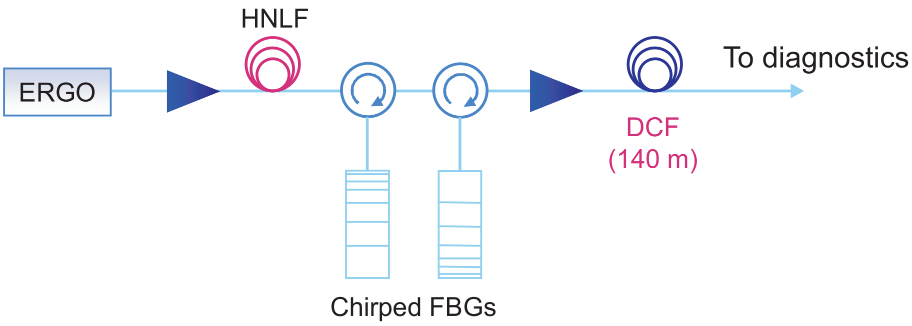

FIGURE 4.4: Experimental setup used to generate linearly-chirped rectangular-like pulses.

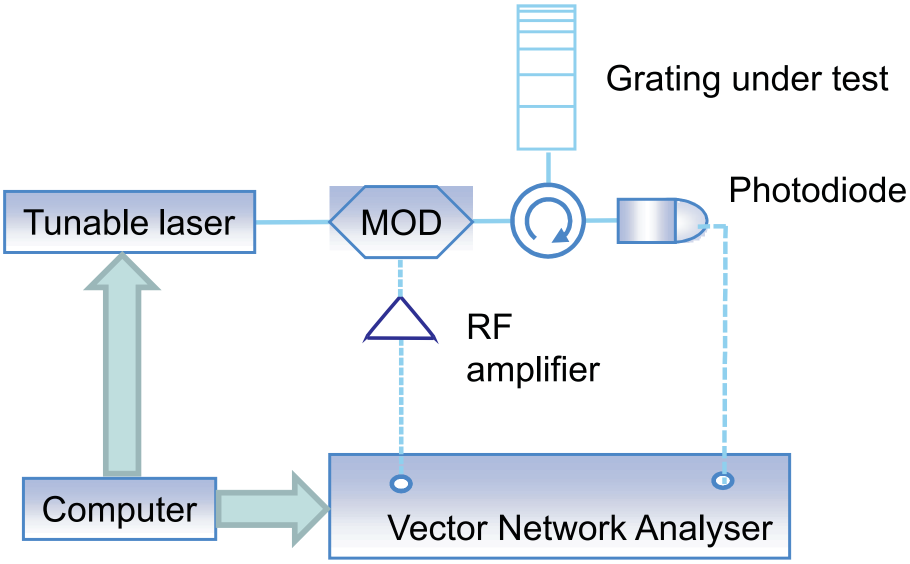

FIGURE 4.5: Experimental setup used to generate linearly-chirped rectangular-like pulses.

Modulation phase shift method [O'Sullivan 09] was used to characterise the spectral response of the linear-chirp fibre Bragg gratings, and the experimental setup is shown in Figure 4.5. A computer was used to control a tunable laser which can sweep across the wavelength window in which the chromatic dispersion needs to be measured. The output of the tunable laser is modulated by an electro-optic intensity modulator driven by a RF signal at frequency f_m which was sent from a vector network analyser. The modulated signal was circulated to the chirped fibre Bragg grating and reflected back. The signal was then measured by a photodiode and converted to a RF signal. The phase of the RF signal sent from the vector network analyser and the RF signal received from the photodiode were compared in the vector network analyser, and the resultant RF phase delay is

$\phi(\lambda)$ which is a function of the source wavelength. $\phi(\lambda_r)$ is RF phase delay at a reference wavelength λ_r. Then the group delay as a function of wavelength λ is given by

$$\Delta\tau_g(\lambda) = \frac{\phi(\lambda) - \phi(\lambda_r)}{360^o}\frac{1}{f_m} \tag{4.2}$$

where $\phi(\lambda) - \phi(\lambda_r)$ is the RF phase difference measured between wavelength λ and a reference wavelength λ_r.

These two linear-chirp FBGs had almost identical spectral response (see Fig. 4.7), but two opposite ends of the FBGs were chosen as the input ports for the incident signals so that each of them induced an opposite chirp to the reflected output signal. After reflected from the first FBG, the filtered pulses acquired a chirp of $\sim$ 20 ps/nm. A second chirped FBG was then used to remove the chirp as well as to further slice the spectrum, increasing the band extinction ratio to $\sim$ 40 dB, as shown in the spectral trace in Fig. 4.6(b).

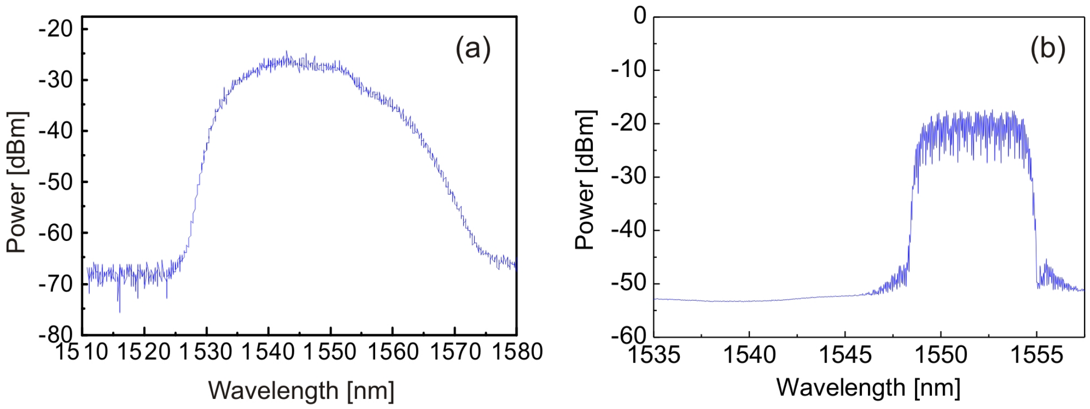

FIGURE 4.6: (a): Optical spectrum after the 490-m long HNLF. (b): Spectral traces after the spectrum slicing by two cascaded FBGs.

After that, the pulses were stretched in time by propagation through 140 m of dispersion compensating fibre (DCF) with a dispersion of $D \approx$ -107 ps/nm/km at 1550 nm, resulting in a rectangular-like envelope of $\sim$ 85 ps FWHM which was sufficiently long to overlap with all four tributaries of the 40 Gbit/s signal as shown in Fig. 4.8(a). The pulses were observed to have sharp trailing and leading edges and a good flat-top section. Fig. 4.8(b) shows the spectrogram of the linearly chirped pulses measured using an electro-optic modulation-based L-FROG [Vu 08]. The measured chirp was $\sim$ 15 ps/nm. The linear chirp ensured that the mapped WDM channels would be equally spaced from each other in frequency.

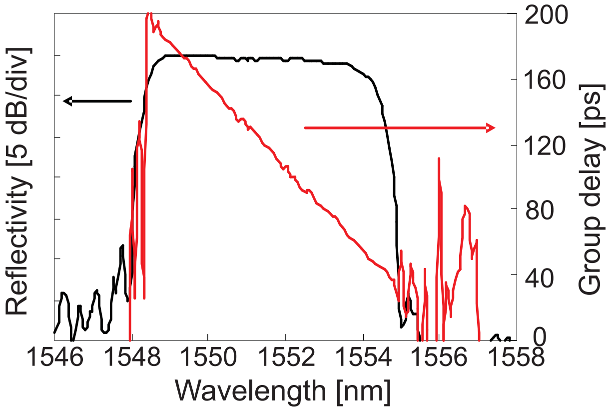

FIGURE 4.7: The spectral response of the linear-chirp FBGs.

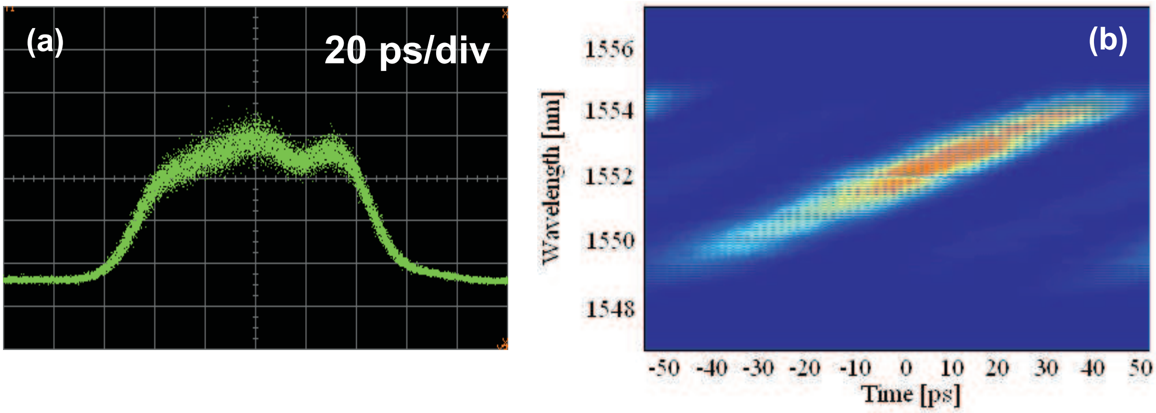

FIGURE 4.8: (a): Temporal trace of linearly-chirped rectangular pulse (for illustrative purposes, when taking this measurement the repetition rate was gated down to 5 GHz). (b): Measured FROG spectrogram traces of the linearly-chirped pulses.

4.3.2 OTDM to mixed TDM-WDM format conversion experiment

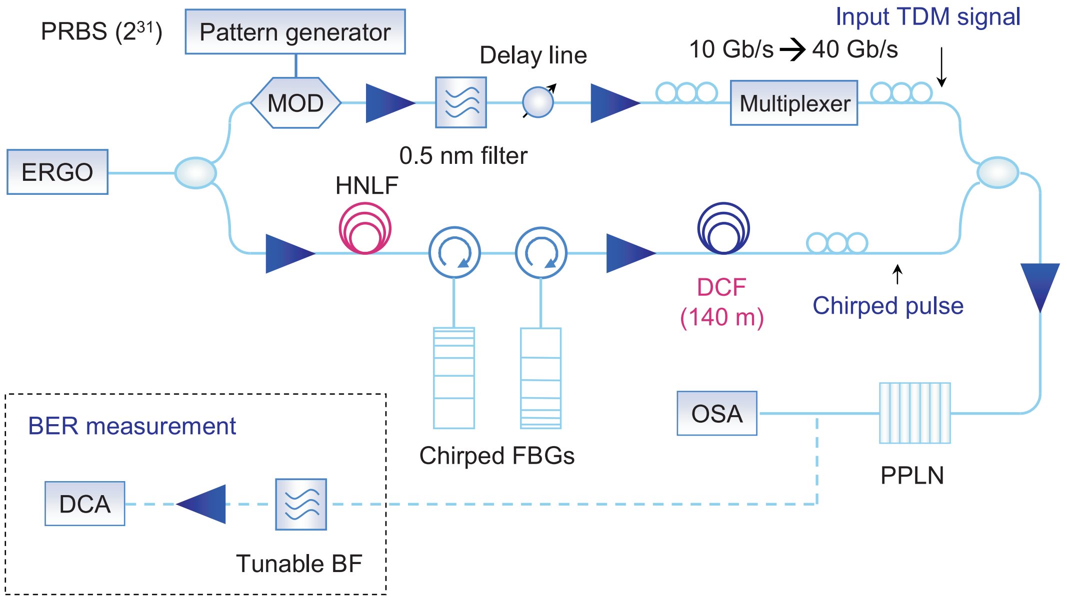

FIGURE 4.9: Experimental setup used to convert the OTDM to mixed TDM-WDM signal. MOD: modulator, EDFA: erbium-doped fiber amplifier, PC: polarization controller, DCA: digital communication analyzer (scope bandwidth of 32GHz).

Fig. 4.9 shows the experimental setup used to convert a 40 Gbit/s OTDM signal to a 4×10 Gbit/s mixed TDM-WDM signal. A 10 GHz, 1.5 ps mode-locked ERGO was first split into two separate paths using a 3-dB coupler to generate the data signal and the linearly-chirped rectangular-like pulses, respectively. The bottom arm was used to generate the 10 GHz linearly-chirped rectangular-like pulses, as introduced in Section 4.3.1. The pulses in the data path were modulated by a $2^{31} - 1$ pseudorandom bit sequence (PRBS) using a lithium niobate modulator, then filtered using a 0.5 nm-bandpass filter (yielding a temporal width of 7 ps) to match the PPLN SHG acceptance bandwidth. The FROG spectrogram traces and corresponding retrieved intensity and phase profiles of the 10 Gbit/s signal are shown in Fig. 4.10. The 10 Gbit/s signal was subsequently multiplexed up to 40 Gbit/s to form a $\sim$ 33% duty cycle RZ-OOK signal as shown in Fig. 4.11.

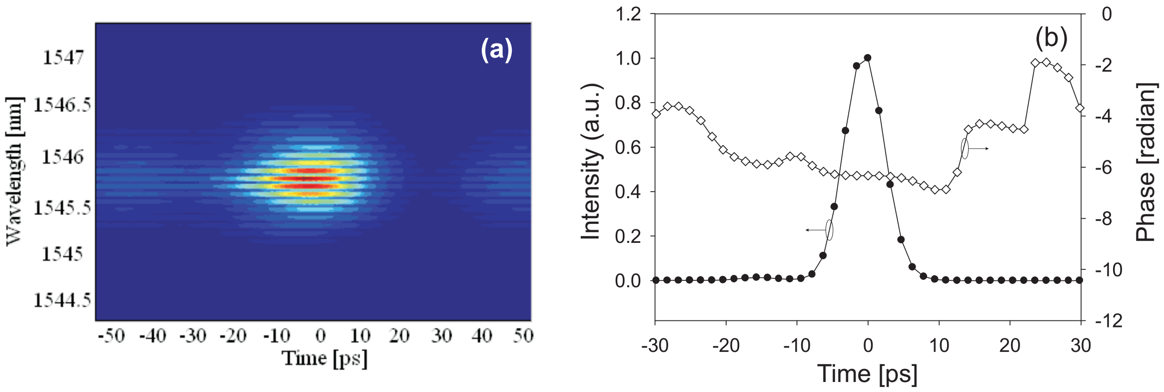

FIGURE 4.10: (a) FROG spectrogram trace and (b) retrieved intensity and phase profile for the input OTDM signal.

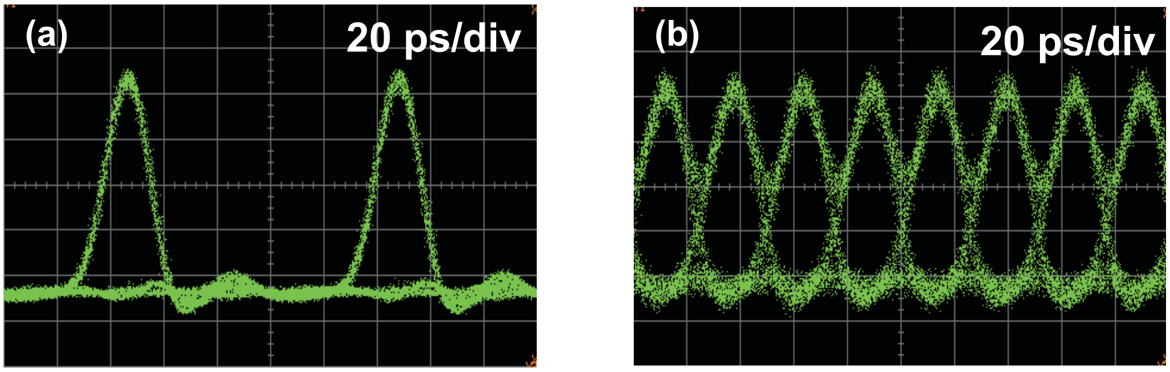

FIGURE 4.11: (a): Eye diagram of the 10-Gbit/s data signal. (b): Eye diagram of the 40-Gbit/s data signal.

A variable delay line was used to adjust the relative delay between the OTDM signal and the linearly-chirped rectangular pulses. The two signals were then combined with a 3-dB coupler and launched into a PPLN waveguide. The 30-mm-long fibre pigtailed PPLN waveguide (HC Photonics Corp.) was used to induce the cSHG/DFG process, and its phase matching wavelength for SHG was 1546 nm at $50^{o}C$. As discussed previously, the 40 Gbit/s data signal generated the second harmonic (at 773 nm) via the SHG process in the PPLN, which then interacted with the linearly chirped pulses via the DFG process to produce the mixed TDM-WDM-format signal as a replica of the original data, as shown in Fig. 4.3. The measured spectrum at the output of the PPLN waveguide is shown in Fig. 4.12(a). The 3-dB bandwidth of each of the four converted WDM channels and the spacing between them were 0.57 nm and 1.42 nm, respectively and their optical signal to noise ratio was more than 22 dB.

A filter, tunable both in bandwidth and central wavelength (Alnair Labs.), was used after the PPLN device to extract either the full converted mixed TDM-WDM signal or one of the four WDM channels separately. The measured spectral trace, eye-diagram and FROG spectrogram of the converted mixed TDM-WDM output are shown in Fig. 4.12(b), Fig. 4.13(a) and Fig. 4.13(b), respectively. The spectrogram in Fig. 4.13(b) shows that it has an opposite slope to that of the original linearly chirped signal [Fig. 4.6(b)]. This is because the higher frequency components of the linearly chirped pulse interact first with the input OTDM pulses which are the then converted to lower frequency components in the mixed TDM/WDM output as sketched in Fig. 4.3.

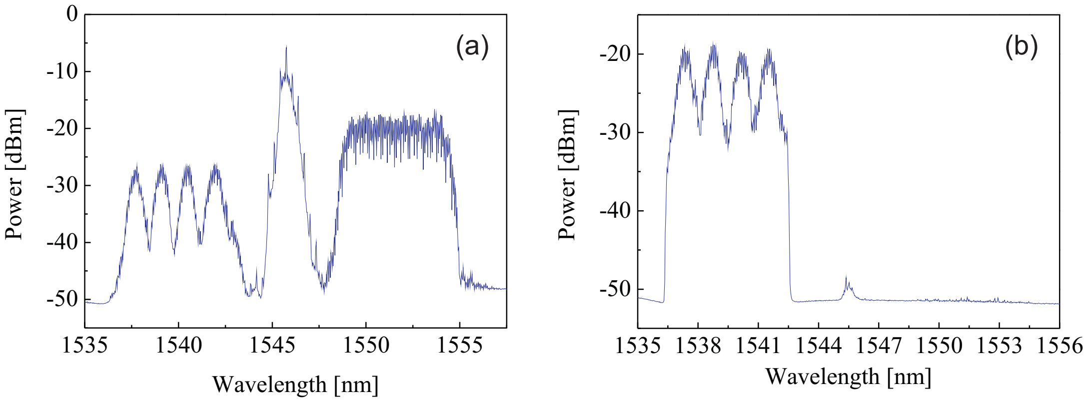

FIGURE 4.12: (a): Optical spectrum after PPLN. (b): Optical spectrum of the converted mixed TDM-WDM signals.

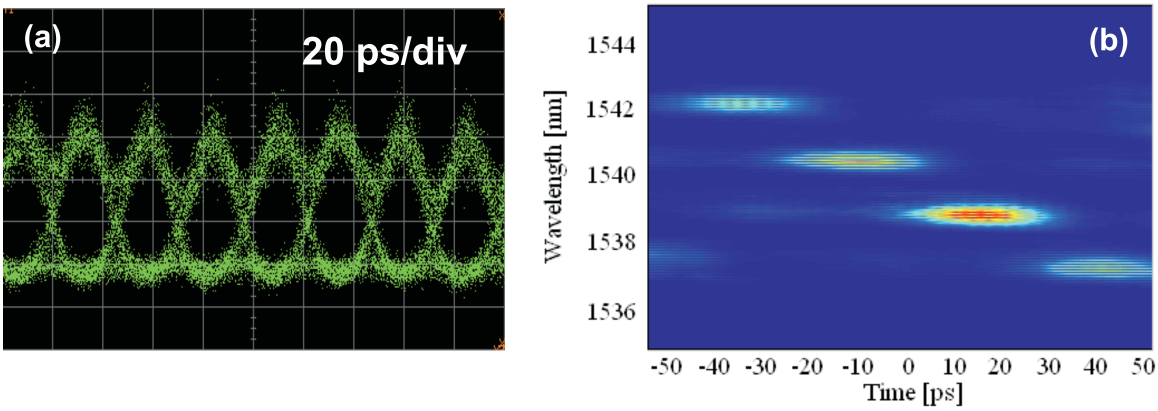

FIGURE 4.13: (a): Eye diagram and spectral trace of converted mixed TDM-WDM signal. (b): Measured FROG spectrogram trace of the converted mixed TDM-WDM signal.

Each of the four WDM channels was then extracted using the Alnair filter. The spectral traces and eye-diagrams of each WDM channel are shown in Fig. 4.14 (a) (b), Fig. 4.15 (a) (b), Fig. 4.16 (a) (b), and Fig. 4.17 (a) (b), respectively. As can be seen, all of the four converted channels show a clear open eye-diagram. The individual pulses of each WDM channel and the input OTDM signal were also characterized using the FROG technique. The FROG spectrogram traces and corresponding retrieved intensity and phase profiles of each WDM channel are shown in Fig. 4.14 (c) (d), Fig. 4.15 (c) (d), Fig. 4.16 (c) (d), and Fig. 4.17 (c) (d), respectively. Compared to the input pulses (Fig. 4.10), the output pulses in each WDM channel had similar pulse widths (7.5 ps, 8.7 ps, 8.6 ps, and 9.0 ps respectively) to the original pulses (7.2 ps), and the 3-dB spectral bandwidth of the output pulses on each channel and the original pulses were also similar (0.57 nm, 0.57 nm, 0.57 nm, 0.57 nm, and 0.6 nm respectively), resulting in time-bandwidth products of 0.53, 0.60, 0.60, 0.63 and 0.54 for each channel and the original pulses. This suggested that the OTDM to WDM conversion has not significantly affected the quality of the signal (the slight increase in the signal pulse width is attributed to the choice of a tight filter bandwidth at the system output).

One of the applications of this OTDM-WDM conversion is to perform the drop operation in OTDM signal add/drop multiplexers, i.e. dropping several tributary channels from the high-speed OTDM signal. To assess the drop operation, the width of the passband of the Alnair filter were adjusted, two of the WDM channels (Ch 1 and Ch 2) simultaneously and three of the WDM channels (Ch 1, Ch 2 and Ch 3) were simultaneously extracted, respectively. Spectral traces and eye-diagrams for each case are shown in Fig. 4.18 (a)(b) and Fig. 4.19 (a)(b), respectively. Both the eye-diagrams show clear, open eyes for the selected channels as well as a good suppression for the unselected channels.

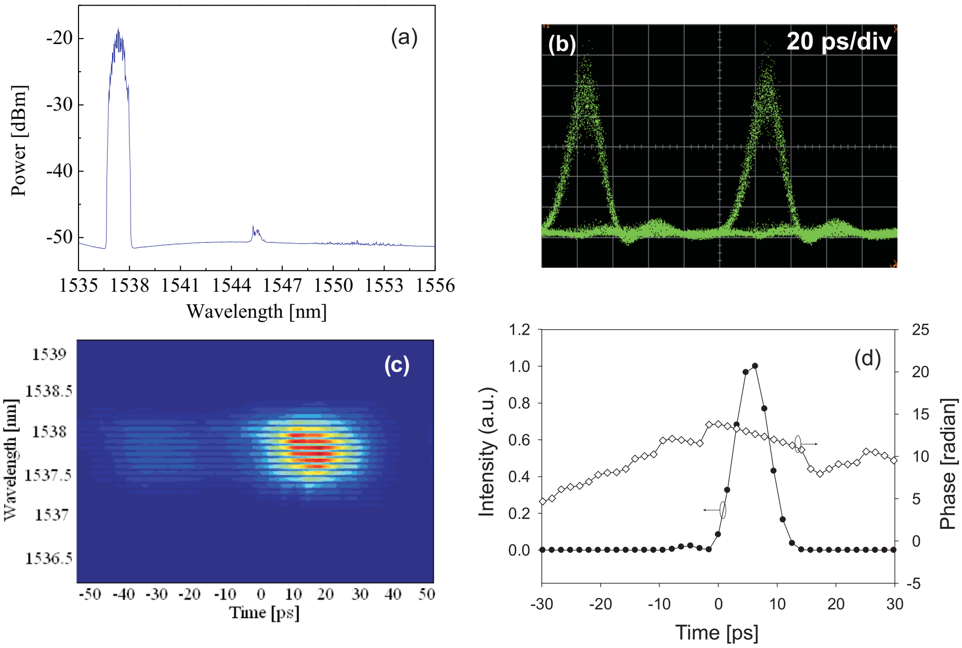

Figure 4.14: (a) Optical spectrum (b) Eye diagram (c) FROG spectrogram trace and (d) retrieved intensity and phase profiles for Channel 1 of the converted mixed TDM-WDM signal.

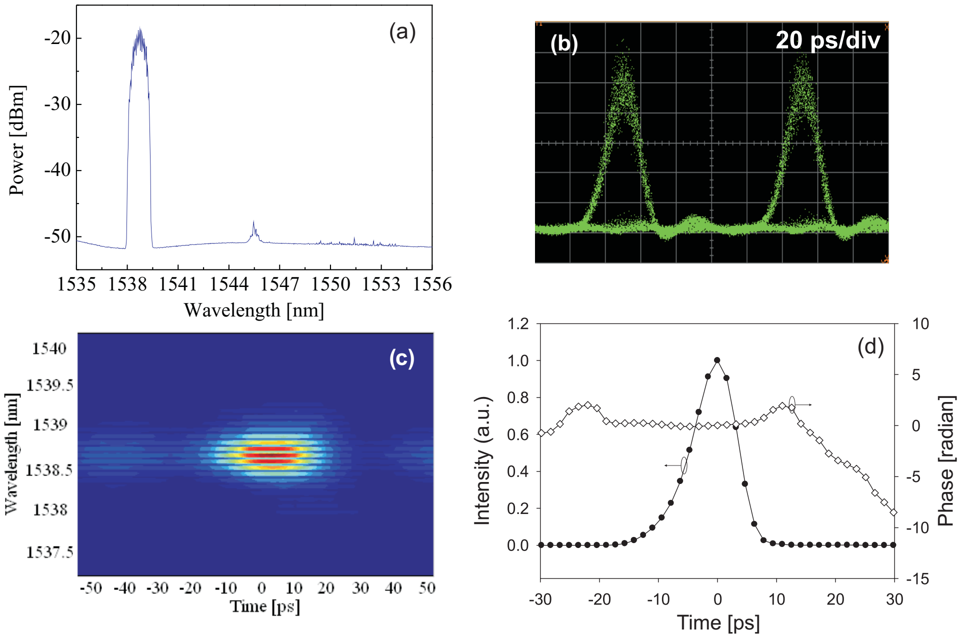

Figure 4.15: (a) Optical spectrum (b) Eye diagram (c) FROG spectrogram trace and (d) retrieved intensity and phase profiles for Channel 2 of the converted mixed TDM-WDM signal.

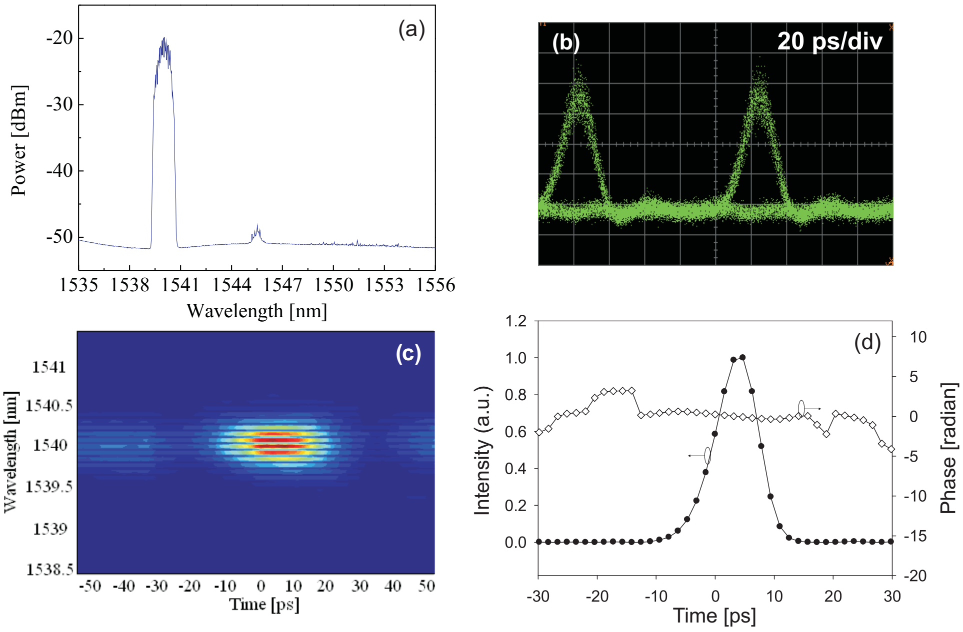

FIGURE 4.16: (a) Optical spectrum (b) Eye diagram (c) FROG spectrogram trace and (d) retrieved intensity and phase profiles for Channel 3 of the converted mixed TDM-WDM signal.

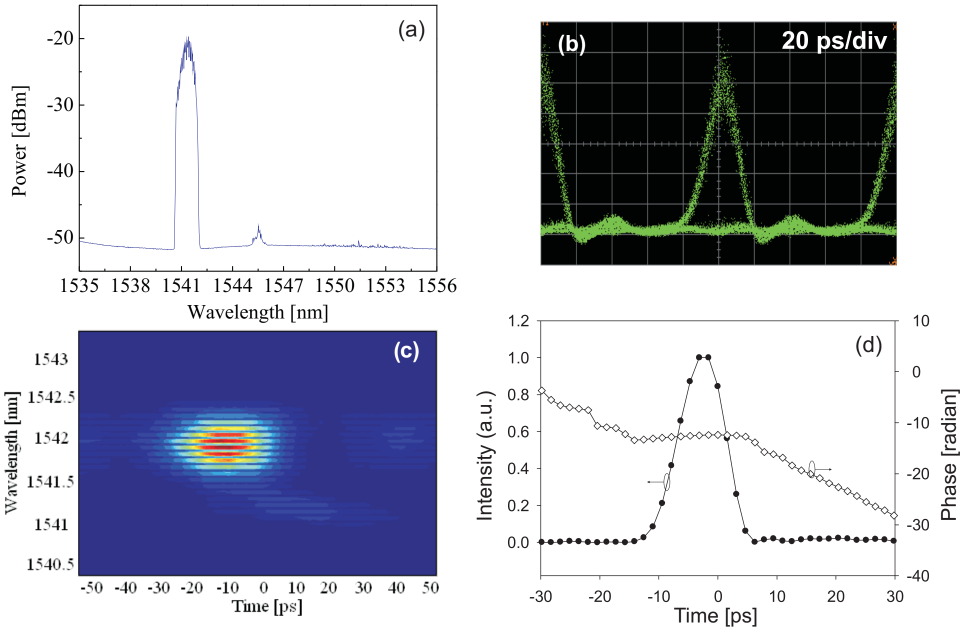

FIGURE 4.17: (a) Optical spectrum (b) Eye diagram (c) FROG spectrogram trace and (d) retrieved intensity and phase profiles for Channel 4 of the converted mixed TDM-WDM signal.

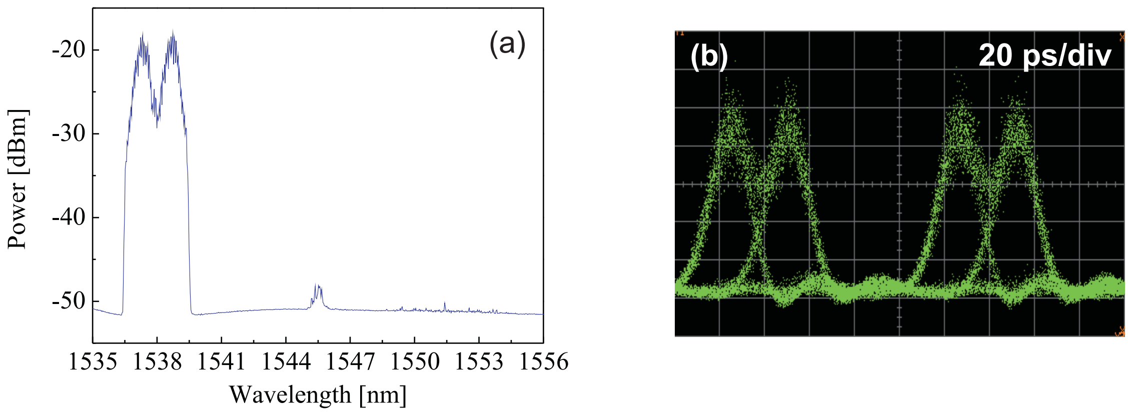

FIGURE 4.18: (a) Optical spectrum (b) Eye diagram for Channel 1 and 2 of the converted mixed TDM-WDM signal.

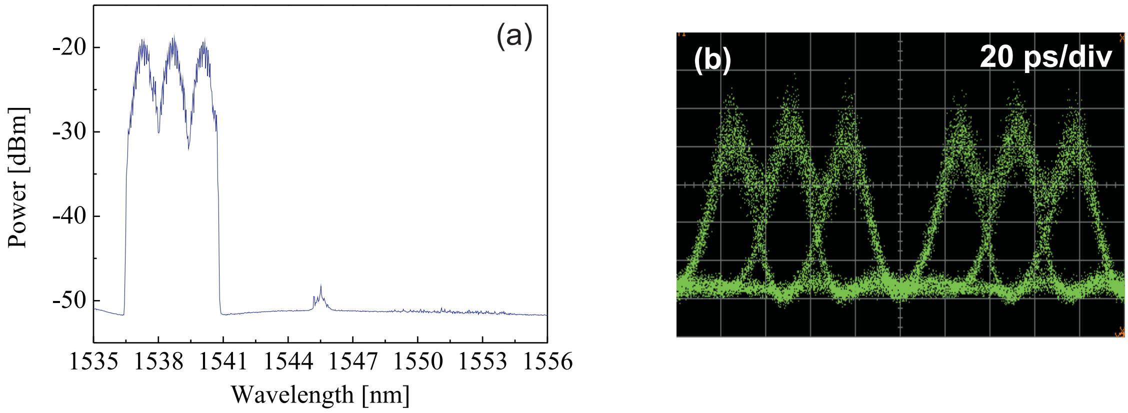

FIGURE 4.19: (a) Optical spectrum (b) Eye diagram for Channel 1, 2 and 3 of the converted mixed TDM-WDM signal.

Finally, we assessed the performance of the conversion system through bit-error rate (BER) measurements, properly filtering and amplifying each WDM channel in the process. Error-free operation (BER$=10^{-9}$) was achieved for all four WDM channels and the power penalty of the four channels was between 1.5 dB and 2 dB as compared to the back-to-back measurements at (10 Gbit/s), as shown in Fig. 4.20.

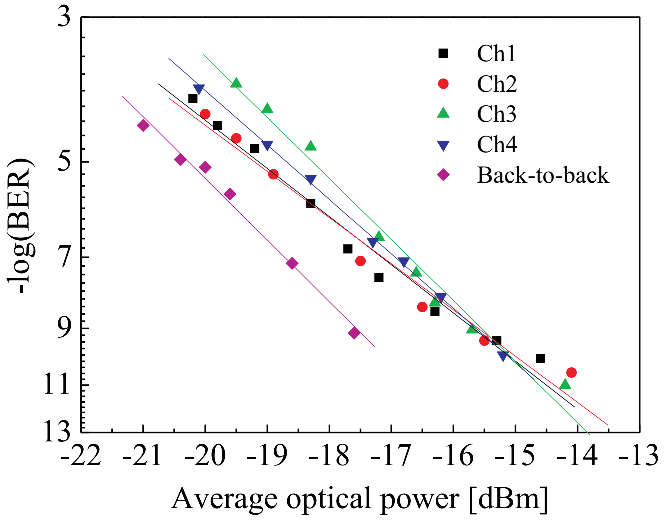

FIGURE 4.20: BER curves for each tributary channel and the back-to-back signal.

4.4 Conclusion

In this chapter, I have successfully presented the conversion of a 40 Gbit/s OTDM signal to a 4 × 10 Gbit/s mixed TDM-WDM signal using cSHG/DFG in a fully fiberized 30-mm-long PPLN waveguide. The technique relies on the generation of spectrally (and temporally) flat linearly chirped pulses which are then optically switched with the short data pulses of the OTDM signal in the nonlinear waveguide. Experimental results showed that the output pulses from the OTDM to mixed TDM-WDM conversion had a good quality and the intersymbol interference in the mixed TDM-WDM signal was low. Error-free operation was obtained for all channels with a power penalty below 2 dB.

References

[Agrawal 07] G. P. Agrawal, Nonlinear fiber optics, Elsevier, 2007.

[Almeida 04] P. J. Almeida, P. Petropoulos, B. C. Thomsen, M. Ibsen & D. J. Richardson, *All-optical packet compression based on time-to-wavelength conversion*, Ieee Photonics Technology Letters, vol. 16, no. 7, pages 1688–1690, July 2004.

[Almeida 06] P. J. Almeida, P. Petropoulos, F. Parmigiani, M. Ibsen & D. J. Richardson, *OTDM add-drop multiplexer based on time-frequency signal processing*, Journal of Lightwave Technology, vol. 24, no. 7, pages 2720–2732, July 2006.

[Gallo 08] K. Gallo, A. Pasquazi, S. Stivala & G. Assanto, *Parametric solitons in two-dimensional lattices of purely nonlinear origin*, Physical Review Letters, vol. 100, no. 5, page 053901, February 2008.

[Hashimoto 00] T. Hashimoto, H. Sotobayashi, K. Kitayama & W. Chujo, *Photonic conversion of OC-192OTDM-to-4 x OC-48WDM by supercontinuum generation*, Electronics Letters, vol. 36, no. 13, pages 1133–1135, June 2000.

[Ishio 84] H. Ishio, J. Minowa & K. Nosu, *Review and Status of Wavelength-division-multiplexing Technology and Its Application*, Journal of Lightwave Technology, vol. 2, no. 4, pages 448–463, 1984.

[Jundt 97] D. H. Jundt, *Temperature-dependent Sellmeier equation for the index of refraction, n(e), in congruent lithium niobate*, Optics Letters, vol. 22, no. 20, pages 1553–1555, October 1997.

[Keiser 99] G. E. Keiser, *A review of WDM technology and applications*, Optical Fiber Technology, vol. 5, no. 1, pages 3–39, January 1999.

[Kilper 04] D.C. Kilper, R. Bach, D.J. Blumenthal, D. Einstein, T. Landolsi, L. Ostar, M. Preiss & A.E. Willner, *Optical performance monitoring*, Lightwave Technology, Journal of, vol. 22, no. 1, pages 294 – 304, jan. 2004.

[Norte 96] D. Norte & A. E. Willner, *All-optical data format conversions and reconversions between the wavelength and time domains for dynamically reconfigurable WDM networks*, Journal of Lightwave Technology, vol. 14, no. 6, pages 1170–1182, June 1996.

[O'Sullivan 09] Rongqing Hui Maurice O'Sullivan, Fiber optic measurement technology, Elsevier Academic Press, 2009.

[Shake 02] I. Shake & H. Takara, *Averaged Q-factor method using amplitude histogram evaluation for transparent monitoring of optical signal-to-noise ratio degradation in optical transmission system*, Lightwave Technology, Journal of, vol. 20, no. 8, pages 1367 – 1373, aug 2002.

[Sotobayashi 01] H. Sotobayashi, W. Chujo & T. Ozeki, *80Gbit/s simultaneous photonic demultiplexing based on OTDM-to-WDM conversion by four-wave mixing with supercontinuum light source*, Electronics Letters, vol. 37, no. 10, pages 640–642, May 2001.

[Sotobayashi 02] H. Sotobayashi, W. Chirio & K. Kitayama, *Photonic gateway: TDM-to-WDM-to-TDM conversion and reconversion at 40 Gbit/s (4 channels X 10 Gbits/s)*, Journal of the Optical Society of America B-optical Physics, vol. 19, no. 11, pages 2810–2816, November 2002.

[Tucker 88] R. S. Tucker, G. Eisenstein & S. K. Korotky, *Optical Time-division Multiplexing For Very High Bit-rate Transmission*, Journal of Lightwave Technology, vol. 6, no. 11, pages 1737–1749, November 1988.

[Uchiyama 01] K. Uchiyama & T. Morioka, *All-optical time-division demultiplexing experiment with simultaneous output of all constituent channels from 100Gbit/s OTDM signal*, Electronics Letters, vol. 37, no. 10, pages 642–643, May 2001.

[von Lerber 07] T. von Lerber, J. Tuominen, H. Ludvigsen, S. Honkanen & F. Küppers, *Investigation of multiwavelength clock recovery based on heterodyne beats of sideband-filtered signal*, Optics Communications, vol. 271, no. 1, pages 87 – 90, 2007.

[Vu 08] K. T. Vu, A. Malinowski, M. A. F. Roelens, M. Ibsen, P. Petropoulos & D. J. Richardson, *Full characterization of low-power picosecond pulses from a gain-switched diode laser using electrooptic modulation-based linear FROG*, Ieee Photonics Technology Letters, vol. 20, no. 5-8, pages 505–507, March 2008.

[Weber 06] H. G. Weber, R. Ludwig, S. Ferber, C. Schmidt-Langhorst, M. Kroh, V. Marembert, C. Boemer & C. Schubert, *Ultrahigh-speed OTDM-transmission technology*, Journal of Lightwave Technology, vol. 24, no. 12, pages 4616–4627, December 2006.

5

Retiming of short pulses based on pre-shaping and quadratic cascading in a periodically poled lithium niobate waveguide

5.1 Introduction

All-optical signal regeneration is expected to play an essential role in future high speed optical communication systems. The cumulative effects of repeater noise amplification and optical nonlinearities in long-haul transmission systems can give rise to both amplitude noise and timing jitter in the transmitted optical signals, resulting in significant performance degradation. Therefore, signal regeneration techniques for the mitigation of both amplitude noise and timing jitter are required to overcome these transmission impairments. In this chapter, an all-optical retiming scheme based on pulse shaping and cSHG/DFG-based switching in a PPLN waveguide will be demonstrated. This chapter starts with a brief description of some types of degradations experienced in fiber-optic communication systems and a review of regeneration techniques which generally involve three basic functions, reamplification, reshaping and retiming. The chapter then focuses on all-optical retiming techniques and an all-optical retiming scheme using pulse shaping and cascaded quadratic interactions in PPLN waveguides for RZ-OOK signals is proposed. The chapter closes with experimental evidence supporting this retiming scheme.

5.1.1 Signal degradation and regeneration in fiber-optic communication systems

Modern fiber-optic communication systems can transmit data at high data rates over long distances. However, optical fiber transmission channels are not ideal, affected by many factors such as amplified spontaneous emission (ASE), dispersion, non-linear effects, and crosstalk [Gordon 86, Chraplyvy 90, Xie 03, Agrawal 07]. First of all, unless amplification is used, the maximum transmission distance between optical transmitter and receiver is mainly determined by fiber loss. Optical amplifiers such as EDFAs and Raman amplifiers are used for the compensation of fibre loss in the transmission link. However, amplification is always accompanied by the generation of ASE noise, which might give rise to other degradations. Second, chromatic dispersion causes optical pulses to broaden as they travel along a fibre. The overlap between neighbouring pulses, namely intersymbol interference (ISI), may create errors at the receiver. The solution that is currently used in practice is to perform dispersion compensation, typically by matching the transmission fibre with another DCF of opposite-sign dispersion so that the dispersion effects cancel out. Another source of degradation is a variety of nonlinear effects such as SPM, XPM, FWM, SBS, and stimulated Raman scattering (SRS). The dispersion compensation with DCFs is ultimately limited by nonlinear effects, such as SPM and XPM, which interact with dispersion to make it very difficult to compensate for the induced nonlinear chirps. Also, the combination of ISI and FWM leads to intrachannel four wave mixing (IFWM) which creates "ghost" pulses at the "0" level as well as generating significant amplitude fluctuations on the "1" level [Essiambre 99]. The ISI effect makes the neighbouring pulses in one channel overlap and results in timing fluctuations of the pulses due to the intrachannel cross phase modulation (IXPM) effect between the the adjacent pulses [Mamyshev 99]. Another origin of timing jitter is that ASE and nonlinear impairments manifest themselves as phase noise shifting the central frequency of the signal by a small random amount, and because of chromatic dispersion the speed of each pulse through the fibre also varies. Hence at the receiver the pulses appear shifted relative to each other, leading to timing jitter [Gordon 86]. Polarization mode dispersion (PMD) is another kind of degradation and becomes prominent typically at data rates of 40 Gbit/s and above [Sunnerud 02, Agrawal 07]. Because of random imperfections and asymmetries of fibres, two different polarization modes in fibres travel at different speeds, resulting in the spreading of optical pulses.

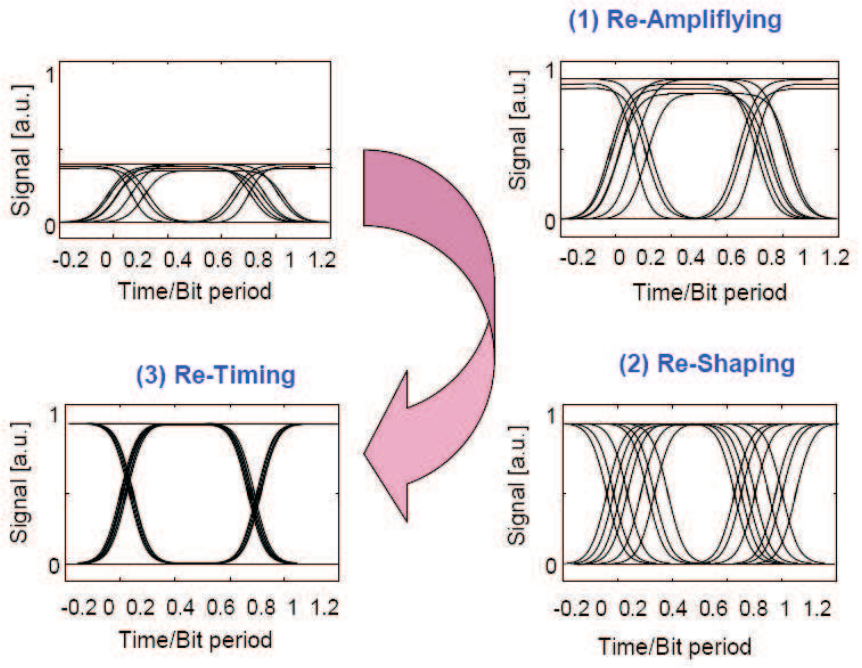

FIGURE 5.1: Principle of 3R regeneration, as applied to NRZ signal: (1) Re-amplifying; (2) Re-shaping; and (3) Re-timing. Reference [Leclerc 03].

These degradations introduced above may eventually make optical signals unrecognizable at the receiver. Therefore, optical signals need to be regenerated, and regenerators are required to be placed periodically in the transmission line. A regenerator transforms the degraded bit stream into its original form by performing three functions known as reamplifying, reshaping, and retiming [Leclerc 03]. Such devices are referred to as "3R regenerators". The block diagram of 3R regeneration is illustrated in Fig. 5.1. Regenerators that only perform reamplifying and reshaping are called "2R regenerators". Optical-electronic-optical conversion is a mature technique used for regeneration. The fundamental principle of optical-electronic-optical regeneration is to convert an optical signal to an electronic format first, so that its time and shape are restored. Forward error correction can also be employed to the electronic signal to detect errors. For instance, the widely used Reed-Solomon RS(255,239) code which has a redundancy of 7 % gives a coding gain of ~ 4.3 dB at an output BER level of 10^{-8} [Kschischang 10]. Then the electronic signal is used to modulate an optical laser to generate a new optical signal. However, optical-electronic-optical regeneration is limited by the speed of electronics, rendering it restricting for high-speed fiber-optic communication systems [Leclerc 03].

It is also possible to carry out all-optical regeneration without the need for electronics. Various configurations for all-optical regeneration have been demonstrated previously. For instance, all-optical 2R regenerators based on SPM in a HNLF have been intensively studied [Mamyshev 98, Raybon 02, Vasilyev 05, Striegler 06, Lee 06, Provost 08, Vasilyev 08]. Mamyshev reported first a 2R regeneration scheme based on the effect of SPM of the data signal in a nonlinear medium with a subsequent optical filtering at a frequency which is shifted with respect to the input data carrier frequency. Noise in "zeros" and amplitude fluctuations in "ones" are suppressed considerably because of a step-like transfer function [Mamyshev 98]. Recently, multi-channel SPM-based regenerations have been reported. The key to this is management of the chromatic dispersion along the device which allows for effective control of the inter-channel cross-talk interactions [Vasilyev 05, Provost 08, Vasilyev 08]. FWM is another nonlinear interaction which can be used for regeneration. Ciaramella *et al.* demonstrated a 2R regeneration scheme which makes use of gain saturation in the FWM effect resulting in a suppression of fluctuations in the peak power of a pulse [Ciaramella 00]. Simos *et al.* reported an all-optical 2R regenerator using FWM in a SOA, based on the nonlinear FWM transfer function [Simos 04]. The XPM effect in either a HNLF or a SOA can also be used for regeneration. Suzuki *et al.* proposed a 3R-regeneration scheme which relies on XPM in a highly nonlinear fibre resulting in a regenerated wavelength-converted signal with a reverse bit pattern [Suzuki 05]. Leuthold *et al.* proposed 3R regenerators based on SOA using cross gain modulation or XPM in an interferometric configuration [Leuthold 02]. All-optical 3R regenerations relying on XPM in a NOLM were reported in [Bogoni 04].

3R regenerators are required in most cases in optical networks, and retiming is an essential functionality in a 3R regenerator to realign a pulse to the clock cycle. Furthermore, even for 2R regenerators which only perform reamplification and reshaping and might be useful in some parts of the transmission systems, the reshaping operation itself sometimes still leads to an increase in the timing jitter which needs to be addressed. For instance, Finot *et al.* reported that operating of Mamyshev regenerators at the "plateau zone" which was ideal from the reshaping point of view induced maximum delay fluctuations on the pulses and resulted in large timing jitter [Finot 08]. Thus retiming is attractive to be added to a 2R regenerator for added functionality. In the next section, I will focus on retiming techniques.

5.1.2 All-optical retiming techniques

In the section above, signal regeneration techniques in fiber-optic communication systems have been briefly reviewed. In the following, I will focus on one of the regeneration functions, retiming, and I will demonstrate a novel all-optical retiming scheme. In a signal affected by timing jitter the pulses are randomly shifted from their nominal slot, causing decision errors at the receiver. Therefore, retiming technologies are of high importance to improve the performance of fiber-optic communication systems. Several all-optical retiming schemes have been demonstrated previously. For instance, an all-optical retiming scheme based on reshaping a pulse into a rectangular pulse before optically switching it with clean, synchronous pulses using XPM in a NOLM was reported in [Watanabe 03, Parmigiani 06a, Parmigiani 09]. Retiming schemes based on either cross-phase modulation in an optical fibre or phase modulation with a single phase modulator, followed by a dispersive element to reposition the data pulse in the time domain were reported in [Parmigiani 06b] and [Jiang 03], respectively. A retiming scheme that relied on the manipulation of the temporal walk-off between the pump and the SH pulses in PPLN was presented in [Hasegawa 04]. In that scheme, the input data pulses affected by timing jitter generated SH pulses through SHG. The slower-propagating SH pulses were subsequently gated by a slightly later incident clock pulse train through DFG, generating an output signal with suppressed timing jitter at a different wavelength. The stability of the systems discussed in [Watanabe 03, Parmigiani 06a, Parmigiani 09], which are based on $\chi^{(3)}$ nonlinearities in optical fibres, is generally compromised by the long fibre lengths required for efficient operation, while PPLN waveguides provide high $\chi^{(2)}$ nonlinear coefficients, and are compact and insensitive to environmental perturbations. However, the retiming scheme discussed in [Hasegawa 04], which is based on $\chi^{(2)}$ nonlinearities in PPLN waveguides, was limited in flexibility since the walk-off is directly related to the physical device length, and also the retiming region had an uneven intensity response which is likely to give rise to large amounts of amplitude noise on the output signal. In the all-optical retiming scheme presented in this chapter, we overcome these limitations by pre-shaping the data pulses into broader flat-top pulses, prior to them being launched into the waveguide, where they are switched with a synchronous clean optical clock. The details of the principle of this retiming scheme will be presented in the next section.

5.2 Operational principle of the retiming scheme

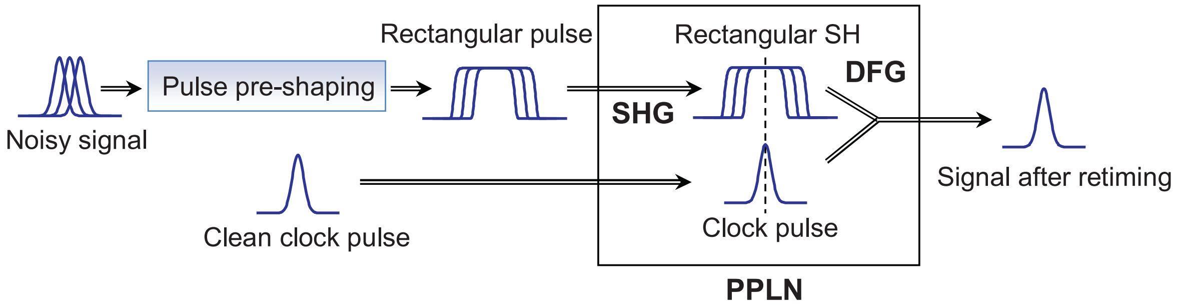

FIGURE 5.2: Illustration of the all-optical pulse retiming scheme based on both pulse pre-shaping and cSHG/DFG in a PPLN waveguide.

The basic idea of the proposed retiming scheme is illustrated in Fig. 5.2. The input data pulses affected by timing jitter noise are first pre-shaped into flat-top pulses and launched into the PPLN device. The flat-top pulses at the fundamental frequency generate flat-top SH pulses by SHG in the PPLN waveguide. The SH pulses are subsequently gated by the locally generated clock pulse train, which is synchronously launched into the PPLN device and temporally aligned to the nominal centre of the SH data pulses, to generate an output signal with suppressed timing jitter at a different wavelength through DFG. Note that clock recovery would normally be required to synchronize the clock pulses to the incoming data stream, but the development of clock recovery techniques is beyond the scope of this thesis.

One 2-ps pulse source and one 7-ps pulse source were available in the lab for these experiments. Because the pulse width of the input signal affected by timing jitter should be ideally comparable to that of the clean clock pulse train, the output of the 2-ps pulse source was first filtered using a 0.5-nm bandpass filter (yielding a temporal width of 7 ps) and then used as the input signal in the following experiment presented in Section 5.3. The 7-ps input signal was designed to be converted into 50 ps rectangular pulses, which means that the timing-jitter tolerance was ∼ ± 25 ps in the designed retiming system. However, it is noted that the retiming performance would be degraded as the two edges of the retiming region are approached, where the rectangular SH pulses and the clock pulses only partially overlapped. The 7-ps pulse source was used as the clock.

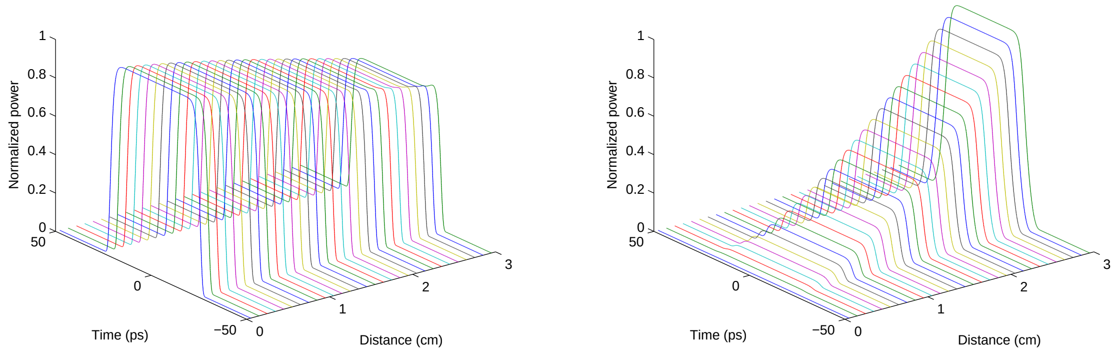

(a) Input rectangular pulse

(b) SH pulse

Figure 5.3: Propagation of (a) the input pulses and (b) the SH pulses along the length of the PPLN waveguide in the SHG process.

In order to predict the behavior of the experiments, simulations were run with 50-ps rectangular input pulses and 7-ps clock pulses. Since the flatness of the top of the generated SH pulses is critical to the performance of the proposed retiming scheme, a simulation of the SHG process involving the input rectangular-like pulses and the generated SH pulses was performed. The simulations used the coupled mode equations of the SHG process as presented in Section 2.1.2.1 in the background chapter and the split-step Fourier algorithm as shown in the Ref. [Agrawal 07]. Also the simulation was performed with the specifications of the PPLN waveguides described in Section 2.2. Figure 5.3 shows the simulation results of the rectangular pump pulses and the generated SH signal along the length of the waveguide. As the generated SH pulse grows gradually along the length of the PPLN waveguide, it still keeps the flat-top shape, and is not severely distorted from the walk-off effect between the fundamental frequency and the SH. As shown in Fig. 5.3(a), the small jump on the top of the rectangular-like input pulse is because the pump depletion in that region is relatively less significant than that in other regions.

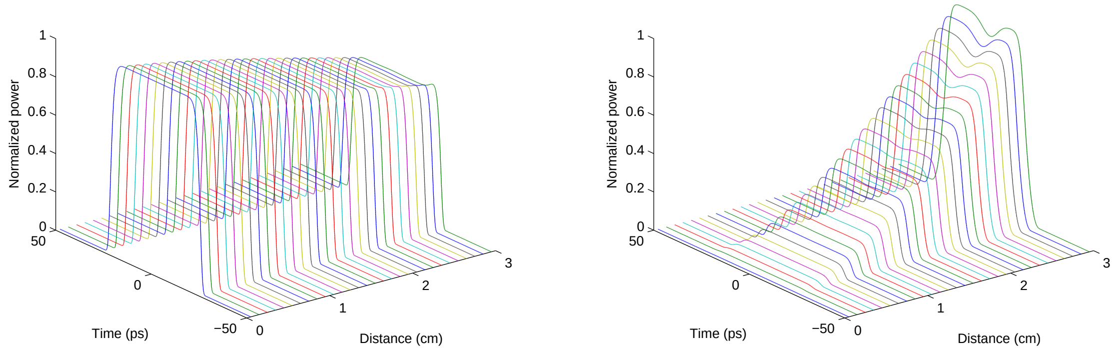

(a) Input rectangular pulse (b) SH pulse

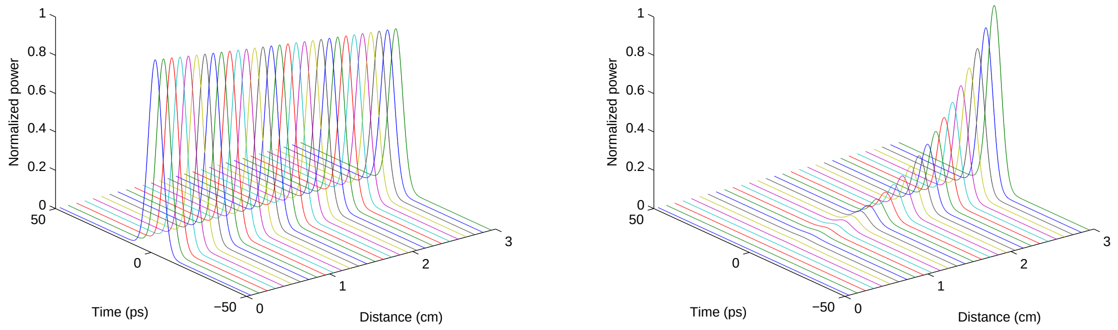

(c) Clock pulse (d) Output pulse

FIGURE 5.4: Propagation of (a) the input pulses (50 ps) and (b) the SH pulses (c) the clock pulses (7 ps) (d) the output pulses along the length of the PPLN waveguide in the cSHG/DFG process.

A full simulation of the cSHG/DFG process involving the initial flat-top, SH, clock, and output pulses was also performed. Fig. 5.4(a-d) show simulations of the propagation of these pulses along the 30-mm-length PPLN waveguide. As can be seen in Fig. 5.4(a) and (b), the initial flat-top pulse also generates a SH pulse with a flat-top shape and without any significant waveform distortion originating from walk-off effects in the device. The small dip on the flat-top region in the SH pulse is caused by the DFG interaction between the SH pulse and the clock pulse, and its position corresponds to the region of temporal overlap between them. The output pulse has a Gaussian profile, similar to the clock pulse, and its peak power grows gradually along the waveguide as shown in Fig. 5.4(d).

The ultimate bandwidth limitation of our technique is imposed by the walk-off between

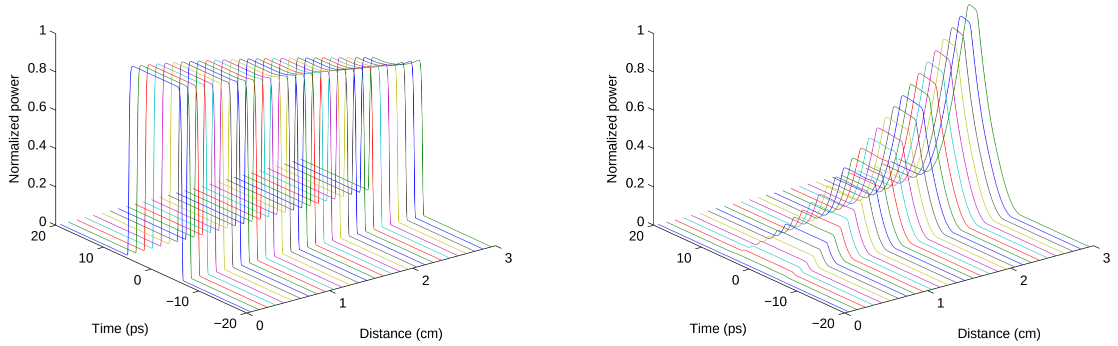

(a) Input rectangular pulse (b) SH pulse

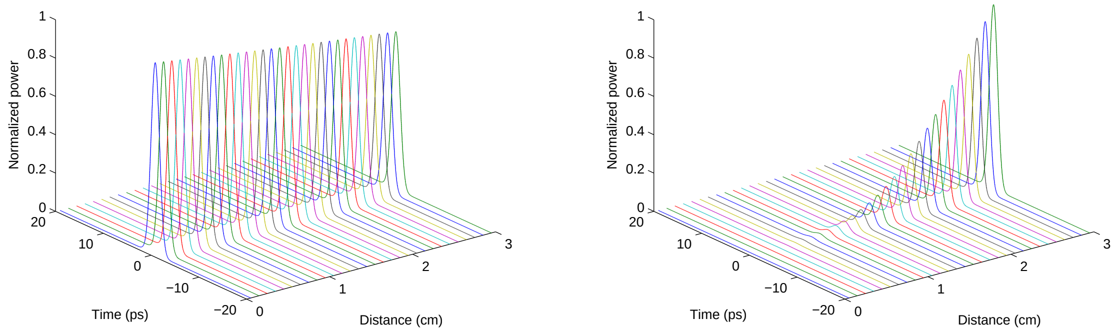

(c) Clock pulse (d) Output pulse

FIGURE 5.5: Propagation of (a) the input pulses (10 ps) and (b) the SH pulses (c) the clock pulses (2 ps) (d) the output pulses along the length of the PPLN waveguide in the cSHG/DFG process.

the data and the SH signal. As illustrated in Fig. 5.5, another set of simulations was run with 10-ps rectangular-like input pulses and 2-ps clock pulses. The SH pulse was generated with a flat-top shape, and the output pulse was generated at the temporal position of the clock pulse with a Gaussian profile, which indicated good operation for this retiming system. However, if the duration of the input rectangular-like pulse is further shortened to less than 10 ps, the duration of the generated SH pulse would still be ∼ 10 ps due to the walk-off effect (as shown in Fig. 5.6), which limits the data period to 10 ps (corresponding to a data rate of 100 Gbit/s) for a 30-mm PPLN device. It is noted that even higher data rates could be achieved using a shorter PPLN device.

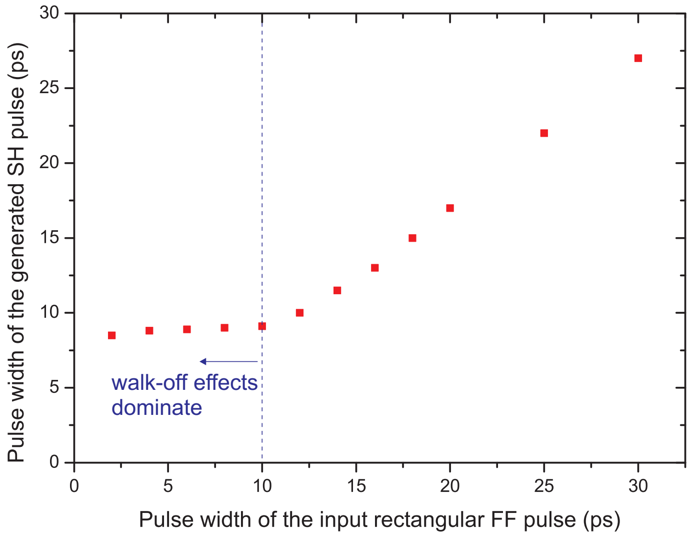

FIGURE 5.6: Pulse width of the input rectangular FF pulse versus pulse width of the generated SH pulse.

5.3 Experiment

5.3.1 Generation of rectangular pulses

Pulse shaping techniques to convert pulses from a Gaussian-like shape to a rectangular-like shape have been well studied, and may rely for example on the superstructure fibre Bragg grating (SSFBG) technique [Petropoulos 01], the PMD effect in a highly birefringent fibre [Watanabe 03] or the use of acousto-optic and spatial light modulators [Weiner 00].

An alternative approach of pulse shaping using a commercial optical processor (Waveshaper) has recently been developed. As introduced in the Background chapter, optical processors are based on high-resolution LCoS techniques, and can be employed as spectral filters allowing individual control of the intensity and phase of spectral components. The model of the optical processor (Finisar WaveShaper 4000E) used in the experiment has a resolution of 4 GHz. In the case that we convert a Gaussian pulse into a rectangular pulse in the time domain, in terms of Fourier transform theory, in the frequency domain we need to shape a spectrum with a Gaussian profile into a spectrum with a profile of a sinc-function consisting of alternating lobes of the inverse phase, as shown in Fig. 5.7. Therefore, in order to achieve a rectangular pulse at the output, we need to design a filter with a spectral response $H(\omega)$ as follows

$$H(\omega) = Y_{rectangular}(\omega)/X_{input}(\omega) \tag{5.1}$$

where $Y_{rectangular}(\omega)$ is the spectrum of the rectangular pulse and $X_{input}(\omega)$ is the spectrum of the input pulse.

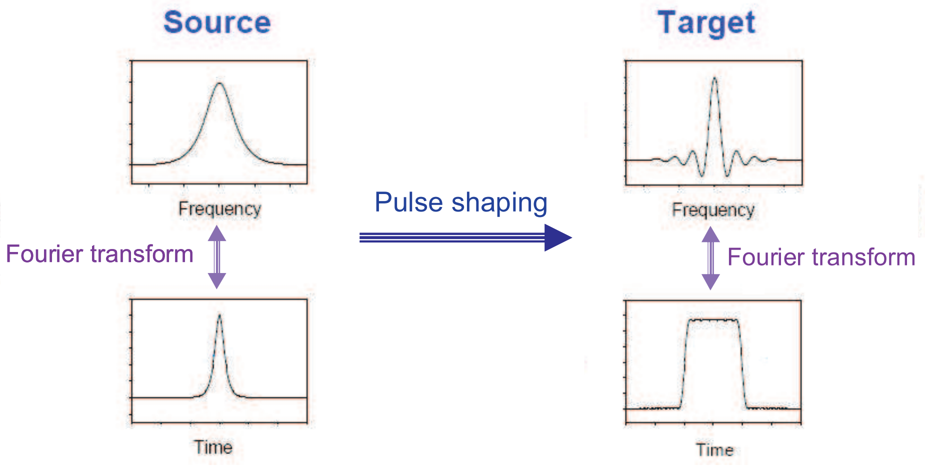

Figure 5.7: Pulse shaping to generate a rectangular pulse from a Gaussian pulse. Reference [Petropoulos 01].

Figure 5.8 shows the experimental setup used to generate the 10 GHz 50-ps rectangular-like pulses. The designed spectrum (pink trace) and the spectrum measured using OSA (blue trace) of the 50-ps rectangular pulses are shown in Fig. 5.9(a). The temporal intensity profile of the rectangular pulses measured using an optical sampling oscilloscope is

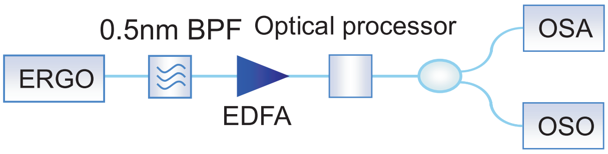

FIGURE 5.8: Schematic of the experimental setup to generate rectangular pulses. ERGO: erbium glass oscillator laser, EDFA: erbium-doped fibre amplifier, BPF: band pass filter, OSO: optical sampling oscilloscope, OSA: optical spectrum analyser.

shown in Fig. 5.9(b). Figure 5.9(b) confirms that the width of the pulses is $\sim$ 50 ps and the pulses have sharp trailing and leading edges. The maximum intensity fluctuation at the flat section of the rectangular pulses is $\sim$ 20% of the height of the rectangular pulses. This relatively large fluctuation is because the bandwidth of 50-ps-long rectangular pulses is too narrow compared to the data rate of 10 Gb/s. In terms of Fourier transform theory, the 50-ps pulse width of the designed rectangular pulse corresponds to a 3-dB bandwidth of $\sim$ 8 GHz for the main lobe of the sinc-function in frequency, but the spectral spacing between the adjacent spectral components for a 10 Gb/s signal is 10 GHz. This means that the main lobe of the sinc-function only comprises two or three spectral lines which are not enough to accurately control the shape of the spectrum. Another reason is that the filtering on the input pulse performed by the optical processor cannot be very accurate due to the finite resolution of the optical processor. However, one should note that our experiments used 7-ps clock pulses, which were much broader relative to these fast intensity fluctuations. It was considered that these fluctuations can be averaged out during the nonlinear interactions in the PPLN waveguide and should have little effect on the performance of the retiming system.

5.3.2 Retiming experiment

Figure 5.10 illustrates the experimental setup to realise our all-optical pulse retiming system. The PPLN waveguide used in the experiment was described in the background chapter. An erbium glass oscillator was filtered using a 0.5-nm filter and used as the pulse source for the data signal which comprised 10 GHz, 7-ps pulses at 1546 nm. The data

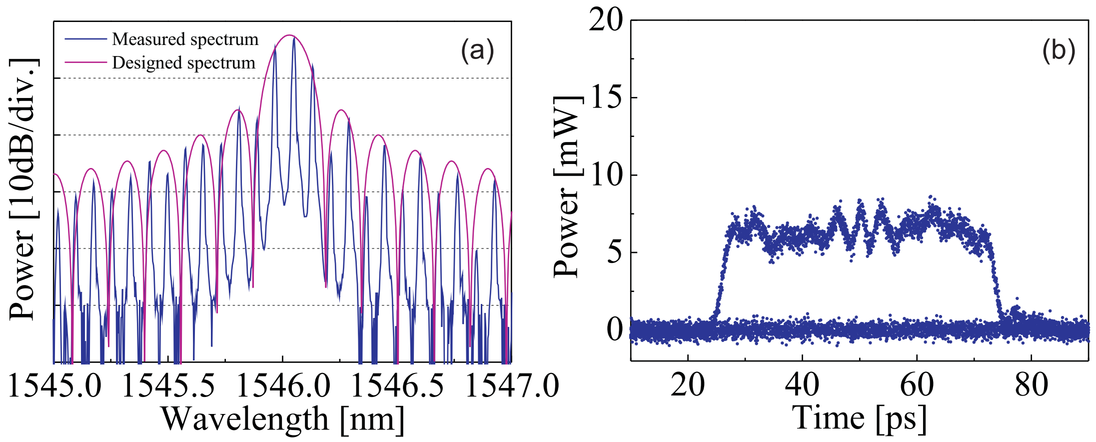

FIGURE 5.9: (a) Designed and measured spectra of the rectangular pulses (measured with a resolution of 0.05 nm). (a) Temporal intensity profile of the rectangular pulses measured using an optical sampling oscilloscope.

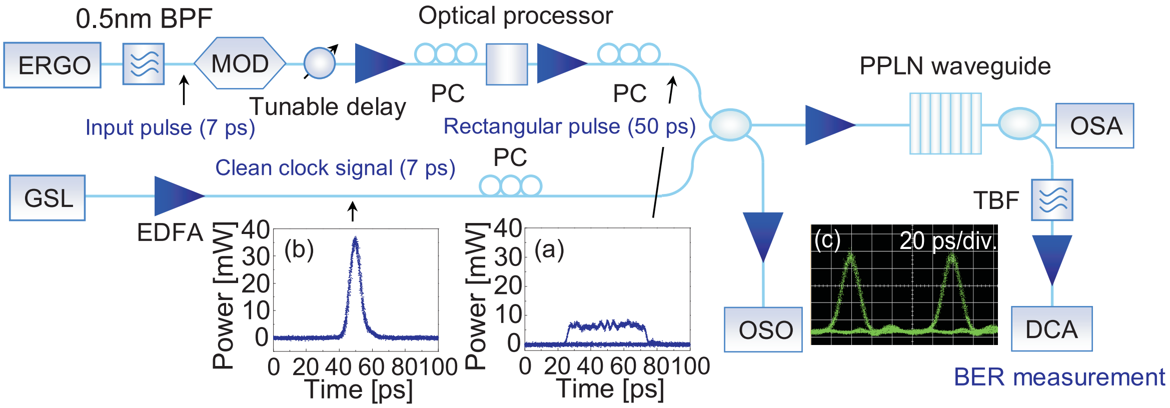

FIGURE 5.10: Schematic of the experimental setup and experimental traces recorded on several points in the system: ERGO: erbium glass oscillator laser, GSL: gain switched laser, MOD: modulator, EDFA: erbium-doped fibre amplifier, PC: polarization controller, DCA: digital communication analyzer, OSO: optical sampling oscilloscope, BPF: band pass filter, TBF: tunable bandpass filter, OSA: optical spectrum analyser. (a) Temporal intensity profile of the rectangular pulses measured by OSO. (b) Temporal intensity profile of the clock pulses measured by OSO. (c) Eye-diagram of the output pulses measured by OSA.

pulses were amplitude modulated by a $2^{31} - 1$ PRBS using a lithium niobate modulator, then amplified and launched into the optical processor to form 50-ps-long (FWHM) rectangular pulses as described previously (Fig. 5.10(a)).

The clean clock pulses at a wavelength of 1550 nm were generated by a 10-GHz, 7-ps gain-switched laser (GSL) [see Fig. 5.10(b)], and amplified before being combined with the flat-top pulses using a 3-dB coupler and launched into the PPLN waveguide. A variable delay line was used to control the relative position between the shaped data and the clean clock pulse trains and to simulate the effects of timing jitter. Polarization controllers were used to align all the optical waves to the optical axis of the PPLN waveguide. The average optical powers of both the data signal and the clock at the PPLN input were 18 dBm, and the OSNR of the data signal was 33 dB. The (noisy) input reshaped pulses at 1546 nm were up-converted to 773 nm by the SHG process in the PPLN waveguide. The SH data stream, which would still have retained any timing jitter present on the data, was then gated by the input clock via DFG to mitigate the jitter and produce a clean replica of the original data at 1542 nm. Fig. 5.11 shows the spectrum at the output of the PPLN waveguide, showing that the output signal had an OSNR of more than 22 dB. A tunable filter (Alnair Labs.) with a flat-top passband of 2 nm was used after the PPLN device to extract the retimed signal at 1542 nm and the corresponding measured eye-diagrams are shown in Fig. 5.10(c).

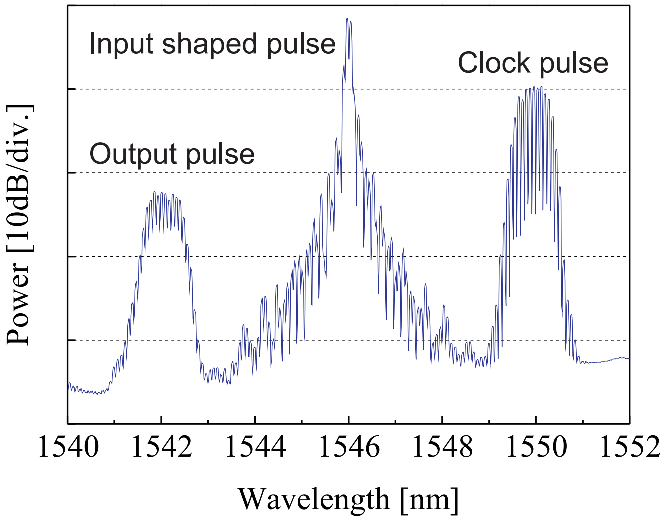

FIGURE 5.11: Spectrum at the output of the PPLN waveguide (measured with a resolution of 0.05 nm).

To assess the retiming performance of the system we varied systematically the relative delay between the clock and data signals and measured the output (Fig. 5.12). In the figure, the temporal displacement $\Delta\tau = 0$ corresponds to the clock pulse aligned to the nominal centre of the flat-top pulse. The temporal position of the output pulse did not change with the temporal offset between input and clock pulses, which means that any timing jitter on the input data pulses would not be transferred to the converted pulses. As long as the clock pulses overlapped with the flat-top region of the SH pulses (50 ps), the peak powers of the output pulses remained constant as shown in Fig. 5.12. However, when the clock pulses moved away from the flat-top regions of the shaped pulses, the output peak powers dramatically decreased. This result indicates that the maximum tolerable input timing jitter is determined by the duration of the flat-top pulses.

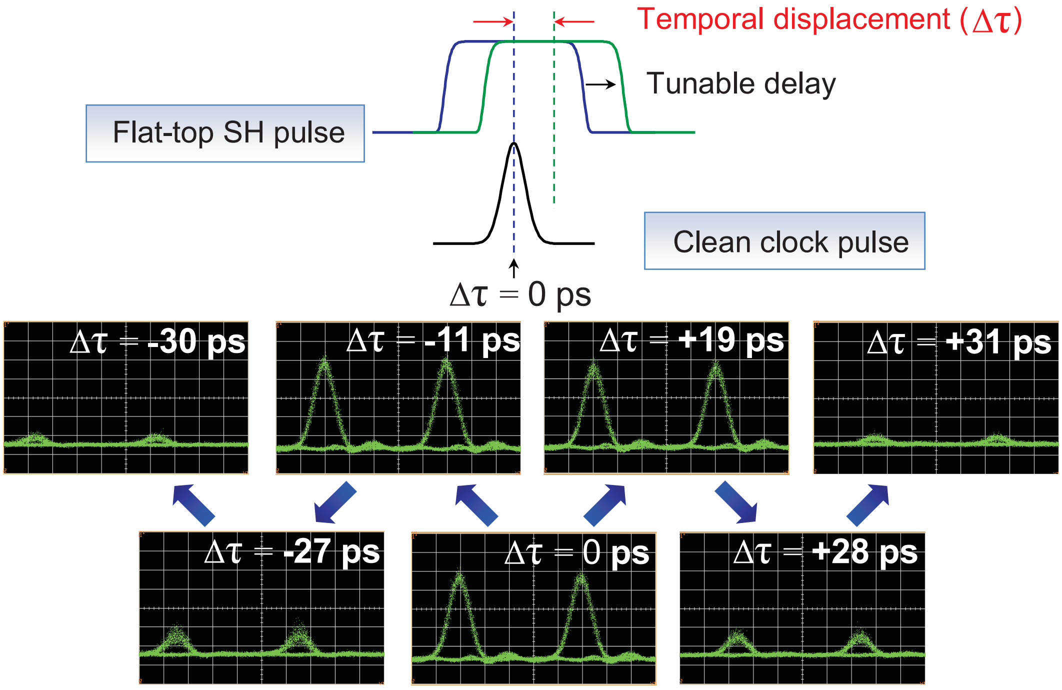

FIGURE 5.12: Eye diagrams of the signal after retiming at various relative positions.

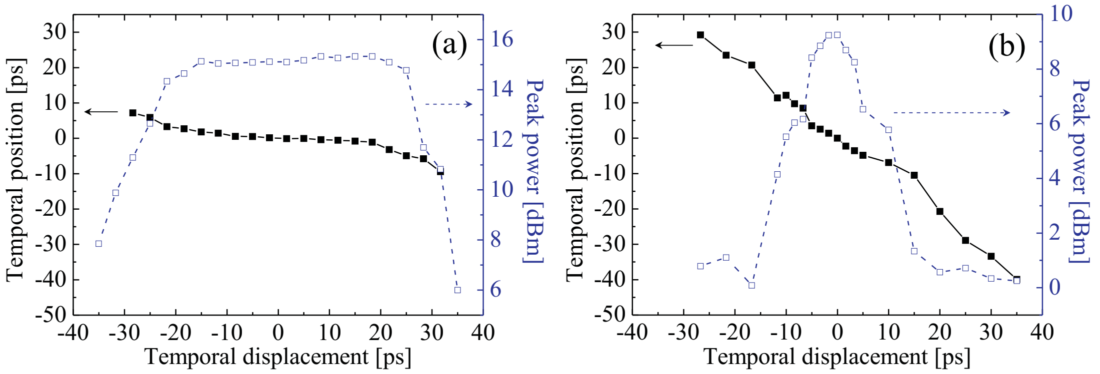

FIGURE 5.13: Temporal position and peak power of the output signal plotted as a function of the input time delay (a) with and (b) without pre-shaping.

The measured peak power and temporal position of the output pulses are plotted in Fig. 5.13 as a function of the temporal offset between the pulse streams. The zero on the horizontal axis was chosen to coincide with the point providing the most efficient conversion (or the maximum peak power). Fig. 5.13(a) corresponds to the case in which the input data pulses have been pre-shaped into flat-top pulses, and shows clearly the retiming performance. Timing jitter ranging from -22 ps to 25 ps could be eliminated by the retiming system, and this retiming region had an even intensity response. In contrast, Fig. 5.13(b) corresponds to the case when no pulse shaping was applied to the input signal. This latter case shows very limited retiming capability because the pulse width of the unshaped SH pulses is comparable to that of the clock pulses.

We finally performed BER measurements at 10 Gbit/s (using an electrically amplified receiver) to ensure that the retiming system did not introduce any amplitude noise on the input pulses. The BER measurement results are shown in Fig. 5.14. Retiming of the output signal was realised with a slight power penalty of 0.6 dB (at BER $= 10^{-9}$) as compared to the back-to-back measurements. This penalty is mainly due to the OSNR degradation from 33 dB in the data signal to 22 dB in the switched output.

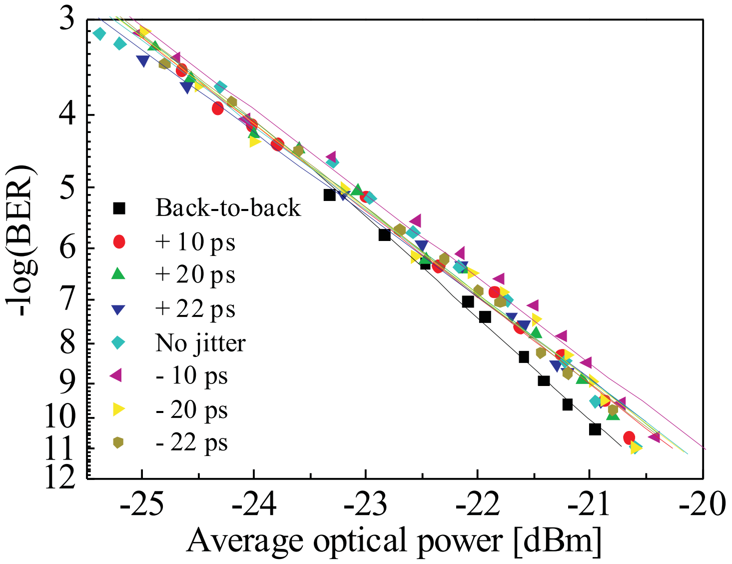

FIGURE 5.14: BER curves for the back-to-back signal and the output signals with various time delays.

5.4 Conclusion

In this chapter, I have demonstrated an all-optical signal retiming system based on pulse shaping and cSHG/DFG-based switching in a fully fiberised 30-mm-long PPLN waveguide. The presented results have shown the benefits of pre-shaping the data pulses into a flat-top waveform, as opposed to feeding them directly into the PPLN waveguide. Retiming was realised with a power penalty of just 0.6 dB at a BER of 10^{-9}. This proof-of-principle experiment operated at 10 Gbit/s with 7 ps clock pulses. In the current retiming scheme, the data signal has to be at the SHG phase matching wavelength of the PPLN device. This requirement could be overcome by employing the cSFG/DFG process instead, in which the data signal would act as one of the pumps for the SFG process.

References

[Agrawal 07] G. P. Agrawal, Nonlinear fiber optics, Elsevier, 2007.

[Bogoni 04] A. Bogoni, P. Ghelfi, M. Scaffardi & L. Poti, *All-optical regeneration and demultiplexing for 160-gb/s transmission systems using a NOLM-based three-stage scheme*, Selected Topics in Quantum Electronics, IEEE Journal of, vol. 10, no. 1, pages 192 – 196, 2004.

[Chraplyvy 90] A. R. Chraplyvy, *Limitations On Lightwave Communications Imposed By Optical-fiber Nonlinearities*, Journal of Lightwave Technology, vol. 8, no. 10, pages 1548–1557, October 1990.

[Ciaramella 00] E. Ciaramella & S. Trillo, *All-optical signal reshaping via four-wave mixing in optical fibers*, Ieee Photonics Technology Letters, vol. 12, no. 7, pages 849–851, July 2000.

[Essiambre 99] R. J. Essiambre, B. Mikkelsen & G. Raybon, *Intra-channel cross-phase modulation and four-wave mixing in high-speed TDM systems*, Electronics Letters, vol. 35, no. 18, pages 1576–1578, September 1999.

[Finot 08] C. Finot, T.N. Nguyen, J. Fatome, T. Chartier, S. Pitois, L. Bramerie, M. Gay & J.-C. Simon, *Numerical study of an optical regenerator exploiting self-phase modulation and spectral offset filtering at 40ăGbit/s*, Optics Communications, vol. 281, no. 8, pages 2252 – 2264, 2008.

[Gordon 86] J. P. Gordon & H. A. Haus, *Random-walk of Coherently Amplified Solitons In Optical Fiber Transmission*, Optics Letters, vol. 11, no. 10, pages 665–667, October 1986.

[Hasegawa 04] T. Hasegawa, X. Wang & A. Suzuki, *Retiming of picosecond pulses by a cascaded second-order nonlinear process in quasi-phase-matched LiNbO3 waveguides*, Optics Letters, vol. 29, no. 23, pages 2776–2778, December 2004.

[Jiang 03] L. A. Jiang, M. E. Grein, H. A. Hans, E. P. Ippen & H. Yokoyama, *Timing jitter eater for optical pulse trains*, Optics Letters, vol. 28, no. 2, pages 78–80, January 2003.

[Kschischang 10] Frank R. Kschischang & Benjamin P. Smith. *Forward error correction (FEC) in optical communication.* In Lasers and Electro-Optics (CLEO) and Quantum Electronics and Laser Science Conference (QELS), 2010 Conference on, pages 1 –2, may 2010.

[Leclerc 03] O. Leclerc, B. Lavigne, E. Balmefrezol, P. Brindel, L. Pierre, D. Rouvillain & F. Seguineau, *All-optical signal regeneration: from first principles to a 40 Gbit/s system demonstration*, Comptes Rendus Physique, vol. 4, no. 1, pages 163–173, January 2003.

[Lee 06] J. H. Lee, T. Nagashima, T. Hasegawa, S. Ohara, N. Sugimoto, Y. G. Han, S. B. Lee & K. Kikuchi, *Output performance investigation of self-phase-modulation-based 2R regenerator using bismuth oxide nonlinear fiber*, Ieee Photonics Technology Letters, vol. 18, no. 9-12, pages 1296–1298, May 2006.

[Leuthold 02] J. Leuthold, G. Raybon, Y. Su, R. Essiambre, S. Cabot, J. Jaques & M. Kauer, *40 Gbit/s Transmission and Cascaded All-Optical Wavelength Conversion over 1 000 000 km*, Electronics Lett, vol. 38, pages 890–892, 2002.

[Mamyshev 98] P. V. Mamyshev. *All-optical data regeneration based on self-phase modulation effect*, 1998.

[Mamyshev 99] P. V. Mamyshev & N. A. Mamysheva, *Pulse-overlapped dispersion-managed data transmission and intrachannel four-wave mixing*, Optics Letters, vol. 24, no. 21, pages 1454–1456, November 1999.

[Parmigiani 06a] F. Parmigiani, P. Petropoulos, M. Ibsen & D. J. Richardson, *All-optical pulse reshaping and retirning systems incorporating pulse shaping fiber Bragg grating*, Journal of Lightwave Technology, vol. 24, no. 1, pages 357–364, January 2006.

[Parmigiani 06b] F. Parmigiani, P. Petropoulos, M. Ibsen & D. J. Richardson, *Pulse retiming based on XPM using parabolic pulses formed in a fiber Bragg grating*, Ieee Photonics Technology Letters, vol. 18, no. 5-8, pages 829–831, March 2006.

[Parmigiani 09] F. Parmigiani, L. K. Oxenlowe, M. Galili, M. Ibsen, D. Zibar, P. Petropoulos, D. J. Richardson, A. T. Clausen & P. Jeppesen, *All-Optical 160-Gbit/s Retiming System Using Fiber Grating Based Pulse Shaping Technology*, Journal of Lightwave Technology, vol. 27, no. 9, pages 1135–1141, May 2009.

[Petropoulos 01] P. Petropoulos, M. Ibsen, A. D. Ellis & D. J. Richardson, *Rectangular pulse generation based on pulse reshaping using a superstructured fiber Bragg grating*, Journal of Lightwave Technology, vol. 19, no. 5, pages 746–752, May 2001.

[Provost 08] L. Provost, C. Kouloumentas, F. Parmigiani, S. Tsolakidis, I. Tomkos, P. Petropoulos & D. J. Richardson. *Experimental investigation of a dispersion-managed multi-channel 2R optical regenerator*, 2008.

[Raybon 02] G. Raybon, Y. Su, J. Leuthold, R. . J. Essiambre, T. Her, C. Joergensen, P. Steinvurzel & K. D. K. Feder. *40 Gbit/s pseudo-linear transmission over one million kilometers*, 2002.

[Simos 04] H. Simos, A. Bogris & D. Syvridis, *Investigation of a 2R All-Optical Regenerator Based on Four-Wave Mixing in a Semiconductor Optical Amplifier*, J. Lightwave Technol., vol. 22, no. 2, page 595, Feb 2004.

[Striegler 06] A. G. Striegler & B. Schmauss, *Analysis and optimization of SPM-based 2R signal regeneration at 40 Gb/s*, Journal of Lightwave Technology, vol. 24, no. 7, pages 2835–2843, July 2006.

[Sunnerud 02] H. Sunnerud, M. Karlsson, Chongjin Xie & P.A. Andrekson, *Polarization-mode dispersion in high-speed fiber-optic transmission systems*, Lightwave Technology, Journal of, vol. 20, no. 12, pages 2204 – 2219, December 2002.

[Suzuki 05] J. Suzuki, T. Tanemura, K. Taira, Y. Ozeki & K. Kikuchi, *All-optical regenerator using wavelength shift induced by cross-phase modulation in highly nonlinear dispersion-shifted fiber*, Ieee Photonics Technology Letters, vol. 17, no. 2, pages 423–425, February 2005.

[Vasilyev 05] M. Vasilyev & T. I. Lakoba, *All-optical multichannel 2R regeneration in a fiber-based device*, Optics Letters, vol. 30, no. 12, pages 1458–1460, June 2005.

[Vasilyev 08] M. Vasilyev, T. I. Lakoba & P. G. Patki. *Multi-wavelength all-optical regeneration*, 2008.

[Watanabe 03] S. Watanabe, F. Futami, R. Okabe, Y. Takita, S. Ferber, R. Ludwig, C. Schubert, C. Schmidt & H. G. Weber. *160 Gbit/s optical 3R-regenerator in a fiber transmission experiment*, 2003.

[Weiner 00] A. M. Weiner, *Femtosecond pulse shaping using spatial light modulators*, Review of Scientific Instruments, vol. 71, no. 5, pages 1929–1960, May 2000.

[Xie 03] C. J. Xie, L. Moller, H. Haunstein & S. Hunsche, *Comparison of system tolerance to polarization-mode dispersion between different modulation formats*, Ieee Photonics Technology Letters, vol. 15, no. 8, pages 1168–1170, August 2003.

6

Phase sensitive amplifiers exploiting cascaded quadratic nonlinearities in periodically poled lithium niobate waveguides

6.1 Introduction

In Chapter 5, a review of regeneration techniques in fibre-optic communication systems was presented, and a novel all-optical retiming scheme for return-to-zero on-off keying (RZ-OOK) signals was demonstrated. In this chapter, I will introduce phase sensitive amplifier (PSA)-based regeneration for phase shift keying (PSK) signals, and will demonstrate two novel configurations of phase sensitive amplification based on cascaded quadratic effects in PPLN waveguides.

This chapter is organised as follows: in Section 6.1.1 I first introduce the benefits of PSK signals, followed by the role of PSAs in regenerating PSK signals in Section 6.1.2. Subsequently, non-degenerated PSA based on cSHG/DFG in a PPLN waveguide is demonstrated in Section 6.2 and phase-regenerative wavelength conversion (PR-WC) is demonstrated in Section 6.3.

6.1.1 The benefits of phase shift keying signals

Fibre-optic communication systems traditionally employ conventional OOK signals which encode data using the intensity of light waves. The signal constellation for OOK is shown in Fig. 6.1(a). It is intuitive to represent modulation formats in a constellation diagram (i.e., in the complex plane, each data pulse is represented by a single point whose radial direction represents the E-field amplitude and the angular direction is the E-field phase). In Fig. 6.1(a), the red dot at the origin represents data "0", and the second red dot represents data "1". It is noted that data "1" can be at any point on the blue circle in the constellation diagram, because OOK signals encode data using the intensity rather than the phase. With the advent of EDFAs, research efforts have been mainly focused on OOK format and OOK systems have been widely deployed in commercial systems.

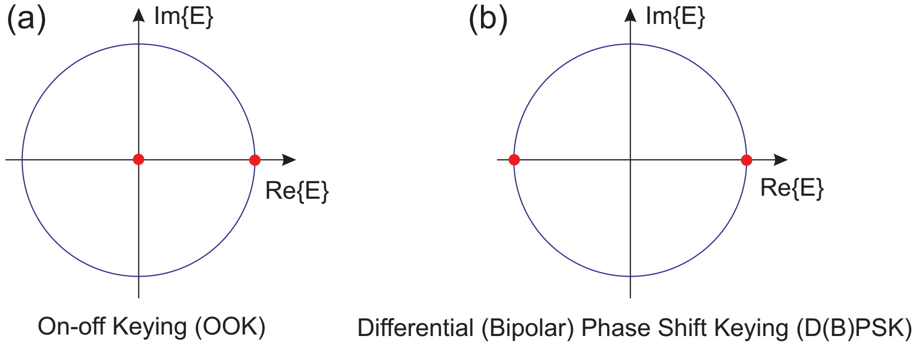

FIGURE 6.1: Constellations of (a) OOK and (b) D(B)PSK.

However, in next-generation systems, PSK formats as well as a number of advanced optical modulation formats which use both the amplitude and phase of the optical carrier will be of great importance. These modulation formats have greater tolerance to chromatic- and polarization-mode dispersion, and enable higher spectral efficiency, i.e. they can accommodate higher data capacities than OOK for the same signal bandwidth [Xu 04, Gnauck 05]. The simplest PSK modulation formats are bipolar phase shift keying (BPSK) and differential phase shift keying (DPSK) whose signal constellations are shown in Fig. 6.1(b). BPSK format encodes the data using two phases of the carrier waves which are separated by 180°. It is noted that it does not particularly matter where the constellation points are exactly positioned on the blue circle, and in this figure they are shown on the real axis, at 0^o and 180^o. DPSK format has the same constellation as BPSK but encodes data with a 0 or π-phase shift between adjacent bits.

DPSK offers considerable advantages over OOK in terms of receiver sensitivity and tolerance to uncompensated dispersion and fibre nonlinearity [Xie 03, Gnauck 05]. A DPSK signal in combination with balanced detection requires a ∼3 dB lower OSNR than OOK to reach a given BER. The lower OSNR requirement of DPSK can be used to reduce the power requirements of fibre-optic communication systems and extend the transmission reach [Gnauck 05]. Also, DPSK offers larger resistance than OOK to transmission impairments such as uncompensated dispersion and nonlinearity [Xie 03, Xu 04, Gnauck 05]. In a 10 Gb/s system DPSK does not outperform OOK [Xu 03, Ishida 03], whereas the performance of DPSK surpasses that of OOK convincingly in 40 Gb/s long-haul systems [Xu 04, Gnauck 05]. The reason is that in 40 Gb/s transmissions intra-channel FWM and intra-channel XPM become prominent [Essiambre 99, Xu 04, Gnauck 05]. Intra-channel XPM results in timing jitter on the pulses [Mamyshev 99], and DPSK greatly reduces the nonlinear intra-channel XPM effect in highly dispersed transmission by the use of pulses of equal energy in all time slots [Wei 03]. Intra-channel FWM transfers power between adjacent bit slots as pulses disperse into each other and mix due to fibre nonlinearity. In OOK systems, intra-channel FWM results in amplitude fluctuations on the "1s", and "ghost pulses" on the "0s" [Essiambre 02]. DPSK suffers less penalty from intra-channel FWM than OOK due to the lower peak power of DPSK for the same average power [Liu 02] and also a correlation between the nonlinear phase shifts experienced by any two adjacent bits [Wei 03]. It is proven that the Intra-channel FWM process that involves adjacent pulses contributes an identical phase shift to these pulses and cancels out in the differential phase error regardless of the bit pattern [Wei 03]. Also, because of the presence of power in every bit slot for DPSK signals, the optical power is more evenly distributed in DPSK than in OOK, so bit-pattern-dependent nonlinear effects are reduced [Gnauck 05].

6.1.2 The role of phase sensitive amplifiers

Since PSK signals carry information in the phase of the optical carrier, the primary limit of a DPSK transmission system is the accumulation of linear and nonlinear phase noise. Linear phase noise originates from imperfections in optical modulators on the transmitter and from ASE in optical amplifiers [Croussore 05]. Nonlinear phase noise originates from intra- and inter-channel nonlinearities such as SPM and XPM that convert amplitude noise to phase noise, which is named as the Gordon-Mollenauer effect [Gordon 90]. As a result, amplitude noise from modulators, ASE, dispersion-induced pattern effects and nonlinearities all introduce nonlinear noise that limits the system performance. Therefore, suppressing the cumulative linear phase noise and the nonlinear phase noise is of great importance in systems employing phase encoded signals. PSAs have the potential to play a critical role in the phase regeneration of phase encoded signals.

Optical amplifiers such as EDFAs, SOAs, and Raman amplifiers are commonly used in optical communication and sensor systems to boost the signal power. These amplifiers are examples of phase-insensitive amplifiers (PIAs), since their gain does not depend on the optical phase of the input signals. The operation of PIAs is illustrated in Fig. 6.2(a). The in-phase and quadrature signal components experience identical gain, and the input phase and the output phase are identical. In contrast to PIAs, PSAs are capable of amplifying or deamplifying input signals according to the phase of the optical signal [Levenson 93, Ou 93]. The operational principle of typical PSAs is shown in Fig. 6.2(b). The in-phase component of the input signal is amplified, while the quadrature component is attenuated. As a result, the output signal is more closely aligned towards the in-phase axis of the amplifier, and the output phase is squeezed compared to the input phase. This gain characteristic is capable of regenerating D(B)PSK signals, as the output data bits have a "squeezed" phase which is close to 0 or π, depending on the input signal. PSAs have another intriguing advantage, that is the noise figure of PSAs can potentially be reduced below the 3 dB quantum limit of phase-insensitive linear amplifier [Caves 82, Tong 10]. Linear amplifiers are those whose gain does not depend on the power of the incoming signal. Phase-insensitive linear amplifiers amplify equally both the signal and any noise on it. Due to Heisenberg's uncertainty principle, amplification introduces some phase and amplitude fluctuations, and this gives rise to the quantum noise limits of linear amplifiers. In EDFAs, the fluctuation comes in the form of ASE, and the ASE spectral density in a single polarisation is given by

$$\rho_{ASE} = n_{sp} h\nu (G - 1) \tag{6.1}$$

where $h\nu$ is the photon energy, n_{sp} is spontaneous emission factor which is a measure of the quality of the inversion of the optical amplifier, and G is the amplifier gain. The noise figure is given by

$$NF = \frac{2\rho_{ASE}}{Gh\nu} + \frac{1}{G} \tag{6.2}$$

Substituting Eq. 6.1 into Eq. 6.2, the noise figure can be expressed as

$$F = 2n_{sp}\frac{G-1}{G} + \frac{1}{G} \tag{6.3}$$

Since $n_{sp} \geq 1$, for large gain, the lower limit of the noise figure of linear amplifiers is 3dB.

The use of PSAs in applications, such as optical phase and amplitude regeneration [Croussore 05, Croussore 08], dispersion compensation [Li 94], and the suppression of modulational instability [Imajuku 97b], has been successfully demonstrated.

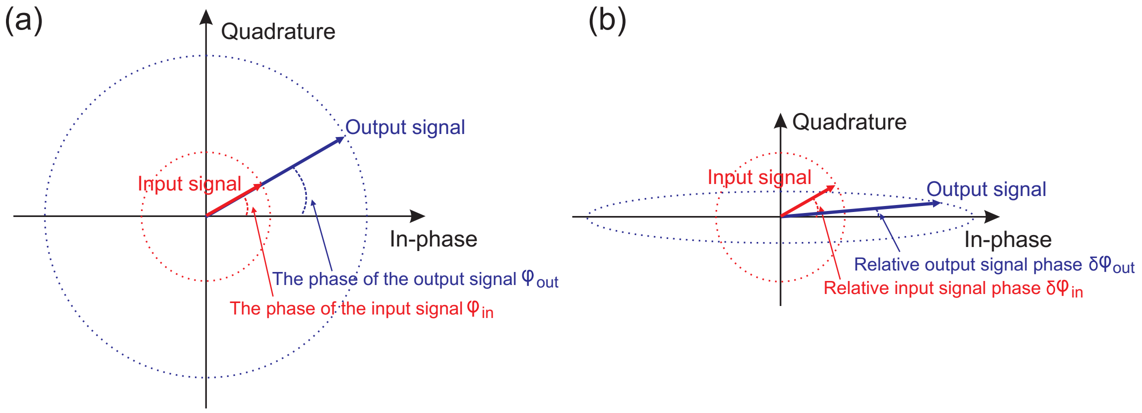

FIGURE 6.2: Illustration of (a) phase-insensitive amplifier and (b) phase sensitive amplifier.

PSAs can be classified into two categories, frequency-degenerate PSA and non-degenerate PSA. Frequency-degenerate PSAs, where the frequencies of the signal and the idler are identical, can only amplify signals within a narrow frequency band for a fixed pump configuration. In contrast, for non-degenerate PSAs the signal and the idler are at different frequencies and simultaneous multichannel amplification is possible [Tong 11]. In order to implement both types of PSAs, pump, signal and idler must be phase-locked to each other at the input of PSAs, using various approaches such as optical phase-locking loop [Imajuku 97a], pump injection-locking [Takada 98], FWM [Tang 05b] and phase modulation [Tang 05a]. Inside the PSA, pump and idler interact with each other and generate a light wave at the signal wavelength. The generated signal adds onto the initial signal either constructively or destructively, resulting in either amplification or deamplification of the signal according to the relative phases between pump, signal and idler.

In this chapter, two novel configurations of phase sensitive amplification based on cascaded quadratic effects in periodically poled lithium niobate waveguides will be demonstrated. The first one is frequency non-degenerate PSA based on the cSHG/DFG process within a single PPLN waveguide, demonstrated in Section 6.2. The theoretical calculation and proof-of-principle experiments of this configuration will be presented. The broad gain bandwidths of this PSA configuration will also be investigated. The second configuration of PSA is PR-WC which is based on a combination of the cSHG/DFG process and the cSFG/DFG process within PPLN waveguides, demonstrated in Section 6.3. Compared to other PSA configurations, signals are both phase-regenerated and converted to a new wavelength in a PR-WC. Theoretical analysis and experiments of this PR-WC configuration will be presented.

6.2 Frequency non-degenerate phase sensitive amplification based on quadratic cascading in a periodically poled lithium niobate waveguide

6.2.1 Introduction

Various schemes to achieve PSA have been reported previously, including degenerate FWM in a $\chi^{(3)}$ medium [Yuen 79, Kumar 84, McKinstrie 04] and degenerate parametric amplification (PA) (or squeezed-state generation) in a $\chi^{(2)}$ medium [Tajima 05, Eto 07, Eto 08]. In the latter scheme where two PPLN waveguides were employed, a FF wave was frequency doubled in the first PPLN waveguide. The generated SH wave and the residual FF wave were used as pump and probe lights respectively for degenerate PA in the second PPLN waveguide. The PA output was then at the same wavelength as the probe beam. Recently, frequency non-degenerate PSAs based on nonlinear fibre optic PAs have been demonstrated offering potential important advantages relative to their frequency degenerate counterparts [Tang 05b, Tang 08, Lundstrom 09]. In particular, frequency non-degenerate PSAs can be operated as multi-channel devices, which are compatible with WDM systems.

Here I report on a new scheme for frequency non-degenerate PSA based on the cSHG/DFG process in a PPLN waveguide. PPLN-based PSA offers a number of attractive features relative to fibre-based PSA implementations including the prospect of compact devices, large operational bandwidths, and importantly a far greater immunity to the effects of SBS of the pump beams which imposes performance limitations and adds complexity to silica fibre-based PSA devices. In the following, I will describe in detail the theoretical model developed for the quadratic cascading interaction, and then experimentally validate the model.

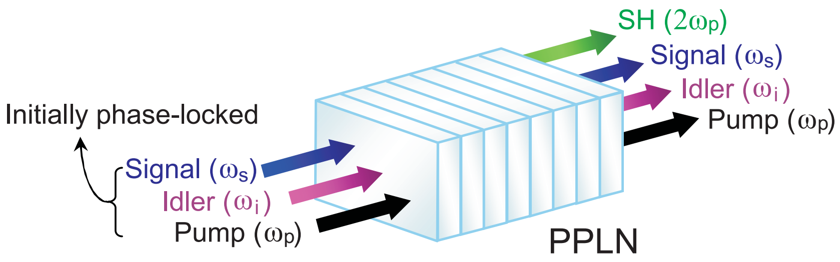

Figure 6.3: Schematic diagram of phase sensitive amplifier based on the cSHG/DFG process in a PPLN waveguide. The relative phases among the input waves need to be initially locked.

6.2.2 Theoretical calculation

Figure 6.3 shows the schematic diagram of the cSHG/DFG interaction in a single PPLN waveguide for frequency non-degenerate PSA. Three waves: a pump, a signal, and an idler, with frequencies of ω_p, ω_s, and ω_i are injected with a fixed phase relation into the waveguide [Tang 05b, Tang 08, Lundstrom 09]. The signal, the pump and the idler have the same frequency spacing between them (i.e. $\omega_s+\omega_i = 2\omega_p$). The frequency arrangement is shown in Figure 6.4. The pump generates a wave at the second harmonic frequency ($2\omega_p$), which interacts with the other two input waves via the DFG process. The phases of the input signal, pump and idler are denoted as ϕ_s, ϕ_p, ϕ_i, respectively. The phase of the generated signal through the cSHG/DFG process is $2\phi_p - \phi_i$. In the case that the difference in the phases of the initial signal and the generated signal is in the range of $[-\pi/2, \pi/2]$, the initial signal adds onto the generated signal constructively. In the particular case that the phase of the initial signal equals the phase of the generated signal (i.e. $2\phi_p - \phi_i = \phi_s + 2m\pi$, where m is an integer), the PSA maximally amplifies the signal. In the case that the difference in the phases of the initial signal and the generated signal is in the range of $[\pi/2, 3\pi/2]$, the initial signal adds onto the generated signal destructively. In the particular case that the difference in the phases of the initial signal and the generated signal is π (i.e. $2\phi_p - \phi_i = \phi_s + (2m+1)\pi$, where m is an integer), the PSA maximally attenuates the signal.

In the following, a frequency non-degenerate PSA based on the cSHG/DFG process in a PPLN waveguide will be investigated analytically. Under the slowly varying envelope approximation, the coupled-mode equations describing the cSFG/DFG process can be

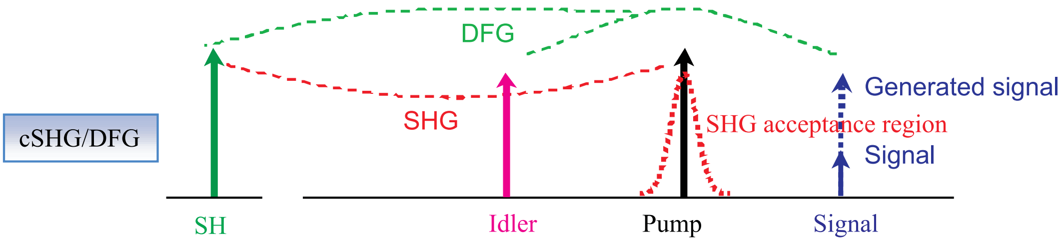

FIGURE 6.4: Frequency arrangement of cSHG/DFG based phase sensitive amplifier in a PPLN waveguide.

derived as follows [Gallo 99, Liberale 02]:

$$\frac{dE_p(z)}{dz} = -\frac{\alpha_p}{2}E_p(z) + i\kappa_{pp}\omega_p E_{SH}(z)E_p^*(z)e^{i\Delta k_{pp}z} \tag{6.4}$$

$$\frac{dE_{SH}(z)}{dz} = -\frac{\alpha_{SH}}{2}E_{SH}(z) + i\kappa_{pp}\omega_p E_p^2(z)e^{-i\Delta k_{pp}z} + 2i\kappa_{si}\omega_p E_s(z)E_i(z)e^{i\Delta k_{si}z} \tag{6.5}$$

$$\frac{dE_s(z)}{dz} = -\frac{\alpha_s}{2}E_s(z) + i\kappa_{si}\omega_s E_{SH}(z)E_i^*(z)e^{-i\Delta k_{si}z} \tag{6.6}$$

$$\frac{dE_i(z)}{dz} = -\frac{\alpha_i}{2}E_i(z) + i\kappa_{si}\omega_i E_{SH}(z)E_s^*(z)e^{-i\Delta k_{si}z} \tag{6.7}$$

where E_p, E_{SH}, E_s, and E_i denote the normalized complex electric fields of the pump, SH, signal, and idler waves propagating along the axis (z) of the waveguide, respectively. Each α represents the linear propagation loss coefficients for the corresponding wave. The coupling coefficients for the SHG (κ_{pp}) and the DFG process (κ_{si}) are expressed as,

$$\kappa_{pp} = d_{eff}\sqrt{\frac{2\mu_0}{cn_p^2 n_{SH}A_{eff}}} \tag{6.8}$$

$$\kappa_{si} = d_{eff}\sqrt{\frac{2\mu_0}{cn_s n_i n_{SH}A_{eff}}} \tag{6.9}$$

where, d_{eff}, μ_0, c, A_{eff}, and n_j represent the effective nonlinear coefficient, the permeability of free space, the speed of light, the effective mode area in the PPLN waveguide (assumed to be the same for both the SHG and DFG cases), and the refractive indices of each wave, respectively. In Type-0 (e : e + e) QPM geometry which is considered here, the d_{33} coefficient couples z polarized fundamental frequency waves to z polarized second harmonic wave, and the refractive indices these waves see are all the extraordinary refractive indices. Thus d_{eff} is given by $(2/\pi)d_{33}$ ($d_{33} = 27$ pm/V for the SHG at 1064 nm) [Shoji 97]. The phase mismatches for the SHG (Δk_{pp}) and the DFG processes (Δk_{si}) are expressed as,

$$\Delta k_{pp} = k_{SH} - 2k_p - \frac{2\pi}{\Lambda} \tag{6.10}$$

$$\Delta k_{si} = k_s + k_i - k_{SH} + \frac{2\pi}{\Lambda} \tag{6.11}$$

where, Λ is the period of the QPM grating and each k is the wave vector at the corresponding frequency. The coupled wave equations [Eqs. 6.4, 6.5, 6.6, 6.7] can be conveniently rewritten in terms of amplitudes and phases of the waves by introducing the following complex notation as in [Armstrong 62],

$$E_j(z) = A_j(z)e^{i\phi_j(z)} \tag{6.12}$$

where, A_j and ϕ_j denote the modulus and phase of the complex field amplitude for a generic interacting wave j, respectively. If we substitute Eq. 6.12 into Eqs. 6.4, 6.5, 6.6, 6.7, the coupled wave equations can be expressed as the following set of six equations:

$$\frac{dA_p(z)}{dz} = -\frac{\alpha_p}{2}A_p(z) - \kappa_{pp}\omega_p A_{SH}(z)A_p(z)sin\theta(z) \tag{6.13}$$

$$\frac{dA_{SH}(z)}{dz} = -\frac{\alpha_{SH}}{2}A_{SH}(z) + \kappa_{pp}\omega_p A_p^2(z)sin\theta(z) - 2\kappa_{si}\omega_p A_s(z)A_i(z)sin\psi(z) \tag{6.14}$$

$$\frac{dA_s(z)}{dz} = -\frac{\alpha_s}{2}A_s(z) + \kappa_{si}\omega_s A_{SH}(z)A_i(z)sin\psi(z) \tag{6.15}$$

$$\frac{dA_i(z)}{dz} = -\frac{\alpha_i}{2}A_i(z) + \kappa_{si}\omega_i A_{SH}(z)A_s(z)sin\psi(z) \tag{6.16}$$

$$\frac{d\theta(z)}{dz} = (\kappa_{pp}\omega_p\frac{A_p^2(z)}{A_{SH}(z)} - 2\kappa_{pp}\omega_p A_{SH}(z))cos\theta(z) + 2\kappa_{si}\omega_p\frac{A_s(z)A_i(z)}{A_{SH}(z)}cos\psi(z) + \Delta k_{pp} \tag{6.17}$$

$$\begin{aligned}\frac{d\psi(z)}{dz} =&(\kappa_{si}\omega_s\frac{A_{SH}(z)A_i(z)}{A_s(z)} + \kappa_{si}\omega_i\frac{A_{SH}(z)A_s(z)}{A_i(z)} - 2\kappa_{si}\omega_p\frac{A_s(z)A_i(z)}{A_{SH}(z)})cos\psi(z)\\ &- \kappa_{pp}\omega_p\frac{A_p^2(z)}{A_{SH}(z)}cos\theta(z) + \Delta k_{si}\end{aligned} \tag{6.18}$$

where, two kinds of relative phase relationships between the interacting waves can also be defined as follows:

$$\theta(z) = \phi_{SH}(z) - 2\phi_p(z) + \Delta k_{pp} z \tag{6.19}$$

$$\psi(z) = \phi_s(z) + \phi_i(z) - \phi_{SH}(z) + \Delta k_{si} z \tag{6.20}$$

Here, θ and ψ denote the relative phase variation between the interacting waves in the beam propagation direction (z) for the SHG and DFG processes, respectively. In the case that the signal, the pump and the idler waves are phase-locked at the input of the PPLN, the evolutions of these waves depend on the input relative phase, and can be described by the set of Equations 6.13 to 6.20.

The coupled-mode equations (Eqs. 6.13 - 6.18) were numerically solved by considering the same parameters for the PPLN waveguide as used in the experiments described in Section 6.2.3. I acknowledge the following simulations were mainly done by my colleague Kwang Jo Lee. The PPLN waveguide was designed for SHG at the pump wavelength (λ_p) of 1546.0 nm, while the signal (λ_s) and idler (λ_i) wavelengths were set at 1541.4 nm and 1550.6 nm, respectively. The effective mode area and the linear loss coefficients for the PPLN waveguide were $A_{eff} = 52\mu\text{m}^2$, $\alpha_p = \alpha_s = \alpha_i = 0.35$ dB/cm, and $\alpha_{SH} = 2\alpha_p$, respectively. The PSA signal gain (G) is defined as the ratio of the signal powers at the input ($z = 0$) and the output ($z = L$) of the waveguide as follows:

$$G \equiv \frac{[A_s(L)]^2}{[A_s(0)]^2} \tag{6.21}$$

The input powers of each interacting wave at the waveguide facet were assumed to be 33 dBm for the pump wave (P_p) and -4 dBm for the signal and idler wave (P_s, P_i), respectively. The calculated signal gain [Eq. 6.21] is plotted in Fig. 6.5(a) as a function of the phase of the pump wave (ϕ_p). The results show that the maximum signal gain is 19.0 dB and 30.1 dB for crystal lengths (L) of 30 mm and 50 mm, respectively. These correspond to peak-to-peak gain differences of 41.3 dB and 48.4 dB, respectively. As indicated in Fig. 6.5(a), the gain of the signal depends on the relative phase, which implies the possibility to realize a PSA which can amplify or deamplify the input signal according to its phase. Figure 6.5(b) shows the maximum and minimum PSA gain (maximum deamplification) and the PIA gain without the input idler power as a function of the input pump power for the 30-mm-long device. As can be appreciated from the graph, the PSA gain increases quadratically with the pump power. The difference between PSA and PIA gain reaches the theoretical limit of ∼ 6 dB at an input pump power of 33 dBm, as indicated in the figure [Choi 99].

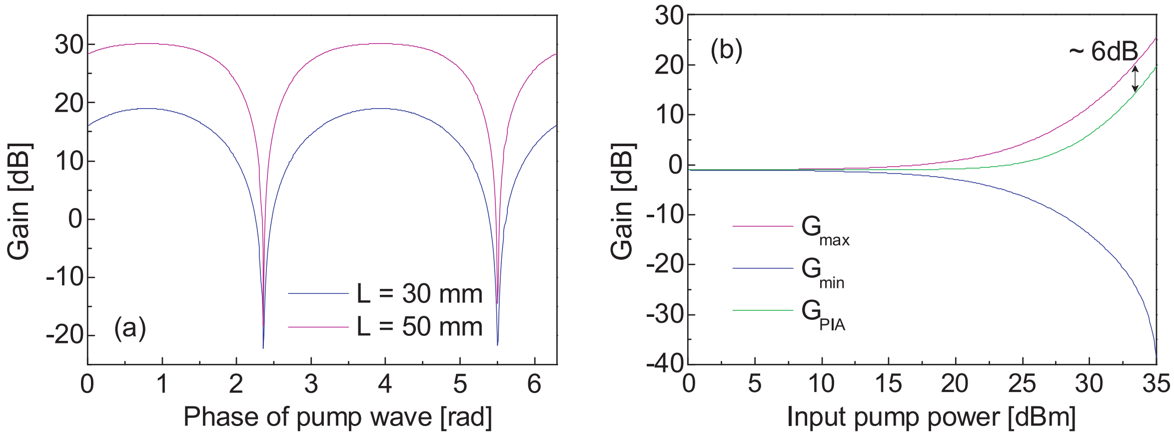

FIGURE 6.5: (a): Calculated signal gain plotted as a function of the initial relative pump phase for a crystal length of 30 mm and 50 mm at an input pump power of 33 dBm. (b): Variation of maximum, minimum PSA gain and PIA gain as a function of the input pump power for a crystal length of 30 mm.

The maximum PSA signal gain is also plotted in Fig. 6.6(a) as a function of the crystal length for an input pump power of 33 dBm. The result clearly shows that the gain increases with the crystal length due to the longer interaction length. In particular, the maximum gain is proportional to the fourth-power of the crystal length until the PSA gain starts to saturate. As presented in Ref. [Umeki 11], following our work Umeki *et al.* have demonstrated a PSA based on 5-cm-long PPLN waveguides and with an input pump power of 31.5 dBm, achieving an in-phase gain of +11 dBm and a phase sensitive peak-to-peak gain difference of 21 dB in their experiments.

Fig. 6.6(b) shows the calculated maximum PSA gain plotted as a function of the signal wavelength ($\lambda_s - \lambda_p$) at an input pump power of 33 dBm. The calculated 3-dB bandwidths are 88 nm and 77 nm for crystal lengths of 30 mm and 50 mm, respectively. This indicates that the proposed PSA scheme is applicable to broadband operation and the amplification of multiple WDM data signals.

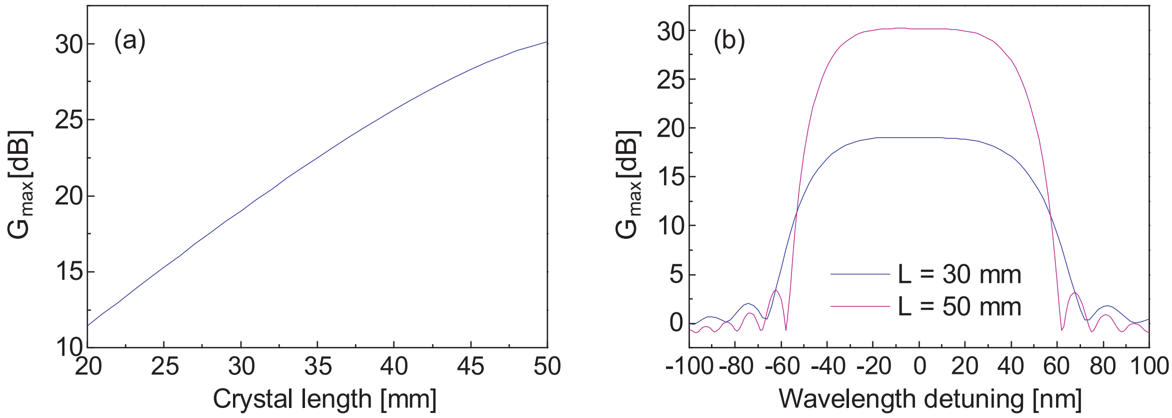

FIGURE 6.6: (a): Maximum signal gain as a function of crystal length for an input pump power of 33 dBm. (b): Calculated maximum PSA gain plotted as a function of the signal wavelength at an input pump power of 33 dBm.

6.2.3 Experiments

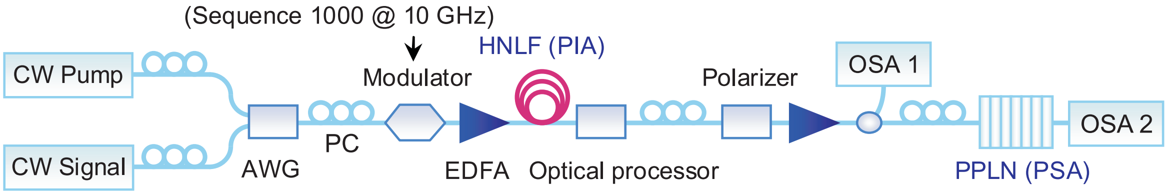

FIGURE 6.7: Schematic for the proposed frequency non-degenerate PSA based on the cSHG/DFG process in the PPLN waveguide.

Since the signal and pumps at the input of a PSA are required to be phase-locked to each other, either of two methods is conventionally used to produce the PSA pumps: modulation (phase or amplitude) of a continuous-wave (CW) light to create phase-coherent sidebands [Tang 05a], or FWM to generate a phase-locked idler [Tang 05b]. The former option is simple to implement but is limited by electronics and can only produce optical waves separated by at most a few hundred gigahertz. In this experiment, I used the second approach to generate phase-locked optical waves. Figure 6.7 shows the experimental setup that I used to validate the proposed PSA approach and associated model. It comprised of two stages: Firstly, a $\chi^{(3)}$-based fibre PIA was used to generate a phase-locked but conjugated idler. The resulting phase-locked pump, signal and idler waves were then passed through a programmable optical filter that allowed a controlled adjustment of the relative phase between them, before being injected into a cascaded $\chi^{(2)}$-based parametric amplifier (PPLN waveguide) used to obtain PSA operation. Two wavelength tunable CW lasers were used as the pump and the signal sources operating at 1546.0 nm and 1541.4 nm, respectively. The two beams were combined together into a single fibre at the input to the system using an arrayed waveguide grating. The pump-to-signal power ratio was set to $\sim$ 20 dB and the combined beams were launched into an amplitude modulator to generate 100-ps pulses at a repetition rate of 2.5 GHz, thereby allowing for a four-fold increase in the peak power of the signals after onward amplification in an EDFA. After amplification the signal and pump beams were coupled into the fibre PIA, formed by a 500-m long HNLF with a nonlinear coefficient of $\gamma = 20$ $(\mathrm{W{\cdot}km})^{-1}$, a dispersion of 0.06 ps/nm/km, and a dispersion slope of 0.0035 ps/nm^2/km. The resulting three waves (pump, signal, and idler) were subsequently passed through an optical processor (Finisar Waveshaper 4000E) allowing for individual filtering, attenuation, and phase-shifting relative to each other. A polarizer, EDFA, and appropriate polarization control elements were used to amplify and align all three waves to the optical axis of the PPLN waveguide for the cSHG/DFG process. The total power at the waveguide input was 14 dBm with the pump signal completely dominating the power (coupling loss of $\sim$ 1.4 dB).

Figure 6.8(a) shows the measured output spectra for amplification and deamplification of the signal and idler wave. The maximum gain achievable for this pump power level was 0.65 dB and the peak-to-peak signal gain variation was measured to be 3.4 dB, which agrees well with the theoretical gain curve plotted in Fig. 6.8(b) as a function of the relative phase of the signals. The gain profiles clearly indicate the phase-sensitive behaviour showing both the maximum amplification and deamplification with a period of π-phase. Note that the input and output coupling losses are not taken into account in measuring the gain. In the same figure I also report the corresponding PIA gain in the PPLN, i.e. in the absence of the input idler signal. To achieve this, the HNLF in the first stage was removed, while ensuring that the same absolute and relative power levels as in the PSA case were maintained at the input of the PPLN. As shown in Fig. 6.8(b), the difference between the PSA and PIA gain is about 1.7 dB. The negative PIA gain of ∼ 1 dB is due to the beam propagation loss (α) within the waveguide, which agrees well with the theoretical estimation at this input power level.

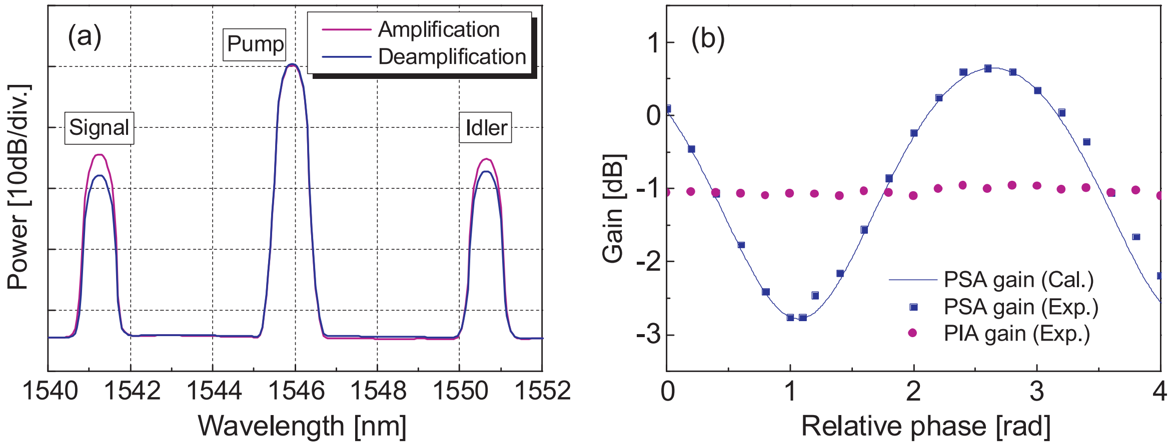

FIGURE 6.8: (a): Measured output spectra of three interacting waves showing amplification and deamplification. (b): Measured and calculated phase-sensitive gain plotted as a function of initial pump phase for PIA and PSA operation.

For these first proof-of-principle experiments, we kept the excitation levels of the PPLN waveguide well within the restrictions imposed by the pigtailing of this specific device (maximum input power of 14 dBm). Improvements in current pigtailing technology mean that currently available devices are now able to handle peak pulse powers of up to 33 dBm. In light of the excellent agreement between our first experiments and the theoretical predictions [Fig. 6.8(b)], we can reasonably expect to reach a differential PSA-PIA gain of ∼ 6 dB with a pump power of 33 dBm, as expected from Fig. 6.5(b), from state-of-the-art PPLN devices.

Finally I investigated broadband PSA operation. To do this, I tuned the CW signal source to the following wavelengths: 1529.82 nm, 1534.47 nm, 1536.07 nm, and 1538.3 nm, respectively. Fig. 6.9 shows the calculated and measured maximum and minimum PSA signal gain for each signal wavelength. As can be seen, the measured phase-sensitive gains were almost constant (with a variation of less than 0.5 dB across the whole 16 nm wavelength range, which was limited by the tuning range of our input signal source). Since symmetric operation around the pump wavelength is expected, broadband operation of the process exceeding the 32 nm effective measurement bandwidth can be inferred. The theoretical device bandwidth predicted in Fig. 6.6(b) is 88 nm - significantly broader than can routinely be obtained for a fibre based single-pump, non-degenerate PSA.

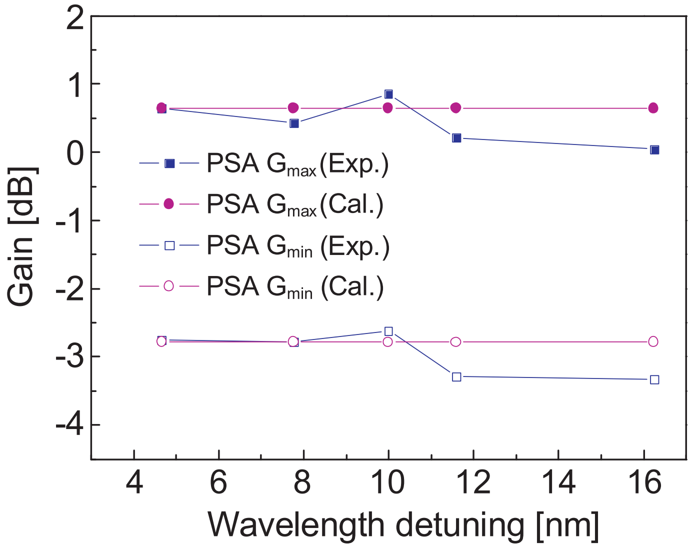

FIGURE 6.9: Variation of the maximum and minimum points of the phase-sensitive signal gain for several signal wavelengths.

6.2.4 Conclusion

I have theoretically investigated and experimentally demonstrated a frequency non-degenerate PSA based on cSHG/DFG occurring in a single PPLN waveguide. The PSA performance was demonstrated and characterised by exploiting a combination of a $\chi^{(3)}$-based PIA to create the initial phase-locking among the waves followed by a $\chi^{(2)}$-based PSA based on the cSHG/DFG process. I verified the very good agreement between the theoretical predictions and the performance of the cSHG/DFG PSA, achieving a maximum gain of 0.65 dB with a peak-to-peak gain variation of 3.4 dB for a $\sim$ 100-ps duration, 2.5 GHz pulsed signal in a 3-cm PPLN waveguide with an input pump of 14 dBm. These first proof-of-principle experiments show also the potential of the process as a broadband PSA mechanism. Further significant improvements of the PSA gain can be envisaged with improvements in the coupling to the PPLN waveguides, enabling higher pump powers. The calculations show that PSA gains in excess of 30 dB can be achieved in practical device lengths (50 mm) for launched power levels of 33 dBm. Finally, it is worth emphasising that the compact size and the fact that no SBS suppression techniques are required as major advantages of the PPLN approach relative to silica fibre based PSA implementations.

6.3 Phase regenerative wavelength conversion based on cascaded quadratic processes in periodically poled lithium niobate waveguides

6.3.1 Introduction

Several PSA configurations have been demonstrated based on a number of technologies, such as FWM in HNLFs [McKinstrie 04, Croussore 07, Croussore 09, Slavik 10], Kerr effects in nonlinear interferometers [Shirasaki 90, Marhic 91], as well as the technique based on cascaded second-order nonlinearities in PPLN waveguides which I described earlier [Lee 09]. A new kind of PSA based on FWM in a HNLF has recently been experimentally demonstrated which provides PR-WC [Croussore 07, Croussore 09]. In that configuration, two idlers at two new wavelengths are generated in a phase-sensitive fashion during a single stage of FWM interaction. Thereby, in principle perfect phase regeneration of differential (bipolar) phase-shift keying (D(B)PSK) signals is achieved without requiring a large FWM conversion efficiency, whereas compared to other PSA implementations an additional important network function is performed at the same time, i.e. wavelength conversion. Hence PR-WC is of considerable interest for next generation meshed transparent networking systems.

I will report two different implementations of a novel scheme for PR-WC based on combinations of cSHG/DFG and cSFG/DFG in PPLN waveguides in this section. The basic operational principle of this scheme can be intuitively represented in the complex plane of the E-field, as shown in Fig. 6.10. The scheme operates by generating two copies of the incoming signal. One copy (generated through cSFG/DFG) is a phase-preserving replica of the input, whereas the other (generated through cSHG/DFG) is its phase conjugate. These two outputs are equalized in power and combined. In the complex plane of the E-field, the combined output is aligned to the in-phase axis. Therefore, a noisy input D(B)PSK signal is phase-regenerated to an output signal which in principle has an exact phase value of either 0 or π. PR-WC exploiting cascaded second-order nonlinearities in PPLN waveguides offers a number of advantages over the corresponding FWM-based approach. PPLN waveguides are compact and effectively immune to stimulated Brillouin scattering of the pump beams. Furthermore, in contrast to fiber-based implementations, the operation of PR-WC exploiting cascaded second-order nonlinearities in PPLN waveguides is less susceptible to the generation of pump-pump and pump-signal harmonics [McKinstrie 06, McKinstrie 07], or even to self-phase and cross-phase modulation [Croussore 07].

In the following, I am going to present experimental demonstrations of this scheme, which employ either two discrete PPLN waveguides for the implementation of the cSFG/DFG and cSHG/DFG processes or just one, where the nonlinear processes develop simultaneously. The section is organized as follows. An analytical presentation of the two schemes is given in Section 6.3.2; I have chosen to describe the two-stage PR-WC implementation first (Section 6.3.2.1), because its analytical treatment is simpler. The presentation of the single-stage PR-WC implementation follows in Section 6.3.2.2. The experimental demonstrations are presented in Section 6.3.3. This time, I change the order in which the two implementations are presented. Due to the relatively simpler experimental setup, the experiment of the single-stage PR-WC implementation is shown first (Section 6.3.3.1) followed by the two-stage PR-WC implementation (Section 6.3.3.2), which includes the demonstration of the phase regeneration results.

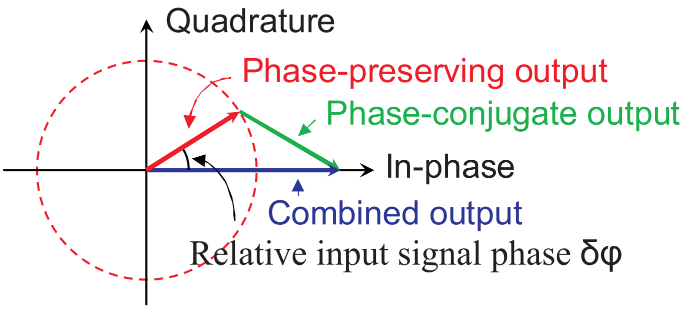

Figure 6.10: Operational principle of phase-regenerative wavelength conversion.

6.3.2 Theory

6.3.2.1 Two-stage implementation

Figure 6.11 illustrates the wavelength arrangement for the two-stage PR-WC implementation based on a combination of cascaded second-order nonlinearities in two separate PPLN waveguides (i.e. cSFG/DFG in the first PPLN and cSHG/DFG in the second PPLN).

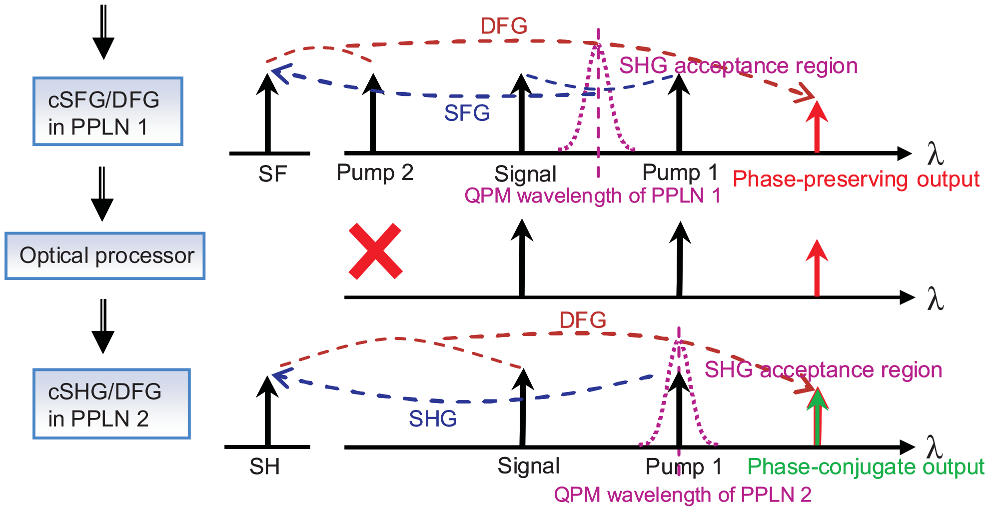

FIGURE 6.11: Illustration of two-stage phase-regenerative wavelength conversion based on cSFG/DFG and cSHG/DFG in two separate PPLN waveguides.

The QPM wavelengths of the first (PPLN 1) and the second PPLN waveguides (PPLN 2) are detuned relative to each other, and arranged so that Pump 1 and the input signal are placed symmetrically around the QPM wavelength of PPLN 1. Also the wavelength of Pump 1 coincides with the QPM wavelength of PPLN 2. Pump 2 is set at a frequency such that Pump 2, Signal, and Pump 1 have the same frequency spacing between them. The input Signal, Pump 1, and Pump 2 are phase-locked relative to each other and launched into PPLN 1. As shown in Fig. 6.11, the input Signal and Pump 1 generate the SF wave by SFG in PPLN1, followed by the DFG process between the SF wave and Pump 2, which generates the phase-preserving output at a new wavelength. The evolution of the interacting waves associated with the cSFG/DFG process in PPLN 1 can be described through the following set of coupled mode equations [Suhara 03]:

$$\begin{aligned}
\frac{dA_{p1}}{dz} &= i\omega_{p1}\kappa_{SFG}A_{sf}A_s^*exp(i\Delta k_{SFG}z)\\
\frac{dA_s}{dz} &= i\omega_s\kappa_{SFG}A_{sf}A_{p1}^*exp(i\Delta k_{SFG}z)\\
\frac{dA_{sf}}{dz} &= i\omega_{sf}\kappa_{SFG}A_sA_{p1}exp(-i\Delta k_{SFG}z) + i\omega_{sf}\kappa_{DFG}A_{p2}A_{out}exp(-i\Delta k_{DFG}z)\\
\frac{dA_{p2}}{dz} &= i\omega_{p2}\kappa_{DFG}A_{sf}A_{out}^*exp(i\Delta k_{DFG}z)\\
\frac{dA_{out}}{dz} &= i\omega_{out}\kappa_{DFG}A_{sf}A_{p2}^*exp(i\Delta k_{DFG}z)
\end{aligned} \tag{6.22}$$

where A_j ($j = p1$, $p2$, sf, s, out) are the complex amplitudes of Pump 1, Pump 2, the SF, the signal and the output respectively, ω_j are the angular frequencies, κ_{SFG} and κ_{DFG} are the nonlinear coupling coefficients of the SFG process and the DFG process respectively, and Δk_{SFG} and Δk_{DFG} are the phase mismatches of the SFG process and the DFG process respectively. $\Delta k_{SFG} = 0$ since Pump 1 and the input signal are placed symmetrically around the QPM wavelength. Δk_{DFG} is also close to zero because of the low dispersion of lithium niobate crystal in the wavelength region around 1550 nm. Note that for simplicity the waveguide loss has not been taken into account in Eq. 6.22. By integrating the coupled-mode equations for cSFG/DFG under the non-depletion approximation, the complex amplitude of the cSFG/DFG output can be approximated as:

$$\begin{aligned}
A_{cSFG/DFG} &\approx \frac{1}{2}\omega_{out}\omega_{sf}\kappa_{SFG}\kappa_{DFG}A_{p1}A_sA_{p2}^*L^2\\
&= \frac{1}{2}\omega_{out}\omega_{sf}\kappa_{SFG}\kappa_{DFG}|A_{p1}||A_s||A_{p2}|L^2e^{i(\varphi_{p1}-\varphi_{p2}+\varphi_s)}\\
&= \frac{1}{2}\omega_{out}\omega_{sf}\kappa_{SFG}\kappa_{DFG}|A_{p1}||A_s||A_{p2}|L^2e^{i(\frac{3}{2}\varphi_{p1}-\frac{1}{2}\varphi_{p2}+\delta\varphi)}
\end{aligned} \tag{6.23}$$

where L is the length of PPLN 1. φ_{p1}, φ_{p2}, and φ_s also denote the phases of Pump 1, Pump 2, and Signal respectively. The relative input signal phase, $\delta\varphi$, is defined as $(\delta\varphi_1 + \delta\varphi_2)/2$, where $\delta\varphi_1 = \varphi_s - \varphi_{p1}$ is the relative phase between Signal and Pump 1, and $\delta\varphi_2 = \varphi_s - \varphi_{p2}$ is the relative phase between Signal and Pump 2.

Pump 2 is suppressed after PPLN 1, and the rest of the optical waves are subsequently launched into PPLN 2. In the cSHG/DFG process occurring within PPLN 2, the SH wave of Pump 1 is generated by the SHG process, and this is accompanied by the DFG process between the SH wave and the input signal which produces its phase-conjugate output. The evolution of the interacting waves associated with the cSHG/DFG process in PPLN2 can be described through the following set of coupled mode equations [Gallo 97]:

$$\begin{aligned}\frac{dA_{p1}}{dz} &= i\omega_{p1}\kappa_{SHG}A_{sh}A_{p1}^{*}exp(i\Delta k_{SHG}z)\\ \frac{dA_{sh}}{dz} &= \frac{i}{2}\omega_{sh}\kappa_{SHG}A_{p1}^{2}exp(-i\Delta k_{SHG}z)+i\omega_{sh}\kappa_{DFG}A_{s}A_{out}exp(-i\Delta k_{DFG}z)\\ \frac{dA_{s}}{dz} &= i\omega_{s}\kappa_{DFG}A_{sh}A_{out}^{*}exp(i\Delta k_{DFG}z)\\ \frac{dA_{out}}{dz} &= i\omega_{out}\kappa_{DFG}A_{sh}A_{s}^{*}exp(i\Delta k_{DFG}z)\end{aligned} \tag{6.24}$$

where A_j (the subscript $j = p1$, sh, s, out) are the complex amplitudes of Pump 1, the SH, the signal and the output respectively, κ_{SHG} is the nonlinear coupling coefficient of the SHG process, and Δk_{SHG} is the phase mismatch of the SHG process. Note that $\Delta k_{SHG} = 0$ as Pump 1 is set at the SHG QPM wavelength, whereas as before, $\Delta k_{DFG} \approx 0$. Under the non-depletion approximation and by integrating the coupled-mode equations for cSHG/DFG, the complex amplitude of the cSHG/DFG output can be approximated as:

$$\begin{aligned}A_{cSHG/DFG} &\approx \frac{1}{4}\omega_{out}\omega_{sh}\kappa_{SHG}\kappa_{DFG}A_{p1}^{2}A_{s}^{*}L^{2}\\ &= \frac{1}{4}\omega_{out}\omega_{sh}\kappa_{SHG}\kappa_{DFG}|A_{p1}|^{2}|A_{s}|L^{2}e^{i(2\varphi_{p1}-\varphi_{s})}\\ &= \frac{1}{4}\omega_{out}\omega_{sh}\kappa_{SHG}\kappa_{DFG}|A_{p1}|^{2}|A_{s}|L^{2}e^{i(\frac{3}{2}\varphi_{p1}-\frac{1}{2}\varphi_{p2}-\delta\varphi)}\end{aligned} \tag{6.25}$$

where L is the length of PPLN 2. Since Pump 2, Signal, and Pump 1 have the same frequency spacing between them, the outputs from cSHG/DFG and cSFG/DFG are generated at the same wavelength. Thus these two outputs are combined. If for simplicity, we assume that the two waveguides have the same length, and the intensities of the two outputs are equalised by adjusting the power of Pump 2, then the complex amplitude of the combined output can be approximated as:

$$\begin{aligned}A &\approx \frac{1}{2}\omega_{out}\omega_{sf}\kappa_{SFG}\kappa_{DFG}|A_{p1}||A_{s}||A_{p2}|L^{2}e^{i(\frac{3}{2}\varphi_{p1}-\frac{1}{2}\varphi_{p2}+\delta\varphi)}\\ &+\frac{1}{4}\omega_{out}\omega_{sh}\kappa_{SHG}\kappa_{DFG}|A_{p1}|^{2}|A_{s}|L^{2}e^{i(\frac{3}{2}\varphi_{p1}-\frac{1}{2}\varphi_{p2}-\delta\varphi)}\\ &= \omega_{out}\omega_{sf}\kappa_{SFG}\kappa_{DFG}|A_{p1}||A_{s}||A_{p2}|L^{2}e^{i(\frac{3}{2}\varphi_{p1}-\frac{1}{2}\varphi_{p2})}cos(\delta\varphi)\end{aligned} \tag{6.26}$$

In the ideal case that the phase-conjugate output from cSHG/DFG and the phase-preserving output from cSFG/DFG are perfectly conjugated and have strictly equal power, the combination of these two output results in perfect cancellation of the quadrature component of the output and amplification of the in-phase component, as shown in Eq. 6.26.

6.3.2.2 Single-stage implementation

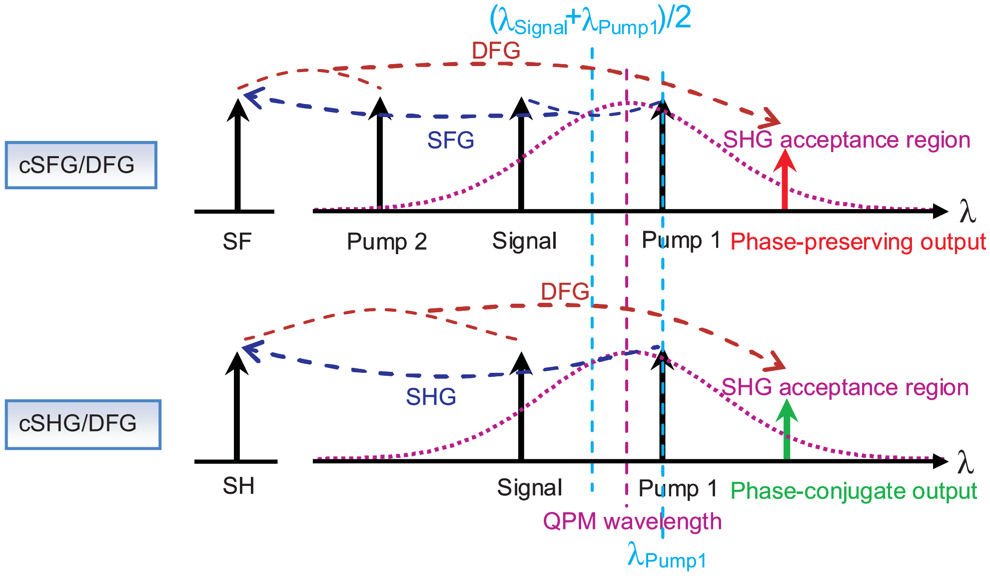

FIGURE 6.12: Illustration of single-stage phase-regenerative wavelength conversion based on cSFG/DFG and cSHG/DFG in a single PPLN waveguide.

The two separate nonlinear stages described above can also be combined within a single PPLN waveguide, thereby benefitting from an implementation that requires fewer components. Figure 6.12 illustrates the wavelength arrangement for the proposed single-stage PR-WC implementation based on the simultaneous combination of the cSHG/DFG and cSFG/DFG processes in a single PPLN waveguide. The input Signal, Pump 1, and Pump 2 are phase-locked relative to each other and launched into the PPLN waveguide. In order to allow the two cascaded processes to occur simultaneously in the same device they need to be detuned from the exact phase-matching conditions. As shown in Fig. 6.12, it is necessary to ensure that Pump 1 still falls within the SHG acceptance bandwidth and that the mean wavelength of the input Signal and Pump 1 also falls within it. In addition, Pump 2 needs to be set at a frequency which equalises the frequency difference between Pump 2 and the Signal, and the Signal and Pump 1.

The input Signal and Pump 1 generate the SF wave by the SFG process. When followed by DFG between the SF wave and Pump 2 a phase-preserving output at a new wavelength [see Fig. 6.12(a)] is generated. At the same time, the SH wave of Pump 1 is generated in the PPLN waveguide as shown in Fig. 6.12(b), and this is accompanied by DFG between this SH wave and the input signal to produce its phase-conjugate output at a new wavelength. Since Pump 2, Signal and Pump 1 are arranged to have the same frequency spacing between them, the outputs from cSHG/DFG and cSFG/DFG are therefore generated at the same wavelength. For simplicity, we assume that the phase mismatches of the SHG and the SFG process are equal but with opposite sign and nonzero ($\Delta k_{SHG} = -\Delta k_{SFG} \neq 0$) due to the detuning of both cSHG/DFG and cSFG/DFG from the exact phase-matching conditions (which is in contrast to the aforementioned two-stage implementation). By integrating the coupled-mode equations for cSFG/DFG under the non-depletion approximation, the complex amplitude of the cSFG/DFG output can be approximated as:

$$\begin{aligned}
A_{cSFG/DFG} &\approx \frac{\omega_{out}\omega_{sf}\kappa_{SFG}\kappa_{DFG}A_{p1}A_sA_{p2}^*}{\Delta k_{SFG}}\int_0^L (e^{-i\Delta k_{SFG}z}-1)e^{i\Delta k_{DFG}z}dz \\
&\approx \frac{\omega_{out}\omega_{sf}\kappa_{SFG}\kappa_{DFG}A_{p1}A_sA_{p2}^*}{(\Delta k_{SFG})^2}(i\Delta k_{SFG}L - e^{i\Delta k_{SFG}L}+1) \\
&= \frac{\omega_{out}\omega_{sf}\kappa_{SFG}\kappa_{DFG}|A_{p1}||A_s||A_{p2}|e^{i(\frac{3}{2}\varphi_{p1}-\frac{1}{2}\varphi_{p2})}}{(\Delta k_{SFG})^2}e^{i\delta\varphi}(i\Delta k_{SFG}L - e^{i\Delta k_{SFG}L}+1) \\
&\approx \omega_{out}\omega_{sf}\kappa_{SFG}\kappa_{DFG}|A_{p1}||A_s||A_{p2}|e^{i(\frac{3}{2}\varphi_{p1}-\frac{1}{2}\varphi_{p2})}L^2 sinc(\Delta k_{SFG}L/2)e^{i\delta\varphi+i\Delta k_{SFG}L/4}
\end{aligned} \tag{6.27}$$

where $\Delta k_{DFG} \approx \Delta k_{SFG}$ because of the low dispersion feature of lithium niobate crystal in the wavelength region around 1550 nm, and $sinc(x) = sin(x)/x$. By integrating the coupled-mode equations for cSHG/DFG under the non-depletion approximation, the complex amplitude of the cSHG/DFG output can be approximated as:

$$\begin{aligned} A_{cSHG/DFG} &\approx \frac{1}{2}\frac{\omega_{out}\omega_{sh}\kappa_{SHG}\kappa_{DFG}A_{p1}^{2}A_{s}^{*}}{\Delta k_{SHG}}\int_{0}^{L}(e^{-i\Delta k_{SHG}z}-1)e^{i\Delta k_{DFG}z}dz \\ &\approx \frac{1}{2}\frac{\omega_{out}\omega_{sh}\kappa_{SHG}\kappa_{DFG}A_{p1}^{2}A_{s}^{*}}{(\Delta k_{SHG})^{2}}(i\Delta k_{SHG}L-e^{i\Delta k_{SHG}L}+1) \\ &= \frac{1}{2}\frac{\omega_{out}\omega_{sh}\kappa_{SHG}\kappa_{DFG}|A_{p1}|^{2}|A_{s}|e^{i(\frac{3}{2}\varphi_{p1}-\frac{1}{2}\varphi_{p2})}}{(\Delta k_{SHG})^{2}}e^{i\delta\varphi}(i\Delta k_{SHG}L-e^{i\Delta k_{SHG}L}+1) \\ &\approx \frac{1}{2}\omega_{out}\omega_{sh}\kappa_{SHG}\kappa_{DFG}|A_{p1}|^{2}|A_{s}|e^{i(\frac{3}{2}\varphi_{p1}-\frac{1}{2}\varphi_{p2})}L^{2}sinc(\Delta k_{SHG}L/2)e^{i\delta\varphi+i\Delta k_{SHG}L/4} \end{aligned} \tag{6.28}$$

where $\Delta k_{DFG} \approx \Delta k_{SHG}$ because of the low dispersion feature of lithium niobate crystals at wavelengths around 1550 nm. We also assume that the intensities of the two outputs are equalized by adjusting the power of Pump 2, then the complex amplitude of the combined output can be approximated as:

$$\begin{aligned} A &\approx \frac{1}{2}\omega_{out}\omega_{sf}\kappa_{SFG}\kappa_{DFG}|A_{p1}||A_{s}||A_{p2}|L^{2}sinc(\Delta k_{SFG}L/2)e^{i(\frac{3}{2}\varphi_{p1}-\frac{1}{2}\varphi_{p2})}e^{i\delta\varphi+i\Delta k_{SFG}L/4} \\ &+\frac{1}{4}\omega_{out}\omega_{sh}\kappa_{SHG}\kappa_{DFG}|A_{p1}|^{2}|A_{s}|L^{2}sinc(\Delta k_{SHG}L/2)e^{i(\frac{3}{2}\varphi_{p1}-\frac{1}{2}\varphi_{p2})}e^{-i\delta\varphi+i\Delta k_{SHG}L/4} \\ &= \omega_{out}\omega_{sf}\kappa_{SFG}\kappa_{DFG}|A_{p1}||A_{s}||A_{p2}|L^{2}sinc(\Delta k_{SFG}L/2)e^{i(\frac{3}{2}\varphi_{p1}-\frac{1}{2}\varphi_{p2})}cos(\delta\varphi') \end{aligned} \tag{6.29}$$

where A_j ($j = p1$, $p2$, s) denote the complex amplitudes of Pump 1, Pump 2 and the Signal respectively. $\delta\varphi' = \delta\varphi + \Delta k_{SFG}L/4$ is the summation of the relative input phase plus the phase shift induced by the nonzero phase-mismatches of the SHG and the SFG processes.

Compared to the two-stage scheme, the conversion efficiency of the cSHG/DFG process and the cSFG/DFG process in the single-stage scheme is compromised by the nonzero phase-mismatches resulting in a lower output power. However, in principle, the combination of the phase-conjugate output and the phase preserving output still results in amplification of the in-phase component of the signal and cancellation of the quadrature component, as shown in Eq. 6.29. This regenerative property is independent of the conversion efficiency of the cSHG/DFG and the cSFG/DFG processes. A limitation of the single-stage implementation is that the operational bit rate of the input signal (i.e. the signal bandwidth) is restricted by the frequency spacing between the signal and the pumps which in turn, is limited by the SHG acceptance bandwidth of the PPLN waveguide.

In the following section, I present two separate experiments that have demonstrated the PR-WC proposed above in either a single- or a two-stage implementation, employing either one or two nominally identical PPLN devices as the nonlinear media respectively. The implementation of the single-stage PR-WC is simpler and is presented first in Section 6.3.3.1. Fuller measurements of the phase-correction performance of the scheme are presented for the more flexible two-stage implementation that follows in Section 6.3.3.2.

6.3.3 Experiments

6.3.3.1 Single-stage implementation

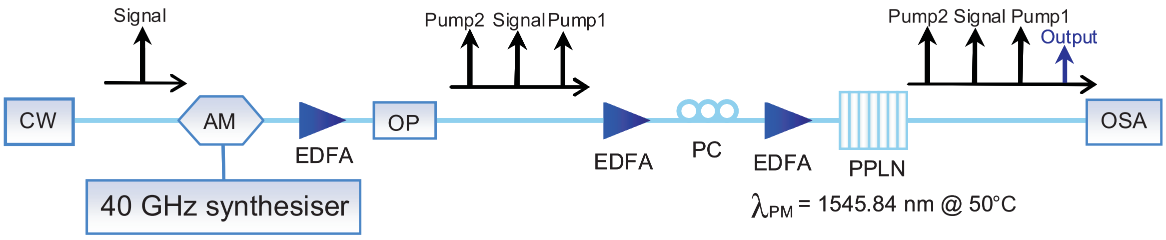

Figure 6.13: Experimental setup for the proposed single-stage PR-WC based on a combination of cSHG/DFG and cSFG/DFG. AM: amplitude modulator, PC: polarization controller, EDFA: erbium-doped fibre amplifier, OSA: optical spectrum analyser, OP: optical processor.

Fig. 6.13 shows the experimental setup used to realize the single-stage PR-WC. A 30-mm-long fibre-pigtailed PPLN waveguide (HC Photonics Corp.) was used to observe both cSHG/DFG and cSFG/DFG in a single stage. Its SHG phase matching wavelength was $\sim$ 1545.84 nm at 50^oC, its insertion loss was 3.5 dB and its normalised (internal) conversion efficiency was 75% W^{-1}cm^{-2}. A CW laser operating at 1545.68 nm was modulated by an amplitude modulator driven by a 40 GHz synthesiser, generating three frequency tones at 1545.36 nm, 1545.68 nm and 1546.00 nm respectively. These three tones were used as Pump 2, the input Signal, and Pump 1, respectively. All of the frequency tones were subsequently passed through an optical processor (Finisar Waveshaper 4000E), which is a programmable filter used to adjust both the relative phase between the three waves and the optical power of Pump 2, thereby controlling the strength of the cSFG/DFG process in the PPLN waveguide. All of the optical waves were aligned to the optical axis of the PPLN waveguide by a polarisation controller, amplified (to a total power of 21 dBm) and subsequently launched into the PPLN waveguide. Both the phase-preserving output of the cSFG/DFG process and the phase-conjugate output of the cSHG/DFG process respectively lie at 1546.32 nm.

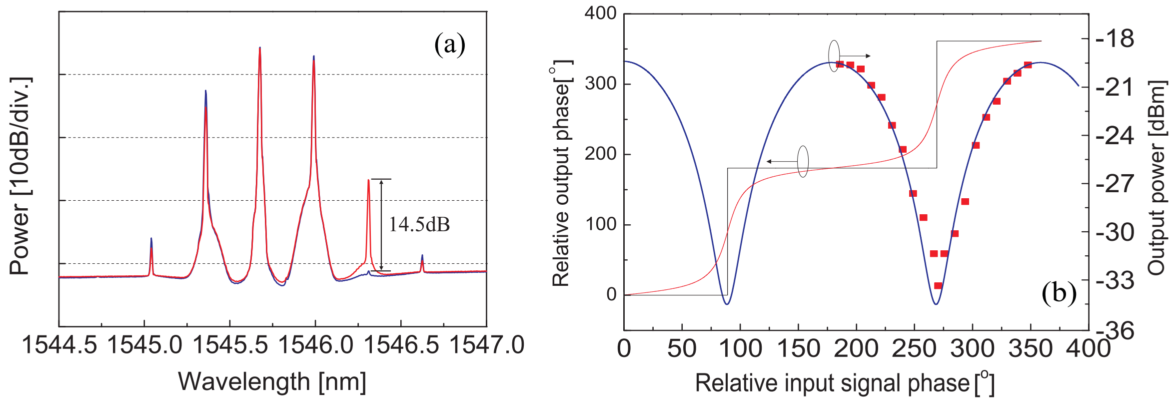

FIGURE 6.14: (a): Measured output spectra of the single-stage PR-WC showing the phase-sensitive swing. (b): Measured (symbols) and calculated phase-sensitive swing (solid line) plotted as a function of the relative input signal phase for the single-stage PR-WC.

Fig. 6.14(a) shows the measured spectra at the output of the PPLN waveguide for the cases of maximum (red trace) and minimum conversion efficiency (blue trace) at the combined output. Note that these measurements were achieved by controlling the relative phase of the signal at 1545.68 nm in the OP. The wavelength conversion loss for the case of maximum conversion was ∼ 19.5 dB. Similar to Section 6.2, I evaluate the performance of the system in terms of its phase-sensitive swing (PSS), i.e. the ratio between the maximum and minimum output power of the converted signal. The PSS of the combined output was ∼ 14.5 dB. From Eq. 6.29 we find that this corresponds to an amplitude ratio of the cSHG/DFG and cSFG/DFG outputs of ∼ 0.7:1. In contrast to the experimental results in Section 6.2, the large PSS of the combined output is due to the strong attenuation of the quadrature component of the signal rather than the amplification of the in-phase component. Fig. 6.14(b) shows the phase-sensitive behaviour of the combined output plotted as a function of the relative phase between the input signal and the pumps. The experimental measurements (red spots) agree well with the theoretical curve calculated using Eq. 6.29 (blue curve). The swing profile clearly indicates the phase-sensitive behaviour with a period of π-phase. Figure 6.14(b) also illustrates the calculated phase regenerative properties of the proposed single-stage PR-WC scheme. The black trace shows the ideal case, where the outputs from cSHG/DFG and cSFG/DFG are perfectly conjugated and have strictly equal powers. The cancellation of the quadrature component of the signal allows close to ideal binary phase regeneration, independent of the overall cSHG/DFG and cSFG/DFG efficiency. The red trace shows the calculated phase regenerative properties of the single-stage PR-WC scheme for a PSS of 14.5 dB as achieved in the experiment.

6.3.3.2 Two-stage implementation

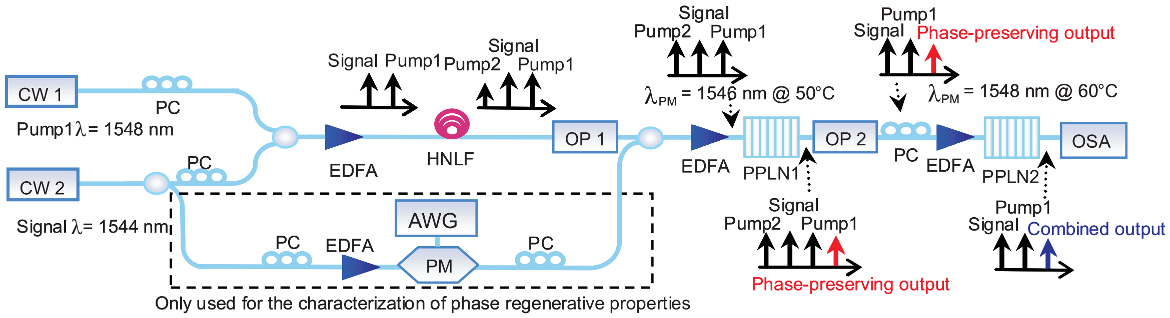

FIGURE 6.15: Experimental setup for the two-stage PR-WC scheme based on a combination of cSHG/DFG and cSFG/DFG in two cascaded PPLN waveguides. CW: continuous wave, PC: polarization controller, EDFA: erbium-doped fibre amplifier, HNLF: highly nonlinear fibre, OP: optical processor, OSA: optical spectrum analyzer, PM: phase modulator, AWG: arbitrary waveform generator.

Figure 6.15 shows the experimental setup used to realise the two-stage PR-WC with two cascaded PPLN waveguides. Both of the PPLN waveguides (HC Photonics Corp.) were nominally identical with parameters as shown in Section 6.3.3.1. The SHG QPM of PPLN 1 was $\sim$ 1546 nm by operating it at $50^{o}C$. The SHG QPM of PPLN 2 was shifted to 1548 nm by operating it at the higher temperature of $60^{o}C$. Two CW lasers were used as the signal source and Pump 1, operating at 1544nm and 1548 nm respectively. The two beams were combined in a 3-dB coupler, amplified and launched into 500 m of a HNLF to generate a phase-correlated idler wave at 1540 nm through FWM which was then used as Pump 2. The HNLF had a dispersion of -0.87 ps/nm/km at 1550 nm and a nonlinear coefficient of 19 $(\mathrm{W{\cdot}km})^{-1}$. All of the optical waves were passed through Optical Processor 1 (OP1), which, as before, was used to adjust the relative phase between the signal and the pumps and to adjust the optical power of Pump 2, thereby controlling the strength of the cSFG/DFG process in PPLN 1. After OP1, all of the optical waves were amplified (to a total power of 21 dBm) and launched into PPLN 1 which induced the cSFG/DFG process to generate the phase-preserving output at 1552 nm. All of the resulting optical waves were subsequently passed through a second optical processor (OP2), which selectively suppressed Pump 2. After OP2, all of the optical waves were amplified (to a total power of 21 dBm) and launched into PPLN 2 which induced the cSHG/DFG process to generate the phase-conjugate output, also at 1552 nm.

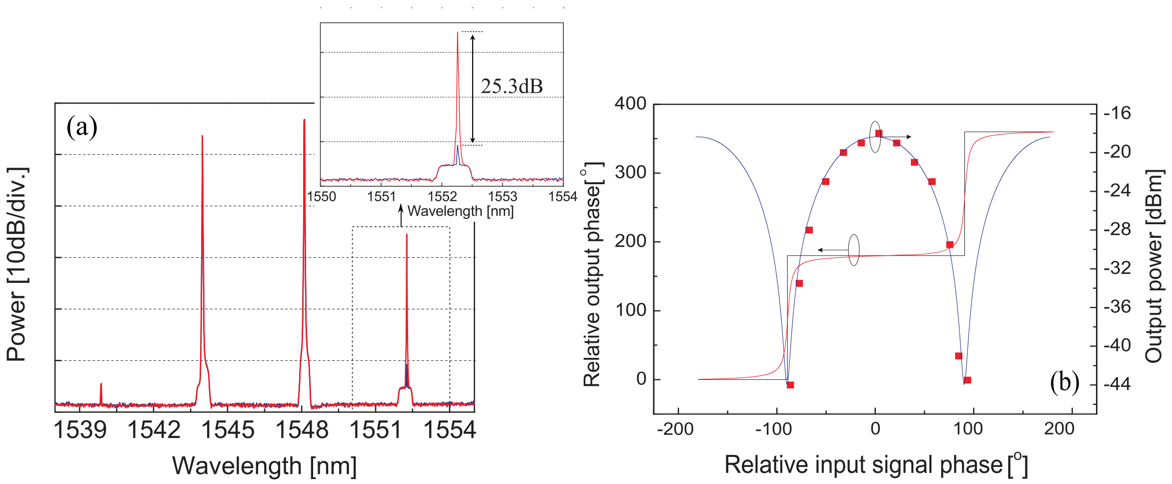

FIGURE 6.16: (a): Measured output spectra of the two-stage PR-WC scheme showing the phase-sensitive swing (measured with a resolution of 0.05 nm). (b): Measured (red spots) and calculated phase-sensitive swing (blue curve) plotted as a function of the relative input signal phase, and the calculated input-output phase relationship of ideal case (black trace) and the two-stage PR-WC scheme (red trace).

Figure 6.16(a) shows the measured spectra at the output of PPLN 2 for the cases of maximum (red trace) and minimum conversion efficiency (blue trace) at the combined output. Note that these measurements were achieved by controlling the relative phase of the signal at 1544 nm in OP1. The wavelength conversion loss for the case of maximum conversion was $\sim$ 18 dB. The PSS of the combined output was $\sim$ 25.3dB. From Eq. 6.26 we find that this corresponds to an amplitude ratio of the cSHG/DFG and cSFG/DFG outputs of $\sim$ 0.91:1.

Figure 6.16(b) shows the phase-sensitive behaviour of the combined output plotted as a function of the relative phase between the input signal and the pumps. The experimental measurements (red spots) agree well with the theoretical curve (blue curve). The swing profile clearly indicates the phase-sensitive behaviour with a period of π-phase. Figure 6.16(b) also illustrates the calculated phase regenerative properties of the proposed two-stage PR-WC scheme. The black trace shows the ideal case, where the outputs from cSHG/DFG and cSFG/DFG are perfectly conjugated and have strictly equal powers. The red trace shows the calculated phase regenerative properties of the two-stage PR-WC scheme for a PSS of 25.3 dB as achieved in the experiment. Phase noise ranging between $\pm 30^o$ at an input D(B)PSK signal can be suppressed to $\sim \pm 1.5^o$ at the output. As with all basic PSA configurations, phase regeneration in this PR-WC scheme is achieved at the expense of some added amplitude noise. In our PR-WC scheme, a phase fluctuation of $\pm 30^o$ is converted into an amplitude fluctuation of 0.62 dB. (This amplitude noise can be reduced e.g. by increasing the conversion efficiency of the PPLN waveguides and saturating the gain of the outputs. However, this was not possible in my experiment, due to the maximum permissible power I could launch to the PPLN waveguides.)

To characterize the phase regenerative capabilities of the system, the signal was split into two arms as illustrated in the dashed box shown in Fig. 6.15. The input Signal in the top arm was suppressed by OP1 after FWM, and a phase modulator was first used to emulate phase noise degradation of a binary phase modulated signal in the bottom arm. The modulator was driven by an electrical signal comprising the sum of a binary (signal) at 4 Gbit/s, and a broadband random noise waveform, generated using a 24 GS/s arbitrary waveform generator (Tektronix AWG7122B). To measure the phase characteristics, the input signal and the idler were assessed using a homodyne coherent receiver. Because the homodyne receiver requires a local oscillator at the original signal wavelength, the output was first converted back to the original signal wavelength using a parametric fibre wavelength converter using the output and Pump 1. The parametric fibre wavelength converter relied on FWM in a 500-m-long HNLF with a nonlinear coefficient of $\gamma = 20$ $(\mathrm{W{\cdot}km})^{-1}$, a dispersion of 0.06 ps/nm/km, and a dispersion slope of 0.0035 ps/nm^2/km. The phase information was retrieved using digital signal processing, and the results are displayed in Fig. 6.17. I acknowledge the help from my colleague Joseph Kakande for the signal post-processing. The data were sampled at the sampling rate of 48 GHz, and one in every 12 samples was recorded in the digital signal processing (i.e. one recorded sample per bit). Phase histograms (20000 recorded samples) of the input signal and the (converted) output are shown in Fig. 6.17(a) and Fig. 6.17(b) respectively. The input signal phase at the 0^o peak is distributed with a 3 dB width of $\pm 30^o$, while at the output the phase fluctuations have been considerably reduced, with a 3 dB distribution width of $< 10^o$. We attribute the difference between the experimental and calculated performance based on the response function shown in Fig. 6.16 to be due to relative phase drift/noise between the pump and signal arms induced by environmental perturbations. Such effects mean that it is not possible to guarantee that the PR-WC was operating at its optimal operating point during the measurement (i.e. inputs with 0^o relative phase experiencing the maximum gain). To make more reliable measurements (and most certainly for any practical application) it would be necessary to ensure that the signal and pump beams were accurately phase-locked - for example using an active phase lock loop (see e.g. Ref. [Slavik 10]). The final 500 m-long fibre-based wavelength conversion stage, which we required to allow us to implement the homodyne coherent receiver, also presents an additional potential source of measurement noise. Nevertheless, these proof-of-principle measurements demonstrate significant phase noise reduction and validate the approach.

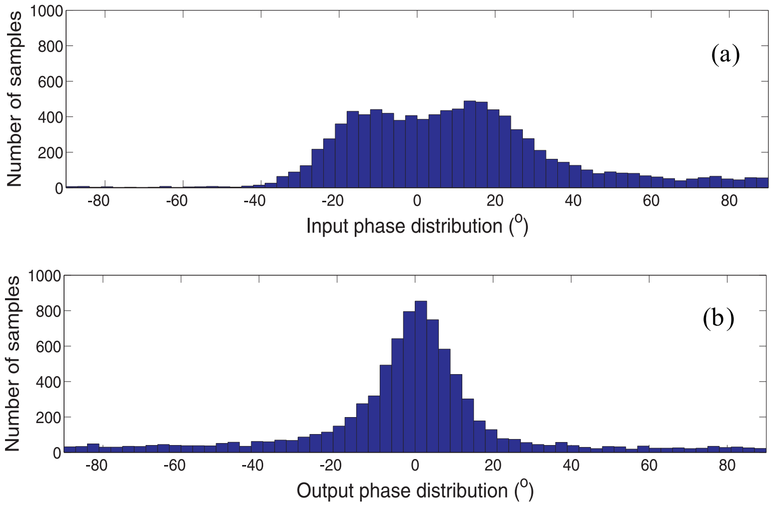

FIGURE 6.17: (a) Measured phase distribution at the input and (b) the output.

6.3.4 Conclusion

In this section, I have demonstrated both theoretically and experimentally a novel scheme for PR-WC based on a combination of cSHG/DFG and cSFG/DFG processes. This scheme can be implemented in either a single PPLN waveguide, or two separate PPLN waveguides. I first demonstrated a single-stage PR-WC using a single PPLN waveguide with a uniform poling period. A PSS of 14.5 dB was achieved in this experiment. In order to achieve the best regenerative performance both cSHG/DFG and cSFG/DFG need to be detuned from the exact phase-matching conditions and the maximum permissible signal bandwidth is restricted by the requirement to fit both the signal and one of the pumps within the SHG bandwidth of the PPLN device. These limitations could in principle be overcome by employing a superstructured PPLN waveguide exhibiting two QPM peaks [Hum 07]. In this case, both cSFG/DFG and cSHG/DFG could operate at the exact phase-matching conditions by placing Pump 1 and the input signal symmetrically around the first QPM wavelength of the PPLN waveguide, as well as placing Pump 1 at the second QPM wavelength of the PPLN waveguide.

The limitations imposed by the single-stage implementation were overcome by separating the two cascaded quadratic operations in two different PPLN waveguides. By doing this, a PSS of 25.3 dB was achieved. I verified the very good agreement between the theoretical predictions and the performance of the PR-WC scheme. The phase-regenerative properties of the wavelength converter were also verified using a purpose-built homodyne detection system. These proof-of-principle experiments of the phase regenerative properties show the potential of the PR-WC scheme as a D(B)PSK phase regenerator.

6.4 Conclusion

In this chapter, two novel configurations of phase sensitive amplification based on cascaded quadratic effects in periodically poled lithium niobate waveguides were demonstrated. The first one was a frequency non-degenerate PSA based on the cSHG/DFG process within a single waveguide. A maximum gain of 0.65 dB with a peak-to-peak gain variation of 3.4 dB for a 100-ps duration, 2.5 GHz pulsed signal was achieved in the experiments with a 3-cm-long PPLN waveguide. The second PSA configuration was a PR-WC which is based on a combination of the cSHG/DFG process and the cSFG/DFG process within PPLN waveguides. Theoretical analysis and experiments of two implementations of this PR-WC configuration were presented, in either a single PPLN waveguide, or two separate PPLN waveguides. Peak-to-peak gain variations of 14.5 dB and 25.3 dB were achieved in the experiments for these two implementations respectively. Finally, the experiments showed the potential of the PR-WC scheme as a D(B)PSK phase regenerator.

References

[Armstrong 62] J. A. Armstrong, N. Bloembergen, J. Ducuing & P. S. Pershan, *Interactions between Light Waves in a Nonlinear Dielectric*, Phys. Rev., vol. 127, no. 6, pages 1918–1939, Sep 1962.

[Caves 82] Carlton M. Caves, *Quantum limits on noise in linear amplifiers*, Phys. Rev. D, vol. 26, pages 1817–1839, Oct 1982.

[Choi 99] S. K. Choi, M. Vasilyev & P. Kumar, *Noiseless optical amplification of images*, Physical Review Letters, vol. 83, no. 10, pages 1938–1941, September 1999.

[Croussore 05] K. Croussore, I. Kim, Y. Han, C. Kim, G. F. Li & S. Radic, *Demonstration of phase-regeneration of DPSK signals based on phase-sensitive amplification*, Optics Express, vol. 13, no. 11, pages 3945–3950, May 2005.

[Croussore 07] K. Croussore & G. F. Li. *Phase-regenerative DPSK wavelength conversion*, 2007.

[Croussore 08] K. Croussore & G. F. Li, *Phase and amplitude regeneration of differential phase-shift keyed signals using phase-sensitive amplification*, Ieee Journal of Selected Topics In Quantum Electronics, vol. 14, no. 3, pages 648–658, May 2008.

[Croussore 09] K. A. Croussore & G. F. Li, *Phase-Regenerative Wavelength Conversion for BPSK and DPSK Signals*, Ieee Photonics Technology Letters, vol. 21, no. 1-4, pages 70–72, January 2009.

[Essiambre 99] R. J. Essiambre, B. Mikkelsen & G. Raybon, *Intra-channel cross-phase modulation and four-wave mixing in high-speed TDM systems*, Electronics Letters, vol. 35, no. 18, pages 1576–1578, September 1999.

[Essiambre 02] R. J. Essiambre, G. Raybon, B. Mikkelsen, I. P. Kaminow & T. Li. *Pseudo-linear transmission of high-speed TDM signals 40 and 160 Gb/s.* In Proc. Optical Fiber Telecommunications IVB, pp.233 - 304., 2002.

[Eto 07] Yujiro Eto, Takashi Tajima, Yun Zhang & Takuya Hirano, *Observation of squeezed light at 1.535 μm using a pulsed homodyne detector*, Opt. Lett., vol. 32, no. 12, pages 1698–1700, Jun 2007.

[Eto 08] Y. Eto, T. Tajima, Y. Zhang & T. Hirano, *Observation of quadrature squeezing in chi((2)) nonlinear waveguide using a temporally shaped local oscillator pulse*, Optics Express, vol. 16, no. 14, pages 10650–10657, July 2008.

[Gallo 97] K. Gallo, G. Assanto & G. I. Stegeman, *Efficient wavelength shifting over the erbium amplifier bandwidth via cascaded second order processes in lithium niobate waveguides*, Applied Physics Letters, vol. 71, no. 8, pages 1020–1022, August 1997.

[Gallo 99] K. Gallo & G. Assanto, *Analysis of lithium niobate all-optical wavelength shifters for the third spectral window*, Journal of the Optical Society of America B-optical Physics, vol. 16, no. 5, pages 741–753, May 1999.

[Gnauck 05] A. H. Gnauck & P. J. Winzer, *Optical phase-shift-keyed transmission*, Journal of Lightwave Technology, vol. 23, no. 1, pages 115–130, January 2005.

[Gordon 90] J. P. Gordon & L. F. Mollenauer, *Phase Noise In Photonic Communications-systems Using Linear-amplifiers*, Optics Letters, vol. 15, no. 23, pages 1351–1353, December 1990.

[Hum 07] D. S. Hum & M. M. Fejer, *Quasi-phasematching*, Comptes Rendus Physique, vol. 8, no. 2, pages 180–198, March 2007.

[Imajuku 97a] W. Imajuku & A. Takada, *In-line phase-sensitive amplifier with optical-PLL-controlled internal pump light source*, Electronics Letters, vol. 33, no. 25, pages 2155–2156, December 1997.

[Imajuku 97b] W. Imajuku & A. Takada, *Reduction of fiber-nonlinearity-enhanced amplifier noise by means of phase-sensitive amplifiers*, Optics Letters, vol. 22, no. 1, pages 31–33, January 1997.

[Ishida 03] K. Ishida, T. Kobayashi, J. Abe, K. Kinjo, S. Kuroda & T. Mizuochi. *A comparative study of 10 Gb/s RZ-DPSK and RZ-ASK WDM transmission over transoceanic distances*, 2003.

[Kumar 84] P. Kumar & J. H. Shapiro, *Squeezed-state Generation Via Forward Degenerate 4-wave Mixing*, Physical Review A, vol. 30, no. 3, pages 1568–1571, 1984.

[Lee 09] K. J. Lee, F. Parmigiani, S. Liu, J. Kakande, P. Petropoulos, K. Gallo & D. Richardson, *Phase sensitive amplification based on quadratic cascading in a periodically poled lithium niobate waveguide*, Optics Express, vol. 17, no. 22, pages 20393–20400, October 2009.

[Levenson 93] J. A. Levenson, I. Abram, T. Rivera & P. Grangier, *Reduction of Quantum-noise In Optical Parametric Amplification*, Journal of the Optical Society of America B-optical Physics, vol. 10, no. 11, pages 2233–2238, November 1993.

[Li 94] R. D. Li, P. Kumar & W. L. Kath, *Dispersion Compensation With Phase-sensitive Optical Amplifiers*, Journal of Lightwave Technology, vol. 12, no. 3, pages 541–549, March 1994.

[Liberale 02] C. Liberale, I. Cristiani, L. Razzari & V. Degiorgio, *Numerical study of cascaded wavelength conversion in quadratic media*, Journal of Optics A-pure and Applied Optics, vol. 4, no. 4, pages 457–462, July 2002.

[Liu 02] X. Liu, C. Xu & X. Wei. *Nonlinear phase noise in pulse-overlapped transmission based on return-to-zero differential-phase-shift-keying.* In Optical Communication, 2002. ECOC 2002. 28th European Conference on, volume 4, pages 1 –2, sept. 2002.

[Lundstrom 09] C. Lundstrom, J. Kakande, P.A. Andrekson, Zhi Tong, M. Karlsson, P. Petropoulos, F. Parmigiani & D.J. Richardson. *Experimental comparison of gain and saturation characteristics of a parametric amplifier in phase-sensitive and phase-insensitive mode.* In Optical Communication, 2009. ECOC '09. 35th European Conference on, pages 1 –2, sept. 2009.

[Mamyshev 99] P. V. Mamyshev & N. A. Mamysheva, *Pulse-overlapped dispersion-managed data transmission and intrachannel four-wave mixing*, Optics Letters, vol. 24, no. 21, pages 1454–1456, November 1999.

[Marhic 91] M. E. Marhic, C. H. Hsia & J. M. Jeong, *Optical Amplification In A Nonlinear Fiber Interferometer*, Electronics Letters, vol. 27, no. 3, pages 210–211, January 1991.

[McKinstrie 04] C. J. McKinstrie & S. Radic, *Phase-sensitive amplification in a fiber*, Optics Express, vol. 12, no. 20, pages 4973–4979, October 2004.

[McKinstrie 06] C. J. McKinstrie & M. G. Raymer, *Four-wave-mixing cascades near the zero-dispersion frequency*, Optics Express, vol. 14, no. 21, pages 9600–9610, October 2006.

[McKinstrie 07] C. J. McKinstrie, S. Radic, M. G. Raymer & L. Schenato, *Unimpaired phase-sensitive amplification by vector four-wave mixing near the zero-dispersion frequency*, Optics Express, vol. 15, no. 5, pages 2178–2189, March 2007.

[Ou 93] Z. Y. Ou, S. F. Pereira & H. J. Kimble, *Quantum Noise-reduction In Optical Amplification*, Physical Review Letters, vol. 70, no. 21, pages 3239–3242, May 1993.

[Shirasaki 90] M. Shirasaki & H. A. Haus, *Squeezing of Pulses In A Nonlinear Interferometer*, Journal of the Optical Society of America B-optical Physics, vol. 7, no. 1, pages 30–34, January 1990.

[Shoji 97] I. Shoji, T. Kondo, A. Kitamoto, M. Shirane & R. Ito, *Absolute scale of second-order nonlinear-optical coefficients*, Journal of the Optical Society of America B-optical Physics, vol. 14, no. 9, pages 2268–2294, September 1997.

[Slavik 10] R. Slavik, F. Parmigiani, J. Kakande, C. Lundstrom, M. Sjodin, P. A. Andrekson, R. Weerasuriya, S. Sygletos, A. D. Ellis, L. Gruner-Nielsen, D. Jakobsen, S. Herstrom, R. Phelan, J. O'Gorman, A. Bogris,

D. Syvridis, S. Dasgupta, P. Petropoulos & D. J. Richardson, *All-optical phase and amplitude regenerator for next-generation telecommunications systems*, Nature Photonics, vol. 4, no. 10, pages 690–695, October 2010.

[Suhara 03] T. Suhara & M. Fujimura, Waveguide nonlinear-optic devices, Springer, 2003.

[Tajima 05] T. Tajima, Y. Etou & T. Hirano. *Parametric amplification in a periodically poled lithium niobate waveguide at telecommunication wavelength.* In International Quantum Electronics Conference, 2005., pages 1331 – 1332, 11, 2005.

[Takada 98] A. Takada & W. Imajuku, *In-line optical phase-sensitive amplifier employing pump laser injection-locled to input signal light*, Electronics Letters, vol. 34, no. 3, pages 274–276, February 1998.

[Tang 05a] R. Tang, P. Devgan, P. L. Voss, V. S. Grigoryan & P. Kumar, *In-line frequency-nondegenerate phase-sensitive fiber-optical parametric amplifier*, Ieee Photonics Technology Letters, vol. 17, no. 9, pages 1845–1847, September 2005.

[Tang 05b] R. Tang, J. Lasri, P. S. Devgan, V. Grigoryan, P. Kumar & M. Vasilyev, *Gain characteristics of a frequency nondegenerate phase-sensitive fiber-optic parametric amplifier with phase self-stabilized input*, Optics Express, vol. 13, no. 26, pages 10483–10493, December 2005.

[Tang 08] R. Tang, P. S. Devgan, V. S. Grigoryan, P. Kumar & M. Vasilyev, *In-line phase-sensitive amplification of multi-channel CW signals based on frequency nondegenerate four-wave-mixing in fiber*, Optics Express, vol. 16, no. 12, pages 9046–9053, June 2008.

[Tong 10] Z. Tong, A. Bogris, M. Karlsson & P. A. Andrekson, *Full characterization of the signal and idler noise figure spectra in single-pumped fiber optical parametric amplifiers*, Optics Express, vol. 18, no. 3, pages 2884–2893, February 2010.

[Tong 11] Z. Tong, C. Lundstrom, P. A. Andrekson, C.J. McKinstrie, M. Karlsson, D.J. Blessing, E. Tipsuwannakul, B.J. Puttnam, H. Toda & L. Gruner-Nielsen, *Towards ultrasensitive optical links enabled by low-noise phase-sensitive amplifiers*, Nature Photonics, pages –, June June, 2011.

[Umeki 11] Takeshi Umeki, Osamu Tadanaga, Atsushi Takada & Masaki Asobe, *Phase sensitive degenerate parametric amplification using directly-bonded PPLN ridge waveguides*, Opt. Express, vol. 19, no. 7, pages 6326–6332, Mar 2011.

[Wei 03] X. Wei & X. Liu, *Analysis of intrachannel four-wave mixing in differential phase-shift keying transmission with large dispersion*, Optics Letters, vol. 28, no. 23, pages 2300–2302, December 2003.

[Xie 03] C. J. Xie, L. Moller, H. Haunstein & S. Hunsche, *Comparison of system tolerance to polarization-mode dispersion between different modulation formats*, Ieee Photonics Technology Letters, vol. 15, no. 8, pages 1168–1170, August 2003.

[Xu 03] C. Xu, X. Liu, L. Mollenauer & X. Wei. *Comparison of return-to-zero phase shift keying and on-off keying in long haul dispersion managed transmissions*, 2003.

[Xu 04] C. Xu, X. Liu & X. Wei, *Differential phase-shift keying for high spectral efficiency optical transmissions*, Ieee Journal of Selected Topics In Quantum Electronics, vol. 10, no. 2, pages 281–293, March 2004.

[Yuen 79] H. P. Yuen & J. H. Shapiro, *Generation and Detection of 2-photon Coherent States In Degenerate 4-wave Mixing*, Optics Letters, vol. 4, no. 10, pages 334–336, 1979.

7

Elimination of the chirp of optical pulses with PPLN waveguides

7.1 Introduction

Picosecond optical pulses are widely used in diverse applications, such as optical communications, optical sensors, and optical imaging systems. Such short optical pulses can be generated using a variety of means including mode-locked lasers, gain-switched laser diodes, and even externally modulated CW light sources. However, the generated optical pulses often have some associated intrinsic frequency chirp and the cumulative effects of dispersion and various optical nonlinearities often experienced during onward transmission in fibre systems can either intensify this chirp, or induce additional nonlinear degradation, leading to compromised performance for many applications.

Several methods have been employed to eliminate the frequency chirp in short pulses. For instance, suitable lengths of fibre are usually employed to remove the linear chirp component associated with non transform-limited optical pulses. However, the length of the DCF has to be matched to the exact chirp characteristics [Takeda 96]. Another technique based on fibre Bragg grating (FBG) is capable to eliminate both the linear and nonlinear phase components associated with non transform-limited optical pulses.

However, the spectral profile of the FBG typically needs to be determined on a case-by-case basis [Hill 94]. Recently, a compensation scheme to reduce the frequency chirp associated with directly modulated sampled grating distributed Bragg reflector tunable lasers through simultaneous modulation of the laser's phase section was also demonstrated [Maher 09].

In this chapter, I propose and demonstrate an effective method to remove frequency chirps induced in ps-optical pulses with PPLN waveguides. The technique relies on the generation of a conjugated replica of the input chirped pulse in a first PPLN waveguide via cSHG/DFG, followed by the nonlinear interaction of the two phase-conjugated signals through cSFG/DFG in a second PPLN waveguide: a process which eventually yields chirp-free pulses at the system output. This scheme has the distinct advantage that even unknown or nonlinear chirps can be erased without requiring detailed knowledge of the input pulse form.

7.2 Principle of operation

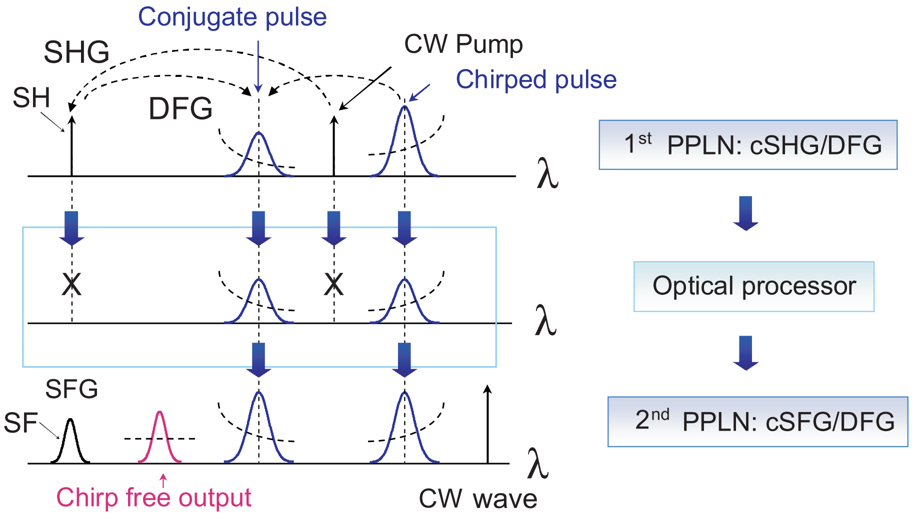

FIGURE 7.1: Illustration of chirp elimination in a short pulse based on both cSHG/DFG and cSFG/DFG in two cascaded PPLN waveguides.

In Section 6.3 in Chapter 6, I presented a PR-WC scheme based on a combination of the cSHG/DFG and cSFG/DFG processes. The summation of the phase preserving replica of the input signal and the phase-conjugated replica of the input signal can give a phase-regenerated output. Again using the combination of the cSHG/DFG and cSFG/DFG processes, I will present a chirp elimination scheme which relies on the product of the input signal and its phase-conjugated replica instead of the summation.

Figure 7.1 illustrates my scheme for the elimination of chirp in pulses based on the combination of cSHG/DFG and cSFG/DFG in two cascaded PPLN waveguides. E_{cp}, E_{cj}, E_{sf}, and E_{out} in the following text denote the optical fields of the input chirped pulse, conjugated replica, SF waves, and chirp-free output waves, respectively. The first PPLN waveguide performs phase-conjugation ($E_{cj} = E_{cp}^*$) and wavelength conversion of the original chirped input pulse by means of the cascaded SHG/DFG process. The SH wave of an input CW is first generated by SHG in the first PPLN waveguide, which is followed by DFG between this SH wave and the initially chirped input pulse to produce the phase-conjugate counterpart with opposite chirp. All of the resulting optical waves after the first PPLN sample are passed through an optical processor. The optical processor is a programmable amplitude filter as introduced in the background chapter. The optical processor rejects both the pump and the SH waves, and equalises the optical power of the input pulse with that of its conjugate. Equalization of the intensities of the two signals is required in order to optimise the efficiency of the cascaded SFG/DFG process in the second PPLN waveguide. In the cSFG/DFG process, the two pulses interact with each other as two synchronised pulsed pumps to generate the SF wave by SFG. The optical field of the SF wave is expressed by the product of the two original optical fields $E_{sf} \sim E_{cp}E_{cj}$, which means that the imaginary part of the input field is cancelled out and thus any frequency chirp is erased. The generated chirp-free SF pulses subsequently interact with a second CW beam via the DFG process, and mapped back into the telecommunication band.

In the cSHG/DFG process at the first PPLN stage, no apparent walk-off effect occurs between the chirped input pulses and the generated conjugated pulses, because they are in the same wavelength band and have similar values of group velocity. Therefore, neglecting the pump depletion, the conjugated pulses are truly conjugated replicas of the chirped input pulses. For the cSFG/DFG process at the second PPLN stage, in a simplified picture (neglecting pump depletion and walk-off), the generated SF field will be proportional to the modulus squared of the original signal ($E_{sf} \sim E_{cp}E_{cj} = |E_{cp}|^2$). However, in the cSFG/DFG process, a significant walk-off effect occurs between the pulses in the telecommunication band (the chirped input signal and the conjugated signal) and the generated SF wave because of the group velocity mismatch, resulting in pulse broadening of the SF wave. To simulate the actual response of the second PPLN stage with the presence of pump depletion and group velocity mismatch, the following coupled mode equations were used:

$$\begin{aligned}
&\frac{\partial A_{cp}}{\partial z} + \frac{1}{v_{cp}}\frac{\partial A_{cp}}{\partial t} = -i\kappa_{SFG}\omega_{cp}A_{sf}A_{cj}^{*}exp(-i\Delta k_{SFG}z)\\
&\frac{\partial A_{cj}}{\partial z} + \frac{1}{v_{cj}}\frac{\partial A_{cj}}{\partial t} = -i\kappa_{SFG}\omega_{cj}A_{sf}A_{cp}^{*}exp(-i\Delta k_{SFG}z)\\
&\frac{\partial A_{cw}}{\partial z} + \frac{1}{v_{cw}}\frac{\partial A_{cw}}{\partial t} = -i\kappa_{DFG}\omega_{cw}A_{sf}A_{out}^{*}exp(-i\Delta k_{DFG}z)\\
&\frac{\partial A_{out}}{\partial z} + \frac{1}{v_{out}}\frac{\partial A_{out}}{\partial t} = -i\kappa_{DFG}\omega_{out}A_{sf}A_{cw}^{*}exp(-i\Delta k_{DFG}z)\\
&\frac{\partial A_{sf}}{\partial z} + \frac{1}{v_{sf}}\frac{\partial A_{sf}}{\partial t} = -i\kappa_{SFG}\omega_{sf}A_{cp}A_{cj}exp(i\Delta k_{SFG}z) - i\kappa_{DFG}\omega_{sf}A_{cw}A_{out}exp(i\Delta k_{DFG}z)
\end{aligned} \tag{7.1}$$

where $A_{cp,cj,sf,cw,out}$ and $v_{cp,cj,sf,cw,out}$ denote the slowly varying envelopes and the group velocities of the input chirped pulse, conjugated replica, SF, CW-wave, and chirp-free output waves, respectively. κ_{SFG} and κ_{DFG} denote the nonlinear coupling coefficients of SFG and DFG respectively. $\Delta k_{SFG} = k_{sf} - k_{cp} - k_{cj} - 2\pi/\Lambda$ and $\Delta k_{DFG} = k_{cw} + k_{out} - k_{sf} + 2\pi/\Lambda$ are the phase-mismatches of SFG and DFG respectively, and Λ is the period of the QPM grating and each k is the wave vector at the corresponding frequency.

In the simulation, the values of the group velocities and the nonlinear coupling coefficients matched those used in the experiments that will be described in the following section (Sec. 7.3) and previously given in the background chapter (Chapter 2). The PPLN waveguide is 3 cm long with a normalized efficiency $\eta_{nor} = 75\%\mathrm{W}^{-1}\mathrm{cm}^{-2}$. The peak power of chirped input pulses is $P_{cp} = P_{cj} = 30$ mW, and the power of CW wave is $P_{cw} = 1$ mW. For the 3-cm PPLN waveguides used in the experiments, the walk-off limit of the pulse duration is ~ 10 ps. In order to investigate the impact of the walk-off effect on the chirp elimination scheme, the durations of the input pulses were chosen as 7 ps which is a slightly shorter than the walk-off limit (10 ps) and 2 ps which is far shorter than that respectively. In the case that the input is 7-ps Gaussian chirped pulses with a chirp of 3.5 ps/nm, and a time-bandwidth product of 1.63 (as achieved in the experiments shown in the following section, Sec. 7.3), the propagation of the chirped input, conjugate, SF and output pulses in the PPLN waveguide is shown in Fig. 7.2, and the normalized powers and phases of the chirped input, conjugate and output pulses are shown in Fig. 7.3. The numerical simulations were based on Eqns. 7.1 and the symmetric split-step Fourier method was employed. As shown in Fig. 7.2, the chirped input pulse and the conjugate pulse interact with each other, generating the SF wave through SFG. In the absence of the walk-off effect, the SF pulse would be shortened because the generated SF field is proportional to the modulus squared of the original signal. The SFG process is followed by the DFG process between the SF wave and the CW, generating the output pulse at a new wavelength. As shown in Fig. 7.3, the durations of the input and output pulses are $\sim$ 7 ps and $\sim$ 6.2 ps respectively. Such a similarity between the pulse durations stems from a balance between pulse shortening in SFG and pulse broadening due to walk-off in the second PPLN waveguide. The temporal displacement between the input and the output pulses is because the SF is delayed relative to the input pulse due to the walk-off effect and the temporal position of the delayed SF pulse is subsequently converted to the output pulse through the DFG process. The numerical simulations confirmed the capability of the scheme to remove the chirp of the pulses, even in the presence of moderate walk-off between the original and SF signals in the PPLN waveguide.

Next, the input signal was changed to un-chirped Gaussian pulses with the same pulse duration. The propagation of chirped input, conjugate, SF and output pulses in the PPLN waveguide is shown in Fig. 7.4, and the normalized powers and phases of the chirped input, conjugate and output pulses are shown in Fig. 7.5. The output pulse duration was again $\sim$ 6.2 ps, i.e. the same as in the previous case. Along with the previous chirped input pulse case, these two simulations confirm that the chirp elimination scheme eventually yields chirp-free pulses at the system output with similar pulse durations to the input pulses, and operates independently of the spectral phase characteristics of the input pulses.

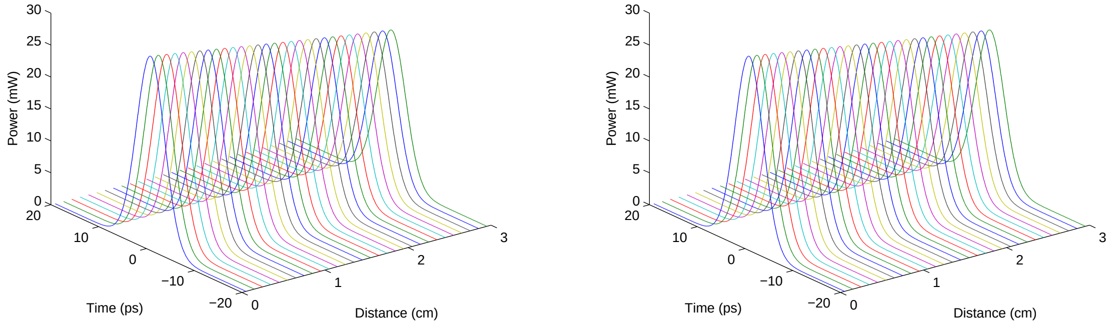

(a) Chirped input pulse (b) Conjugate pulse

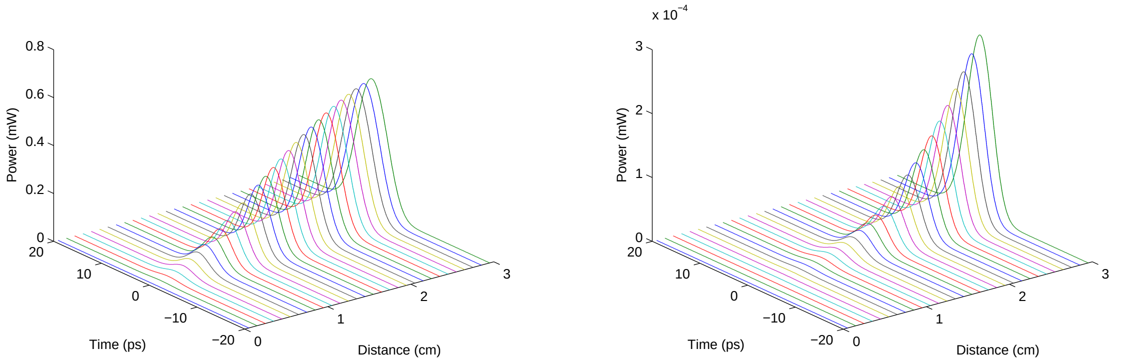

(c) SF wave (d) Output pulse

FIGURE 7.2: Propagation of the pulses along the PPLN waveguide for the 7-ps Gaussian chirped input pulses case.

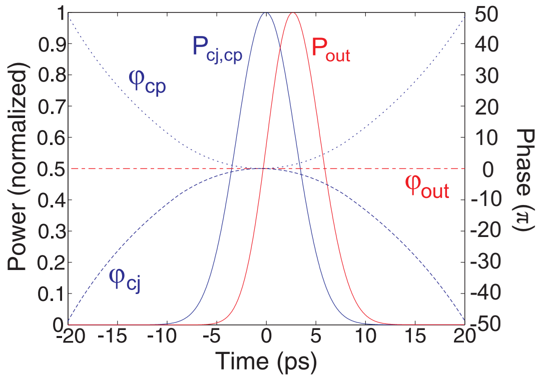

FIGURE 7.3: Normalized powers (P_{cp},P_{cj} and P_{out} denote the normalized powers of the chirped input, conjugate and output pulses respectively) and phases (φ_{cp},φ_{cj},φ_{out} denote the phases of the chirped input, conjugate and output pulses respectively) for the 7-ps Gaussian chirped input pulses case.

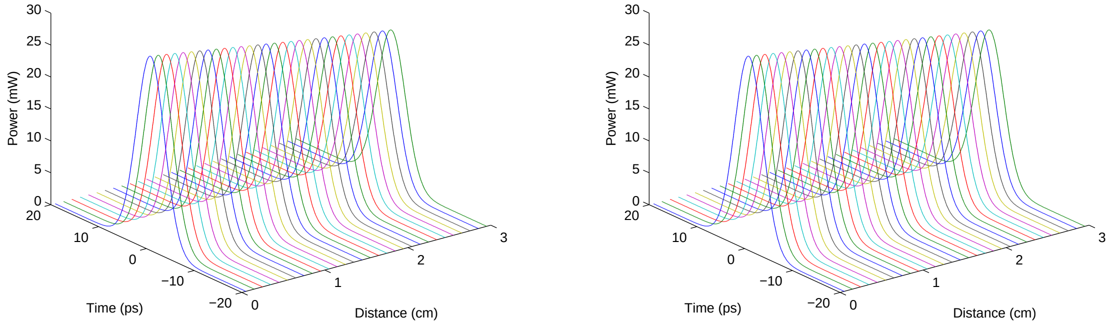

(a) Chirped input pulse (b) Conjugate pulse

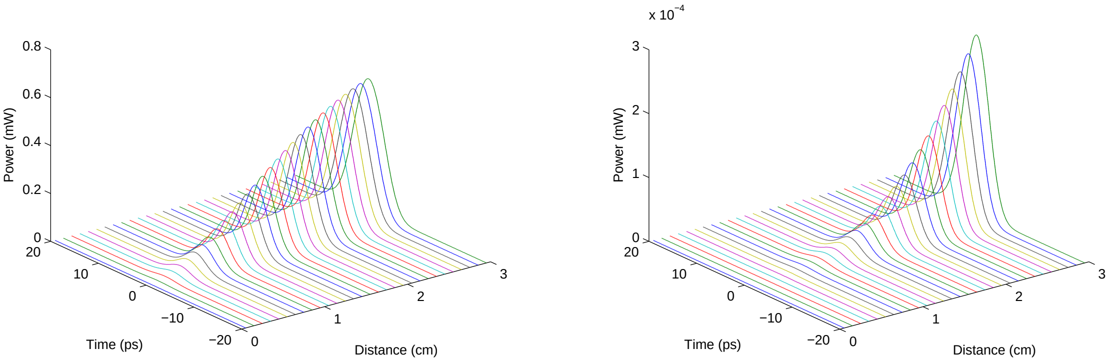

(c) SF wave (d) Output pulse

FIGURE 7.4: Propagation of the pulses along the PPLN waveguide for the 7-ps Gaussian un-chirped input pulses case.

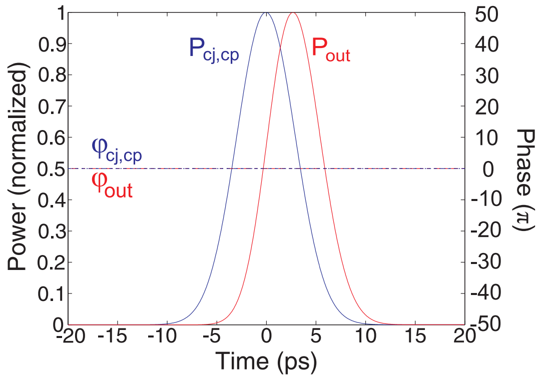

FIGURE 7.5: Normalized powers (P_{cp},P_{cj} and P_{out} denote the normalized powers of the chirped input, conjugate and output pulses respectively) and phases (φ_{cp},φ_{cj},φ_{out} denote the phases of the chirped input, conjugate and output pulses respectively) for the 7-ps Gaussian un-chirped input pulses case.

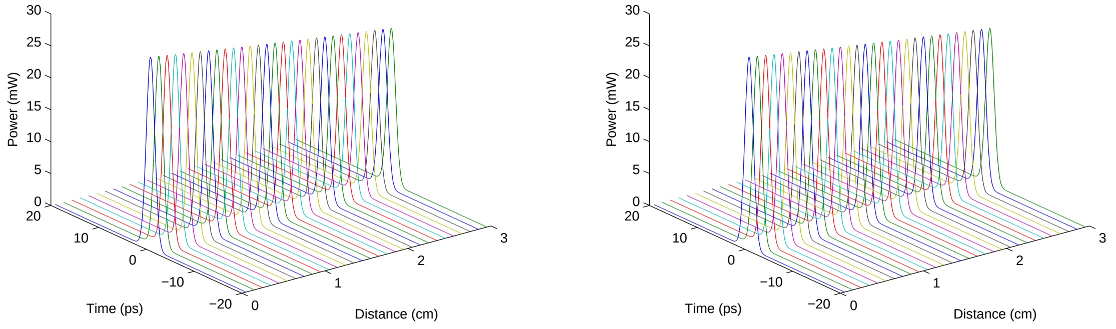

(a) Chirped input pulse

(b) Conjugate pulse

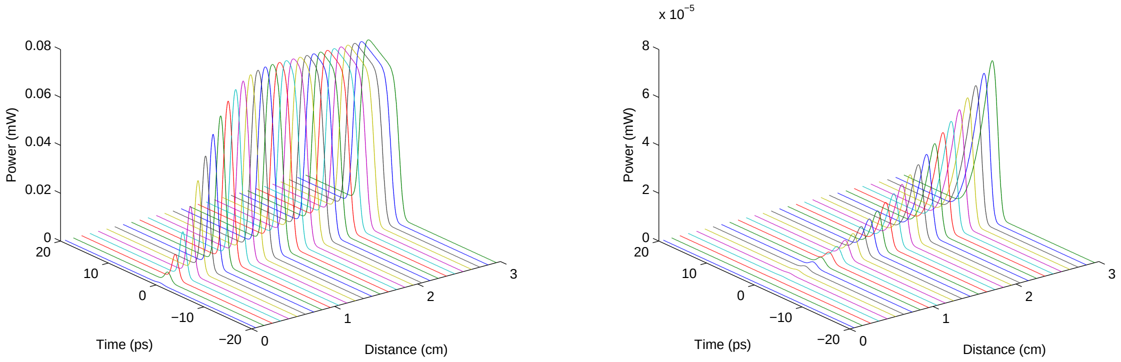

(c) SF wave

(d) Output pulse

FIGURE 7.6: Propagation of the pulses along the PPLN waveguide for the 2-ps Gaussian chirped input pulses case.

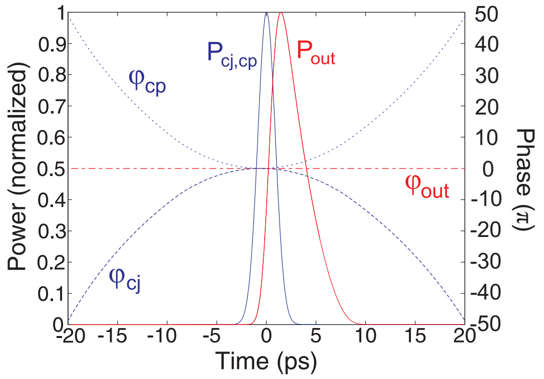

FIGURE 7.7: Normalized powers (P_{cp},P_{cj} and P_{out} denote the normalized powers of the chirped input, conjugate and output pulses respectively) and phases (φ_{cp},φ_{cj},φ_{out} denote the phases of the chirped input, conjugate and output pulses respectively) for the 2-ps Gaussian chirped input pulses case.

In the next simulation, the input signal was changed to 2-ps Gaussian chirped pulses with a chirp of 3.5 ps/nm. The propagation of the chirped input, conjugate, SF and output pulses in the PPLN waveguide is shown is Fig. 7.6, and the normalized powers and phases of the chirped input, conjugate and output pulses are shown in Fig. 7.7. The input and output pulse durations were 2 ps and ~ 3.8 ps respectively. The simulation results indicate that the presence of a significant walk-off effect yields a broadening to the pulses, but no significant chirp at the output. The variation of pulse durations due to walk-off can be analysed using a semi-analytical approach, as presented in the bandwidth comparison chapter (Chapter 3) and in Ref. [Prawiharjo 05]. The output field in the frequency domain can be expressed as the product between the PPLN filter function (which depends on the group velocity mismatch between the pumps and the SF) and the Fourier Transform of the modulus squared of the input signal $[FT\{|E_{cp}|^2\}]$. This yields a response which is insensitive to the phase of the input field and an acceptance bandwidth corresponding to SHG from an "equivalent" un-chirped pump with the same intensity distribution as the input signal (i.e., $|E_{cp}|$).

7.3 Experimental results

Figure 7.8 shows the experimental setup used to realise the chirp-free pulse generation system. Both chirped and un-chirped pulses were used at the input to investigate the performance of this system. Two 30-mm-long fibre-pigtailed PPLN waveguides (HC Photonics Corp.) as described in the background chapter were used for the cSHG/DFG and cSFG/DFG steps. Their SHG phase matching wavelength was 1546 nm at 50^{o}C and 42^{o}C, respectively. A CW laser operating at 1546.0 nm was used as the pump for the first PPLN device. A mode locked ERGO generated 10-GHz, 2-ps pulses at 1552 nm. The temporal intensity profile of the ERGO laser output measured with an OSO (EXFO PSO-100) is shown in Fig. 7.9(a) and the spectrum of the ERGO laser measured with an OSA is shown in Fig. 7.9(b). The pulse width of the ERGO laser output is ~ 2.0 ps.

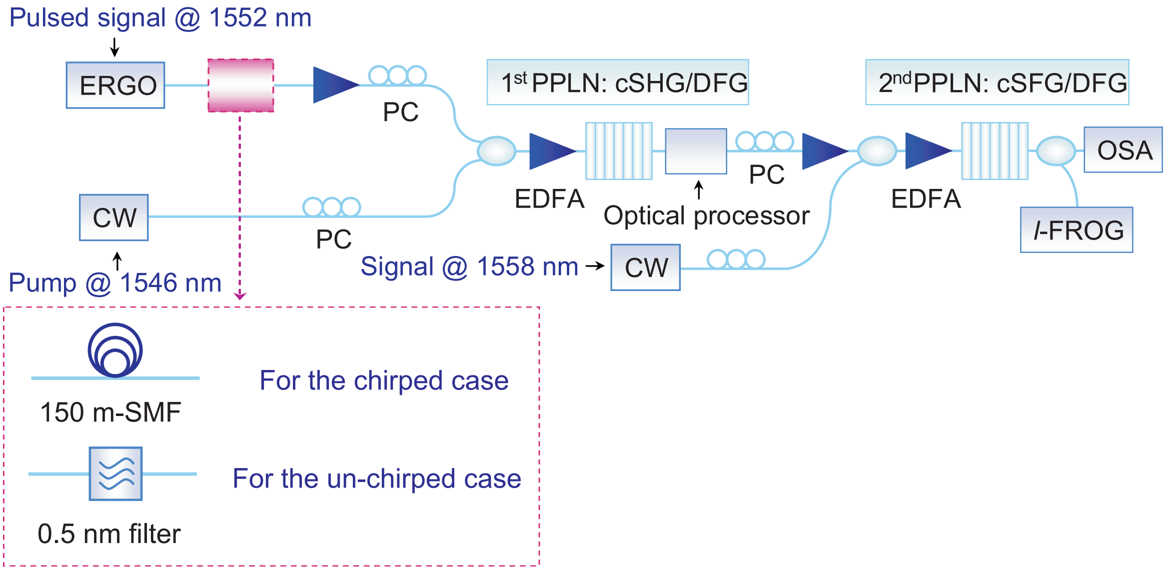

FIGURE 7.8: Experimental setup used to realise the proposed chirp-elimination scheme. PC: polarization controller, EDFA:erbium-doped fibre amplifier, TBF:tunable bandpass filter, OSO:optical sampling oscilloscope, OSA:optical spectrum analyser.

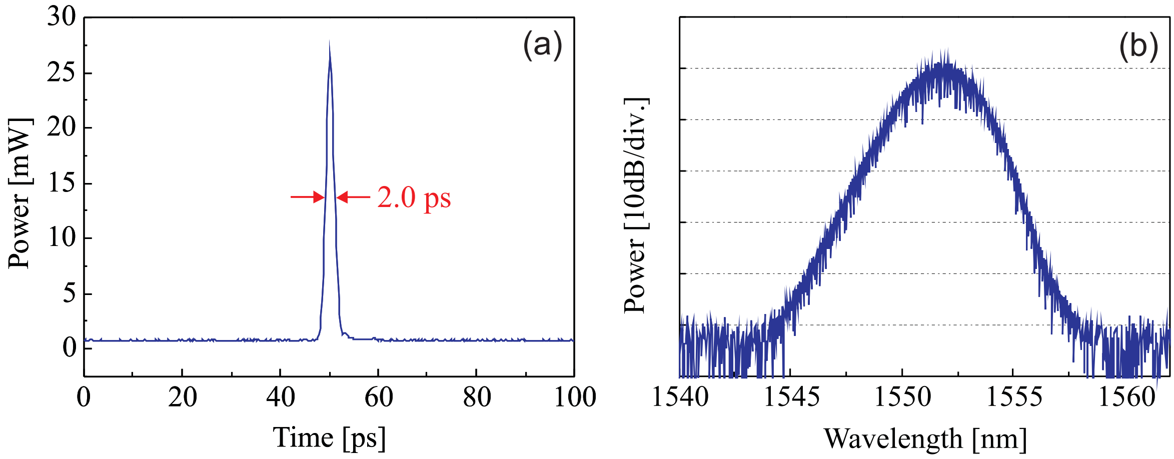

FIGURE 7.9: (a): Temporal intensity profile of the ERGO laser output measured by OSO. (b): Spectrum of the ERGO laser measured by OSA (measured with a resolution of 0.05 nm).

In the chirped input pulse case, the output of ERGO laser was launched into 150-m of a single mode fibre (SMF) to generate the input chirped pulses. The temporal intensity profile and the spectrum after the SMF are shown in Fig. 7.10. The pulse width is stretched to ∼ 6.5 ps due to the dispersion induced by the SMF. Figure 7.11 shows the FROG spectrogram and the retrieved normalized intensity and phase profiles of the

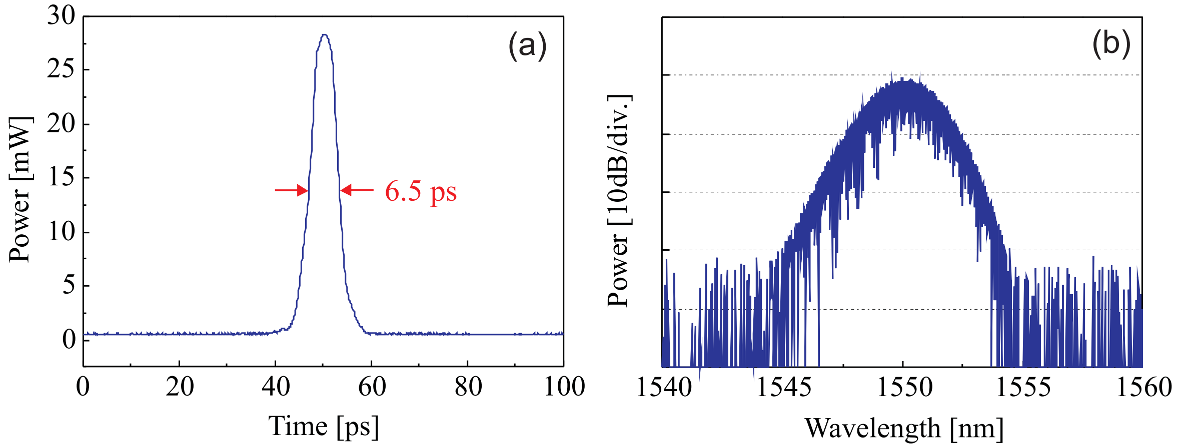

FIGURE 7.10: (a): Temporal intensity profile of the chirped input pulse measured by OSO. (b): Spectrum of the chirped input pulse measured by OSA (measured with a resolution of 0.05 nm).

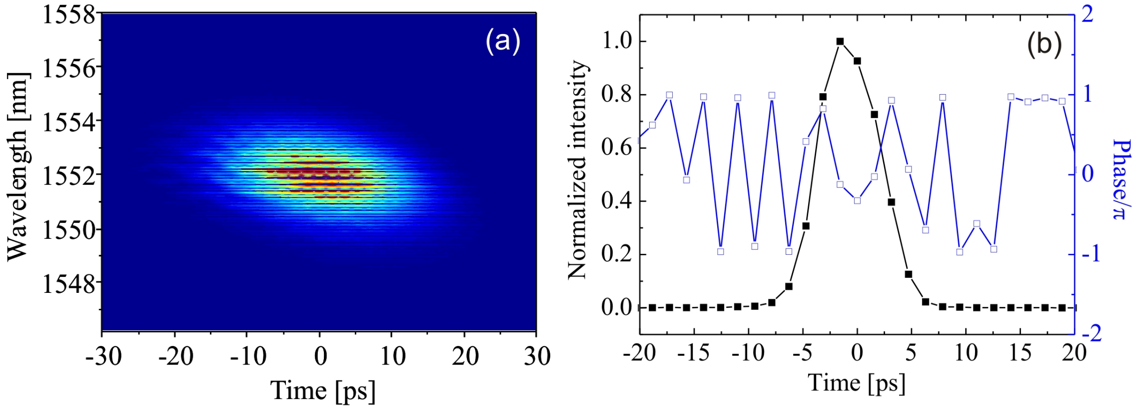

FIGURE 7.11: (a): Measured FROG spectrogram of the chirped input pulse. (b): Retrieved normalized intensity and phase profiles of the chirped input pulse.

input chirped pulses. The FROG measurement was taken using a L-FROG as introduced in the background chapter. The measured chirp of the input pulses was 3.5 ps/nm, and the phase profile of the chirped input signal $\phi(t)$ was retrieved from the spectrogram as shown in Fig. 7.11(b).

The CW pump and the chirped pulses were combined in a 3-dB coupler and then amplified before being launched into the first PPLN waveguide. The total power at the input of the waveguide was restricted to 21 dBm to protect its coupling connectors. Figure 7.12(a) shows the measured spectrum of the signals at the output of the first PPLN waveguide (pump, chirped input signal and conjugated pulse). A filter, tunable both in bandwidth

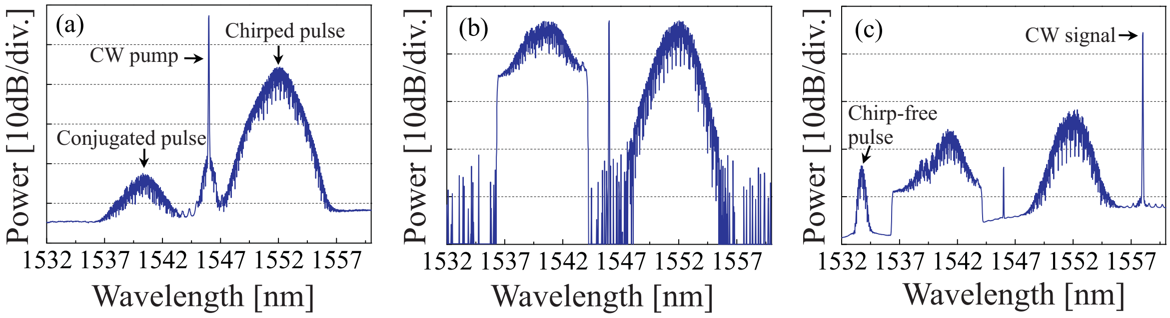

FIGURE 7.12: Spectral traces measured after (a) the first PPLN waveguide, (b) the optical processor, and (c) the second PPLN waveguide in the chirped input pulses case.

and centre wavelength (Alnair Labs.), was used after the first PPLN waveguide to extract and characterise the conjugate signal. The temporal intensity profile and the spectrum of the conjugate signal are shown in Fig. 7.13. Figure 7.14 shows the measured FROG spectrogram and the retrieved normalized intensity and phase profiles of the conjugate signal. The conjugated pulses had a pulse width of ∼ 6.8 ps which was similar to that of the chirped input pulses, while the chirp of the conjugated pulses is opposite to that of the original signal as shown in the retrieved phase profiles (Fig. 7.11(b) and Fig. 7.14(b)).

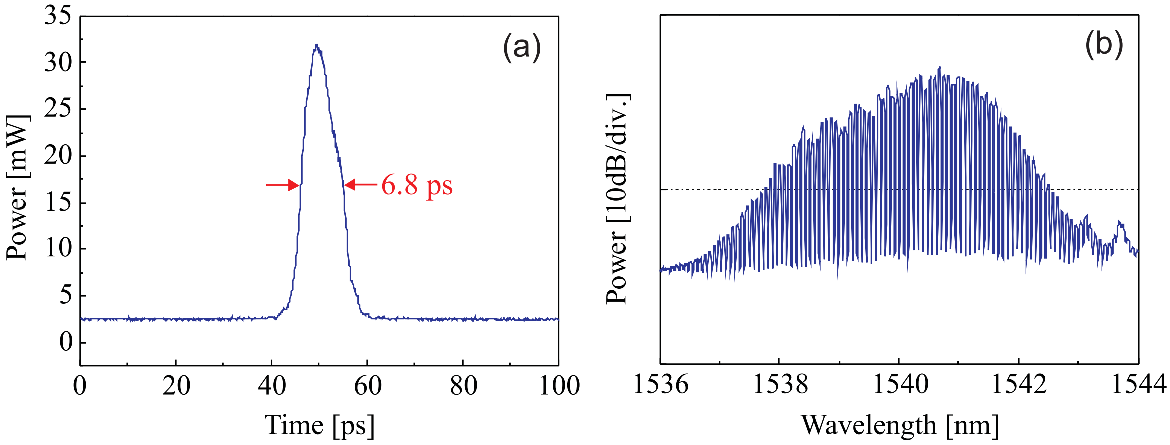

FIGURE 7.13: (a): Temporal intensity profile of the conjugated replica measured by OSO. (b): Spectrum of the conjugated replica measured by OSA (measured with a resolution of 0.05 nm).

After that, an optical processor (Finisar WaveShaper 4000E) filtered out both the pump and the SH waves, and equalised the optical power of the input chirped pulses with that of the conjugate pulses. The spectral trace measured after the optical processor is shown in Fig. 7.12(b). The two signals were then amplified and combined with a 1558-nm CW

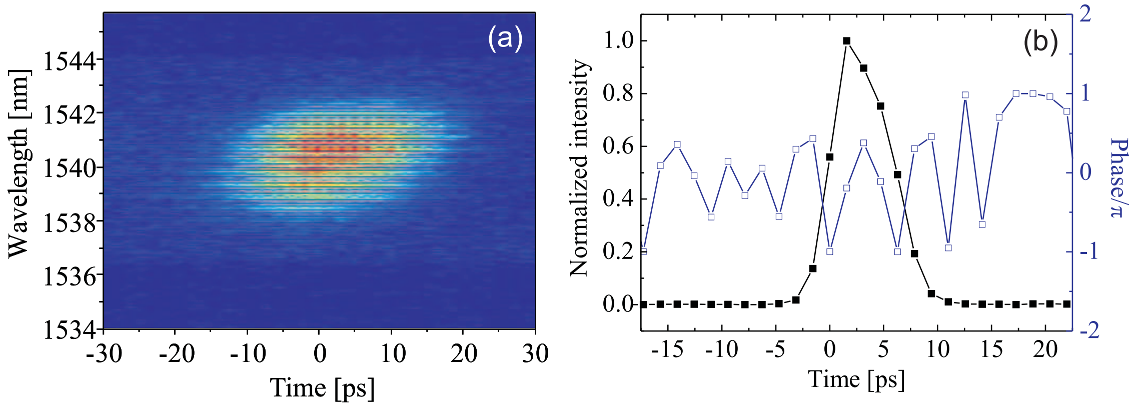

FIGURE 7.14: (a): Measured FROG spectrogram of the conjugated replica. (b): Retrieved normalized intensity and phase profiles of the conjugated replica.

beam in a second 3-dB coupler. All three waves were then amplified further to 21 dBm and launched into the second PPLN waveguide to interact with each other via cSFG/DFG as described in Fig. 7.1. The resultant spectrum, measured after the second PPLN device, is shown in Fig. 7.12(c). The measured OSNR of the cSFG/DFG output signal at 1533.7 nm was 14 dB. The previously used tunable filter (Alnair Labs.) was used again after the second PPLN waveguide to extract and characterise the output signal. The temporal traces of the output pulses measured with an OSO is shown in Fig. 7.15(a). The measured pulse width of the output pulse was ∼ 6.6 ps which was close to that of the input pulse (∼ 6.5 ps). The time-bandwidth product for the chirp-free output was 0.48, which indicates good quality, close to transform-limited pulses. Figure 7.16 shows the measured FROG spectrogram and the retrieved normalized intensity and phase profiles of the output pulse. The chirp in the output pulses has been cancelled out after the cSFG/DFG process. The measured chirp rate parameters of the output pulses was zero within the resolution limit of the FROG.

The experiment was repeated for an unchirped input. In this case, the output of ERGO laser was filtered by a 0.5-nm bandpass filter to achieve a similar input pulse duration as in the experiment above. The temporal intensity profile and the spectrum after the filter are shown in Fig. 7.17. The pulse width is broadened to ∼ 6.7 ps due to the spectral filtering. Figure 7.18 shows the FROG spectrogram and the retrieved normalized intensity and phase profiles of the un-chirped input pulses. The measured chirp of the input pulses was

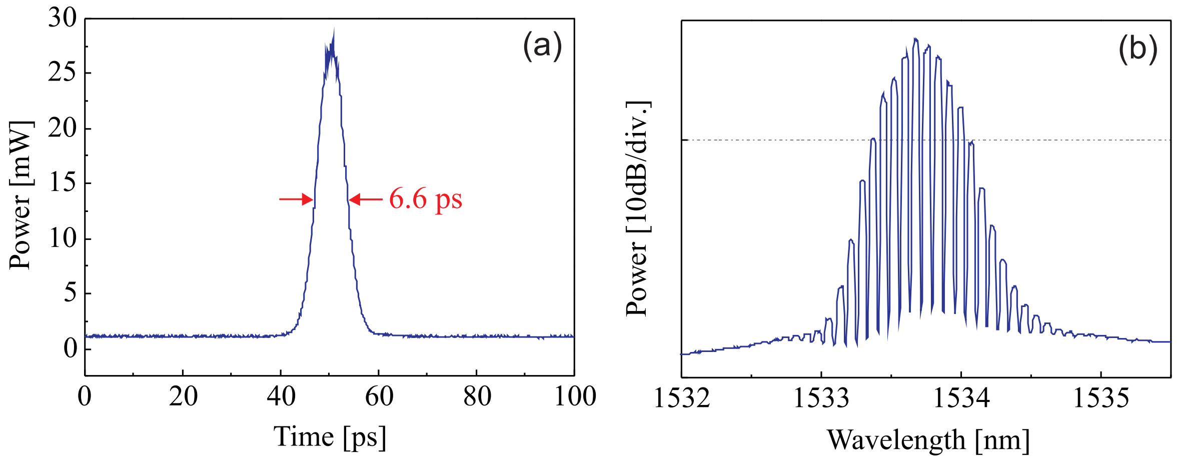

FIGURE 7.15: (a): Temporal intensity profile of the resultant chirp-free pulse measured by OSO. (b): Spectrum of the resultant chirp-free pulse measured by OSA (measured with a resolution of 0.05 nm).

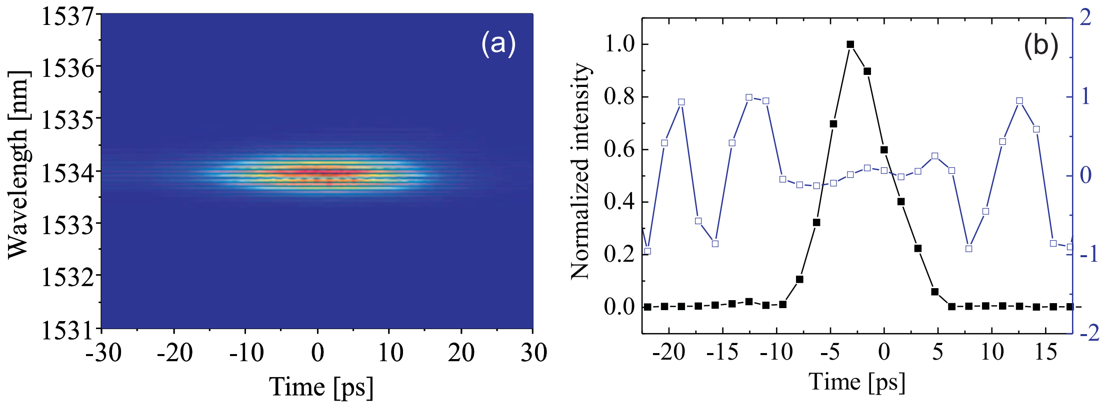

FIGURE 7.16: (a): Measured FROG spectrogram of the resultant chirp-free pulse. (b): Retrieved normalized intensity and phase profiles of the resultant chirp-free pulse.

close to zero. Subsequently, the pulses were combined with the CW pump, amplified and launched into the first PPLN waveguide. Figure 7.19(a) shows the measured spectrum of the signals at the output of the first PPLN waveguide. The temporal intensity profile and the spectrum of the conjugate signal are shown in Fig. 7.20. Figure 7.21 shows the measured FROG spectrogram and the retrieved normalized intensity and phase profiles of the conjugate signal. In this case, the conjugated pulses had a pulse width of $\sim$ 6.7 ps and a close to zero chirp.

After that, an optical processor filtered out both the pump and the SH waves, and equalised the optical power of the input chirped pulses with that of the conjugate pulses.

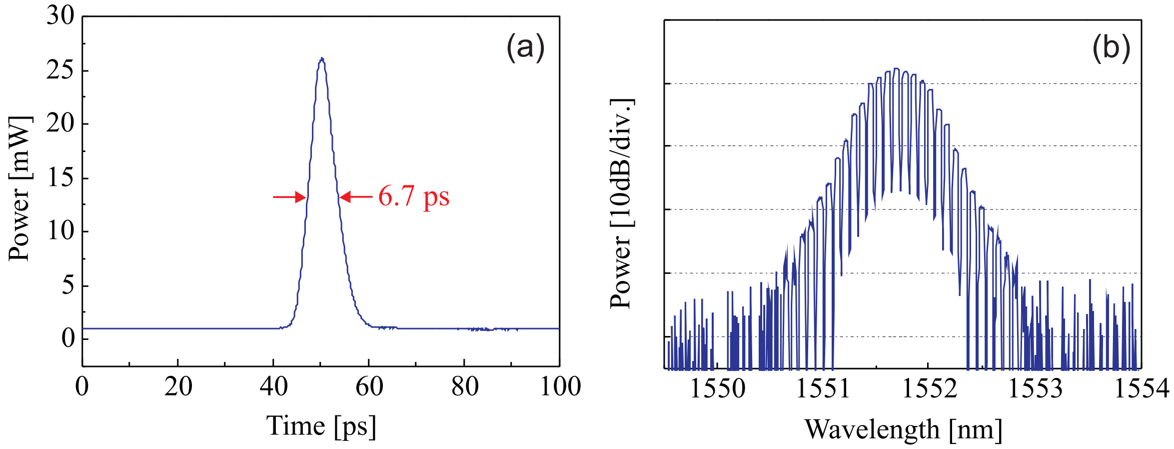

FIGURE 7.17: (a): Temporal intensity profiles of the un-chirped input pulse measured by OSO. (b): Spectrum of the un-chirped input pulse measured by OSA (measured with a resolution of 0.05 nm).

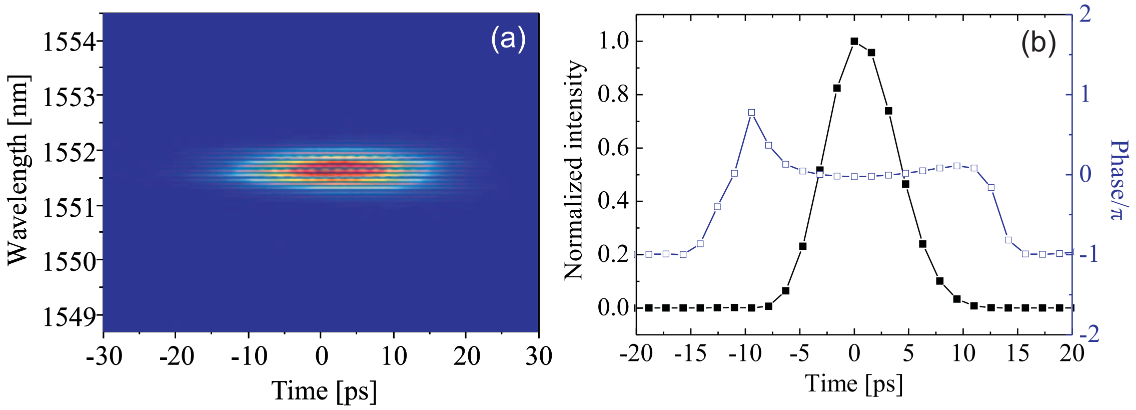

FIGURE 7.18: (a): Measured FROG spectrogram of the un-chirped input pulse. (b): Retrieved normalized intensity and phase profiles and the un-chirped input pulse.

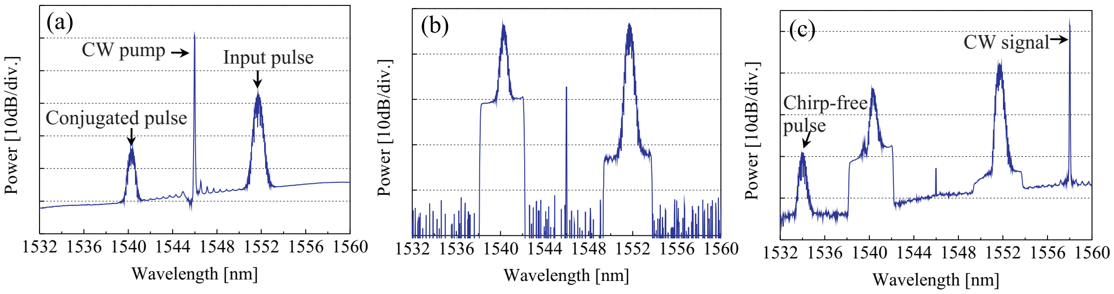

FIGURE 7.19: Spectral traces measured after (a) the first PPLN waveguide, (b) the optical processor, and (c) the second PPLN waveguide in the un-chirped input pulses case.

The spectral trace measured after the optical processor is shown in Fig. 7.19(b). The two signals were then amplified and combined with a 1558-nm CW beam in a second 3-dB coupler. All three waves were then launched into the second PPLN waveguide to interact with each other via cSFG/DFG as described in Fig. 7.1. The resultant spectrum, measured after the second PPLN device, is shown in Fig. 7.19(c). The measured OSNR of the cSFG/DFG output signal at 1533.7 nm was 15 dB. Figure 7.22 shows the temporal intensity profile and the spectrum of the output pulses, and Figure 7.23 shows the measured FROG spectrogram and the retrieved normalized intensity and phase profiles of the output pulses. As can be seen in Fig. 7.23, the measured chirp of the output pulses was zero within the resolution limit of the FROG. The measured pulse width of the output pulses was $\sim$ 6.4 ps which was close to that of the input pulse ($\sim$ 6.7 ps). The time-bandwidth product for the output pulses was 0.47. These experimental results confirmed the operational principle and the simulation results shown in Section 7.2 that input pulses emerge out of this system chirp-free and with similar temporal intensity profiles as at the input, independently of the input chirp characteristics.

For the case of launching 2-ps input pulses into 3-mm-long PPLN waveguides as modelled in Section 7.2, it is expected that the output pulses are significantly broadened and the temporal intensity profiles of the output pulses are severely distorted compared to the input pulses due to the walk-off effect. Therefore, the case of 2-ps input pulses was not demonstrated experimentally.

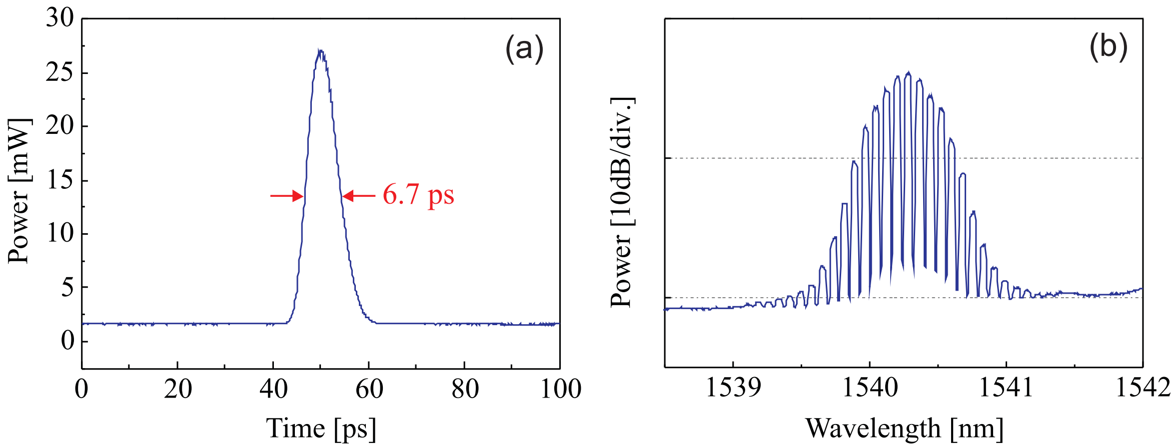

Figure 7.20: (a): Temporal intensity profile of the conjugated replica measured by OSO. (b): Spectrum of the conjugated replica measured by OSA (measured with a resolution of 0.05 nm).

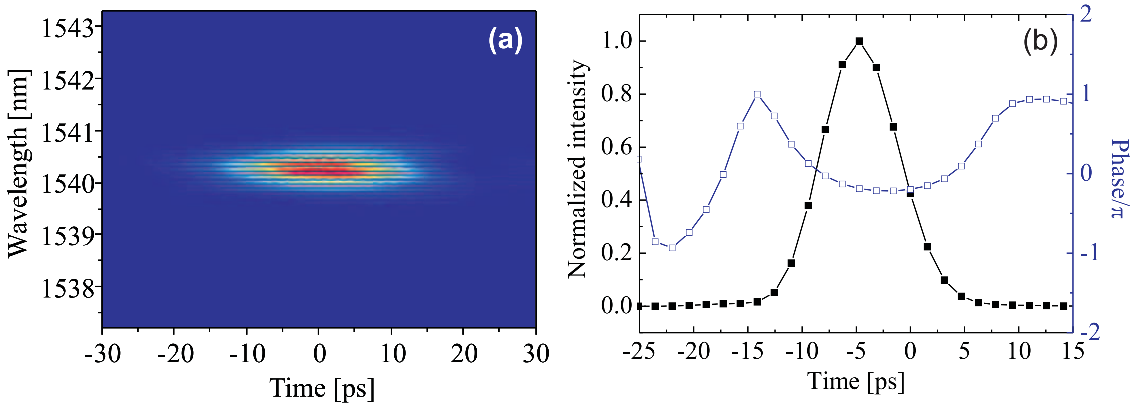

FIGURE 7.21: (a): Measured FROG spectrogram of the conjugated replica. (b): Retrieved normalized intensity and phase profiles of the conjugated replica.

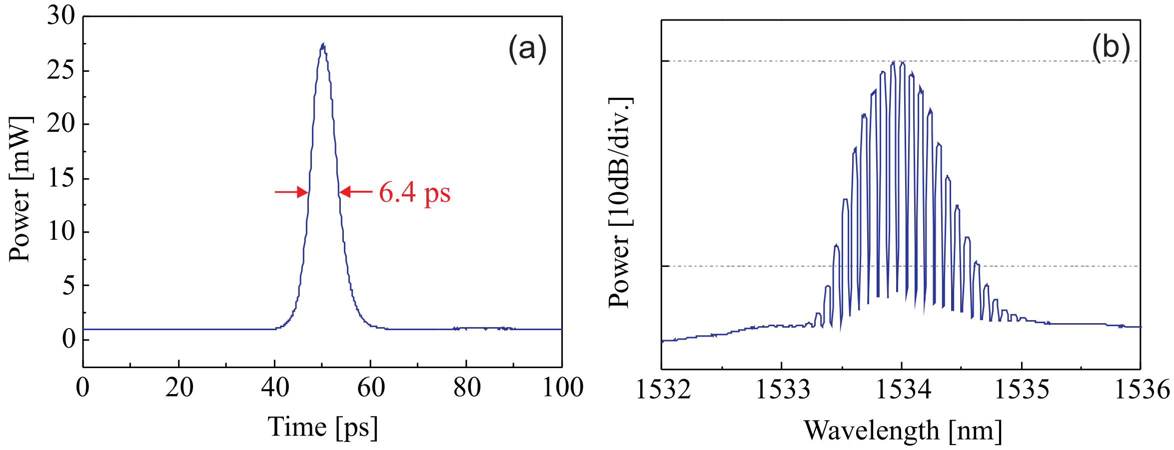

FIGURE 7.22: (a): Temporal intensity profile of the resultant output pulse measured by OSO. (b): Spectrum of the resultant output pulse measured by OSA (measured with a resolution of 0.05 nm).

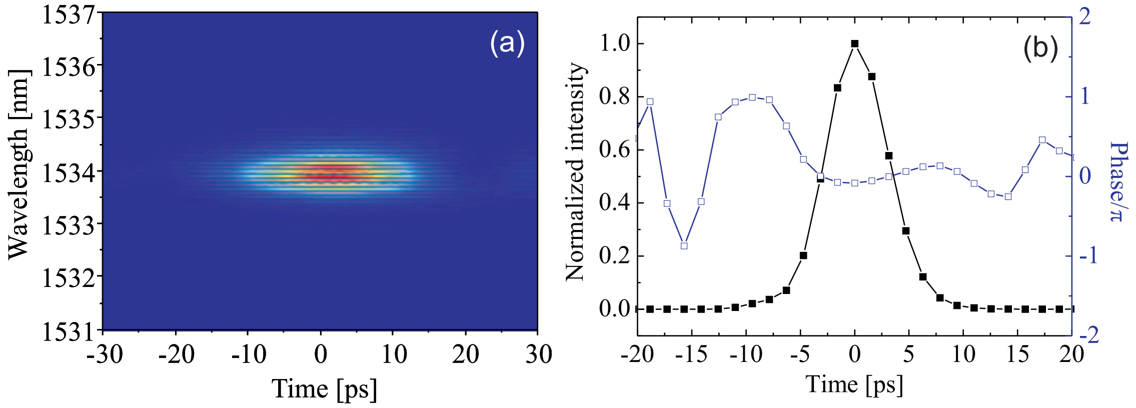

FIGURE 7.23: (a): Measured FROG spectrogram of the resultant output pulse. (b): Retrieved normalized intensity and phase profiles of the resultant output pulse.

7.4 Conclusion

In this chapter, I proposed an effective method to erase the chirp of ps-long pulses and generate chirp-free output pulses. The technique, which is based on a combination of cascaded nonlinear effects in two different PPLN waveguides, operates independently of the input chirp characteristics and requires only limited knowledge of the input pulse shape. Simulations with different input chirp profiles have been performed, all resulting in chirp-free output pulses after this chirp-elimination system. The experimental results validated the simulations and confirmed the capability of this scheme.

This chapter concludes the work I have performed on PPLN waveguides. In the following chapter, which is the last chapter reporting technical work in this thesis, I will present some work I have carried out on the generation of short pulses based on an optical frequency comb generator. As the name suggests, these sources have commonly been attractive for their spectral properties. In my work, I have focused instead on their temporal characteristics.

References

[Hill 94] K. O. Hill, S. Theriault, B. Malo, F. Bilodeau, T. Kitagawa, D. C. Johnson, J. Albert, K. Takiguchi, T. Kataoka & K. Hagimoto, *Chirped In-fiber Bragg Grating Dispersion Compensators - Linearization of Dispersion Characteristic and Demonstration of Dispersion Compensation In 100-km, 10-gbit/s Optical-fiber Link*, Electronics Letters, vol. 30, no. 21, pages 1755–1756, October 1994.

[Maher 09] R. Maher, Kai Shi, P.M. Anandarajah, A. Kaszubowska, L.P. Barry & Yonglin Yu, *Novel Frequency Chirp Compensation Scheme for Directly Modulated SG DBR Tunable Lasers*, Photonics Technology Letters, IEEE, vol. 21, no. 5, pages 340 –342, march1, 2009.

[Prawiharjo 05] J. Prawiharjo, K. Gallo, N. G. R. Broderick & D. J. Richardson, *Frequency-resolved optical gating in the 1.55 mu m band via cascaded ((2))(chi) processes*, Journal of the Optical Society of America B-optical Physics, vol. 22, no. 9, pages 1985–1993, September 2005.

[Takeda 96] N. Takeda, S. Ryu & S. Akiba, *2.5Gbit/s, 8-channel, 1056km densely spaced coherent WDM transmission experiment*, Electronics Letters, vol. 32, no. 10, pages 907–908, May 1996.

8

Conclusion and future work

8.1 Conclusion

The main aim of this thesis was to investigate the use of cascaded quadratic nonlinearities in PPLN waveguides and realise several all-optical signal processing techniques for telecom applications.

After the introduction of PPLN waveguides and five types of second-order nonlinear interactions in PPLN waveguides, namely SHG, SFG, DFG, cSHG/DFG and cSFG/DFG in Chapter 2, I reported a systematic and comparative study of the acceptance bandwidths of cSHG/DFG and cSFG/DFG in PPLN waveguides in both the CW and pulsed-pump regimes in Chapter 3. The theoretical and experimental results show that the SHG bandwidth is approximately half that of the SFG process in the CW regime, whereas the tuning bandwidths of both cSHG/DFG and cSFG/DFG processes should be similar in the pulsed pump regime.

In Chapter 4, I demonstrated a format conversion scheme of a 40 Gbit/s OTDM signal to 4 × 10 Gbit/s WDM channels based on the cSHG/DFG process in a PPLN waveguide. The technique relies on the generation of spectrally (and temporally) flat linearly chirped pulses which are then optically switched with short data pulses in the nonlinear waveguide. Error-free operation was obtained for all channels with a power penalty below 2 dB.

In Chapter 5, I demonstrated an all-optical signal retiming system based on pulse shaping and cSHG/DFG-based switching in a fully fiberised 30-mm-long PPLN waveguide. The original data pulses were shaped into flat-top pulses to avoid conversion of their timing jitter into pulse amplitude noise at the output of the waveguide. Pulse retiming was confirmed by temporal measurements, while bit-error rate measurements confirmed good noise performance for the system with a power penalty of 0.6 dB at a BER of 10^{-9}.

In Chapter 6, two novel configurations of phase sensitive amplification based on cascaded quadratic effects in PPLN waveguides were demonstrated. The first one is a frequency non-degenerate PSA based on the cSHG/DFG process within a single PPLN waveguide. Using a 3-cm-long PPLN waveguide, a maximum gain of 0.65 dB with a peak-to-peak gain variation of 3.4 dB was achieved for a 100-ps duration, 2.5 GHz pulsed signal in the experiments. The second configuration of PSA is PR-WC which is based on a combination of the cSHG/DFG process and the cSFG/DFG process within PPLN waveguides. Two implementations of this PR-WC configuration were presented, in either a single PPLN waveguide, or two separate PPLN waveguides. Peak-to-peak gain variations of 14.5 dB and 25.3 dB were achieved in the experiments for these two implementations respectively. Finally, the phase regeneration experiment showed the potential of the PR-WC scheme as a D(B)PSK phase regenerator.

In Chapter 7, I proposed and demonstrated a novel method for the elimination of arbitrary frequency chirp from short optical pulses. The technique is based on the combination of the cSHG/DFG process and the cSFG/DFG process in two individual periodically poled lithium niobate waveguides. The proposed scheme operates independently of the spectral phase characteristics of the input pulse, producing a near-transform-limited output.

Apart from my PhD project relating to PPLN waveguides, I also investigated the use of OFCGs as telecommunication sub-picosecond pulse sources in Chapter A. I theoretically analysed the working mechanism of the OFCG in both the frequency and the time domain. I experimentally investigated the intensity and phase characteristics of pulses generated from a commercial OFCG when filtered with a wavelength and bandwidth tunable filter. The experimental results agreed well with the predictions from the simulations and verified the models I set up to describe the operation of the source. I also proposed two approaches to compensate for the intrinsic chirp of pulses generated from the OFCG. A filter design that compensated for the slope of the OFC was able to yield a periodic train of identical pulses with pulse width of 1.5 ps at a 10 GHz repetition rate. Finally, by using a free-space delay line interferometer to overlap the pulse pairs generated at the output of an OFCG, a continuous, uniform and noise-free pulse train at a 20 GHz repetition rate with pulse width of ~ 0.62 ps was obtained.

8.2 Future work

Several future directions from this research work can be readily envisaged. First, if state-of-art PPLN waveguides with longer lengths and a higher tolerance to input pump power are available, the frequency non-degenerate PSA configuration relying on cSHG/DFG in PPLN waveguides, as presented in Chapter 6, could be demonstrated as a D(B)PSK phase regenerator. Furthermore, if the conversion efficiency of the PPLN waveguides is high enough allowing the PPLN devices to operate at the gain saturation regime, this frequency non-degenerate PSA configuration can even be demonstrated to regenerate both the phase and the amplitude of D(B)PSK signal. Importantly, PPLN-based PSA offers a far greater immunity to the effects of SBS of the pump beams which imposes performance limitations and adds complexity to silica fibre-based PSA devices. Eventually, the ultimate test for a regenerator like these described in this thesis would be in a transmission environment.

Another interesting direction is to implement the all-optical signal processing concepts and subsystems I developed with other nonlinear devices instead of PPLN waveguides. All-optical signal processing technologies based on quadratic nonlinearities in both silica and soft-glass poled fibres are very attractive. The benefits of poled fibres is that the device length can be tailored according to the requirements of individual applications, making for a more flexibly engineered signal processing system. Moreover, being made from fibre, these devices can be readily integrated into fibre based systems with minimal interconnection loss. The combination of poled fibre technology with soft glasses has the potential to offer devices with much higher nonlinearities than currently available in silica.

Approaches I have previously demonstrated in PPLN can be immediately extended to the poled fibre environment.

Appendix A

Optical frequency comb generator as a short-pulse source

A.1 Introduction

Outside the main scope of my PhD project relating to PPLN waveguides, I also did some works on the investigation of using optical frequency comb generators (OFCGs) as telecom sub-picosecond pulse sources. Our lab had acquired a commercial OFCG and I studied its main properties, and also investigated ways to use it as a short pulse source. My studies on the OFCG are presented in this chapter.

OFCGs, which are based on the resonant driving of a lithium niobate phase modulator placed inside a high-finesse Fabry-Perot (FP) cavity, were first proposed in 1972 [Kobayashi 72]. Starting from a CW source, an OFCG is able to generate a series of equally spaced modes that is well known as an optical frequency comb (OFC) in frequency. Nowadays, OFCGs have been developed to generate tens of THz broad OFC, and are widely used for many applications, such as accurate laser frequency measurements [Kourogi 93, Slyusarev 97] and optical coherence tomography [Kourogi 01].

OFCGs can also be treated as stable picosecond pulse sources for optical fibre communication applications due to the wide spectral span and the spectral stability of the OFCG output [Macfarlane 96, Kourogi 96, Durand 96, Kovacich 00, Kourogi 01]. A short pulse train can be viewed as the superposition of many CW phase-locked modes. In general, the two factors that determine the width of the generated laser pulses arise mainly from the limited gain bandwidth of the laser medium and the intra-cavity dispersion. In the operation of a short pulse laser, the modes outside the bandwidth of the gain medium cannot absorb energy from it, and thus the bandwidth of a short pulse usually cannot be wider than the bandwidth of the gain medium. In addition, due to the broad bandwidth of a short pulse, the dispersive effects of the modes resonating in the cavity would broaden the pulse width, which is referred to as intra-cavity dispersion. OFCGs do not suffer from the first problem, and the span of an OFC generated by an OFCG is only ultimately limited by the material dispersion of the short electro-optic crystal [Kourogi 95]. So far, OFCGs have been demonstrated to generate a few hundred femtoseconds pulses for telecommunication applications [Kourogi 01]. In addition, the pulse train generated by OFCGs can achieve wide wavelength tunability because the optical signal is external.

However, previous studies into the short pulses generated by these OFCGs have mainly focused on the spectral envelope and the temporal intensity profiles of the pulses [Kourogi 94, Macfarlane 96, Kovacich 00, Kato 05], and only a few have studied their temporal phase characteristics [Saitoh 98]. Ref. [Saitoh 98] presented the electric field of the pulses generated from an OFCG in time, but the phase profile of the generated pulses was not easily interpretable in that paper. Insufficient knowledge of the phase profile of the generated pulses limits the application of OFCGs as telecommunication pulse sources. In this chapter, I present a theoretical and experimental study of the intensity and phase properties of the pulses generated by an OFCG. Such a study will aid the use of OFCGs as short pulse sources for communication applications. In the experiment, I demonstrate that the combination of an OFCG, and a wavelength- and bandwidth-tunable spectral filter, results in a pulse source that is widely tuneable in both pulse width and central wavelength. Furthermore, two approaches are proposed to compensate for the intrinsic chirp of the OFCGs, which use either a properly designed compensating filter or a free-space delay line interferometer.

This chapter is organized as follows: In Section A.2, the operational principle of OFCGs is analysed. In Section A.3, a numerical simulation of OFCGs is presented. Section A.4 presents three studies on pulse generation based on the OFCG. In the first experiment, the spectrum of the OFCG is sliced experimentally to validate the numerical modelling. Furthermore, two approaches are used to compensate for the intrinsic chirp of the OFCGs. Section A.5 concludes the chapter.

A.2 Principle of operation

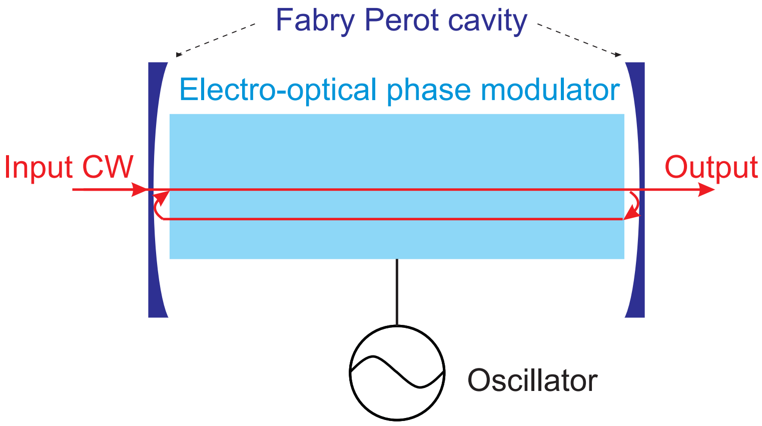

Figure A.1: Illustration of OFCGs.

As shown in Fig. A.1, an OFCG consists of an electro-optic phase modulator inside a FP cavity. The operation of an OFCG can be analysed from two different angles. One way is to view it as a FP cavity with a constant distance between the two cavity mirrors, containing the electro-optic phase modulator by which the sidebands are generated in the frequency domain, in resonance with the FP cavity. Alternatively, the OFCG can be considered as a FP cavity with a periodically varying spacing between its two cavity mirrors. This variation is due to the modulation of the refractive index of the EOM crystal. Most of the studies found in the literature to date have focused on the first approach, which analyses the operation of the OFCG in the frequency domain [Kourogi 93, Macfarlane 96, Musha 04]. The EOM's modulation frequency f_m is adjusted to an integer multiple of the free spectral range (FSR) of the Fabry-Perot cavity, so that all sidebands generated by the phase modulation are in resonance with the cavity. Thus the energy is transferred from the CW to sidebands in the OFCG. To represent this procedure mathematically, we consider a stable CW laser centred at frequency f_o is injected into the OFCG. The optical field inside the OFCG after circulating N times in the cavity can be expressed as

$$E^{(N)}(t) = \sum_k E_k^{(N)} exp[2i\pi(f_0 + kf_m)t] \tag{A.1}$$

where $E_k^{(N)}$ is the complex electric field amplitude of the k-th order sideband after N round trips in the cavity. After each circulation in the cavity, the energy transferred from the k-th to the q-th order sideband by phase modulation can be expressed as

$$E_{(q,k)}^{(N+1)} = r_1 r_2 exp(2i\phi_k) J_{k-q}(2\beta) E_k^{(N)} \tag{A.2}$$

where J_{k-q} is the $(k-q)$-th Bessel function, r_1 and r_2 are the amplitude reflectivities of mirror one and mirror two, respectively. ϕ_k is the round-trip phase shift and is induced by the dispersion in the EOM, the detuning of the modulation frequency from the FSR of the cavity and the detuning of the carrier from the cavity resonance [Kourogi 93, Kovacich 00]. Therefore, after $N+1$ round trips in the cavity, the field amplitude of the k-th order sideband can be expressed as [Kourogi 93]

$$E_k^{(N+1)} = r_1 r_2 exp(2i\phi_k) \sum_q J_{k-q}(2\beta) E_{(q,k)}^{(N)} + t_1 E_{in} \delta(k) \tag{A.3}$$

where E_{in} is the field amplitude of incident CW laser, $\delta()$ is delta function, and t_1 is the amplitude transmittance of mirror one.

Neglecting the dispersion of the EOM, the detuning of the modulation frequency and the detuning of the carrier frequency, the OFCG has a symmetric spectrum consisting of discrete spectral lines separated by f_m, with wings that decay exponentially in the frequency domain. The power of the k-th sideband P_k of the OFCG is approximately expressed as [Kourogi 93]

$$P_k = \eta_{FP}(\frac{\pi}{2\beta F})^2 exp(-\frac{|k|\pi}{\beta F}) P_{in} \tag{A.4}$$

where η_{FP} is the efficiency of the Fabry-Perot cavity, β is the single pass modulation index, F is the finesse of the optical cavity and P_{in} is the input laser power. On one half of the spectrum, all spectral lines have 0 spectral phase, while on the other half, the spectral lines have alternating 0 and π spectral phases. Each of those halves generates a pulse train with repetition rate f_m, such that the complete spectrum gives two pulses for each time period $T_m = 1/f_m$, separated by a half-period from each other. However, the adjacent pulses generated by different halves of spectrum have opposite chirps [Jiang 07]. From Fourier Transform theory, we find that each half of the exponentially decaying spectrum generates a pulse with a root squared Lorentzian shape in the electric field, and the phase of the pulse has a *arctan* shape. The electric field of the pulses $E_{out}(t)$ can be expressed as

$$E_{out} \propto \begin{cases} \frac{\sqrt{\eta_{FP}P_{in}}}{1-i4\beta F f_m(t-mT_m)}, & 2\pi f_m t \approx 2m\pi \\ \frac{\sqrt{\eta_{FP}P_{in}}}{1+i4\beta F f_m(t-(m+\frac{1}{2})T_m)}, & 2\pi f_m t \approx (2m+1)\pi \end{cases} \tag{A.5}$$

$$E_{out} \propto \begin{cases} \frac{\sqrt{\eta_{FP}P_{in}}}{\sqrt{1+16\beta^2F^2f_m^2(t-mT_m)^2}} exp(i\arctan^{-1}(4\beta F f_m(t-mT_m))), \\ \qquad 2\pi f_m t \approx 2m\pi \\ \frac{\sqrt{\eta_{FP}P_{in}}}{\sqrt{1+16\beta^2F^2f_m^2(t-(m+\frac{1}{2})T_m)^2}} exp(-i\arctan^{-1}(4\beta F f_m(t-(m+\frac{1}{2})T_m))), \\ \qquad 2\pi f_m t \approx (2m+1)\pi \end{cases} \tag{A.6}$$

where t is the time. The expression of $E_{out}(t)$ consists of two parts, each of which describes a pulse originating from either half of the spectrum. Furthermore, the phase terms of each part can be seen to be time reversed, highlighting that they originate from and depend directly on the decay rate of the OFC spectrum or equivalently, its slope on a logarithmic scale.

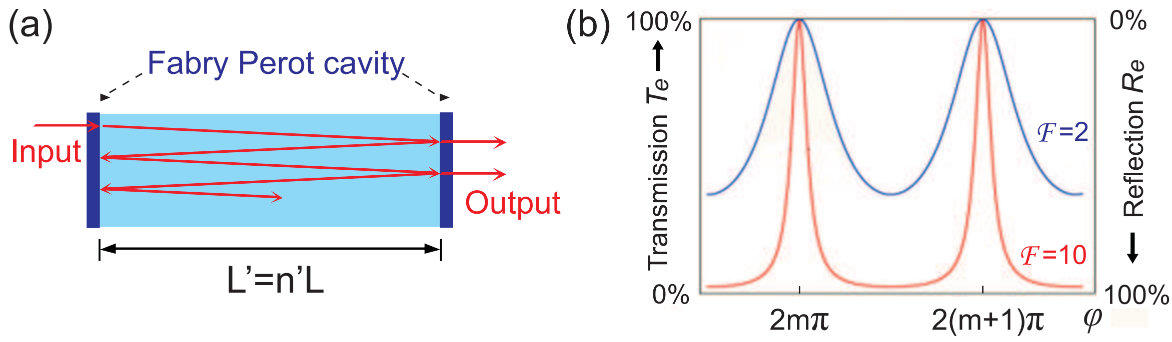

FIGURE A.2: (a): Illustration of a FP cavity. (b): Transmission function of FP cavity.

The operation of the OFCG can also be analysed in the time domain. This analysis is presented below and constitutes an original contribution of my work. As shown in Fig. A.2(a), the OFCG is considered as a FP cavity with a periodically varying cavity spacing, as determined by the phase modulation on the EOM. Neglecting the material dispersion of the electro-optic crystal, the output electrical field of the electro-optic phase modulator is given by

$$\begin{aligned} E(t) &= Acos[\omega t - \frac{\omega}{c}(n_0 - \frac{1}{2}n_0^3 r_{63} E_m \sin(2\pi f_m t))L] \\ &= A\cos[\omega t - \frac{\omega n_0 L}{c} + \beta \sin(2\pi f_m t)] \end{aligned} \tag{A.7}$$

where n_0 is the refractive index of the LiNbO$_3$ crystal, $\beta = \omega n_0^3 r_{63} E_m L/2c$ is the modulation index, E_m is the amplitude of the electric field of the modulation signal, L is the distance between the two mirrors of the FP cavity, and r_{63} is the electro-optic effect coefficient of the LiNbO$_3$ crystal [Volk 08]. $\omega n_0 L/c$ is set to be a multiple of 2π. The equivalent refractive index which takes into account the effect of the modulation can be expressed as $n' = n_0 - \Delta n' = n_0 - n_0^3 r_{63} E_m \sin(2\pi f_m t)/2$, and the equivalent length of the FP cavity is $L' = n'L$. The phase difference between the beam which is transmitted through the FP cavity and the beam which is circulated once through the FP cavity can be expressed as $\varphi = 2kL' = 2kn'L$. It is convenient to express the temporal variation of φ as $\delta = 2k\Delta n' L = 2\beta \sin(2\pi f_m t)$. Following basic expressions that can be applied to FP cavities, the amplitude of the transmitted beam A_T and the transmission function T_e can be written as

$$\begin{aligned} A_T &= T\sum_{m=0}^{\infty} R^m e^{im\delta} = \frac{T}{1 - Re^{i\delta}} \\ &= \frac{T}{1 - R + 2R\sin^2\frac{\delta}{2} - 2iR\sin\frac{\delta}{2}\cos\frac{\delta}{2}} \\ &\approx \frac{T}{1 - R - 2iR\sin\frac{\delta}{2}} \propto \frac{T}{1 - i\frac{2F}{\pi}\sin\frac{\delta}{2}} \end{aligned} \tag{A.8}$$

where $R = r_1 r_2$, $T = 1 - R$ and $F \approx \frac{\pi R^{1/2}}{1-R} \approx \frac{\pi R}{1-R}$ is the finesse of the cavity. The transmission function is given by

$$T_e = A_T A_T^* \propto \frac{T^2}{1 + \frac{4R}{(1-R)^2}\sin^2(\frac{\delta}{2})} \tag{A.9}$$

The periodic variation of the equivalent length of the FP cavity makes the peaks of the transmission function sweep periodically across the incident CW laser frequency f_0. If we assume that the modulation index is within the range $0 < \beta \leq \pi$, then only one of the peaks of the transmission function sweeps across the incident CW laser frequency twice in each modulation period T_m, generating two pulses in each modulation period in the time domain. For large values of R ($> 98\%$) and F, the peaks of the transmission function become sharp, as shown in Fig. A.2(b). Hence, the transmission function plays an important role in determining the intensity and chirp profiles of the output pulse train, only when the sharp peak of the transmission function sweeps across the incident CW laser at frequency f_0. At that instance, the value of phase difference variation δ can be approximated by $\delta = 2\beta \sin 2\pi f_m t \approx 4\pi\beta f_m t$. Thus the incident laser is almost linearly swept by the sharp peak of the transmission function, and the intensity profile of the waveform at the output of the FP cavity has the same shape as the transmission function of the cavity. Following from Eq. A.8 and A.9, A_T and T_e can be approximated by the following expressions:

$$A_T \propto \frac{T}{1 - i\frac{2F}{\pi}\sin\frac{\delta}{2}} = \begin{cases} = \frac{T}{1 - i4\beta F f_m (t - mT_m)}, & 2\pi f_m t \approx 2m\pi \\ = \frac{T}{1 + i4\beta F f_m (t - (m + \frac{1}{2})T_m)}, & 2\pi f_m t \approx (2m+1)\pi \end{cases} \tag{A.10}$$

$$T_e = \frac{T^2}{1 + \frac{4R}{(1-R)^2}\sin^2(\frac{\delta}{2})} \propto \frac{T^2}{t^2 + (\frac{1}{4\beta F f_m})^2} \tag{A.11}$$

As shown in the above expressions, the transmission function of the FP cavity has a Lorentzian shape, so the pulse generated by an OFCG also has a Lorentzian shape. In addition, the adjacent pulses in each time period have opposing chirps. Finally, the output electric field can be expressed as

$$E_{out}(t) \propto \begin{cases} \sqrt{T_e(t) P_{in}} exp(i\angle A_T) \propto \frac{T\sqrt{P_{in}}}{1 - i4\beta F f_m (t - mT_m)}, 2\pi f_m t \approx 2m\pi \\ \sqrt{T_e(t) P_{in}} exp(i\angle A_T) \propto \frac{T\sqrt{P_{in}}}{1 + i4\beta F f_m (t - (m + \frac{1}{2})T_m)}, 2\pi f_m t \approx (2m+1)\pi \end{cases} \tag{A.12}$$

This conclusion matches the derivation result of the first model that analysed the OFCG in the frequency domain. The numerical implementation of these two models is presented in the following section.

A.3 Numerical simulation

In the following simulation, the OFC spectrum will first be generated based on the frequency domain analysis in the previous section. CW laser light was injected continuously into the OFCG at wavelength 1560 nm, defining the central wavelength of the comb. After each circulation in the cavity, energy is transferred from the central spectral line to other sidebands by means of the coupling equation A.3. The spectral profile of the sidebands reach a steady state after a number of circulations in the cavity. The full spectrum of the OFCG generated from the simulation is shown in Fig. A.3(b) and is in good agreement with that measured using an OSA and shown in Fig. A.3(a).

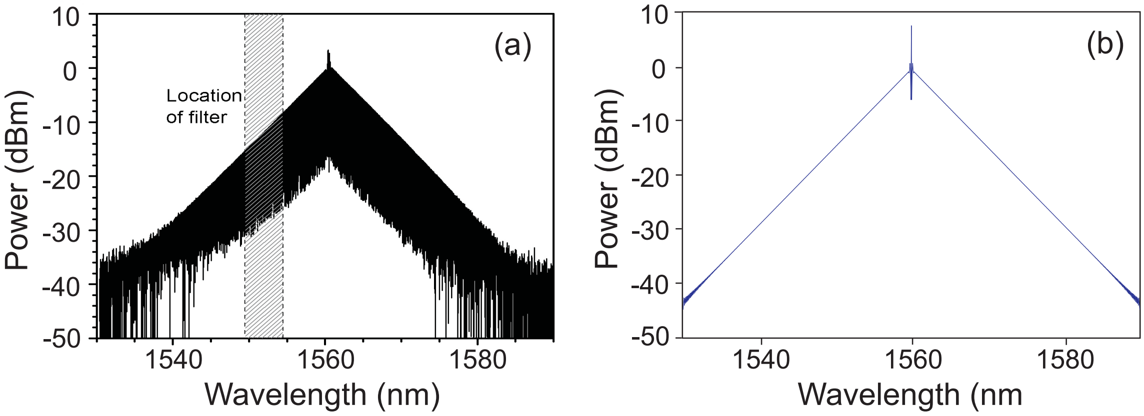

Figure A.3: (a): The full unamplified spectrum of the OFCG measured on an optical spectrum analyser. (b): The full spectrum of the OFCG generated from the simulation in the frequency domain

Following the time domain analysis in the previous section, the OFC can also be generated in the time domain. CW light at wavelength 1560 nm was once again injected into a FP cavity with a periodically varying spacing between its two cavity mirrors. The output is the sum of the transmitted waves at different times of round trips in the FP cavity. The phase profile associated with the Fabry-Perot cavity is applied on the output light, and this gives a time-varying phase shift. The intensity and chirp profile of the pulses obtained from this model are depicted as the blue traces in Fig. A.4(a) and (b). The adjacent pulses in each time period have opposing chirps. The intensity profile of the pulses generated by each half of the simulated spectrum has a Lorentzian shape, because each half of the spectrum generates a pulse with root squared Lorentzian shape in the electric field, as shown in Eq. A.12. As shown in Fig. A.4, the time domain modelling curves (blue traces) match the frequency domain modelling curves (red traces) which were obtained through inverse Fourier transformation of the spectrum generated in frequency. Therefore, these two modellings were consistent with each other. By avoiding the use of the computation consuming mode-coupling equation (Eq. A.3), the computation speed of the modelling in the time domain is faster than the modelling in the frequency domain.

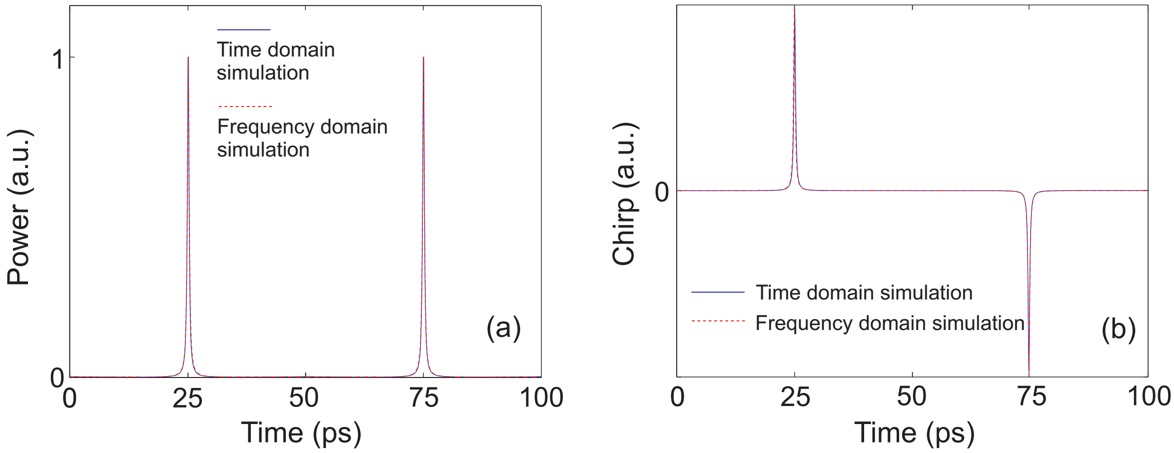

FIGURE A.4: (a): Intensity profile of the pulse generated by an OFCG in one time period from simulations in the time domain (blue trace) and in the frequency domain (red trace). (b): Chirp profile of the pulse generated by an OFCG in one time period from the simulations in the time domain (blue trace) and in the frequency domain (red trace).

A.4 Experiments

A.4.1 Characterisation of the OFCG output

In this section, the output of an OFCG was experimentally characterised. A commercially available OFCG from Optical Comb Inc. (model LP-5011), operating at 10 GHz and fed with an external CW laser at 1556.5 nm, was used. Fig. A.5 shows the full spectrum of the OFC measured using an OSA ,which exhibits stable 10 GHz spectral lines, with an exponentially decaying envelope. Fig. A.6 shows the spectrogram of the OFCG, obtained using an EOM-based L-FROG set-up as introduced in the background chapter (Chapter 2). As shown in Fig. A.6, the spectrogram of the OFCG output clearly shows the pair of time-offset pulses that comprise the OFC waveform.

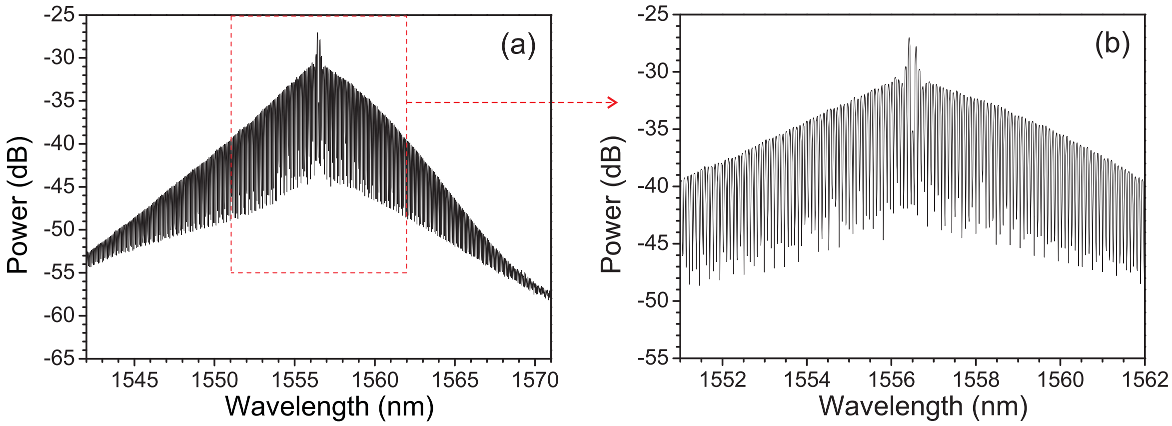

FIGURE A.5: (a): Measured full spectrum of the OFCG on OSA (resolution = 0.05nm). (b): Enlarged spectrum.

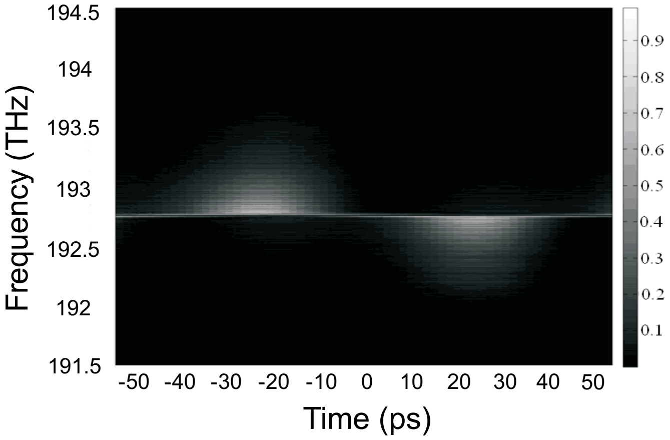

FIGURE A.6: Spectrogram measured at the output of the OFCG.

As shown in Fig. A.7(a) and (b), an autocorrelation measurement of the pulses at the output of the OFCG results in a pulse width estimation of ~ 0.84 ps (assuming a Lorentzian pulse, the pulse width is half of the autocorrelation width for a Lorentzian pulse shape), which is wider than expected for the broad bandwidth and spectral shape of the source (0.40 ps). This is due to the dispersion of the lithium niobate crystal within the OFCG cavity, as well as some dispersion given by the SMF fibres between the OFCG output and the autocorrelator. In the autocorrelation trace of the pulses at the output of the OFCG as shown in Fig. A.7(a), the three peaks are $\sim$ 50 ps apart from each other, which represents that although driven by a 10 GHz RF signal, the output signal has a 20 GHz repetition rate, because there are two pulses in each time period. The most important feature is that the three peaks of the autocorrelation trace do not have the same intensity, even though the measurement is made on a continuous pulse train. This can be understood if one considers that the pulse pairs have opposite chirps and develop mirror symmetric shapes under the influence of dispersion. The DCA trace of the pulse train at the output of the OFCG measured with a fast photoreceiver is shown in Fig. A.7(c).

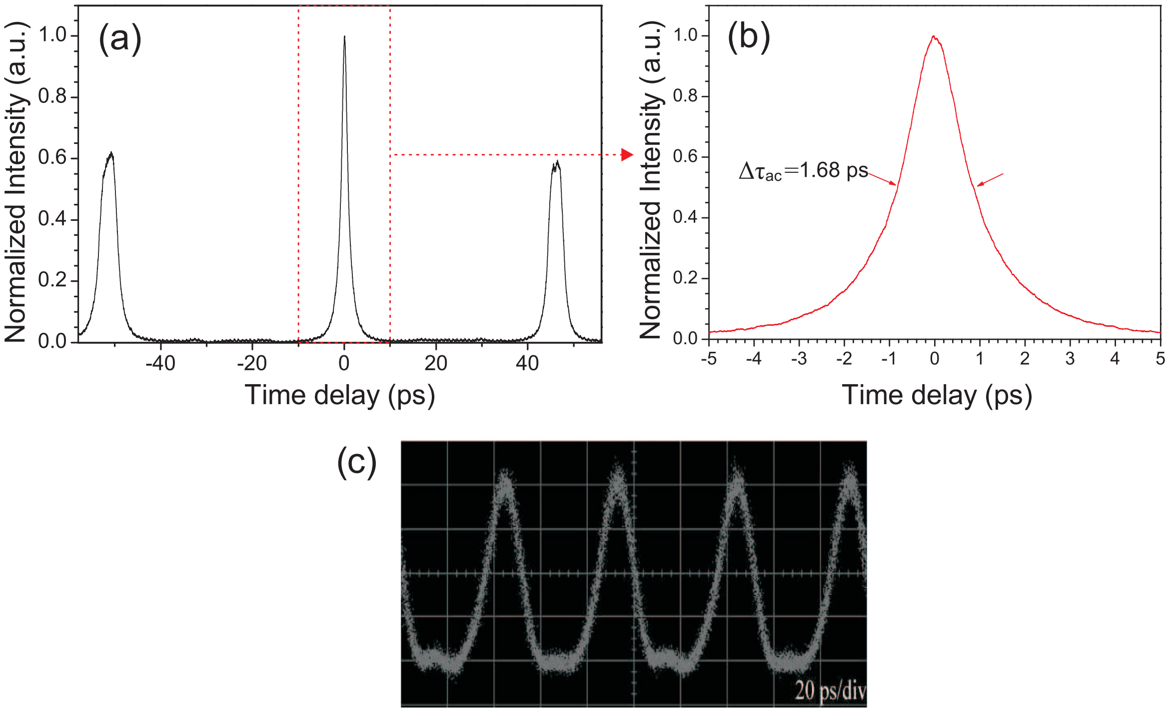

FIGURE A.7: (a): Autocorrelation trace of the OFCG. (b): Enlarged autocorrelation trace. (c): DCA trace of the OFCG.

A.4.2 Slicing the spectrum of the OFCG

In order to verify the numerical modelling presented in Section A.3, the intensity and phase characteristics of the pulses generated by spectral slicing of the OFC were experimentally investigated. The experimental setup is shown in Fig. A.8. I investigated the

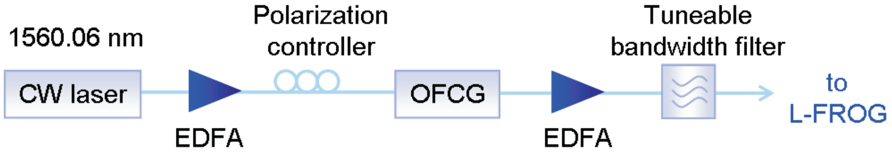

Figure A.8: Experimental setup for slicing the spectrum of the OFCG.

dependence of the output pulse characteristics on the bandwidth of the spectral slice by passing the OFC through different filter bandwidths. Due to the relatively high loss of the OFCG (29.9 dB), both the CW seed and the OFCG output were amplified with EDFAs. The filter used in the experiments was a Santec flat-top bandwidth-tunable filter (OTF-950) which could be continuously and independently tuned in bandwidth and wavelength across the C-band. The dotted lines in Fig. A.3(a) denote the location of the filter in the experiments (centred around 1552 nm). The wavelengths of the CW laser and the filter were chosen such that the part to be filtered experienced a flat gain across its bandwidth as it passed through the EDFA, and the shape of the OFC spectrum was preserved. Pulses were measured with filter bandwidths from 0.5 nm to 5 nm on the short wavelength side of the OFC spectrum allowing to pick out one component of the pulse pair. I analysed the filtered output on the L-FROG measurement setup, and the measured pulses are shown along with simulations in Fig. A.9, A.10 and A.11. In the simulation, the pulses were generated in the frequency domain, as introduced in Sec. A.3. Figure A.9(a), A.10(a) and A.11(a) show the output pulses resulting from 0.5 nm, 3 nm, and 5 nm filter bandwidths respectively. Both the measured pulse intensity and phase profiles (dots) can be seen to match very well with the theory (lines). Their corresponding spectra are shown in the figures to the right. The filtered pulses can be seen to be of high quality and very short, with pulse widths of 10.5 ps, 2.3 ps and 1.6 ps respectively. Note that the linear chirp observed on the pulses is mainly due to the dispersion of the fibre ($\sim$ 60 m of a SMF) between the OFCG output and the L-FROG which has been accounted for in the simulations, rather than intrinsic chirp originated from the slope of the OFC. The intrinsic chirp originated from the slope of the OFC is actually very small ($<$ 100 GHz across the full pulse-width in all cases examined). Side ringing can be observed on the pulses and which is due to the super-Gaussian shape of the tunable filter. Indeed, it is observed that the ringing is reduced for the case of the 0.5 nm filter which has a more rounded spectrum.

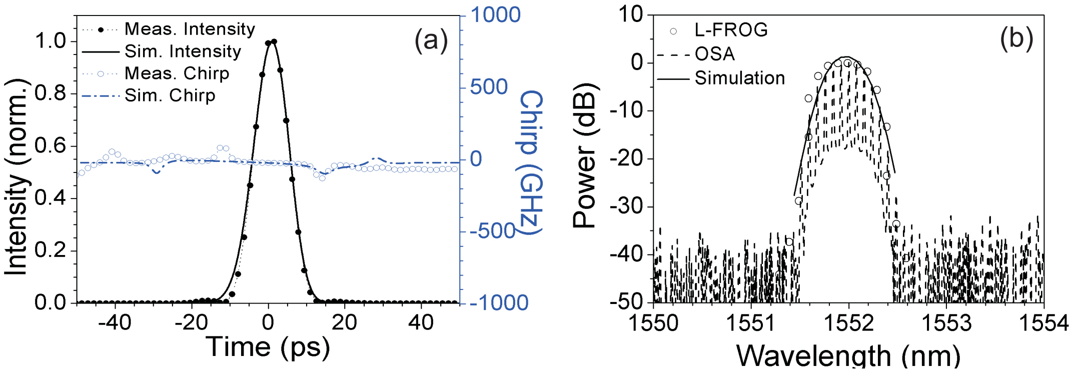

FIGURE A.9: (a): Filtered output pulse profiles for bandwidths of 0.5 nm. (b): Corresponding spectrum for bandwidths of 0.5 nm.

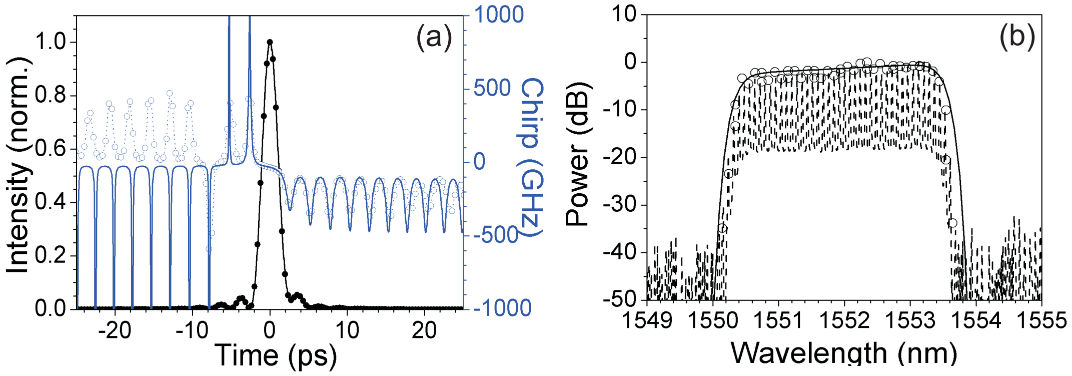

FIGURE A.10: (a): Filtered output pulse profiles for bandwidths of 3 nm. (b): Corresponding spectrum for bandwidths of 3 nm.

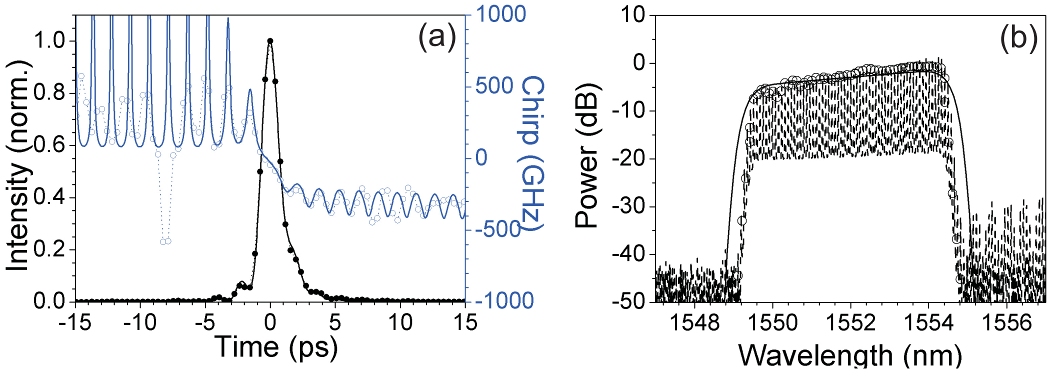

FIGURE A.11: (a): Filtered output pulse profiles for bandwidths of 5 nm. (b): Corresponding spectrum for bandwidths of 5 nm.

A.4.3 Chirp compensation with a compensating filter

OFCGs are attractive for several applications that require a stable array of spectral lines spanning a wide range of frequencies. However, despite their broad bandwidth, the use of OFCGs as pulse sources remains relatively unexplored. A major reason for this is that the comb generation mechanism results in the emission of two pulses of opposing chirp for each cavity modulation cycle, as shown in the previous section. One pulse accounts for the blue-shifted frequency components in the spectrum, and the other accounts for the red-shifted frequency components [Jiang 07, Ng 08]. This unusual temporal/spectral structure limits the application of such sources since a perfectly periodic train of identical pulses is generally preferred for most applications, including telecommunications.

In order to avoid this limitation, it is possible to design an (amplitude-only) filter to slice only half of the full spectrum to generate a periodic train of identical pulses and correct for the spectral slope which gives rise to the chirp (see Eq. A.5). A filter with controllable amplitude response relying on either SSFBG technologies or LCoS technology (optical processor), as introduced in the background chapter (Chapter 2) and employed in the previous chapters of the thesis, can be used to implement such filtering. The passband of the designed filter should not exceed the half-bandwidth of the OFC and should be sufficiently wide in order to make full use of the power. In addition, the shape of the filter's passband should be specially designed to suppress the side lobes of the pulses in the time domain. The shape of a potential compensating filter is shown in Fig. A.12(a). The filter design incorporates a *sech*^{2} profile, skewed with an opposite slope to that of the OFC, and apodized with a 5 nm 6th-order super-Gaussian spectral envelope. The resulting filtered spectrum and calculated pulse profile are shown in Fig. A.12(a) and (b) respectively. The 1.5 ps pulse is seen to be chirp free and have a smooth profile with no evidence of side lobes down to the -30 dB level. It is interesting to note that the strictly flat chirp profile of the pulse originates purely from the amplitude shaping of the spectrum. It is noted that a programmable wave shaper filter was not available at the time, and the special SSFBG required for this operation was eventually not fabricated. Therefore experimental results are not available for this short study.

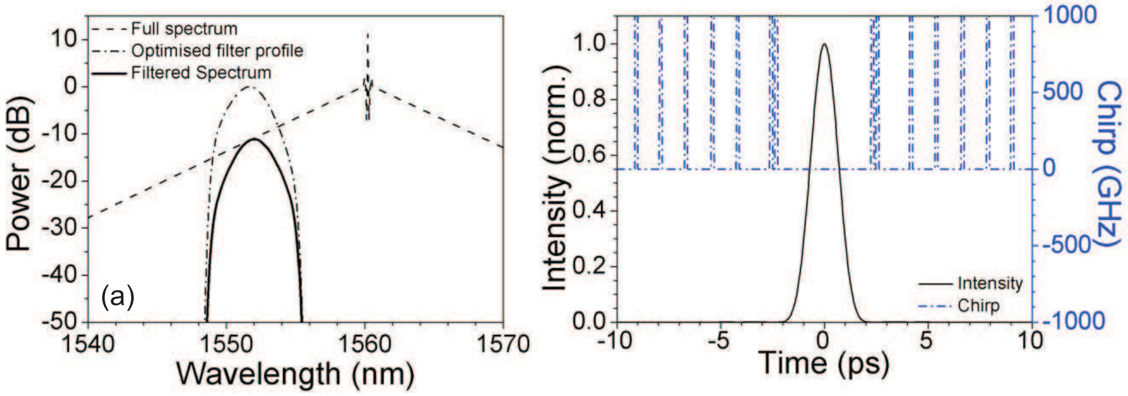

FIGURE A.12: (a): Spectral profile of a filter that provides apodised pulses, and the corresponding filtered output. (b): Output pulses from the compensating filter.

A.4.4 Chirp compensation with a free-space interferometer

Several approaches have been proposed to generate uniform trains of individual pulses from portions of an OFCG spectrum, for example, using a properly designed compensating filter which is presented in the previous section, or using a line-by-line pulse shaper which is presented in [Jiang 07]. These means rely either on intensity filtering or complex line-by-line phase filtering. However, these approaches generally result in a loss of power through filtering and the generation of longer pulses than should be possibly given from the inherent spectral bandwidth of the OFCG. In the following experiment, I will investigate a neat and simple solution based on passing the comb output through a delay-line interferometer. By doing this, a uniform train of close to transform-limited pulses (with respect to the full source bandwidth) at twice the driving frequency of the OFCG is generated without incurring significant filtering losses. The electric fields of the pulse pairs generated at the output of the OFCG are given by Eq. A.10. We can see that it is possible to cancel the chirp of the pulses by overlapping them in time with a delay-line interferometer, yielding:

$$E(t) \approx \frac{T}{1 - i4\beta F f_m t} + \frac{T}{1 + i4\beta F f_m t} = \frac{2T}{1 + (4\beta F f_m t)^2} \tag{A.13}$$

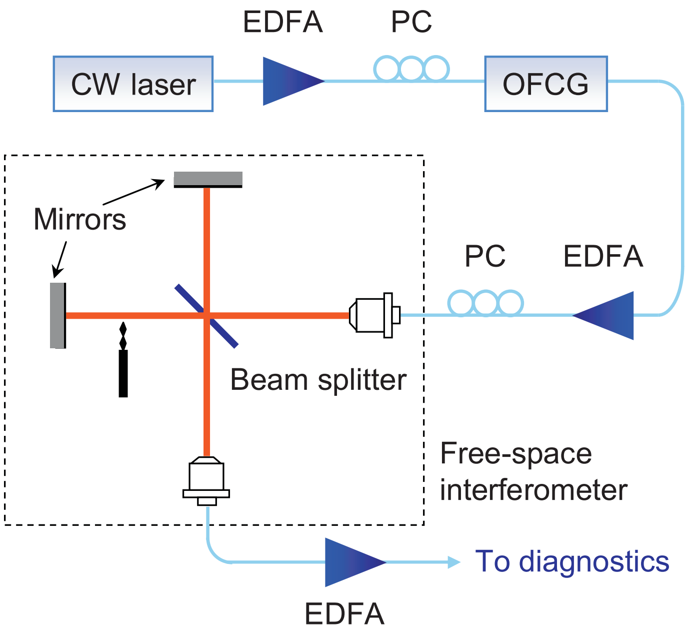

Figure A.13: Experimental set-up to cancel the chirp of the OFCG output using an delay-line interferometer.

As shown in Fig. A.13, the experimental set-up was constructed to use a free-space delay line interferometer to overlap the pairs of pulses in time and obtain a train of transform-limited pulses at the output which occupy the full spectrum of the OFCG. A CW laser operating at 1556.5 nm was fed to the OFCG driven at $f_m = 10$ GHz.

To cancel the chirp of the pulse pairs generated by the OFCG, the signal was fed to a free-space delay line interferometer, based on a Michelson configuration, with its two mirrors placed on 1-D translation stages for precise control of the relative delay between the two arms. The condition described in Eq. A.13 above is obtained by carefully adjusting the position of the mirrors to yield a precise 50 ps (or $mT_m \pm 50$ ps) delay between the two paths, resulting in a spectrogram as shown in Fig. A.14. When this is achieved, all autocorrelation peaks at 0 and ±50 ps time delay have the same intensity, denoting a uniform pulse train (Fig. A.15(a)), whereas the pulse width contracts to $\sim$ 0.62 ps (see Fig. A.16, blue dashed line, assuming a Lorentzian pulse, the pulse width is half of the autocorrelation width for a Lorentzian pulse shape). An observation of the spectrum reveals that instead of consisting of two distinct halves with a phase difference between the two, it now exhibits a broadband 20 GHz spectrum with every second of the original 10 GHz spectral lines suppressed by more than $\sim$ 10 dB, as shown in Fig. A.17 (this is in contrast to the spectrum measured without the interferometer, which exhibits 10 GHz spectral lines as shown in Fig. A.5). Detection of the pulses with a fast photoreceiver reveals a continuous and noise-free 20 GHz pulse train, as shown on the DCA trace in Fig. A.15(b).

The practicality and long term performance of the source is somewhat compromised by the use of a free-space interferometer in these proof of principle experiments. However, replacing this with a compact DPSK demodulator would greatly enhance its long term stability.

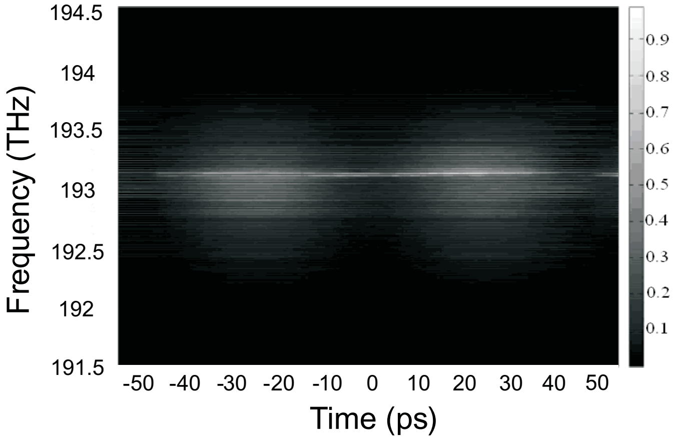

FIGURE A.14: Spectrograms measured at the output of the interferometer (delay=50 ps)

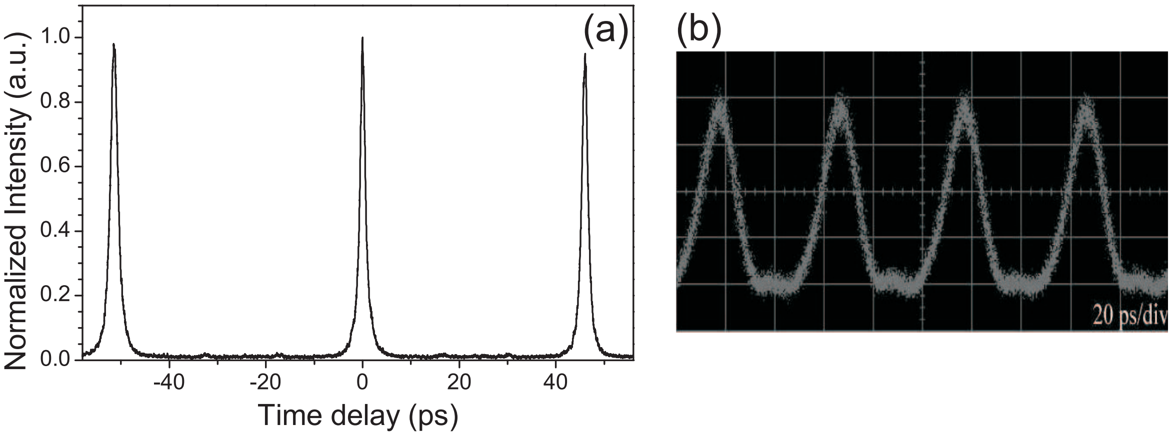

FIGURE A.15: (a): Autocorrelation trace after delay line interferometer. (b): DCA trace of after delay line interferometer.

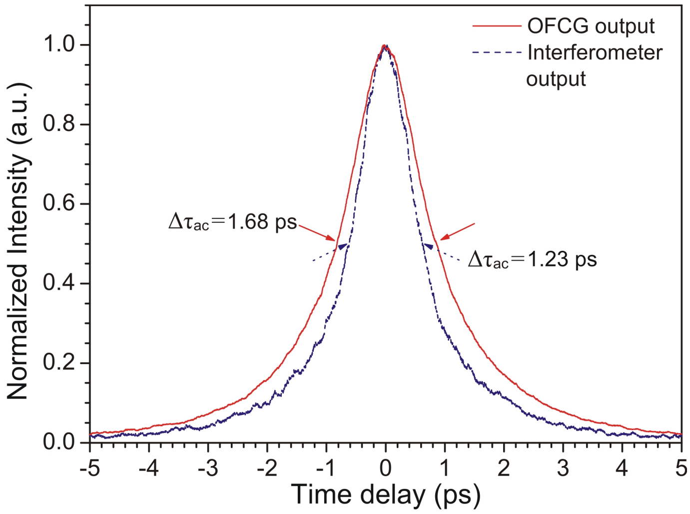

Figure A.16: Autocorrelation traces showing the reduction in pulse width after the free-space interferometer (measurements of the autocorrelation widths are marked on the plot).

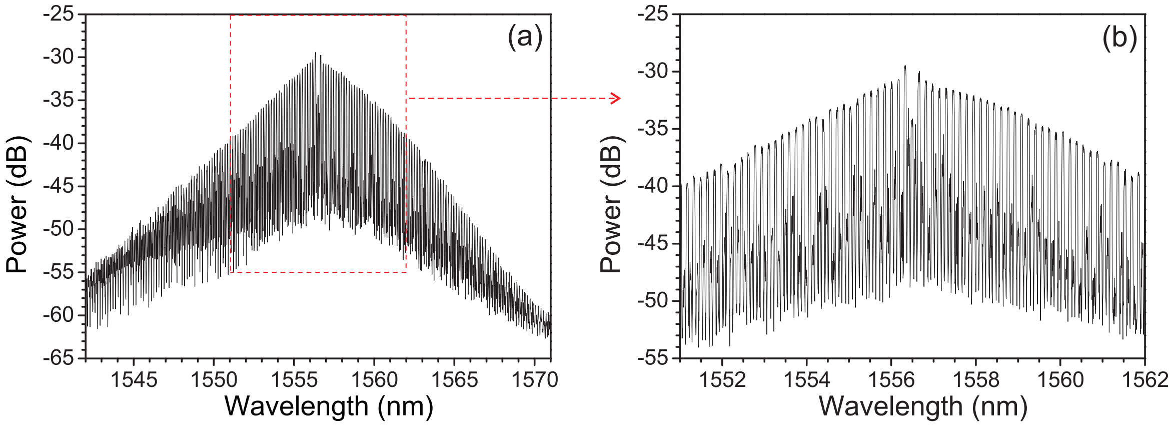

Figure A.17: (a): Measured spectrum after delay line interferometer (resolution = 0.05nm). (b): Enlarged spectrum.

A.5 Conclusion

In this chapter, I theoretically analysed the working mechanism of the OFCG in both the frequency and the time domain. I experimentally investigated the intensity and phase characteristics of pulses generated from a commercial OFCG and filtered with a wavelength and bandwidth tunable filter. The experimental results agree well with the simulation and verify the two models. In addition, I demonstrated the combination of the OFCG and a wavelength- and bandwidth-tunable spectral filter allows the generation of a high quality and ultra-stable 10 GHz pulse train with pulse widths tunable from 1.6 to 10.5 ps. I also proposed two approaches to compensate for the intrinsic chirp of pulses generated from the OFCG. A filter design that compensates for the slope of the OFC is able to yield a periodic train of identical pulses with pulse width of 1.5 ps at a 10 GHz repetition rate. Finally, using a free-space delay line interferometer to overlap the pulse pairs generated at the output of an OFCG, a continuous, uniform and noise-free pulse train at a 20 GHz repetition rate with pulse width of $\sim$ 0.62 ps is obtained. Unlike previous demonstrations, this technique does not resort to any type of phase [Jiang 07], or amplitude filtering [Ng 08], which will restrict the overall bandwidth of the signal. Additionally, this process allows the whole frequency comb spectrum to be treated as a single entity, rather than in two halves, thereby greatly enhancing its applicability. Replacing the free-space interferometer with a compact, pigtailed alternative, such as a commercial DPSK demodulator, could greatly enhance the practicality of the source, whereas suitable dispersion compensation would help reduce the observed pulse width even further.

References

[Durand 96] E. Durand, T. Saitoh, M. Kourogi & M. Ohtsu, *0.4-THz frequency offset locking between two optical frequency combs*, Ieee Photonics Technology Letters, vol. 8, no. 1, pages 163–165, January 1996.

[Jiang 07] Z. Jiang, D. E. Leaird, C. B. Huang, H. X. Miao, M. Kourogi, K. Imai & A. M. Weiner, *Spectral line-by-line pulse shaping on an optical frequency comb generator*, Ieee Journal of Quantum Electronics, vol. 43, no. 11-12, pages 1163–1174, November 2007.

[Kato 05] M. Kato, K. Fujiura & T. Kurihara, *Generation of a superstable Lorentzian pulse train with a high repetition frequency based on a Fabry-Perot resonator integrated with an electro-optic phase modulator*, Applied Optics, vol. 44, no. 7, pages 1263–1269, March 2005.

[Kobayashi 72] T. Kobayashi, T. Sueta, Y. Matsuo & Y. Cho, *High-repetition-rate Optical Pulse-generator Using A Fabry-perot Electrooptic Modulator*, Applied Physics Letters, vol. 21, no. 8, pages 341–&, 1972.

[Kourogi 93] M. Kourogi, K. Nakagawa & M. Ohtsu, *Wide-span Optical Frequency Comb Generator For Accurate Optical Frequency Difference Measurement*, Ieee Journal of Quantum Electronics, vol. 29, no. 10, pages 2693–2701, October 1993.

[Kourogi 94] M. Kourogi, T. Enami & M. Ohtsu, *A Monolithic Optical Frequency Comb Generator*, Ieee Photonics Technology Letters, vol. 6, no. 2, pages 214–217, February 1994.

[Kourogi 95] M. Kourogi, B. Widiyatomoko, Y. Takeuchi & M. Ohtsu, *Limit of Optical-frequency Comb Generation Due To Material Dispersion*, Ieee Journal of Quantum Electronics, vol. 31, no. 12, pages 2120–2126, December 1995.

[Kourogi 96] M. Kourogi, T. Enami & M. Ohtsu, *A coupled-cavity monolithic optical frequency comb generator*, Ieee Photonics Technology Letters, vol. 8, no. 12, pages 1698–1700, December 1996.

[Kourogi 01] M. Kourogi & M. Ohtsu. *Past, Present, and future of optical comb generation.*, 2001.

[Kovacich 00] R. P. Kovacich, U. Sterr & H. R. Telle, *Short-pulse properties of optical frequency comb generators*, Applied Optics, vol. 39, no. 24, pages 4372–4376, August 2000.

[Macfarlane 96] G. M. Macfarlane, A. S. Bell, E. Riis & A. I. Ferguson, *Optical comb generator as an efficient short-pulse source*, Optics Letters, vol. 21, no. 7, pages 534–536, April 1996.

[Musha 04] M. Musha, A. Ueda, M. Horikoshi, K. Nakagawa, M. Ishiguro, K. Ueda & H. Ito, *A highly stable mm-wave synthesizer realized by mixing two lasers locked to an optical frequency comb generator*, Optics Communications, vol. 240, no. 1-3, pages 201–208, October 2004.

[Ng 08] Trina T. Ng, Sheng Liu, Periklis Petropoulos & David J. Richardson, *A filtered optical frequency comb generator as a stable and tunable short pulse source*, European Conference on Optical Communication (ECOC) 2008, Brussels, Belgium, 2008.

[Saitoh 98] T. Saitoh, S. Mattori, S. Kinugawa, K. Miyagi, A. Taniguchi, M. Kourogi & M. Ohtsu, *Modulation characteristic of waveguide-type optical frequency comb generator*, Journal of Lightwave Technology, vol. 16, no. 5, pages 824–832, May 1998.

[Slyusarev 97] S. Slyusarev, T. Ikegami, S. Ohshima & E. Sakuma, *Frequency measurement of accurate sidebands of an optical frequency comb generator*, Optics Communications, vol. 135, no. 4-6, pages 223–226, February 1997.

[Volk 08] Tatyana Volk & Manfred Wohlecke, Lithium niobate-defects, photorefraction and ferroelectric switching, Springer-Verlag Berlin Heidelberg, 2008.

Matlab code for pulse evolution in a PPLN waveguide

```
clc; clear all; close all;

i=sqrt(-1);
pi=3.1415926535;
c = 3e5;                                    %km/s

T = -50e-12:100e-12/2048:50e-12-100e-12/2048;   % time window
dt = 100e-12/2048;
lambda = 1550;                              % wavelength (nm)

ln=1;
i=sqrt(-1);
Po=0.015*1.4; %input pwr in watts
alpha=0.0003; % Fiber loss value in dB/km

to=100000000*0.62e-12; %initial pulse width in second
C=0; %Input chirp parameter for first calculation
b2=-0.1e-24; %2nd order disp. (s2/m)
Ld=(to^2)/(abs(b2)); %dispersion length in meter
pi=3.1415926535;
Ao=sqrt(Po); %Amplitude

%---------------------------------------------------------
tau =- 50e-12:100e-12/2048: 50e-12-100e-12/2048;%  dt=t/to
dt=100e-12/2048;
rel_error=1e-5;
h=1000;% step size

z=Ld;
   u=Ao*exp(-((1+i*(-C))/2)*(tau/to).^20);%page#47 G.P.AGrawal
   figure(11)
   plot(abs(u),'r');
   title('Input Pulse'); xlabel('Time'); ylabel('Amplitude');
```

```

tos=1000000000000*0.62e-12; %initial pulse width in second
Pos=0.008*1.4;
Aos=sqrt(Pos); %Amplitude
us=Aos*exp(-((1+i*(-C))/2)*(tau/tos).^2);%page#47 G.P.AGrawal

figure(2)
plot(T,(abs(u)/max(abs(u))).^2);

% PPLN PARAMETERS
L = 0.03;                                    % m

alpha_dB = 30;                          % dB/m
alpha = alpha_dB/4.343;                  % per m
alpha_dBSH = 60;                          % dB/m
alphaSH = alpha_dBSH/4.343;          % per km
%   CALCULATIONS

l = max(size(u));

%   PULSE PROPAGATION --- SPLIT STEP FOURIER METHOD
step = 0.0001;                                          % step size (m)

jj = step;

df = 1/dt;
dw = ((2*pi)*df)/l;
wref=2*pi*3*10^8/(1550*10^(-9));
w=(l/2:-1:-l/2+1)*dw;
w=fftshift(w);
spectrum1=fft(u);                      %Pulse spectrum
spectrum2=fft(rand(1,length(u))/10000000000);
spectrum3=fft(us);                      %Pulse spectrum
spectrum4=fft(rand(1,length(u))/10000000000);

figure(10)
plot([1:length(u)],rand(1,length(u))/10000000000)

df = 1/dt;
dl=((df*(lambda*1e-9)^2)/3e8)/l;
lam=(-1*l/2:1:l/2-1)*dl;
lamr=(lambda*1e-9)+lam;

u1=1.318089*10^8;
u2=1.37386*10^8;
u3=1.318089*10^8;
u4=1.318089*10^8;
```

```

beta1=1/u1;
beta21=1/u2;
beta31=1/u3;
beta41=1/u4;

ln=1;
x=0;

kk1=7.3932e-014;
kk2=7.3932e-014;
kk3=7.3932e-014;
kk4=7.3932e-014;

for jj = step:step:L
spectrum1=spectrum1.*exp(-alpha/2*(step/2)) ;
spectrum2=spectrum2.*exp(-alphaSH/2*(step/2)+i*((beta1-beta21)*w)*(step/2)) ;
spectrum3=spectrum3.*exp(-alpha/2*(step/2)) ;
spectrum4=spectrum4.*exp(-alpha/2*(step/2)) ;
A1=ifft(spectrum1);
A2=ifft(spectrum2);
A3=ifft(spectrum3);
A4=ifft(spectrum4);

k1=i*wref*kk1*(conj(A1).*A2)*exp(i*jj*x);
k2=i*wref*kk1*(conj(A1)+step/2*k1).*(A2+step/2*k1)*exp(i*(jj+step/2)*x);
k3=i*wref*kk1*(conj(A1)+step/2*k2).*(A2+step/2*k2)*exp(i*(jj+step/2)*x);
k4=i*wref*kk1*(conj(A1)+step*k3).*(A2+step*k3)*exp(i*(jj+step)*x);

A1=A1+step/6*(k1+2*k2+2*k3+k4);

k21=i*wref*kk2*conj(A1).*A1*exp(-i*jj*x)+2*i*wref*kk2*(A4).*A3*exp(-i*jj*x);
k22=i*wref*kk2*(conj(A1)+step/2*k21).*(A1+step/2*k21)*exp(-i*(jj+step/2)*x)+2*i*wref*kk2
    *((A4)+step/2*k21).*(A3+step/2*k21)*exp(-i*(jj+step/2)*x);
k23=i*wref*kk2*(conj(A1)+step/2*k22).*(A1+step/2*k22)*exp(-i*(jj+step/2)*x)+2*i*wref*kk2
    *((A4)+step/2*k22).*(A3+step/2*k22)*exp(-i*(jj+step/2)*x);
k24=i*wref*kk2*(conj(A1)+step*k23).*(A1+step*k23)*exp(-i*(jj+step)*x)+2*i*wref*kk2*((A4)
    +step*k23).*(A3+step*k23)*exp(-i*(jj+step)*x);

A2=A2+step/6*(k21+2*k22+2*k23+k24);

k31=i*wref*kk3*conj(A4).*A2*exp(-i*jj*x);
k32=i*wref*kk3*(conj(A4)+step/2*k31).*(A2+step/2*k31)*exp(-i*(jj+step/2)*x);
k33=i*wref*kk3*(conj(A4)+step/2*k32).*(A2+step/2*k32)*exp(-i*(jj+step/2)*x);
k34=i*wref*kk3*(conj(A4)+step*k33).*(A2+step*k33)*exp(-i*(jj+step)*x);

A3=A3+step/6*(k31+2*k32+2*k33+k34);
```

```

k41=i*wref*kk4*conj(A3).*A2*exp(-i*jj*x);
k42=i*wref*kk4*(conj(A3)+step/2*k41).*(A2+step/2*k41)*exp(-i*(jj+step/2)*x);
k43=i*wref*kk4*(conj(A3)+step/2*k42).*(A2+step/2*k42)*exp(-i*(jj+step/2)*x);
k44=i*wref*kk4*(conj(A3)+step*k43).*(A2+step*k43)*exp(-i*(jj+step)*x);

A4=A4+step/6*(k41+2*k42+2*k43+k44);

spectrum1=fft(A1);
spectrum2=fft(A2);
spectrum3=fft(A3);
spectrum4=fft(A4);
spectrum1=spectrum1.*exp(-alpha/2*(step/2)) ;
spectrum2=spectrum2.*exp(-alphaSH/2*(step/2)+i*((beta1-beta21)*w)*(step/2)) ;
spectrum3=spectrum3.*exp(-alpha/2*(step/2)) ;
spectrum4=spectrum4.*exp(-alpha/2*(step/2)) ;
op_pulse(ln,:)=abs(A1);%saving pulses at all intervals

op_pulse2(ln,:)=abs(A2);

op_pulse3(ln,:)=abs(A3);

op_pulse4(ln,:)=abs(A4);

XXX(ln)=max(abs(A1));

ln=ln+1;
end

figure(500);
[X,Y]=meshgrid([step:step*2:L]*100000,tau*10^(12));
Z=(op_pulse(1:2:ln-1,:)').^2*1000;
plot3(X,Y,Z);
% title('Pulse Evolution');
ylabel('Time (ps)'); xlabel('Distance (cm)'); zlabel('Power (mW)');

figure(501);
[X,Y]=meshgrid([step:step*2:L]*100000,tau*10^(12));
Z=(op_pulse2(1:2:ln-1,:)').^2*1000;
plot3(X,Y,Z);
% title('Pulse Evolution');
ylabel('Time (ps)'); xlabel('Distance (cm)'); zlabel('Power (mW)');

figure(502);
[X,Y]=meshgrid([step:step*2:L]*100000,tau*10^(12));
Z=(op_pulse3(1:2:ln-1,:)').^2*1000;
plot3(X,Y,Z);
```

```
% title('Pulse Evolution');
ylabel('Time (ps)'); xlabel('Distance (cm)'); zlabel('Power (mW)');

figure(503);
[X,Y]=meshgrid([step:step*2:L]*100000,tau*10^(12));
Z=(op_pulse4(1:2:ln-1,:)').^2*1000;
plot3(X,Y,Z);
% title('Pulse Evolution');
ylabel('Time (ps)'); xlabel('Distance (cm)'); zlabel('Power (mW)');
```

List of Publications

1. **S. Liu**, J. Lee, J. Kakande, F. Parmigiani, K. Gallo, P. Petropoulos, D. J. Richardson, "Phase-regenerative wavelength conversion in periodically poled lithium niobate waveguides," Optics Express, Vol. 19, Issue 12, pp. 11705-11715, 2011.

2. J. Lee, **S. Liu**, K. Gallo, P. Petropoulos, D. J. Richardson, "Analysis of acceptable spectral windows of quadratic cascaded nonlinear processes in a periodically poled lithium niobate waveguide," Optics Express, Vol. 19, Issue 9, pp. 8327-8335, 2011.

3. **S. Liu**, Lee, J. Kakande, F. Parmigiani, K. Gallo, P. Petropoulos, D. J. Richardson, "Phase-sensitive wavelength conversion based on cascaded quadratic processes in periodically poled lithium niobate waveguides," OFC 2011, Los Angeles, Mar 2011.

4. **S. Liu**, K. J. Lee, F. Parmigiani, K. Gallo, P. Petropoulos, D. J. Richardson, "Retiming of short pulses using quadratic cascading in a periodically poled lithium niobate waveguide," IEEE Photonics Technology Letters, vol.23, pp.94-96, 2011.

5. S. Dasgupta, F. Poletti, **S. Liu**, P. Petropoulos, D. J. Richardson, "Modelling Brillouin gain spectrum of solid and microstructured optical fibers using finite element method," Journal of Lightwave Technology, vol.29, pp.22-29, 2011.

6. **S. Liu**, K. J. Lee, K. Gallo, P. Petropoulos, D. J. Richardson, "Elimination of the chirp of optical pulses through cascaded nonlinearities in periodically poled lithium niobate waveguides," Optics Letters, vol.35, pp.3724-3726, 2010.

7. K. J. Lee, **S. Liu**, K. Gallo, P. Petropoulos, D. J. Richardson, "Elimination of the chirp of optical pulses through cascaded nonlinearities in periodically poled lithium niobate waveguides," European Conference on Optical Communication (ECOC) 2010, Turin, Sep 2010.

8. M. Ghandour, **S. Liu**, D. K. Hunter, D. Simeonidou, R. Nejabati, P. Petropoulos "Ultra high performance media multicasting scheme over wavelength-routed networks," OFC 2010, San Diego, JThA40, Mar 2010.

9. P. Petropoulos, **S. Liu**, K. J. Lee, F. Parmigiani, K. Gallo, D. J. Richardson, "Processing of telecommunications signals using periodically poled lithium niobate waveguides," ICTON 2010, Munich, Mo.D2,2, Jul 2010 (Invited).

10. K. J. Lee, **S. Liu**, F. Parmigiani, M. Ibsen, P. Petropoulos, K. Gallo, D. J. Richardson, "OTDM to WDM format conversion based on quadratic cascading in a periodically poled lithium niobate waveguide," Optics Express, vol.18(10), pp.10282-10288, 2010.

11. K. J. Lee, **S. Liu**, F. Parmigiani, P. Petropoulos, D. J. Richardson, K. Gallo, "All-optical pulse retiming based on quadratic cascading in a periodically poled lithium niobate waveguide," Nonlinear Photonics, Karlsruhe, Germany, NMB5, Jun 2010.

12. **S. Liu**, K. J. Lee, F. Parmigiani, M. Ibsen, P. Petropoulos, D. J. Richardson, K. Gallo, "OTDM to WDM format conversion based on cascaded SHG/DFG in a single PPLN waveguide," OFC/NFOEC 2010, San Diego, OWF4, Mar 2010.

13. F. Parmigiani, K. J. Lee, **S. Liu**, J. Kakande, P. Petropoulos, K. Gallo, D. J. Richardson, "Phase sensitive amplification based on cascaded SHG/DFG process in a periodically poled lithium niobate waveguide," Institute of Physics Meeting, London, Sep 2009.

14. K. J. Lee, F. Parmigiani, **S. Liu**, J. Kakande, P. Petropoulos, K. Gallo, D. J. Richardson, "Phase sensitive amplification based on quadratic cascading in a periodically poled lithium niobate waveguide," Optics Express, vol.17(22), pp.20393-20400, 2009.

15. **S. Liu**, T. N. Ng, D. J. Richardson, P. Petropoulos, "An optical frequency comb generator as a broadband pulse source," OFC 2009, San Diego, Mar 2009.

16. T. T. Ng, **S. Liu**, P. Petropoulos, and D. J. Richardson, "A filtered optical frequency comb generator as a stable and tuneable short pulse source," European Conference on Optical Communication (ECOC) 2008. Tu.3.D.1, 2008.